

修士論文

Formation and evolution of star clusters and galaxies
in the early Universe

宇宙最初期における星団形成と輝線銀河進化

2023年1月

東京大学大学院理学系研究科物理学専攻

仲里佑利奈

Abstract

Recent observations by Atacama Large Millimeter/ submillimeter Array (ALMA) and James Webb Space Telescope (JWST) have revealed the infant Universe the first billion years after the BigBang. According to the standard Λ CDM model, small density fluctuations of matter grow hierarchically and form small halos with masses of $10^6 M_{\odot}$. The cosmic primordial gas cools and condenses inside the dark matter halos and starts the first star formation at $z \sim 30 - 20$. Massive stars with no heavy elements are thought to be formed then. Such massive stars end their lives in a few million years, and release metals into the inter-stellar medium. Metal-enriched gases bear the second generation of stars and stellar clusters, which finally assemble to form galaxies. Galaxies experience mergers and active star formation, and grow in mass by $z \sim 6$. ALMA and JWST can observe such massive high-redshift galaxies and the latest JWST observation reports several galaxy candidates at $z > 10$. It is urgent to develop theoretical models to be compared with the recent observation.

In this thesis, we aim to reveal formation of star clusters in the early Universe and chemical evolution of high-redshift galaxies which are observable by ALMA and JWST. First, we perform numerical simulations and propose a new formation path of star clusters at $z \sim 20 - 15$ theoretically. Next, we calculate the emission lines from simulated galaxies at $z \sim 9 - 6$ and compare them with the observational results. We discuss in detail the chemical evolution of high-redshift galaxies.

We first study the formation processes of star clusters by considering relative streaming motions between baryons and dark matter. The relative motion is super-sonic and has significant impacts on the formation of the first gravitationally bounded objects around $z \sim 30$. The relative motion can cause a physical offset between the baryon and the dark matter over-densities, which leads to the formation of gas-rich objects collapsing outside their parent dark matter halos. We call them "Supersonically Induced Gas Objects (SIGOs)" and expect dark matter deficient SIGOs to be the progenitors of globular clusters. In order to follow the formation of SIGOs in primordial gas clouds, we run three-dimensional cosmological simulations incorporating the aforementioned relative motions and non-equilibrium chemical reactions. We identify particular gas clouds that are located outside dark matter halos owing to the relative velocities and contract by molecular hydrogen cooling, which is the most important cooling process in a primordial gas. These SIGOs finally become Jeans unstable with the corresponding mass of $\sim 10^5 M_{\odot}$, which is consistent with that of globular clusters.

Next, we study the chemical evolution of high-redshift galaxies which are observable with strong emission lines from doubly ionized oxygen. Recent observations by James Webb Space Telescope discovered a number of high-redshift galaxies, including the most distant galaxy candidates at $z > 10$. JWST and ALMA can observe rest-frame optical and far-infrared [OIII] emission lines, respectively, and combing these multi lines allows probing the physical conditions of inter-stellar medium. We use the FirstLight simulation suite, which provides outputs of 62 high-resolution, zoom-in galaxy simulations. We devise a physical model of HII regions and calculate spatially resolved [OIII] line emission. We show that massive galaxies with stellar masses of

$M_\star > 10^9 M_\odot$ chemically evolve rapidly to $z = 9$. Young stellar populations in the star-forming galaxies boost the [OIII] line emission, rendering the ratio of line luminosity to star formation rate larger than that for low-redshift galaxies, which is consistent with recent observations. Measuring the flux ratios of rest-frame optical and far-infrared lines allows us to estimate the physical conditions such as density and metallicity of the star-forming gas in high-redshift [OIII] emitters.

Contents

1	Cosmic Structure Formation	1
1.1	The Standard Cosmological Model	1
1.1.1	The Friedmann–Lemaître–Robertson–Walker metric	1
1.1.2	Friedmann Equation	2
1.1.3	Equation of State of the Universe	3
1.1.4	Cosmological Parameter	4
1.1.5	Redshift	6
1.2	Structure formation	7
1.2.1	Linear-growth of density fluctuations	8
1.2.2	Non-linear model for spherical collapse	9
1.2.3	Virial equilibrium in a spherical model	10
2	Formation of the First Stars	12
2.1	The minimum collapse mass	12
2.2	Physics of self-gravitating gas	16
2.2.1	Virial theorem	16
2.2.2	Jeans instability	18
2.2.3	Runaway collapse	20
2.2.4	Critical Γ at cloud collapse	21
2.3	The gas dynamics in primordial gas	23
2.3.1	H_2 chemistry	23
2.3.2	cooling process in primordial gas	24
2.4	Stellar feedback to accretion	25
2.5	Mass distribution of Population III stars	26
2.5.1	Life pathways of Pop III stars	27
2.5.2	Remained uncertainty of Pop III mass distribution	28
2.6	Chapter Summary	28
3	Formation and evolution of Supersonically Induced Gas Objects	29
3.1	Stream Velocity	29
3.1.1	Growth of small-scale structure including stream velocity	29
3.1.2	Numerical simulations including stream velocity	32
3.1.3	Supersonically Induced Gas Objects (SIGOs)	33
3.2	Methods	35
3.2.1	Cosmological simulation	35
3.2.2	Chemistry and cooling	35
3.2.3	Definition of SIGOs	36
3.2.4	High-resolution simulation with smaller Box Size	37

3.3	Result	38
3.3.1	Density distribution for each run	38
3.3.2	Evolution of SIGO (S1)	39
3.3.3	Comparison with each run	41
3.3.4	High-resolution simulation with refinement	43
3.3.5	Caveats	45
3.3.6	Comparison with the result of Schauer et al. (2021a)	46
3.4	Statistics of SIGOs	46
3.4.1	SIGOs identified at $z = 25$ in Run 2vH2	47
3.5	Collapse of SIGO candidate clumps	49
3.5.1	Case F1: Hosted by a nearby large DM halo	52
3.5.2	Case F2: Hosted by DM halos through merger	53
3.5.3	Case S1 : Star-forming SIGOs	54
3.6	Star formation in SIGOs	54
3.7	Discussion and summary	56
4	Line emission from galaxies	57
4.1	Chemical evolution of galaxies	57
4.2	Star-forming regions in a galaxy	58
4.2.1	HII regions	59
4.2.2	Photo dissociation regions (PDR)	61
4.2.3	Molecular gas regions	62
4.3	Radiation processes	62
4.3.1	Selection rules and forbidden lines	62
4.3.2	Collisionally excited line emission and critical density	62
4.4	Nebula diagnostics by line ratios	66
4.4.1	T_e estimation	67
4.4.2	Density estimation	69
4.4.3	Metallicity estimation	73
4.5	Observation of high-redshift galaxies	75
4.5.1	Dropout method	75
4.5.2	Detection of $z \sim 6 - 9$ galaxies by ALMA	75
4.5.3	Latest observation by JWST	76
4.5.4	Synergy of JWST and ALMA	79
5	Simulations of high-redshift [OIII] emitters: Chemical evolution and multi-line diagnostics	81
5.1	FirstLight simulation	81
5.1.1	Subgrid physics	83
5.1.2	Definition of notation	84
5.2	Line emissivity calculation	84
5.2.1	Escape fraction f_{esc}	85
5.2.2	Ionization parameter U	86
5.2.3	Ionizing photon rate Q from a populatioin synthesis model	86
5.2.4	CLOUDY calculation	88
5.2.5	$H\beta$ luminosity calculation in case B	89
5.3	Results	89
5.4	$L_{[\text{OIII}]}$ vs SFR	89

5.4.1	Comparison to other simulations	92
5.5	The mass-metallicity relation	93
5.6	Far-IR/optical line ratios	97
5.7	Mock data for NIRSpec observation	100
5.8	Discussion	102
6	Summary and future prospects	104
	Appendix	107
A	Primordial Chemical Reactions	107
B	Subgrid Models in FirstLight	109
B.1	Radiative cooling	110
B.2	Subgrid physics	110
B.2.1	Star formation	110
B.3	Stellar feedback	111
B.4	Metal enrichment	112
B.5	Stellar mass loss	112
B.6	Runaway stars	113
B.7	Radiative Pressure Feedback	113
B.8	Other effects	114
	Appendix	114
C	stellar mass - SFR relationship	115
D	Flux density calculation	118
D.1	Surface flux density calculation	118
D.2	NIRSpec IFU	120
D.2.1	Spectrum in a unit of $[\text{erg/s/cm}^2/\text{\AA}]$	120
D.2.2	Flux density in a unit of MJy/sr	121
D.2.3	Conversion of kpc to arcsec	121
	Acknowledgement	123
	Bibliography	125

Chapter 1

Cosmic Structure Formation

1.1 The Standard Cosmological Model

To describe the Universe, we need to treat four-dimensional space-time in terms of general relativity.

1.1.1 The Friedmann–Lemaître–Robertson–Walker metric

Infinitesimal interval ds^2 is defined at each point in a local inertial frame as

$$ds^2 = g_{\mu\nu}dx^\mu dx^\nu = g_{00}c^2dt^2 + 2cg_{0i}dtdx^i + g_{ij}dx^i dx^j, \quad (\mu, \nu = 0, 1, 2, 3, \quad i, j = 1, 2, 3) \quad (1.1)$$

where dx^μ is an infinitesimal coordinate displacement of four-dimensional spacetime and $g_{\mu\nu}$ is a metric tensor. Let us assume that the universe is isotropic and homogeneous at large length-scales of over tens of mega-parsec, and there is no specific places. This assumption is called the cosmological principle. From the principle, t and x are orthogonal and the metric tensor satisfies $g_{i0} = g_{0i} = 0$. The proper time for a fundamental observer is the same as the cosmic time and ds^2 is expressed as $ds^2 = -c^2dt^2$ in the case of $dx^i = 0$. Then, we obtain $g_{00} = -1$. The uniform assumption requires that space expands (contracts) with time and the space metric is expressed as $g_{ij} = a(t)\gamma_{ij}$. Here, $a(t)$ is scale factor and represents the relative size of the universe at time t . According to the above description, ds^2 is written as

$$ds^2 = -c^2dt^2 + a(t)\gamma_{ij}dx^i dx^j. \quad (1.2)$$

Let us work with polar coordinates, where the angular direction $d\phi$, $d\theta$ and radial direction dr are orthogonal. We can separate those variables as in the following,

$$\gamma_{ij}dx^i dx^j = W(r)dr^2 + r^2(d\theta^2 + \sin^2\theta d\phi^2) \quad (1.3)$$

$$\therefore ds^2 = -c^2dt^2 + a(t)[W(r)dr^2 + r^2(d\theta^2 + \sin^2\theta d\phi^2)]. \quad (1.4)$$

2 Cosmic Structure Formation

In order to derive $W(r)$, we introduce a scalar curvature R , which is calculated as follows,

$$R \equiv R_{\mu}^{\mu} = g^{\alpha\beta} R_{\alpha\beta} \quad (1.5)$$

$$= g^{00} R_{00} + g^{ij} R_{ij} \quad (1.6)$$

$$= -R_{00} + \frac{\gamma_{ij}}{a^2} \left(\tilde{R}_{ij} + \frac{1}{c^2} (a\ddot{a} + 2\dot{a}^2) \gamma_{ij} \right) \quad (1.7)$$

$$= \frac{3}{c^2} \frac{\ddot{a}}{a} + \frac{3}{c^2} \left(\frac{\ddot{a}}{a} + 2 \left(\frac{\dot{a}}{a} \right)^2 \right) + \frac{1}{a^2} \gamma_{ij} \tilde{R}_{ij} \quad (1.8)$$

$$= \frac{6}{c^2} \frac{\ddot{a}}{a} + \frac{6}{c^2} \left(\frac{\dot{a}}{a} \right)^2 + \frac{1}{a^2} \left[\frac{\tilde{R}^{rr}}{W(r)} + \frac{\tilde{R}^{\theta\theta}}{r^2} + \frac{\tilde{R}^{\phi\phi}}{r^2 \sin^2 \theta} \right] \quad (1.9)$$

$$= \frac{6}{c^2} \frac{\ddot{a}}{a} + \frac{6}{c^2} \left(\frac{\dot{a}}{a} \right)^2 + \frac{1}{a^2} \left[\frac{W'}{rW^2} + \frac{2}{r^2} \left(\frac{rW'}{2W^2} + 1 - \frac{1}{W} \right) \right]. \quad (1.10)$$

Here we define two notations for differentiation, $\cdot \equiv \frac{d}{dt}$ and $' \equiv \frac{d}{dr}$. Ricci tensor for γ_{ij} is denoted \tilde{R}_{ij} . The third term in eq. 1.10 should be independent on place and the term in the square bracket is replaced by introducing constant K ,

$$\frac{2W'}{rW^2} + \frac{2}{r^2} \left(1 - \frac{1}{W} \right) = 6K. \quad (1.11)$$

Solving eq. 1.11, we obtain

$$W(r) = \frac{1}{1 - Kr^2}. \quad (1.12)$$

Thus, the metric for an isotropic and homogeneous universe is given by

$$ds^2 = -c^2 dt^2 + a(t)^2 \left[\frac{dr^2}{1 - Kr^2} + r^2 (d\theta^2 + \sin^2 \theta d\phi^2) \right]. \quad (1.13)$$

This metric is called Friedmann-Lemaitre-Robertson-Walker (FLRW) metric. Spatial curvature K determines the curvature of the universe. The scale factor at the current time is often normalized such that $a(t_0) = 1$.

The two coordinate systems \mathbf{r} and \mathbf{x} with the relation $\mathbf{r} = a(t)\mathbf{x}$ are called proper coordinate and comoving coordinate, respectively. The former system changes with time as the universe expands with $a(t)$, whereas the contribution of cosmic expansion is subtracted for the latter coordinate.

1.1.2 Friedmann Equation

This subsection derives an equation describing the time evolution of $a(t)$ from FLRW metric. Einstein equation is written as,

$$R_{\mu\nu} - \frac{1}{2} g_{\mu\nu} R + \Lambda g_{\mu\nu} = \frac{8\pi G}{c^4} T_{\mu\nu}. \quad (1.14)$$

We consider an ideal fluid¹, and then the energy-momentum tensor is

$$T_{\mu\nu} = (\rho_E + P) u_{\mu} u_{\nu} + P g_{\mu\nu}, \quad (1.15)$$

¹A viscosity term works as an anisotropic effect.

where u_μ, ρ_E, P are four-velocity of matter, energy density of matter, and pressure of matter respectively. Substituting eq. 1.15 into the Einstein equation (eq. 1.14), (0,0) component is written as

$$\frac{3}{c^2} \left(\frac{\dot{a}}{a} \right)^2 + \frac{3}{c^2} \frac{K}{a^2} - \Lambda = \frac{8\pi G}{c^4} \rho_E \quad (1.16)$$

$$\therefore \left(\frac{\dot{a}}{a} \right)^2 = \frac{8\pi G}{3c^2} \rho_E - \frac{Kc^2}{a^2} + \frac{\Lambda c^2}{3}. \quad (1.17)$$

This equation is called Friedmann equation. For (i, j) component, we obtain

$$-\frac{1}{c^2} \left(2\frac{\ddot{a}}{a} + \left(\frac{\dot{a}}{a} \right)^2 + \frac{c^2 K}{a^2} \right) g_{ij} + \Lambda g_{ij} = \frac{8\pi G}{c^4} P g_{ij} \quad (1.18)$$

$$\therefore \frac{\ddot{a}}{a} = -\frac{1}{2} \left[\left(\frac{\dot{a}}{a} \right)^2 + \frac{c^2 K}{a^2} \right] + \frac{\Lambda c^2}{2} - \frac{4\pi G}{c^2} P \quad (1.19)$$

$$\therefore \frac{\ddot{a}}{a} = -\frac{4\pi G}{3c^2} (\rho_E + 3P) + \frac{\Lambda c^2}{3} \quad (\text{Substituting eq. 1.17 into eq. 1.19}) \quad (1.20)$$

$$\therefore \ddot{a} = -\frac{G}{a^2} \frac{4\pi}{3} \left(\frac{\rho_E}{c^2} + \frac{3P}{c^2} - \frac{\Lambda c^2}{4\pi G} \right) a^3. \quad (1.21)$$

Eq. 1.21 can be regarded as the equation of motion for a uniform density sphere with radius a . The first term in RHS is the contribution of mass of matter, the second term shows the effective gravity increases with pressure, and the third term is the cosmological constant representing “repulsion” of the universe.

1.1.3 Equation of State of the Universe

Differentiating Friedmann equation (eq. 1.17) with respect to time t yields

$$\frac{\ddot{a}}{a} = \frac{4\pi G}{3c^2} \left(\frac{a}{\dot{a}} \dot{\rho}_E + 2\rho_E \right) + \frac{\Lambda c^2}{3} \quad (1.22)$$

Comparing this equation with eq. 1.20, we obtain

$$\dot{\rho}_E = -3\frac{\dot{a}}{a}(\rho_E + P), \quad (1.23)$$

which describes the evolution of energy density of matter.

Two equations (1.17, 1.21) contain three variables ρ_E, P, a , and thus another equation, often an equation of state (EoS), is required to be considered. Introducing a constant w , we consider a generalized EoS $P = w\rho_E$. From eq. 1.23, we have

$$\rho_E \propto a(t)^{-3(1+w)}, \quad (1.24)$$

where $w = 0, \frac{1}{3}, -1$ correspond to matter, radiation and dark energy respectively. We consider the following specific cases.

(i) non-relativistic matter with negligible pressure (collisionless particle)

Eq. 1.23 is re-written as

$$\dot{\rho}_E = -3\frac{\dot{a}}{a}\rho \quad \rightarrow \quad \frac{\rho_E}{c^2} = \rho_m \sim mn(t) \propto a^{-3}, \quad (1.25)$$

where ρ_m is mass density of matter and $n(t)$ is number density of matter with mass of m . Eq. 1.25 indicates that the total mass is conserved in a comoving volume.

(ii) relativistic matter (radiation)

Substituting $P = \frac{\rho_E}{3}$ into eq. 1.23, we have

$$\dot{\rho}_E = -4\frac{\dot{a}}{a}\rho_E \quad \rightarrow \quad \rho_E \propto a^{-4} \quad (1.26)$$

This relationship accounts for a constant number density (a^{-3}) and contribution of an increase of wavelength in proportion to the expansion of the universe (a^{-1}).

(iii) cosmological constant

Substituting $P = -\rho_E$ into eq. 1.23, we have

$$\dot{\rho}_E = 0 \quad \rightarrow \quad \rho_E \propto \text{const.} \quad (1.27)$$

Here we define

$$\rho_\Lambda = \frac{\Lambda c^4}{8\pi G}, \quad P_\Lambda = -\frac{\Lambda c^4}{8\pi G}. \quad (1.28)$$

Then, Einstein equation (eq. 1.14) is re-written as

$$R_{\mu\nu} - \frac{1}{2}g_{\mu\nu}R = \frac{8\pi G}{c^4}(T_{\mu\nu} + T_{\Lambda\mu\nu}), \quad (1.29)$$

where $T_{\Lambda\mu\nu}$ is described by ρ_Λ and P_Λ . In this description, cosmological constant can be regarded as *fluid* which satisfies EoS $\rho_\Lambda = -P_\Lambda$.

1.1.4 Cosmological Parameter

We summarize the basic parameters that characterize the isotropic and homogeneous universe model. In the following, the index 0 is used to denote the value at the present epoch.

Hubble constant

Hubble's law is written as

$$v_0 = H_0 d_0, \quad (1.30)$$

where v_0, d_0 are recession velocity and distance from a galaxy respectively. The proportional constant H_0 is called Hubble constant and is defined as $H_0 = \frac{\dot{a}}{a} |_{t=t_0}$, which determines the expansion rate of the present-day universe. The dimensionless Hubble constant h is normalized by 100 km/s/Mpc,

$$h = \frac{H_0}{100 \text{ km/s/Mpc}} \quad (1.31)$$

Density parameter

Friedmann equation (eq. 1.17) at $t = t_0$ is written as

$$H_0^2 = \frac{8\pi G}{3c^2} \rho_{E,0} - Kc^2 + \frac{\Lambda c^2}{3}. \quad (1.32)$$

Consider a flat, matter-dominant universe, i.e., $K = 0, \Lambda = 0, \rho \propto a^{-3}$, which is termed Einstein-de Sitter Universe. Non-relativistic matter accounts for energy density, and then eq. 1.32 becomes

$$\rho_{E,crit0} = \frac{3H_0^2 c^2}{8\pi G} \quad (1.33)$$

$$\therefore \rho_{c0} \equiv \frac{\rho_{E,crit0}}{c^2} = \frac{3H_0^2}{8\pi G} \sim 1.88 \times 10^{-29} h^2 \text{ g/cm}^3, \quad (1.34)$$

where ρ_{c0} is called the critical density.

Next, consider the case where there exist radiation, matter, and a cosmological constant, with non-zero curvature. This universe is called Friedmann universe. Normalizing each energy density by the critical density gives

$$\Omega_{m0} \equiv \frac{\rho_{m0}}{\rho_{c0}} = \frac{8\pi G \rho_{m0}}{3H_0^2 c^2}, \quad \Omega_{r0} \equiv \frac{\rho_{r0}}{\rho_{c0}} = \frac{8\pi G \rho_{r0}}{3H_0^2 c^2}, \quad \Omega_{\Lambda 0} \equiv \frac{\rho_{\Lambda 0}}{\rho_{c0}} = \frac{\Lambda c^2}{3H_0^2}. \quad (1.35)$$

Eq. 1.32 becomes

$$\frac{Kc^2}{H_0^2} = \Omega_{m0} + \Omega_{r0} + \Omega_{\Lambda 0} - 1. \quad (1.36)$$

Thus, Friedmann equation at $t = t$ is re-written by introducing Hubble parameter $H \equiv \frac{\dot{a}}{a} |_{t=t}$, and using the relationship of $\rho_m \propto a^{-3}$ ($\rho_r \propto a^{-4}$);

$$H^2 = H_0^2 \left(\frac{\Omega_{r0}}{a^4} + \frac{\Omega_{m0}}{a^3} + \frac{1 - \Omega_{r0} - \Omega_{m0} - \Omega_{\Lambda 0}}{a^2} + \Omega_{\Lambda 0} \right). \quad (1.37)$$

In the case of flat universe ($K = 0$), density parameter satisfies $\Omega_m + \Omega_r + \Omega_\Lambda = 1$. From eq. 1.25, eq. 1.26, and eq. 1.27, we can derive the evolution of each density parameter as follows,

$$\Omega_r = \frac{\Omega_{r0}}{\Omega_{r0} + \Omega_{m0}a + \Omega_{\Lambda 0}a^4}, \quad \Omega_m = \frac{\Omega_{m0}a}{\Omega_{r0} + \Omega_{m0}a + \Omega_{\Lambda 0}a^4}, \quad \Omega_\Lambda = \frac{\Omega_{\Lambda 0}a^4}{\Omega_{r0} + \Omega_{m0}a + \Omega_{\Lambda 0}a^4} \quad (1.38)$$

Figure 1.1 shows the evolution of density parameters as a function of scale factor $a(t)$.

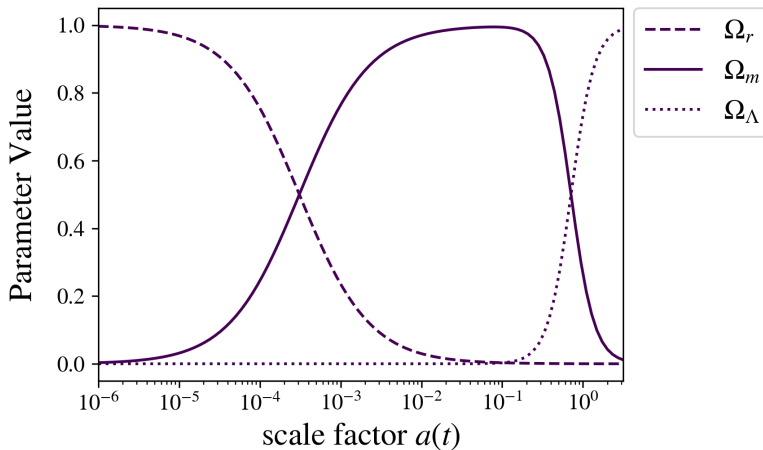


Figure 1.1: Density parameter Ω_r , Ω_m , and Ω_Λ as a function of scale factor $a(t)$. The present-day values are $\Omega_{r0} = 8.05 \times 10^{-5}$, $\Omega_{m0} = 0.27$, $\Omega_{\Lambda0} = 0.73$ (Komatsu et al. 2009).

From Figure 1.1, the matter-dominant phase corresponds roughly to $0.5 < z < 3000$. When redshift is $z \sim 500 - 10$, radiation and dark energy term, and curvature are negligible ($\Omega_{r0} = \Omega_{\Lambda0} = K = 0$). Eq. 1.37 is rewritten as

$$H^2 = H_0^2 \frac{\Omega_{m0}}{a^3} \quad (1.39)$$

$$\therefore a = \left(\frac{3}{2} H_0 t \right)^{2/3} \quad (1.40)$$

Since non-relativistic matter satisfies $\rho \propto a^{-3}$ (eq. 1.25), the energy density at $t = t$ is

$$\rho_E = \rho_m = \frac{\rho_{m0}}{a^3} = \frac{c^2}{6\pi G t^2}. \quad (1.41)$$

1.1.5 Redshift

The wavelength λ of a photon emitted from an object at $t = t$ is stretched by the expansion of the universe. This phenomenon is called redshift. The parameter that evaluates the degree of this wave shift is also called redshift and is defined as

$$z = \frac{\lambda_0 - \lambda}{\lambda}. \quad (1.42)$$

We normalize the current scale factor as $a(t_0) = 1$, and thus a and z have the following relationship:

$$a = \frac{1}{z + 1} \quad (1.43)$$

By estimating the density ratio of the present universe observationally, we can trace the time evolution of expansion or contraction of the universe. However, in order to study the evolution of non-linear structure of the universe, we need to consider the evolution of density perturbation.

1.2 Structure formation

Non-relativistic matter can form large-scale cosmological structures from the initial small fluctuations. This is because relativistic components (radiation) have too large streaming length to proceed sufficient structure formation. Here, we consider the expanding universe as a background spacetime and treat the matter as an ideal fluid. Thus, physical properties of matter can be determined by density ρ , pressure P and velocity \mathbf{v} .

The continuity equation and the fluid equation in the flat, unexpanded spatial coordinate \mathbf{r} are

$$\frac{\partial \rho}{\partial t} + \nabla \cdot (\rho \mathbf{v}) = 0 \quad (1.44)$$

$$\frac{\partial \mathbf{v}}{\partial t} + (\mathbf{v} \cdot \nabla) \mathbf{v} = -\frac{\nabla P}{\rho} - \nabla \phi \quad (1.45)$$

, which consider hydrodynamic pressure and gravitational interaction.

Next, we consider the case of comoving \mathbf{x} . \mathbf{r} and \mathbf{x} has the following relationships,

$$\mathbf{r} = a\mathbf{x} \quad (1.46)$$

$$\dot{\mathbf{r}} = \dot{a}\mathbf{x} + a\dot{\mathbf{x}} \quad (1.47)$$

The first term of the second equation indicates that mater at rest in the comoving coordinate is in motion in the proper coordinate. Thus we can replace $\mathbf{v} \rightarrow \mathbf{v} + \dot{a}\mathbf{x}$ and fluid equations in the comoving coordinate are written as²

$$\begin{aligned} \frac{\partial \rho}{\partial t} + 3\frac{\dot{a}}{a}\rho + \frac{1}{a}\nabla \cdot (\rho \mathbf{v}) &= 0 \\ \frac{\partial \mathbf{v}}{\partial t} + \frac{\dot{a}}{a}\mathbf{v} + \frac{1}{a}(\mathbf{v} \cdot \nabla)\mathbf{v} &= -\frac{1}{a}\nabla \Phi - \frac{1}{a\rho}\nabla P \\ \Delta \Phi &= 4\pi G a^2(\rho_{\text{tot}} - \bar{\rho}_{\text{tot}}) \end{aligned} \quad (1.49)$$

Density and pressure fluctuation $\delta(\mathbf{x}, t)$ and $\delta p(\mathbf{x}, t)$ are defined as follows;

$$\delta(\mathbf{x}, t) = \frac{\rho(\mathbf{x}, t) - \bar{\rho}(t)}{\bar{\rho}(t)} \quad (1.50)$$

$$\delta p(\mathbf{x}, t) = p(\mathbf{x}, t) - \bar{p}(t) \quad (1.51)$$

Thus, eq. 1.49 can be rearranged as

$$\frac{\partial \delta}{\partial t} + \frac{1}{a}\Delta \cdot [(1 + \delta)\mathbf{v}] = 0 \quad (1.52)$$

$$\frac{\partial \mathbf{v}}{\partial t} + \frac{\dot{a}}{a}\mathbf{v} + \frac{1}{a}(\mathbf{v} \cdot \Delta)\mathbf{v} = -\frac{1}{a}\Delta \Phi - \frac{\Delta(\delta p)}{a\bar{\rho}(1 + \delta)}. \quad (1.53)$$

²The gravitatioinal potential in the comoving coordinate is $\Phi = \phi + \frac{1}{2}a\ddot{a}|\mathbf{x}|^2$. Notice that partial differentiation is also replaced:

$$\frac{\partial}{\partial t} \Big|_r \rightarrow \frac{\partial}{\partial t} \Big|_x - \frac{\dot{a}}{a}\mathbf{x} \cdot \nabla_x, \quad \nabla_r \rightarrow \frac{1}{a}\nabla_x \quad (1.48)$$

$$\left(\frac{\partial}{\partial t} + 2\frac{\dot{a}}{a}\right) (1.52) \rightarrow \frac{\partial^2 \delta}{\partial t^2} + \frac{\partial}{\partial t} \left[\frac{1}{a} \Delta \cdot [(1 + \delta)\mathbf{v}] \right] + \frac{2\dot{a}}{a} \frac{\partial \delta}{\partial t} + \frac{2\dot{a}}{a^2} \Delta \cdot [(1 + \delta)\mathbf{v}] = 0 \quad (1.54)$$

$$-\frac{1}{a} \Delta \cdot (1.53) \rightarrow -\frac{1}{a} \frac{\partial}{\partial t} - \frac{\dot{a}}{a^2} \Delta \cdot \mathbf{v} - \boxed{\frac{1}{a^2} \Delta \cdot [(\mathbf{v} \cdot \Delta)\mathbf{v}]} = \frac{1}{a^2} \frac{1}{a^2} \Delta \Phi + \frac{\Delta(\delta p)}{a^2 \bar{\rho}(1 + \delta)} \quad (1.55)$$

1.2.1 Linear-growth of density fluctuations

The third term surrounded by a box is a non-linear term and we neglect it in linear approximation. We get

$$\begin{aligned} \frac{\partial^2 \delta}{\partial t^2} + \frac{2\dot{a}}{a} \frac{\partial \delta}{\partial t} - \frac{\Delta(\delta p)}{a^2 \bar{\rho}} &= \frac{1}{a^2} \Delta \Phi \\ &= \frac{4\pi G}{c^2} (\bar{\rho}_{\text{E,tot}} \delta_{\text{tot}} + 3\delta p_{\text{tot}}), \end{aligned} \quad (1.56)$$

where $\bar{\rho}_{\text{E,tot}}$ is energy density for total fluids and δ_{tot} is the density fluctuation for total fluids. Pressure fluctuations are expressed by using $\delta\rho$ and δS in a linear approximation,

$$\delta p = \left(\frac{\partial p}{\partial \rho} \right)_s \delta \rho + \left(\frac{\partial p}{\partial S} \right)_\rho, \quad (1.57)$$

where S is entropy per unit mass and the speed of sound is defined as $c_s^2 \equiv \left(\frac{\partial p}{\partial \rho} \right)_s$. Thus, eq 1.56 is rewritten as

$$\frac{\partial^2 \delta}{\partial t^2} + \frac{2\dot{a}}{a} \frac{\partial \delta}{\partial t} - \left(4\pi G \bar{\rho} \delta + \frac{c_s^2}{a^2} \Delta \delta \right) = \left(\frac{\partial p}{\partial S} \right)_\rho \frac{\Delta(\delta S)}{a^2 \bar{\rho}} + \frac{4\pi G}{c^2} [\bar{\rho}_{\text{tot}} \delta_{\text{tot}} - \bar{\rho} \delta + 3(\delta p_{\text{tot}} - \delta p)] \quad (1.58)$$

If we assume a self-gravitational system with $\delta S = 0$, we can neglect rhs;

$$\frac{\partial^2 \delta}{\partial t^2} + \frac{2\dot{a}}{a} \frac{\partial \delta}{\partial t} - \left(4\pi G \bar{\rho} \delta + \frac{c_s^2}{a^2} \Delta \delta \right) = 0. \quad (1.59)$$

Fourier transform of $\delta(\mathbf{x}, t) \rightarrow \tilde{\delta}(\mathbf{k}, t)$ gives the following equation,

$$\frac{\partial^2 \tilde{\delta} t^2}{\partial t^2} + 2\frac{\dot{a}}{a} \frac{\partial \tilde{\delta}}{\partial t} - \left(4\pi G \bar{\rho} - \frac{c_s^2 k^2}{a^2} \right) \tilde{\delta} = 0. \quad (1.60)$$

The second term works as "friction" due to the cosmic expansion. The third term is potential term. This linear-equation implies that each Fourier mode with different k evolves independently. When $\left(4\pi G \bar{\rho} - \frac{c_s^2 k^2}{a^2} \right) \tilde{\delta} < 0$, δ does not grow and approaches 0 with damping oscillation. When $\left(4\pi G \bar{\rho} - \frac{c_s^2 k^2}{a^2} \right) \tilde{\delta} > 0$, gravity is stronger than pressure and density fluctuations can grow, and the matter finally collapses gravitationally. There is a threshold wavenumber $k_J \equiv \frac{a\sqrt{4\pi G \bar{\rho}}}{c_s}$, which is called Jeans scale.

From here, we consider the evolution of dark matter fluctuations in linear theory. Fluctuations can grow when $k < k_J$, and $c_s = 0$ because dark matter is collisionless. Then the equation of evolution for dark matter is

$$\ddot{\delta} + 2\frac{\dot{a}}{a} \dot{\delta} - 4\pi G \bar{\rho} \delta = 0. \quad (1.61)$$

Considering Einstein-de Sitter universe, i.e. $\frac{\dot{a}}{a} = \frac{2}{3t}$ and $\rho = \frac{1}{6\pi Gt^2}$ (from eq. 1.41), we can re-arrange eq. 1.61;

$$\ddot{\delta} + \frac{4}{3t}\dot{\delta} - \frac{2}{3t^2}\delta = 0. \quad (1.62)$$

The solution is expressed by the superpositions for two solutions,

$$\delta = At^{2/3} + Bt^{-1}. \quad (1.63)$$

The first and second terms are called "growing mode" and "decaying mode" respectively. We can focus on only the first term and it follows that density fluctuations grow as $\delta \propto t^{2/3}$, proportional to scale factor a in the matter-dominant epoch.

1.2.2 Non-linear model for spherical collapse

The linear approximation in the previous section is valid when $\delta \ll 1$. However, as δ increases, non-linear structure formation should be considered. In the present-day universe, density fluctuations evolve non-linearly in the scale of $\lesssim 10 h^{-1}\text{Mpc}$. We firstly use a simple spherical collapse model. Let us assume a sphere with mass M , constant density, and radius r . We treat the sphere in Einstein de Sitter universe. The equation of motion is

$$\ddot{r} = -\frac{GM(< r)}{r^2}. \quad (1.64)$$

From energy conservation,

$$\frac{1}{2}\dot{r}^2 - \frac{GM(< r)}{r} = E(= \text{const.}) \quad (1.65)$$

The cases of $E < 0$ and $E > 0$ correspond to bounded solution with contracting r and unbounded one with expanding r . By integrating eq. 1.65, we can express r and t with a parameter θ :

$$\begin{cases} r = (GM)^{1/3}A^2(1 - \cos \theta) \\ t = A^3(\theta - \sin \theta) \end{cases} \quad (E < 0) \quad (1.66)$$

$$\begin{cases} r = (GM)^{1/3}A^2(\cosh \theta - 1) \\ t = A^3(\sinh \theta - \theta) \end{cases} \quad (E > 0), \quad (1.67)$$

where A is constant. The density in the sphere is $\rho = \frac{3M}{4\pi r^3}$ and the mean density of Einstein-de-Sitter universe is $\bar{\rho} = \frac{1}{6\pi Gt^2}$. Therefore, the density fluctuation is

$$\delta \equiv \frac{\rho}{\bar{\rho}} - 1 = \begin{cases} \frac{9}{2} \frac{(\theta - \sin \theta)^2}{(1 - \cos \theta)^3} - 1 & (E < 0) \\ \frac{9}{2} \frac{(\sinh \theta - \theta)^2}{(\cosh \theta - 1)^3} - 1 & (E > 0) \end{cases} \quad (1.68)$$

We plot eq. 1.66, eq. 1.67, and eq. 1.68 in Figure 1.2.

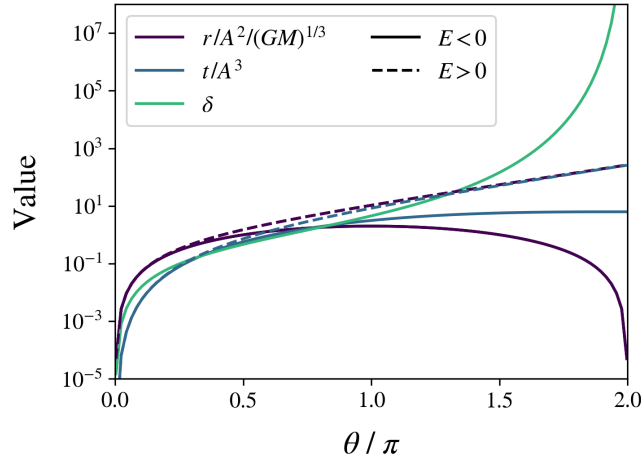


Figure 1.2: Radius r (purple), time t (blue), over density δ (green) as a function of θ . Solid and dashed lines represent bounded and unbounded case, respectively.

For the unbounded solution, the radius expands monotonically and the density is lower than the average density. However, for the bounded solution, the sphere expands and turns into collapse. The turning point from expansion to contraction has a maximum radius and corresponds to $\theta = \pi$. Time, radius and density fluctuations at the turning point are

$$t_{\text{turn}} = \pi A^2, \quad r_{\text{turn}} = 2(GM)^{1/3} A^2, \quad \delta_{\text{turn}} = \frac{9\pi^2}{16} - 1. \quad (1.69)$$

The point where $r \rightarrow 0$ is a collapse point and corresponds to $\theta = 2\pi$. Time at the collapsing point is

$$t_{\text{coll}} = 2t_{\text{turn}} = 2\pi A^2. \quad (1.70)$$

At that time, density fluctuations diverge, $\delta \rightarrow \infty$.

1.2.3 Virial equilibrium in a spherical model

In reality, the density does not diverge and a sphere is gravitationally bound and becomes in equilibrium. In a gravitationally bounded system in equilibrium, total energy E and potential energy U have a following relationship,

$$E = \frac{1}{2} \langle U \rangle, \quad (1.71)$$

where $\langle U \rangle$ is time averaged potential energy. We consider a sphere with uniform density, gravitationally bounded, and in equilibrium. The density is expressed by using mass M and radius R , $\rho = \frac{3M}{4\pi R^3}$. The mass within radius r ($0 < r < R$) and the shell at $r \sim r + dr$ are $\frac{4\pi r^3}{3}$ and $4\pi r^2 dr$ respectively. Thus, the gravitational potential inside the sphere is

$$U = - \int_0^R \frac{G}{r} \frac{4\pi r^3}{3} \cdot 4\pi r^2 dr = - \int_0^R \frac{G}{r} \frac{Mr^3}{R^3} \frac{3Mr^2 dr}{R^3} = - \frac{3}{5} \frac{GM^2}{R}. \quad (1.72)$$

We follow the non-linear collapse for a density-uniformed sphere by using virial theorem. Non-linear growth of spherical symmetry model is already explained in section 1.2.2. A sphere has the maximum radius R_{turn} at the turning point and the total energy is

$$E = U = -\frac{3}{5} \frac{GM^2}{R_{\text{turn}}}. \quad (1.73)$$

After the turning point, the sphere starts to contract. In section 1.2.2, we assume that velocity dispersion can be ignored. However, in reality, velocity dispersion itself supports gravity and the sphere finally becomes in virial equilibrium. The potential energy at the virial equilibrium is

$$U_{\text{vir}} = -\frac{3}{5} \frac{GM^2}{R_{\text{vir}}}. \quad (1.74)$$

According to virial theorem $E = \frac{1}{2}U_{\text{vir}}$, and the virial radius is given by

$$R_{\text{vir}} = \frac{1}{2}R_{\text{turn}}. \quad (1.75)$$

The time to reach virial equilibrium can be considered the same as the time to reach the collapse point, t_{coll} . Thus, the density fluctuation at $t = t_{\text{coll}}$ is

$$\delta_{\text{coll}} = \frac{\rho}{\bar{\rho}} - 1 = \frac{3M}{4\pi R_{\text{vir}}^3} \frac{1}{6\pi G t_{\text{coll}}^2} - 1 \quad (1.76)$$

$$= 18\pi^2 - 1 \simeq 178. \quad (1.77)$$

Chapter 2

Formation of the First Stars

2.1 The minimum collapse mass

Dark matter halos in virial equilibrium cannot contract anymore. Gas in a halo can contract through radiative cooling, and finally forms stars or galaxies. Here, we introduce the minimum halo mass required for the inside gas to collapse. Consider a virialized dark matter halo with mass M and radius R_{vir} . The average density within the halo is

$$\rho_{\text{halo}} = \Delta_c \rho_{c0} (1 + z_{\text{vir}})^3, \quad (2.1)$$

where z_{vir} is the virialization redshift and Δ_c is the overdensity at spherical collapse with uniform density, $\Delta_c = 18\pi^2 \sim 178$ as explained in section 1.2.3. The critical density of the universe denoted ρ_{c0} (see eq. 1.34). The virial radius of the dark matter halo is written as

$$R_{\text{vir}} = \left(\frac{3}{4\pi} \frac{M}{\rho_{\text{halo}}} \right)^{1/3} \quad (2.2)$$

$$\simeq 1 \text{ kpc} \left(\frac{M}{10^8 M_{\odot}} \right)^{1/3} \left(\frac{\Delta_c}{18\pi^2} \right)^{-1/3} \left(\frac{1 + z_{\text{vir}}}{10} \right)^{-1}, \quad (2.3)$$

(Barkana & Loeb 2001a; Bromm et al. 2002; Greif 2015; Tegmark et al. 1997). The corresponding circular velocity V_{circ} is

$$V_{\text{circ}} = \sqrt{\frac{GM}{R_{\text{vir}}}} = 23.4 \left(\frac{M}{10^8 h^{-1} M_{\odot}} \right)^{1/3} \left(\frac{\Delta_c}{18\pi^2} \right)^{1/6} \left(\frac{1 + z_{\text{vir}}}{10} \right)^{1/2} \text{ km s}^{-1}. \quad (2.4)$$

We also define virial temperature

$$T_{\text{vir}} = \frac{\mu m_{\text{p}} V_{\text{circ}}^2}{2k} = 1.98 \times 10^4 \left(\frac{\mu}{0.6} \right) \left(\frac{M}{10^8 h^{-1} M_{\odot}} \right)^{2/3} \left(\frac{\Delta_c}{18\pi^2} \right)^{1/3} \left(\frac{1 + z_{\text{vir}}}{10} \right) \text{ K} \quad (2.5)$$

A gas within a dark matter halo with mass M has the temperature of eq. 2.5. The gas needs to be cooled via radiation within Hubble time in order to contract and form stars. Here we estimate the amount of Hydrogen molecules we need for cooling primordial gas effectively within Hubble time. The Hubble time scale t_{Hubble} is

$$t_{\text{Hubble}} = \int_0^t \frac{1}{a} dt = \int_z^{\infty} \frac{dz}{H} \simeq 6.5 \times 10^6 \left(\frac{1 + z_{\text{vir}}}{100} \right)^{-3/2} h^{-1} \text{ yr}. \quad (2.6)$$

The main cooling process in a primordial gas is H_2 cooling (see details in section 2.3). The H_2 cooling time scale $t_{\text{cool},\text{H}_2}$ is

$$t_{\text{cool},\text{H}_2} \sim \frac{\frac{3}{2}nkT}{\Lambda_{\text{H}_2}}, \quad (2.7)$$

where Λ_{H_2} is the H_2 cooling rate. The values of cooling rates are different from each species. Radiative de-excitation is dominant when the gas density is below the critical density, which is defined as the ratio of radiation and collisional de-excitation, $n_{\text{crit}} \equiv A_{10}/q_{10}$. Here A_{10} is Einstein coefficient and q_{10} is collisional de-excitation rate (see the details in section 2.3). In the case of low-density limit, i.e., $n \ll n_{\text{crit}} \sim 10^5 \text{ cm}^{-3}$, two-level approximation gives the following expression of Λ :

$$\Lambda_{\text{H}_2} = n_{\text{H}_2} C_{01} \Delta E \quad (2.8)$$

$$= n_{\text{H}_2} n_{\text{coll}} q_{01} \Delta E \sim n^2 f_{\text{H}_2} q_{10} \exp\left(-\frac{\Delta E}{kT}\right) \Delta E, \quad (2.9)$$

where ΔE is excitation energy. The collision coefficient is $C_{01} = n_{\text{coll}} q_{01}$, where $n_{\text{coll}} \sim n$ is the number density of the collision partner (mostly hydrogen atom). The fraction of molecular hydrogen is defined as $f_{\text{H}_2} \equiv n_{\text{H}_2}/n$. There is also a relationship between collisional excitation (q_{01}) and de-excitation rate (q_{10}),

$$q_{01} = q_{10} \exp\left(-\frac{\Delta E}{kT}\right) \Delta E. \quad (2.10)$$

The condition that H_2 cooling cools gas within Hubble time is

$$t_{\text{Hubble}} \sim t_{\text{cool},\text{H}_2} \quad (2.11)$$

$$\therefore \frac{2}{3H_0(1+z_{\text{vir}})} \sim \frac{\frac{3}{2}nkT}{n^2 f_{\text{H}_2} q_{10} \exp\left(-\frac{\Delta E}{kT}\right) \Delta E} \quad (2.12)$$

$$\therefore f_{\text{H}_2} \propto (1+z_{\text{vir}})^{-3/2} \frac{T}{q_{10}(T)} \exp\left(\frac{\Delta E}{kT}\right) \quad (2.13)$$

When we consider the rotation transition for H_2 , the corresponding temperature is $\frac{\Delta E}{k} = 512 \text{ K}$. $q_{10}(T)$ is generally power-low of T , thus $f_{\text{H}_2} \propto \exp\left(\frac{\Delta E}{kT}\right)$. For low temperature, f_{H_2} increases because it is difficult to excite H_2 to higher levels.

Furthermore, enough amount of H_2 to cool gas should be formed in a Hubble time. Molecular hydrogen is produced via H^- process (see the section 2.3). When we assume the total number density as $n = n_{\text{H}} + n_{\text{H}^+} + 2n_{\text{H}_2}$, the ionization degree x is $x = \frac{n_{\text{H}^+}}{n}$ and H_2 fraction is determined by $f_{\text{H}_2} \equiv \frac{n_{\text{H}_2}}{n}$. Since the time variation of n_{H^+} is expressed by a recombination rate $\alpha(T)$, time variation of x is

$$\dot{x} = -\alpha(T)nx^2 \quad \left(\because \frac{dn_{\text{H}^+}}{dt} = -\alpha(T)n_e n_{\text{H}^+} \right). \quad (2.14)$$

Integrating eq. 2.14 gets

$$x = \frac{x_0}{1 + n\alpha(T)x_0 t}, \quad (2.15)$$

14 Formation of the First Stars

where x_0 is initial abundances (typically $x_0 \sim 10^{-4}$) and $n\beta(T)x_0$ is equal to the inverse of recombination timescale, $1/t_{\text{rec},0}$. Hydrogen molecule is produced by the following reaction



These reactions are called H^- channel. The reverse reaction of eq. 2.16 is caused by CMB photons (Tegmark et al. 1997). An electron works as a catalyst and its abundance does not change,

$$\frac{dn_{\text{e}}}{dt} = -k_1 n_{\text{H}} n_{\text{e}} + k_3 n_{\text{H}^-} + k_2 n_{\text{H}} n_{\text{H}^-} = 0 \quad (2.18)$$

$$\therefore n_{\text{H}^-} = \frac{k_1 n_{\text{H}} n_{\text{e}}}{k_3 + k_2 n_{\text{H}}} \quad (2.19)$$

The evolution of the molecular fraction f_{H_2} is therefore written as

$$\dot{f}_{\text{H}_2} = \frac{1}{n} \frac{dn_{\text{H}_2}}{dt} \quad (2.20)$$

$$= \frac{1}{n} k_2 n_{\text{H}} n_{\text{H}^-} \quad (2.21)$$

$$= \frac{1}{n} \frac{k_2 k_1 n_{\text{H}}^2 n_{\text{e}}}{k_3 + k_2 n_{\text{H}}} \quad (2.22)$$

$$\sim \frac{k_2 k_1 n_{\text{H}} n_{\text{e}}}{k_3 + k_2 n_{\text{H}}} \cdot n_{\text{H}^+} \quad (\because n \sim n_{\text{H}}, n_{\text{H}^+} \sim n_{\text{e}}) \quad (2.23)$$

$$= k_{\text{H}^-} n_{\text{H}} x \quad \left(k_{\text{H}^-} \equiv \frac{k_2 k_1}{k_3 + k_2 n_{\text{H}}} \right) \quad (2.24)$$

$$= k_{\text{H}^-} \cdot n \frac{x_0}{1 + \frac{t}{t_{\text{rec},0}}}, \quad (2.25)$$

where k_{H^-} is the H_2 formation rate by H^- process. By integrating eq. 2.25, we can get

$$f_{\text{H}_2} \simeq f_{\text{H}_2,0} + \frac{k_{\text{H}^-}}{\alpha(T)} \log \left(1 + \frac{t}{t_{\text{rec},0}} \right) \quad (2.26)$$

$$\simeq \frac{k_{\text{H}^-}}{\alpha(T)}. \quad (2.27)$$

The initial H_2 fraction can be negligible because $f_{\text{H}_2,0} \sim 6 \times 10^7$.

When $t \ll t_{\text{rec},0}$, the fraction becomes

$$f_{\text{H}_2} \simeq \frac{k_{\text{H}^-}}{\alpha(T)} \frac{t}{t_{\text{rec},0}} \propto t. \quad (2.28)$$

The H_2 production rate \dot{f}_{H_2} is constant.

When $t \gg t_{\text{rec},0}$, the fraction increases logarithmically, $f_{\text{H}_2} \propto \log(t/t_{\text{rec},0})$. This is because recombination depletes the electron fraction and H^- channel becomes inefficient.

At the transition time $t = t_{\text{rec},0}$, the H_2 fraction is

$$f_{\text{H}_2} \simeq \frac{k_{\text{H}^-}}{\alpha(T)} \simeq 3.5 \times 10^{-4} \left(\frac{T}{10^3 \text{ K}} \right)^{1.52}. \quad (2.29)$$

Tegmark et al. (1997) derive the above description analytically and show f_{H_2} as a function of T (Figure 2.1).

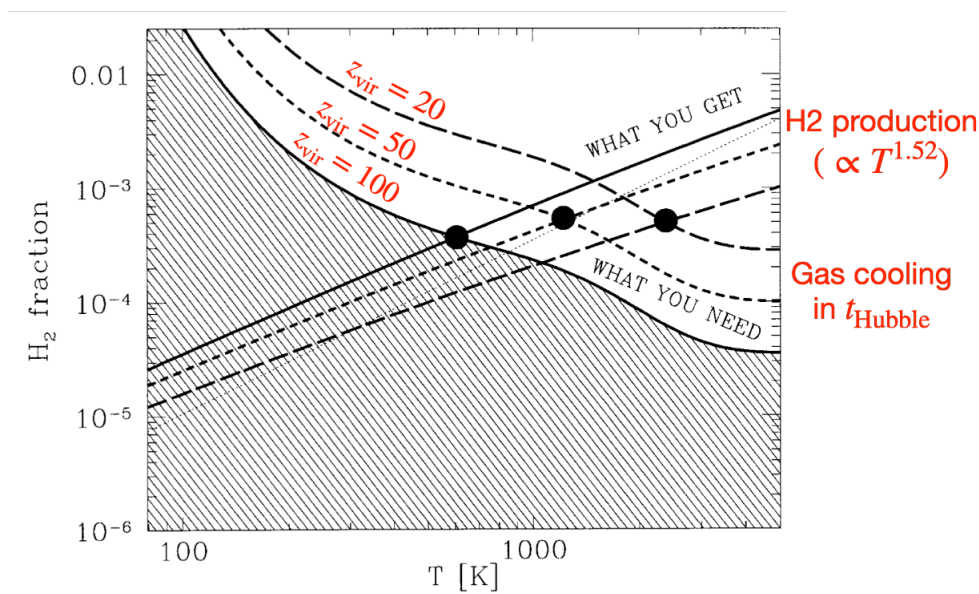


Figure 2.1: H_2 fraction vs. virial temperature. The solid, short-dashed and long-dashed lines are for clumps virializing at $z_{\text{vir}} = 100, 50$, and 25 respectively. Lines with negative slopes indicate the threshold that gas can cool in Hubble time. The shaded region thus shows gas cannot cool in Hubble time. Lines with positive slopes represent the molecular fraction produced in Hubble time. The three intersections (black circles) show the minimum virial temperature for gas to start collapsing. The lines are for $x_0 = 3 \times 10^{-4}$. Adopted from Tegmark et al. (1997) and added a legend.

Yoshida et al. (2003) have conducted cosmological simulations and shown that the distribution of gas halos on $f_{\text{H}_2} - T$ plane is consistent with the analytical results (Tegmark et al. 1997) in Figure 2.2.

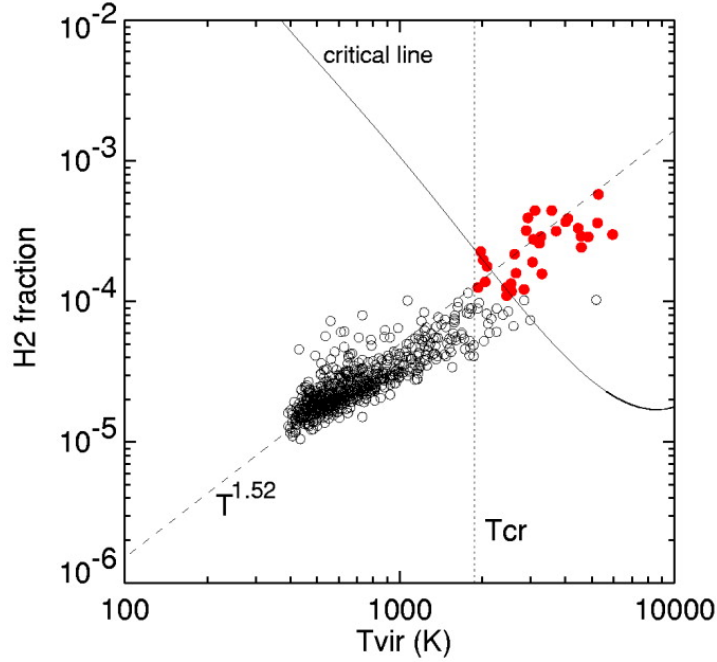


Figure 2.2: The same as Figure 2.1. Filled and open circles are halos that host gas clouds and those that do not at $z = 17$. They identify gas clumps which are cold ($T < 0.5T_{\text{vir}}$) and dens ($n_{\text{H}} > 5 \times 10^2 \text{ cm}^{-3}$) as "gas clouds". Adopted from Yoshida et al. (2003)

2.2 Physics of self-gravitating gas

2.2.1 Virial theorem

Primordial gas is cooled, contracts, and finally reaches hydrostatic equilibrium at some point. From now, we derive the conditions to satisfy hydrostatic equilibrium called Virial theorem (for gas).

The equation of fluid motion is

$$\rho \frac{d\mathbf{v}}{dt} = \nabla p - \rho \nabla \Phi, \quad (2.30)$$

where we neglect magnetic fields. Assuming a spherical gas core, we get

$$\rho \frac{dv}{dt} = -\frac{dp}{dr} - \rho \frac{d\Phi}{r}. \quad (2.31)$$

Multiplying eq. 2.31 by r and integrating it by $dV = 4\pi r^2 dr$ ($r = 0 \rightarrow R$),

$$(\text{LHS of eq. 2.31}) \rightarrow \int \rho \frac{dv}{dt} dV = \int_0^R \left(\frac{1}{2} \frac{d^2 r^2}{dt^2} - v^2 \right) \rho 4\pi r^2 dr \quad (2.32)$$

$$= \frac{1}{2} \frac{d^2}{dt^2} \int_0^R r^2 dM - \int_0^R v^2 dM \quad (2.33)$$

$$= \frac{1}{2} \frac{d^2 I}{dt^2} - 2K, \quad (2.34)$$

where I is moment of inertia and K is kinetic energy. The first term of RHS of eq. 2.31 is re-written as

$$-\int r \frac{dp}{dr} dV = -\int_0^R r \frac{dp}{dr} 4\pi r^2 dr \quad (2.35)$$

$$= -\left\{ [4\pi r^3 p]_0^R - 3 \int_0^R 4\pi r^2 p dr \right\} \quad (2.36)$$

$$= -4\pi R^3 P_{\text{ex}} + 3 \int_0^R p dV \quad (2.37)$$

$$= -4\pi R^3 P_{\text{ex}} + 3(\gamma - 1)U. \quad (2.38)$$

Also, $3 \int_0^R p dV$ is also expressed by the speed of sound and core mass assuming an isothermal core,

$$3 \int_0^R 4\pi r^2 p dr = 3 \int_0^R \frac{k\rho T}{\mu m_{\text{H}}} 4\pi r^2 dr = 3 \int_0^R c_s^2 4\pi r^2 dr \quad \left(\because c_s^2 = \frac{kT}{\mu m_{\text{H}}} \right) \quad (2.39)$$

$$= 3c_s^2 M. \quad (2.40)$$

The second term of RHS of eq. 2.31 becomes

$$-\int \rho r \frac{d\Phi}{dr} dV = -\int \rho \frac{GM_r}{r} dV = -\int \frac{GM_r}{r} dM_r = W \quad (2.41)$$

Also, $-\int \frac{GM_r}{r} dM_r$ is expressed by core mass and radius;

$$-\int \frac{GM_r}{r} dM_r = -a \frac{GM^2}{R}. \quad (2.42)$$

A homogeneous sphere satisfies $a = 3/5$. Therefore,

$$\frac{1}{2} \frac{d^2 I}{dt^2} - 2K = -4\pi R^3 P_{\text{ex}} + 3(\gamma - 1)U + W. \quad (2.43)$$

Virial theorem is defined as $\frac{1}{2} \frac{d^2 I}{dt^2} = 0$ and expressed as

$$\boxed{2K - 4\pi R^3 P_{\text{ex}} + 3(\gamma - 1)U + W = 0}. \quad (2.44)$$

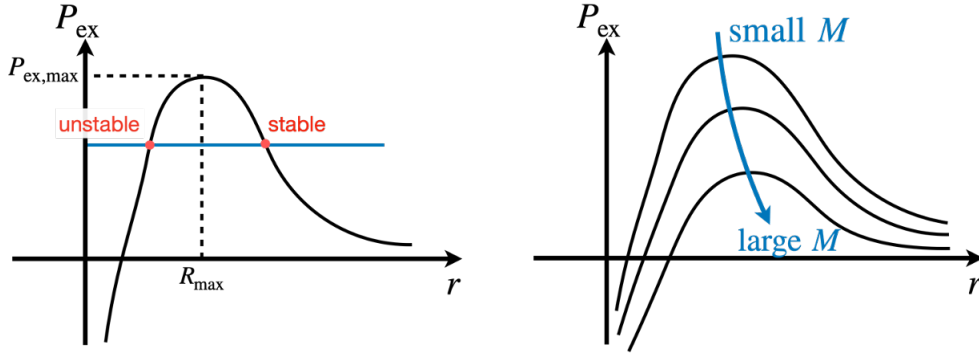
Assuming the system is static ($K = 0$)¹, the virial theorem is re-written as

$$4\pi R^3 P_{\text{ex}} = 3c_s^2 M - a \frac{GM^2}{4\pi R^4} \quad (2.45)$$

$$\therefore P_{\text{ex}} = \frac{3c_s^2 M}{4\pi R^3} - a \frac{GM^2}{4\pi R^4}. \quad (2.46)$$

Thus P_{ex} is expressed as the function of R in Figure 2.3.

¹For hydrostatic equilibrium for stars, we can also neglect the external pressure ($P_{\text{ex}} = 0$)


 Figure 2.3: P_{ex} as a function of R .

From Figure 2.3, P_{ex} has the maximum value at $R = R_{\text{max}}$

$$P_{\text{ex,max}} = \left(\frac{9}{4a}\right)^3 \frac{3}{16\pi} \left(\frac{c_s^8}{G^3 M^2}\right), \quad R_{\text{max}} = \frac{4aGM}{9c_s^2}. \quad (2.47)$$

When a stable solution exist, $P_{\text{ex}} < P_{\text{ex,max}}$ is required. According to the right panel of Figure 2.3, the critical mass should exist which satisfies $P_{\text{ex}} = P_{\text{ex,max}}$. The mass is called "Bonnor-Ebert mass" ;

$$M_{\text{BE}} = 1.18 M_{\odot} \frac{c_s^4}{G^{3/2} P_{\text{ex}}^{1/2}}. \quad (2.48)$$

When the gas temperature is the same inside and outside core²,

$$M_{\text{BE}} \propto \frac{T^2}{G^{3/2} \rho^{1/2} T^{1/2}} \propto \frac{T^{3/2}}{G^{3/2} \rho^{1/2}} \quad (2.49)$$

$$\sim 20 M_{\odot} T^{3/2} n^{-1/2} \mu^{-2} \quad (\text{mean molecular weight } \mu \approx 1.22) \quad (2.50)$$

which corresponds to Jeans mass.

As explained in the next section 2.2.2, Jeans mass considers only the inside gas. Assuming the same temperature inside and outside of the core, we can treat M_J and M_{BE} the same way.

2.2.2 Jeans instability

We have discussed isothermal self-gravitating systems and Boner-Ebert mass M_{BE} , which is the threshold mass of gravitational instability. Here, we discuss the stability of gas in a self-gravitating system adding small perturbations. The basic fluid equations are

$$\frac{\partial \rho}{\partial t} + \nabla \cdot (\rho \mathbf{v}) = 0 \quad (2.51)$$

$$\frac{\partial \mathbf{v}}{\partial t} + (\mathbf{u} \cdot \nabla) \mathbf{v} = -\frac{1}{\rho} \nabla p - \nabla \psi \quad (2.52)$$

$$\Delta \psi = 4\pi G \rho. \quad (2.53)$$

For an arbitral quantity Q , it has small fluctuations Q_1 , i.e., $Q = Q_0 + Q_1$ ($|Q_1| \ll Q_0$). There is an assumption that Q_1 can be expressed as a plane-wave solution, $Q_1 \propto e^{i(kx - \omega t)}$. At

²if the external pressure is the same as the local pressure

the first unperturbed state, gas pressure, density, and velocity are P_0 , ρ_0 and $v_0 = 0$ respectively. When small perturbations are added adiabatically, those properties become $\rho = \rho_0 + \rho_1$ and $v = v_1$. Substituting them to eq. 2.51, 2.52, 2.53, and ignoring the second-order terms, we get

$$\frac{\partial \rho_1}{\partial t} + \rho_0 \nabla \cdot \mathbf{v}_1 = 0 \quad (2.54)$$

$$\frac{\partial \mathbf{v}_1}{\partial t} = -\frac{c_s^2}{\rho_0} \nabla \rho_1 - \nabla \psi_1 \quad (2.55)$$

$$\Delta \psi_1 = 4\pi G \rho_1 \quad (2.56)$$

Executing Fourier transform arranges the above equations to

$$-i\omega \tilde{\rho}_1 + \rho_0 \cdot ik \tilde{v}_1 = 0 \quad (2.57)$$

$$-i\omega \tilde{v}_1 = -\frac{c_s^2}{\rho_0} ik \tilde{\rho}_1 - ik \tilde{\psi}_1 \quad (2.58)$$

$$(ik)^2 \tilde{\psi}_1 = 4\pi G \tilde{\rho}_1 \quad (2.59)$$

In the matrix, we can write

$$\underbrace{\begin{pmatrix} -i\omega & i\rho_0 k & 0 \\ i\frac{kc_s^2}{\rho_0} & -i\omega & ik \\ -4\pi G & 0 & -k^2 \end{pmatrix}}_{\mathbf{A}} \underbrace{\begin{pmatrix} \rho_1 \\ v_1 \\ \psi_1 \end{pmatrix}}_{\mathbf{x}} = \begin{pmatrix} 0 \\ 0 \\ 0 \end{pmatrix} \quad (2.60)$$

Thus, $\mathbf{A} \cdot \mathbf{x} = 0$. If the solution has $\mathbf{x} \neq \mathbf{0}$, \mathbf{A} requires

$$\text{dot} \mathbf{A} = (\omega^2 + 4\pi G \rho_0 - c_s^2 k^2) k^2 = 0 \quad (2.61)$$

$$\therefore \omega^2 = c_s^2 k^2 - 4\pi G \rho_0 \quad (2.62)$$

Eq. 2.62 is a dispersion relationship. k_J is $k_J = \frac{4\pi G \rho_0}{c_s}$. When $k > k_J$, $\omega^2 > 0$ and the system is stable. However, when $k < k_J$, $\omega^2 < 0$ and the system becomes unstable because the perturbation grows exponentially. The threshold wavelength for gravitational instability is

$$\lambda_J = \frac{2\pi}{k_J} = c_s \sqrt{\frac{\pi}{G \rho_0}}. \quad (2.63)$$

If the perturbation wavelength is larger than λ_J , self-gravity overcomes pressure. Jeans mass which radius has Jeans length λ_J is

$$M_J = \frac{4\pi}{3} \left(\frac{\lambda_J}{2} \right)^3 \rho_0 = \frac{\pi}{6} \frac{c_s^3}{G^{3/2} \rho_0^{1/2}} \propto T^{3/2} \rho^{-1/2} \quad (2.64)$$

Once perturbations are added, pressure is exerted on the cloud, which sends out sound waves through the cloud. We can define the time it takes for sound waves to cross the cloud and to re-establish pressure balance. It is called sound crossing time,

$$t_{\text{sc}} = \frac{\lambda}{c_s}. \quad (2.65)$$

Jeans instability is also discussed by comparing the sound crossing time to the free-fall time (t_{ff}), which is the collapse timescale explained in the next section. When $t_{\text{sc}} < t_{\text{ff}}$, the pressure restrains the gravitational collapse. When $t_{\text{sc}} > t_{\text{ff}}$, perturbations continue unabated, resulting in the cloud collapse.

We note that this Jeans analysis set contradictory initial conditions. As an unperturbed state, ρ_0 , $p_0 = \text{const.}$ and $\mathbf{v}_0 = 0$ are assumed. Substituting them into the equation of motion (eq. 2.52) leads $\nabla\psi_0 = 0$. Thus, Poisson equation (eq. 2.53) is not satisfied unless $\rho_0 = 0$. This contradiction is called Jeans swindle.

2.2.3 Runaway collapse

After $M > M_J$, gas clumps begin to collapse gravitationally. The characteristic timescale that the collapse would take is known as the free-fall time. Here we consider a spherical gas cloud without pressure gradient, with only self-gravity. The cloud has a homogeneous density and the shell has radius $r = a$, velocity $v = 0$ at $t = 0$. At $t = t$, we assume the radius $R(t)$ can be written as $R(t) = af(t, a)$ ($0 \leq f \leq 1$). The equation of shell motion at $t = t$ is

$$\frac{d^2R}{dt^2} = a\ddot{f} = -\frac{GM(< a)}{R^2} = -G\frac{1}{(af)^2}\frac{4\pi a^3}{3}\rho(0) \quad (2.66)$$

$$\therefore \ddot{f} = -\frac{4\pi G\rho(0)}{3f^2}. \quad (2.67)$$

In eq 2.67, f is independent of a , which implies that a homogeneous gas sphere, regardless of its size, can contract to the center at the same time if it begins to collapse at the same time.

Integrating eq 2.67 by time, we get

$$\beta + \frac{1}{2}\sin(2\beta) = t\left(\frac{8\pi G\rho(0)}{3}\right)^{1/2} \quad (f = \cos^2\beta) \quad (2.68)$$

When f changes as $f = 1 \rightarrow 0$ (i.e. contract to the center), $\beta = 0 \rightarrow \frac{\pi}{2}$. Substituting $\beta = \frac{\pi}{2}$ into eq 2.67, we obtain

$$t_{\text{ff}} = \left(\frac{3\pi}{32G\rho(0)}\right)^{1/2}, \quad (2.69)$$

which is called free-fall time and represents a required timescale to collapse to infinite density from the state of rest. Equation 2.69 shows high dense inner regions can collapse faster than less dense outer regions. Therefore, the central part contracts and forms a dense core, leaving its envelope. This process is called runaway collapse. Larson (1969) have numerically calculated the collapse of an isothermal spherical gas cloud from uniformed density distribution. Figure 2.4 shows the density distribution of a collapsing gas and the density profile at the envelope follows power law $\rho \propto r^{-2}$. The central part collapses approximately with the free-fall timescale even though pressure gradients exist. The length of the density peak is roughly the same as Jeans length, which is proportional to $\rho^{-1/2}$ (eq. 2.63).

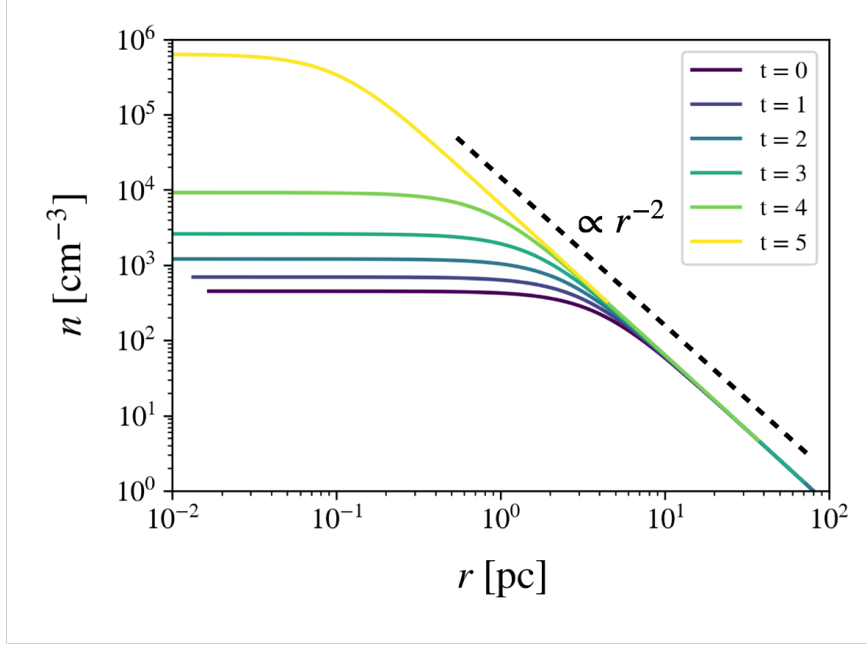


Figure 2.4: The radial profile of density for the collapsing cloud at various times. Each time is normalized by 10^{13} sec. The flat part corresponds to the core with Jeans radius λ_J . The envelope has a density distribution with $\rho \propto r^{-2}$. Calculation adopts asymptotic similarity solution in Larson (1969).

The power-law distribution for the envelope can be explained roughly as follows;

$$\frac{\lambda_J}{c_s} \sim t_{\text{ff}} \sim \frac{1}{\sqrt{G\rho}} \quad (2.70)$$

$$\therefore \rho \propto \frac{c_s}{r^2} \propto \frac{T}{r^2}. \quad (2.71)$$

The more exact derivation is in Larson (1969). The runaway collapse of primordial gas also satisfies Larson's law (e.g. Abel et al. 2002; Hirano et al. 2014; Omukai & Nishi 1998; Ripamonti et al. 2002; Yoshida et al. 2008).

2.2.4 Critical Γ at cloud collapse

Let us assume that pressure is proportional to density to the power of Γ , i.e., $P = K\rho^\Gamma$, where K is constant. For an adiabatic ideal gas, Γ is equal to the specific heat ratio $\gamma (= c_p/c_v)$. The ways of cloud collapse or cloud fragmentation are determined by Γ . Consider the equilibrium condition at the boundary of a cloud sphere. Self gravity F_g and the pressure gradient F_p is

$$F_g = \frac{GM}{R^2} \quad (2.72)$$

$$F_p = \frac{1}{\rho} \frac{dP}{dr} \sim \frac{1}{\rho} \frac{K\rho^\Gamma}{R} \quad (2.73)$$

$$\propto \frac{1}{R^{3\Gamma-2}} \quad (\because \rho \propto 1/R^3) \quad (2.74)$$

22 Formation of the First Stars

Therefore,

$$\frac{F_g}{F_p} \propto R^{2-3\Gamma} R^2 = R^{4-3\Gamma}. \quad (2.75)$$

For spherical symmetry, the critical gamma is $\Gamma_{\text{crit}} = \frac{4}{3}$. There are the following two types of the further evolution of gas clouds.

1. $\Gamma > \Gamma_{\text{crit}} = \frac{4}{3}$: F_p overcomes F_g as density increases and collapse will stop.
2. $\Gamma < \Gamma_{\text{crit}} = \frac{4}{3}$: F_g overwhelms F_p as density increases and collapse will continue.

The value of critical gamma depends on the shape of gas clouds. Consider a sheet-like cloud. The equilibrium state of a sheet-like structure is derived by the following equations:

$$\text{Poisson eq.: } \frac{\partial^2 \psi}{\partial z^2} = 4\pi G \rho(z) \rightarrow \frac{\psi}{R^2} \sim \frac{1}{R} \quad (2.76)$$

$$\text{self-gravity: } F_g = -\frac{d\psi}{dz} \rightarrow F_g \sim \frac{\psi}{R} \propto R^0 \quad (2.77)$$

$$\text{pressure gradient: } F_p = \frac{1}{\rho} \frac{dp}{dz} \rightarrow F_p \propto \frac{K \rho^{\Gamma-1}}{R} \propto R^{-\Gamma}. \quad (2.78)$$

Therefore,

$$\frac{F_p}{F_g} \propto \frac{R^{-\Gamma}}{R^0} = R^{-\Gamma} \quad (2.79)$$

and the critical gamma is $\Gamma_{\text{crit}} = 0$.

The critical gamma for filament structures has a different value. Consider an axisymmetric cylinder. Poisson equation can be written in cylindrical coordinates,

$$\Delta \psi = \frac{1}{r} \frac{d}{dr} r \frac{d\psi}{dr} = 4\pi G \rho. \quad (2.80)$$

Multiplying eq. 2.80 by r and integrating from $r = 0$ to $r = R$, we get

$$\int_0^R \frac{d}{dr} r \frac{d\psi}{dr} dr = \int_0^R 4\pi G \rho r \quad (2.81)$$

$$\left[r \frac{d\psi}{dr} \right]_0^R = 2\pi G \rho R^2 \quad (2.82)$$

$$= 2GM_{\text{line}}, \quad (2.83)$$

where M_{line} is a line mass and constant. Self-gravity and pressure gradient are, thus,

$$F_g = \frac{d\psi}{dr} \Big|_{r=R} = \frac{2GM_{\text{line}}}{R} \propto \frac{1}{R} \quad (2.84)$$

$$F_p = p \frac{dp}{dr} \propto \frac{\rho^{\Gamma-1}}{R} \propto \frac{1}{R^{2\Gamma-1}} \quad \left(\because \rho \propto \frac{1}{R^2} \right) \quad (2.85)$$

$$\therefore \frac{F_p}{F_g} \propto \frac{\frac{1}{R}}{R^{2\Gamma-1}} = R^{-2(\Gamma-1)}. \quad (2.86)$$

Therefore, the critical density for filament structure is $\Gamma_{\text{crit}} = 1$.

Figure 2.5 shows the summary of critical Γ for each shape of gas clouds. Sheet-like clouds

fragment into filamentary structures. Those filamentary clouds fragment into spherical gas clouds.

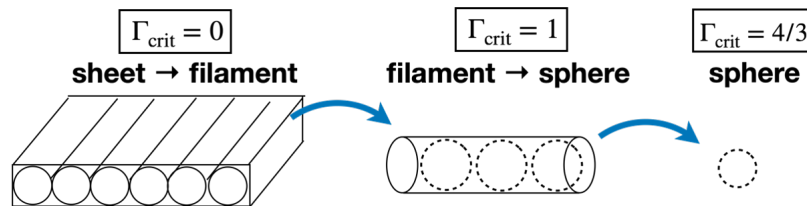


Figure 2.5: Schematic illustration for gas collapse and fragmentation.

2.3 The gas dynamics in primordial gas

2.3.1 H₂ chemistry

Through the BigBang nucleosynthesis, Hydrogen, Helium, and a small amount of Lithium are created. The cosmic primordial gas consists of only these elements. Stars produced by the contraction of primordial gas are known as the first stars or Population III stars. In order to contract primordial gas effectively, cooling by H₂ is the most important coolant in the early universe.

A hydrogen molecule has a symmetry structure and does not have dipole moment. Thus, its radiation is quadrupole radiation by rotational and vibration transition. At present-day star formation, H₂ is formed on the dust surface, however, there is no dust in the primordial gas. There are the gas phase reaction channels for the formation of H₂.

H₂⁺ channel (Saslaw & Zipoy 1967)



H⁻ channel (McDowell 1961; Peebles & Dicke 1968)



H⁻ channel is a much more efficient formation path than H₂⁺ because the binding energy of H⁻ is 0.754 eV, which is much lower than that of H₂⁺, 2.65 eV³. H₂ exists in two states with para-hydrogen or ortho-hydrogen, which are parallel or anti-parallel nuclear spin respectively. Transitions between para- and ortho- are forbidden and the lowest allowed transition is rotational one from $J = 2$ to $J = 0$. This transition occurs only in para-hydrogen and its energy corresponds to a temperature of 512 K. In reality, the Maxwell-Boltzmann tail of the velocity dispersion enables the gas to cool to $T \sim 200$ K (Greif 2015).

³H₂⁺ channel is dominant at $z > 100$.

2.3.2 cooling process in primordial gas

Formation of the first stars depends on the efficient radiation cooling when the primordial gas collapses self-gravitationally. In the present day, the main cooling processes are radiation from metal such as CO or infrared radiation from dust. Figure 2.6 shows cooling functions. The main cooling path in primordial gas depends on the gas temperature.

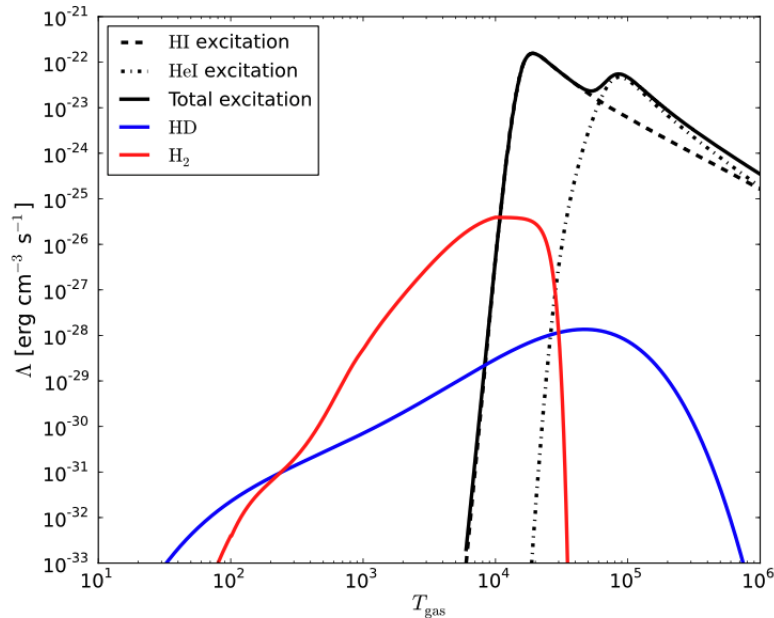


Figure 2.6: cooling function for primordial gas. Red, blue, and black lines show H_2 , HD and atomic cooling respectively. The functions are calculated at $n = 1 \text{ cm}^{-3}$, $x_{\text{H}_2} = 10^{-4}$, $x_{\text{HD}} = 10^{-7}$. Adopted from Bovino & Galli (2019).

When $T_{\text{gas}} \gtrsim 10^6 \text{ K}$, gas is sufficiently ionized and free-free radiation or bremsstrahlung are efficient cooling. When $T \sim 10^5 - 5 \times 10^4 \text{ K}$, collisional excitation of He^+ and H, and the following radiative decay by Lyman α of neutral hydrogen. At $T \sim 10^4 \text{ K}$, the plasma recombines rapidly. Electrons cannot excite the first excited level, which is 10.2 eV above the ground state. Thus, gas temperature becomes stable at $T \sim 10^4 \text{ K}$.

Thermodynamics of primordial gas has been investigated by several studies (Omukai 2000; Omukai & Nishi 1998; Palla et al. 1983; Yoshida et al. 2006). Figure 2.7 shows a temperature and density phase diagram (The Omukai diagram). Distinctive phases are described in A to G.

- (A) Gas enters DM potential well and is adiabatically compressed.
- (B) H_2 is formed via H^- process and molecular cooling begins to work.
- (C) Gas temperature reaches 200 K and H_2 does not work. At that time gas is in local thermal equilibrium (LTE). At this point, gas forms a quasi-hydrostatic core and the corresponding Jeans mass is

$$M_J = 1.75 \times 10^3 M_{\odot} \left(\frac{n}{10^4 \text{ cm}^{-3}} \right)^{-1/2} \left(\frac{T}{200 \text{ K}} \right)^{3/2} \quad (2.91)$$

(D) When $n \sim 10^9 \text{ cm}^{-3}$, H_2 is formed via three body reaction (Palla et al. 1983).



H_2 fraction reaches $x_{\text{H}_2} \sim 1$.

(E) Gas becomes optically thick and cooling is inefficient, which rises temperature.

(F) At $n \sim 10^{14} \text{ cm}^{-3}$, collisional induced emission (CIE) works as a dominant cooling process. In high-density gas, two molecules pair ($\text{H}_2\text{-H}_2$, $\text{H}_2\text{-He}$) approach each other and a temporary dipole is formed. This 'supermolecule' emit dipole radiation and cool gas (Omukai & Nishi 1998; Yoshida et al. 2006).

(G) The gas temperature reaches $T \sim 2000 \text{ K}$ and collisional dissociation of H_2 starts.

(H) At $n > 10^{18} \text{ cm}^{-3}$, gas reaches the final adiabatic phase.

(I) Finally, when the gas density reaches $n \sim 10^{21} \text{ cm}^{-3}$, the protostar forms.

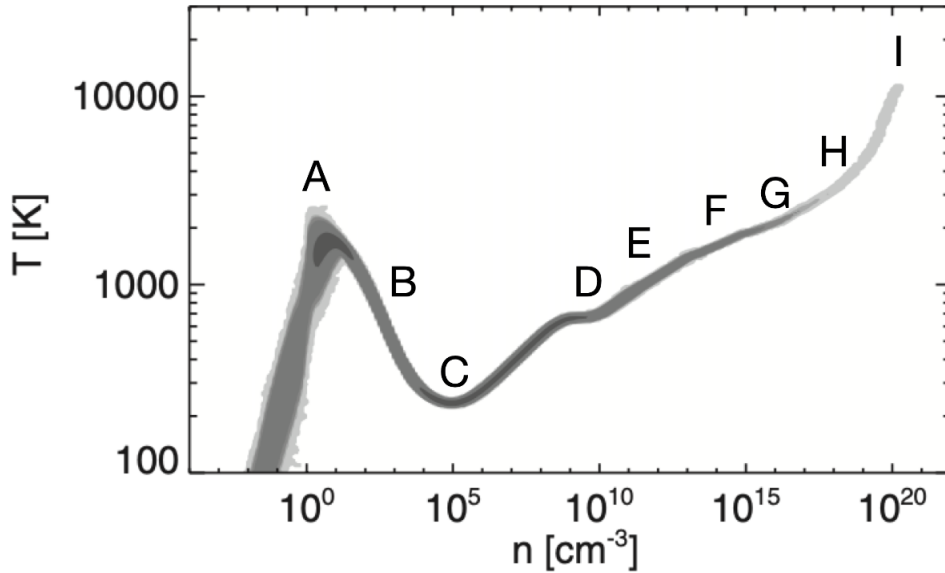


Figure 2.7: Temperature and density phase diagram for primordial gas. Adopted from Yoshida et al. (2012) and added legends.

2.4 Stellar feedback to accretion

As explained above, a protostar is born when the central density reaches $\sim 10^{21} \text{ cm}^{-3}$. A protostar has a mass of $0.01 M_{\odot}$ (Omukai & Nishi 1998; Yoshida et al. 2008) and its envelope has a mass of $\sim 10^3 M_{\odot}$ without cloud fragmentations (e.g. Abel et al. 2002; Yoshida et al. 2006). A protostar grows toward ZAMS by accretion, and its accretion rate is roughly estimated as

$$\dot{M} \sim \frac{M_J}{t_{\text{ff}}} = \frac{c_s^3}{G} \sim 7 \times 10^{-4} M_{\odot}/\text{yr} \left(\frac{T}{300 \text{ K}} \right)^{3/2}. \quad (2.93)$$

Therefore, if mass accretion continues during the lifetime of a massive star, a few Myr, the final mass is thought to be $M \sim 100 - 1000 M_{\odot}$.

In reality, however, feedbacks from the protostars prevents gas accretion and determines the final mass of the first stars. There are two types of feedback to stop accretion; kinematic feedback and radiative feedback. The former comes from outflow by magnetic fields and stellar wind, however, both of them are weak in high-redshift universe. This is because only a primordial magnetic field exists and the strength is thought to be weak ($B \sim 10^{-14}$ G) in a primordial gas cloud, and mass loss through stellar wind is generally low⁴. Therefore, radiative pressure from photoionization and dissociation is a crucial feedback for growth of the first stars.

Hosokawa et al. (2011) perform radiative hydrodynamical simulations, solving the self-consistent stellar evolution at the same time, and investigated a radiative feedback from the primordial protostar and its final mass.

They show that UV photon from the protostar photo-evaporates its accretion disk and stops mass accretion. The final mass of a first star becomes $\sim 40 M_{\odot}$, which is lower than previous expectations of $M = 100 \sim 1000 M_{\odot}$ (e.g. Omukai & Palla 2003; Yoshida et al. 2008, 2006), as shown in Figure 2.8.

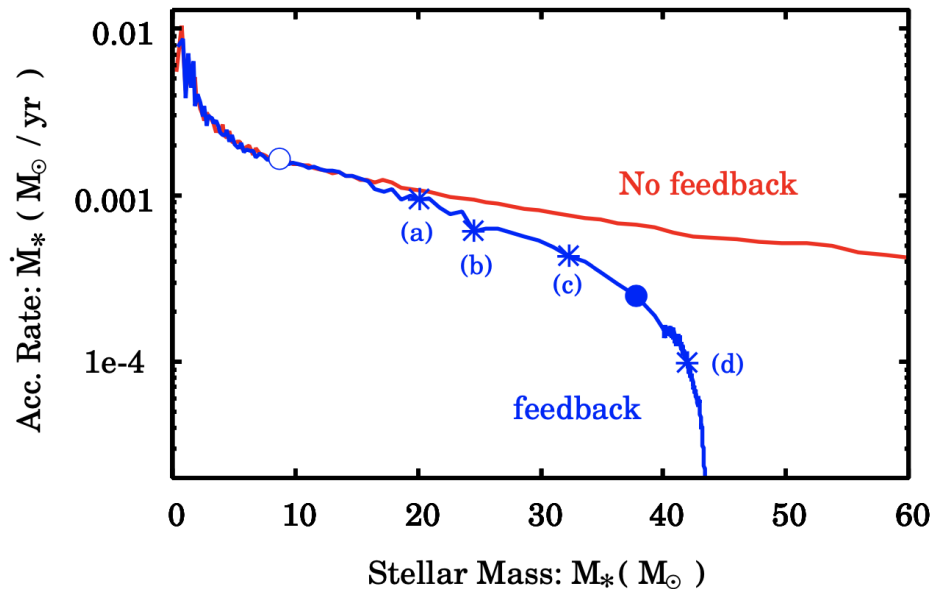


Figure 2.8: Evolution of the accretion rate as a function of stellar mass. A blue (red) line shows a model with (without) radiation feedback. Adopted from Hosokawa et al. (2011).

2.5 Mass distribution of Population III stars

Hosokawa et al. (2011) have examined one halo which exists typically in high-redshift universe (Yoshida et al. 2008). Halo formations have diverse environments, which may lead to various mass distributions of the first stars. Hirano et al. (2014) run cosmological simulations and follow over 100 star-forming clouds and determine the final mass of those first stars by the following

⁴First stars have no heavy elements and small opacity. Therefore, such weak radiation pressure does not induce stellar winds.

RHD simulations as same as Hosokawa et al. (2011). The left figure in Figure 2.9 indicates that star formations start in various timings ($z = 35 - 11$) in DM halos with different virial masses ($M_{\text{vir}} \sim 10^5 - 10^6 M_{\odot}$). The right figure in Figure 2.9 shows a Pop III IMF for ~ 100 first stars and it has a wide mass range from $10 M_{\odot}$ to $1600 M_{\odot}$.

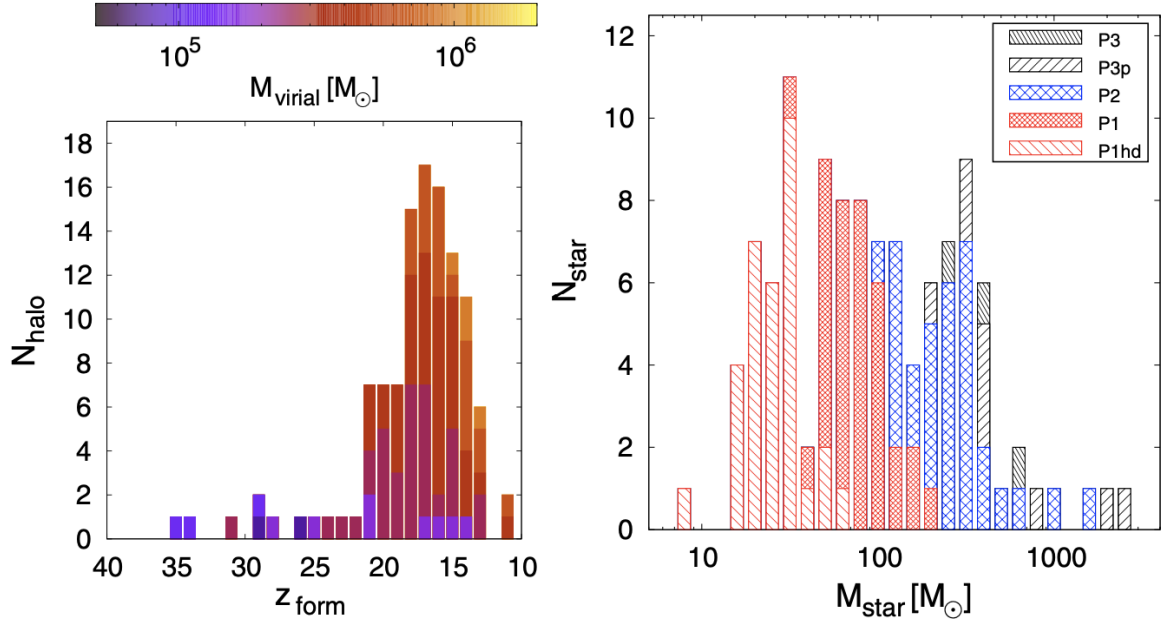


Figure 2.9: Left: Distribution of the timing of star formation. z_{form} is the redshift when a star-forming cloud reaches the density of $\sim 10^6 \text{ cm}^{-3}$. A color bar shows the virial masses of host DM halos. Right: The final mass distribution of the first stars, which corresponds to Pop III IMF. Adopted from Hirano et al. (2014).

2.5.1 Life pathways of Pop III stars

These first stars with different masses have different final pathways as follows.

1. In the case of $M \leq 0.8 M_{\odot}$, stars can survive to the present day because their lifetimes are over cosmic time. These stars are targets for direct observations of Pop III stars in the Milky Way.
2. In the case of $8 M_{\odot} \leq M \leq 40 M_{\odot}$, stars end in core-collapse supernovae (CCSNe). One CCSNe enriches gas to $Z \sim 10^{-3} Z_{\odot}$ (Sluder et al. 2016), thus extremely metal-poor stars might be formed in metal-enriched gas clouds by Pop III star explosions.
3. In the case of $40 M_{\odot} \leq M \leq 140 M_{\odot}$, stars collapse directly to black holes (BHs). Binary Pop III stars within the mass range can form binary BH systems with masses of $20 - 50 M_{\odot}$ (Kinugawa et al. 2014, 2016), whose merger events have been detected as gravitational waves by LIGO and Virgo (e.g. Abbott et al. 2016).
4. In the case of $140 M_{\odot} \leq M \leq 260 M_{\odot}$, stars end in Pair Instability SuperNovae (PISNe).

(Aoki et al. 2014) observe one EMP star which is expected to be formed from metal-enriched gas by PISNe.

5. In the case of $M > 260 M_{\odot}$, helium core directly collapses into a BH.

2.5.2 Remained uncertainty of Pop III mass distribution

There is still uncertainty of Pop III mass distribution with including other effects such as disk fragmentations, magnetic fields, radiation fields, and stream velocity.

Disk fragmentation is found in 3D hydrodynamical simulations and forms secondary stars, which changes Pop III mass distribution significantly. Several simulations have followed the fragmentation processes, but the maximum computational time scale is $\sim 10^3$ yr, not enough to follow the completed evolution for $\sim 10^5$ yr (e.g. Chon & Hosokawa 2019; Clark et al. 2011; Greif et al. 2012; Hirano & Bromm 2017; Inoue & Yoshida 2020; Susa et al. 2014).

Magnetic field might affect disk fragmentations. Primordial magnetic fields are weak ($\sim 10^{-14}$ G) and are thought to be negligible for the first star formation. However, recent studies show that primordial magnetic fields can be amplified in a cloud collapse phase by a small-scale turbulent dynamo. Several current simulations focus on the magnetic field effect in the accretion phase (e.g. Hirano & Machida 2022; Sharda et al. 2021).

Lyman Werner (LW) radiation field as a background or stellar feedback also affects Pop III.2 star formations. This is because LW radiation with energy of 11.2 – 13.6 eV dissociate hydrogen molecule and prevents primordial gas to cool. The dissociation delays the Pop III star formation, or induces the formation of supermassive stars over $10^4 M_{\odot}$ if LW radiation is over the critical value, i.e., $J_{21,\text{crit}} = 100 - 10^3$ (e.g. Bromm & Loeb 2003; Chon et al. 2016; Latif et al. 2021, 2014; Omukai & Palla 2001; O’Shea & Norman 2008; Sugimura et al. 2014).

On the other hand, X-ray or cosmic ray background ionizes hydrogen atoms and increases electrons, which promotes H^- reactions to form H_2 (Hummel et al. 2016, 2015; Inayoshi & Omukai 2012; Park et al. 2021).

Furthermore, relative velocities between baryon and dark matter might have a significant impact on the Pop III star formations and are explained in the next section as a main topic of our research.

2.6 Chapter Summary

Density perturbation originated from inflation grows and forms large-scale filamentary structures in the early universe. DM minihalos with masses of $10^{5-6} M_{\odot}$ are formed in the dense regions at $z \sim 30 - 20$ and primordial clouds form in the DM halo (e.g. Abel et al. 2002; Yoshida et al. 2003). Radiative cooling by H_2 cools gases and enables them to contract to form the protostellar core in the densest center (Yoshida et al. 2008). After the formation of a protostar, gas accretion from an accreting disk or the formation of secondary stars induced by disk fragmentations occur. These stars finally evolve to ZAMS after a few $\times 10^5$ yr.

Chapter 3

Formation and evolution of Supersonically Induced Gas Objects

3.1 Stream Velocity

Structure formation in the early Universe is affected by supersonic relative velocities generated by baryons and dark matter(DM) fluctuations (Tseliakhovich & Hirata 2010). The existence of the relative velocity between baryon and dark matter has already been mentioned in 1970s by Press & Vishniac (1980); Sunyaev & Zeldovich (1970). However, the relative velocity was in second order terms in perturbation theory and was a non-linear effect, thus it has been overlooked until recently. Tseliakhovich & Hirata (2010) show that the relative velocity is supersonic gas flow just after the recombination period which causes a significant impact on the first structure formation in the early universe. Hereafter we call the relative velocity as stream velocity (SV) and explain the impact of SV in the formation of the first object in high-redshift universe.

3.1.1 Growth of small-scale structure including stream velocity

Small fluctuations of matter (e.g. $\delta \sim 10^{-5}$ in CMB) grow gravitationally and finally forms various structures in the universe. The following equations represent the evolution of density fluctuations for baryons (δ_b) and cold dark matter (CDM, δ_c) in comoving coordinates.

$$\frac{\partial \delta_c}{\partial t} + a^{-1} \mathbf{v}_c \cdot \nabla \delta_c = -a^{-1}(1 + \delta_c) \nabla \cdot \mathbf{v}_c \quad (3.1)$$

$$\frac{\partial \delta_b}{\partial t} + a^{-1} \mathbf{v}_b \cdot \nabla \delta_b = -a^{-1}(1 + \delta_b) \nabla \cdot \mathbf{v}_b \quad (3.2)$$

$$\frac{\partial \mathbf{v}_c}{\partial t} + a^{-1} (\mathbf{v}_c \cdot \nabla) \mathbf{v}_c = -\frac{\nabla \Phi}{a} - H \mathbf{v}_c \quad (3.3)$$

$$\frac{\partial \mathbf{v}_b}{\partial t} + a^{-1} (\mathbf{v}_b \cdot \nabla) \mathbf{v}_b = -\frac{\nabla \Phi}{a} - H \mathbf{v}_b - a^{-1} c_s^2 \nabla \delta_b \quad (3.4)$$

$$a^{-2} \nabla^2 \Phi = 4\pi G \bar{\rho}_m \delta_m \quad (3.5)$$

The first two equations are equations of continuity, and the latter two equations are Euler equations for baryons and CDM respectively. The last one is Poisson equation where Φ is total gravitational potential. The baryonic sound speed is denoted c_s . Fourier transforming the above

four equations and eliminating Φ yield

$$\frac{\partial \delta_c}{\partial t} = \boxed{\frac{i}{a} \mathbf{v}_{bc}^{(bg)} \cdot \mathbf{k} \delta_c} - \theta_c \quad (3.6)$$

$$\frac{\partial \theta_c}{\partial t} = \boxed{\frac{i}{a} \mathbf{v}_{bc}^{(bg)} \cdot \mathbf{k} \theta_c} - \frac{3H^2}{2} (\Omega_c \delta_c + \Omega_b \delta_b) - 2H\theta_c \quad (3.7)$$

$$\frac{\partial \delta_b}{\partial t} = -\theta_b \quad (3.8)$$

$$\frac{\partial \theta_b}{\partial t} = -\frac{3H^2}{2} (\Omega_c \delta_c + \Omega_b \delta_b) - 2H\theta_b + \frac{c_s^2 k^2}{a^2} \delta_b \quad (3.9)$$

The two terms in the boxes are stream velocity terms and second order, where \mathbf{v}_{bc} is a relative velocity between baryons and dark matter, $\mathbf{v}_{bc} \equiv \mathbf{v}_b - \mathbf{v}_c$. The terms are negligible at wavenumbers $k \ll k_{vbc} \sim 40 \text{ Mpc}^{-1}$. The variance of SV is

$$\Delta_{vbc}^2(k) = \Delta_\xi^2(k) \left[\frac{\theta_b(k) - \theta_c(k)}{k} \right]^2, \quad (3.10)$$

where $\Delta_\xi^2(k) = 2.42 \times 10^{-9}$ is the initial curvature perturbation variance per $\ln k$. Integrating the variance by $\ln k$ yields the rms SV,

$$\langle v_{bc}^2(x) \rangle = \int \frac{dk}{k} \Delta_{vbc}^2(k). \quad (3.11)$$

Figure 3.1 shows the power-spectrum of stream velocity at the scale of k . The power-spectrum rapidly decreasing at small scale of $k > 0.5 \text{ Mpc}^{-1}$. Thus, stream velocity is constant in a few comoving Mpc. Integration of eq. 3.11 gives the rms velocity σ_{vbc} is $\sigma_{vbc} \sim 30 \text{ km/s}^1$.

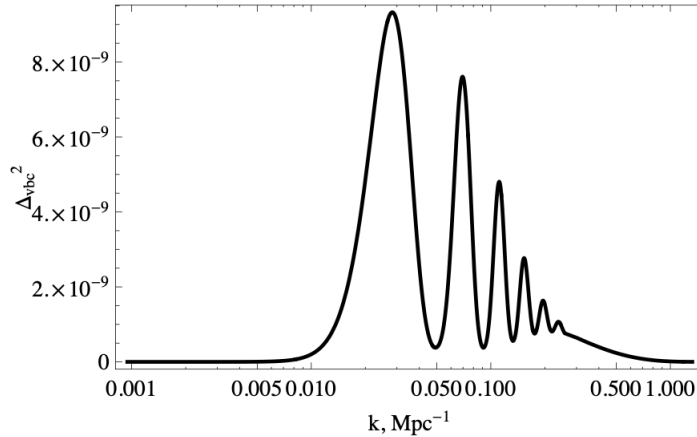


Figure 3.1: The variance of stream velocity perturbation per $\ln k$ as a function of wavenumber. The power spectrum drops rapidly at $k > 0.5 \text{ Mpc}^{-1}$, which indicates that stream velocity is coherent flow in a few comoving Mpc scale. On much larger scale such as $k < 0.01 \text{ Mpc}^{-1}$ (\sim BAO scale), the fluctuations of stream velocity are correlated. Adopted from Tseliakhovich & Hirata (2010)

¹Notice that this rms is evaluated assuming three-dimensional motions.

Before the recombination, baryons and photons are coupled with each other and the baryonic sound speed was relativistic, $c_s = \frac{c}{\sqrt{3}}$. After the recombination, the sound speed of the gas component is equal to the kinetic speed of atomic hydrogen,

$$c_s = \sqrt{\frac{\gamma k T_b}{\mu m_H}}, \quad (3.12)$$

where

$$\gamma = \frac{5}{3} \quad (\text{an ideal monoatomic gas}) \quad (3.13)$$

$$\mu = 1.22 \quad (\text{mean molecular weight with a helium mass fraction of 0.24.}) \quad (3.14)$$

$$m_H = 1.67 \times 10^{-24} \text{ g} \quad (\text{the mass of hydrogen atom}) \quad (3.15)$$

$$T_b = \frac{T_{\text{CMB},0}}{a} = \frac{2.726}{a} \text{ K} \quad (3.16)$$

The calculating the above at the recombination period, i.e., at $z = 1020$ ($a = 0.009794$), the sound speed is $c_s \sim 6 \text{ km/s} = 2 \times 10^{-5} c$. Therefore, rms of stream velocity is five times larger than sound speed at the recombination period and the gas has a supersonic flow relative to CDM. Stream velocity decays with redshift ($1 + z$) and can affect only at very high redshift. Furthermore, the three-dimensional SV field follows Maxwell-Boltzmann distribution,

$$P(v_{\text{bc},3\text{D}}) = \left(\frac{3}{2\pi\sigma_{\text{vbc}}^2} \right)^{3/2} 4\pi v^2 \exp\left(-\frac{3v^2}{2\sigma_{\text{vbc}}^2}\right), \quad (3.17)$$

where σ_{vbc} is rms of three-dimensional stream velocity.

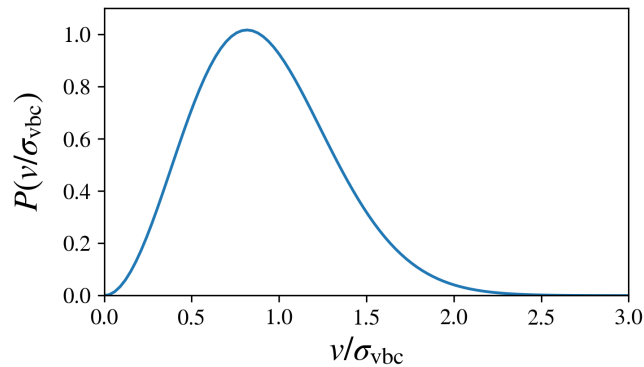


Figure 3.2: The distribution of stream velocity. SV follows three-dimensional Maxwell-Boltzmann distribution.

Visbal et al. (2012) and Fialkov et al. (2013) conduct numerical calculations to see the global distribution of SV and density fluctuation. Figure 3.3 is the sliced distribution within the region of about 400 comoving Mpc.

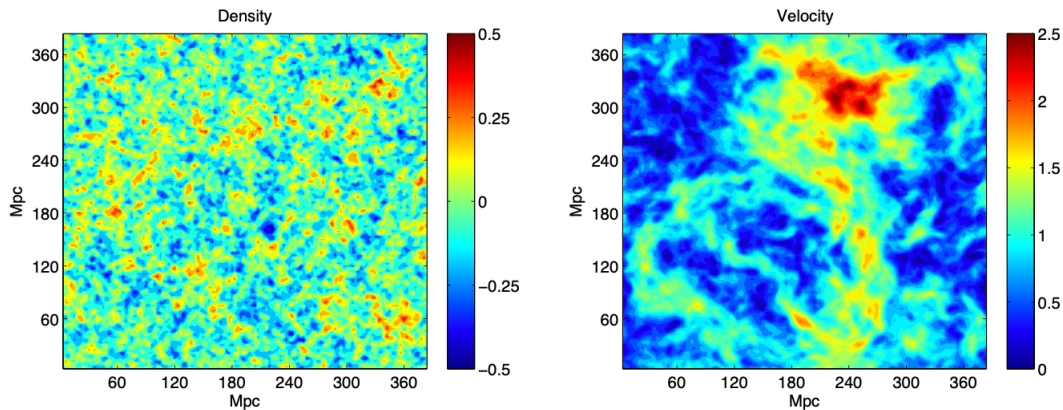


Figure 3.3: Left: The sliced distribution of baryon density fluctuations at $z = 20$. The simulated boxsize is 384 comoving Mpc on a side. Right: The sliced distribution of Stream velocity at $z = 20$. The color bar shows the magnitude of SV in units of its rms(σ_{vbc}). The SV distribution follows Maxwell-Boltzmann distribution in Figure 3.2. Adopted from Fialkov et al. (2013).

Also, including SV term in the Press-Schechter function (Press & Schechter 1974) shows that halo number density is suppressed mostly in $M_{\text{halo}} \sim 10^6 M_{\odot}$ (Tseliakhovich & Hirata 2010). This halo mass is a typical one for the first star formation (Yoshida et al. 2003) and SV has been thought to have a crucial impact on the cosmic structure formation in the early universe.

3.1.2 Numerical simulations including stream velocity

In order to examine the effect of stream velocity at high redshift, several hydrodynamical simulations have been performed with incorporating SV. It is shown that SV lowers the gas fraction in low-mass DM halos and prevents or delays the formation of star-forming clouds (Bovy & Dvorkin 2013; Fialkov et al. 2012; Greif et al. 2011; Naoz et al. 2012; Schauer et al. 2019; Tseliakhovich et al. 2011). For example, Greif et al. (2011) show that the formation of Pop III stars is delayed by $\Delta z \simeq 4$. Figure 3.4 show the delayed collapse timings due to SV. Also, SV can increase the virial mass at the collapse phase, as the same as filtering mass (Naoz et al. 2013).

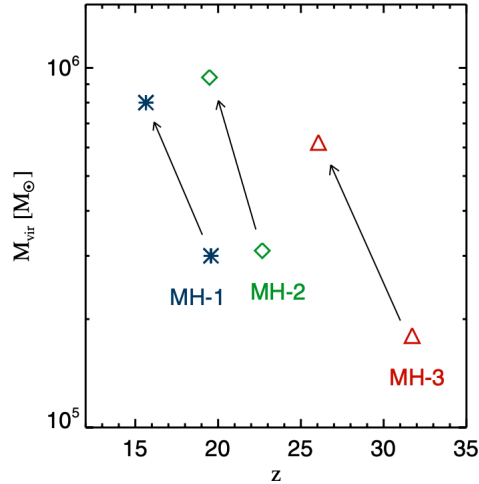


Figure 3.4: Collapse timing and the virial mass at each collapse redshift. MH-1(blue), MH-2 (green) and MH-3(red) represent three different simulated minihalos. Each lower symbol is the case with no stream velocity, and the upper one is the case with $1\sigma_{vbc}$ stream velocity. Adopted from Greif et al. (2011).

The delay of star formation due to SV realizes different physical conditions than previously studied (Hirano et al. 2017, 2018; Kulkarni et al. 2020; Latif et al. 2014; Schauer et al. 2021b; Tanaka & Li 2014). For example, Hirano et al. (2017) find that SV generates strong turbulence in massive gas clouds and increases Jeans mass as the following equation,

$$M_J = \frac{\pi}{6} \frac{(c_s^2 + v_{bc}^2)^{3/2}}{G^{3/2} \rho^{1/2}}. \quad (3.18)$$

The subsequent collapse proceeds rapidly and has a large accretion rate $\dot{M} > 1 M_\odot/\text{yr}$, which is much larger than critical accretion rate of $\dot{M} = 0.04 M_\odot/\text{yr}$. Finally a supermassive star with mass over $10^4 M_\odot$ can be formed in the cloud center, which ends in direct collapse to become a seed of a Super Massive Black Hole (SMBH).

Furthermore, the suppression of low-mass halo formation at high redshift due to SV may change the history of the cosmic reionization and 21 cm signal (Fialkov et al. 2012; Long et al. 2022; McQuinn & O’Leary 2012; Park et al. 2013, 2021; Visbal et al. 2012).

3.1.3 Supersonically Induced Gas Objects (SIGOs)

Intrestingly, the stream velocity suggests a possibility to form peculiar objects in the early universe. Naoz & Narayan (2014) show that SV introduces a phase shift of baryon and DM density fluctuations, which leads spatial offsets between them. In such separated baryon density peak, bayon-dominant object can be formed outside of the DM halos. Figure 3.5 shows the spatial separation between gas clumps and DM halos at $1\sigma_{vbc}$ SV as a function of masses of the gas clumps. We see that s gas clump with mass of $M \leq 10^6 M_\odot$ has a larger separation than the virial radius of the conterpart DM halo.

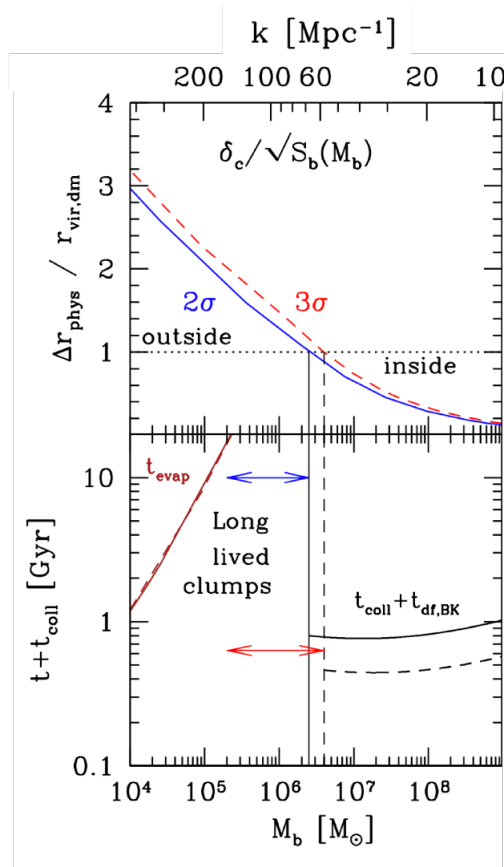


Figure 3.5: (top): The spatial offset between gas clumps and DM halos, normalized by the virial radii of DM halos. Blue and red-dotted lines represent 2σ and 3σ density fluctuation cases as a function of gas clump mass M_b . (bottom): Surviving time scale of gas clumps. Gas clumps outside (inside) halos may experience evaporation (dynamical friction). The red and blue arrows show the mass range of gas clumps that survive as long-lived gas clumps. Adopted from Naoz & Narayan (2014).

Such gaseous objects generated by SV are called Supersonically Induced Gas Objects, short for SIGOs. They may be a new type of progenitors of primordial star clusters. SIGOs have already been identified in several recent simulations. For example, Popa et al. (2016) and Chiou et al. (2018) used hydrodynamical simulations with SV to show that gas-dominated objects are formed in the early universe. Later, Chiou et al. (2019, 2021) incorporated atomic hydrogen cooling in their hydrodynamical simulations and showed that a number of dense SIGOs are formed. However, it remains unclear whether or not, and how, stars are actually formed in SIGOs.

Molecular hydrogen cooling may play a vital role in the early universe (see section 2.3.2). H_2 cooling can lower the temperature of primordial gas clouds to ~ 200 K. Gas clouds with the corresponding Jeans mass of $\sim 1000 M_\odot$ become gravitationally unstable to collapse further to form stars (Yoshida et al. 2008). In this thesis, we perform cosmological simulations with SV in order to study the formation and evolution of SIGOs. We incorporate H_2 cooling and examine if SIGOs can cool and condense to form stars.

3.2 Methods

3.2.1 Cosmological simulation

We use the cosmological simulation code AREPO (Springel 2010). We first run parent simulations with employing 512^3 DM particles with a mass of $1.9 \times 10^3 M_\odot$ and 512^3 Voronoi mesh cells with a mass of $360 M_\odot$. The simulation box size is 1.4 cMpc/h on a side. We use a modified version of the CMBFAST code (Seljak & Zaldarriaga 1996) to generate the transfer functions for the initial conditions. The transfer function calculations incorporate the first-order scale-dependent temperature fluctuations (Naoz & Barkana 2005) and the effect of SV. As in Chiou et al. (2019, 2021), we generate the initial conditions by setting a large density fluctuation amplitude of $\sigma_8 = 1.7$. This choice is aimed at simulating a rare, over-dense region in a large volume where structure forms early.

We run for simulations listed in Table 3.1. “2v” or “0v” represents with/without SV, and “H2” or “H” denotes whether H_2 cooling is turned on/off respectively. For the Run 2vH2 and 2vH, we add a coherent SV with $2\sigma_{\text{vbc}} = 11.8$ km/s in the $+x$ -direction to the baryonic component at the initial redshift $z_{\text{ini}} = 200$. We run the parent simulations to $z = 25$.

Run	v_{bc}	H_2 Cooling
0vH2	0	Yes
0vH	0	No
2vH2	$2\sigma_{\text{vbc}}$	Yes
2vH	$2\sigma_{\text{vbc}}$	No

Table 3.1: Simulation parameters. σ_{vbc} is rms of SV and $\sigma_{\text{vbc}} = 5.6$ km/s at $z_{\text{ini}} = 200$. Cooling “No” represents run with only atomic cooling.

3.2.2 Chemistry and cooling

We follow non-equilibrium chemical reactions and the associated radiative cooling in a primordial gas. We use the chemistry and cooling library GRACKLE (Chiaki & Wise 2019; Smith et al. 2017). The chemistry network includes 49 reactions for 15 primordial species: e, H, H^+ , He, He^+ , He^{++} , H^- , H_2 , H_2^+ , D, D^+ , HD, HeH^+ , D^- , and HD^+ . We include H_2 and HD molecular cooling. The radiative cooling rate by H_2 is calculated by both rotational and vibrational transitions (Chiaki & Wise 2019). The initial abundance of each species at $z_{\text{ini}} = 200$ is based on Galli & Palla (2013) as shown in Figure 3.6. All reactions are described in Appendix 6.

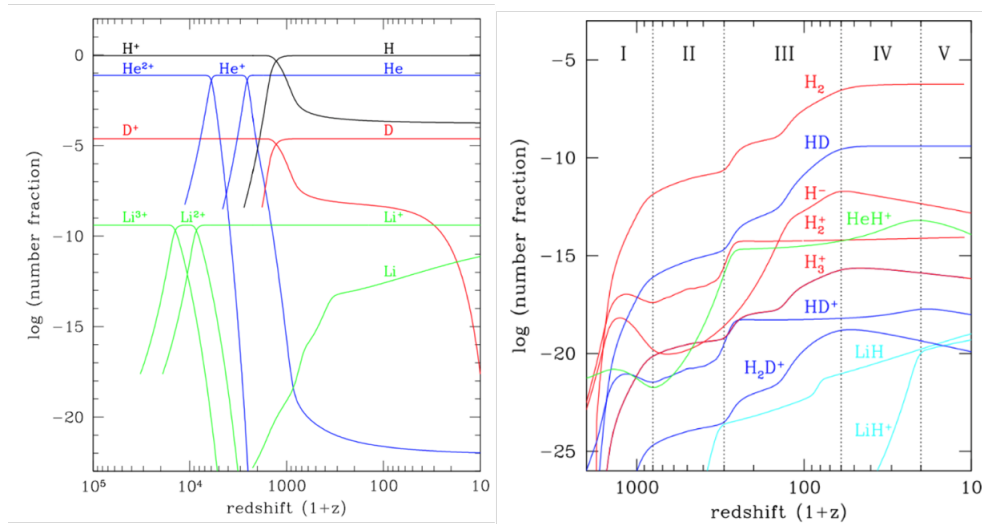


Figure 3.6: Number fraction of primordial chemical species relative to the total number of baryons as a function of redshift. (left): Abundances of H, D, He, and Li through the cosmological recombination. (right): Abundances of main molecules and ions for a primordial gas. Adopted from Galli & Palla (2013).

3.2.3 Definition of SIGOs

We first identify nonlinear objects such as DM halos in essentially the same manner as in Chiou et al. (2018); Popa et al. (2016). We run a Friends-of-Friends(FOF) group finder with a linking length of $b = 0.2$ times the mean particle separation (Dolag et al. 2009). The value of b results in the enclosed overdensity of $\Delta \sim 180$, which is the corresponding overdensity of virialized halos for spherical collapse model (see section 1.2.3). The smallest DM halos contain typically ~ 300 DM particles. We also run the FOF finder to the gas components in order to identify “gas-only” objects that contain over 100 gas cells. The minimum mass of the gas halos and the DM halos are $3.68 \times 10^4 M_\odot$ and $6.04 \times 10^5 M_\odot$ respectively. This threshold excludes small mass halos but allows us to avoid non-physical numerical effects and to calculate the gas fraction in gas-rich region with the accuracy of 10-20% (Naoz et al. 2009).

We calculate the gas mass fraction for the identified DM halos and gaseous clouds. Many of the detected gas clouds are filamentary, and thus it is not appropriate to measure the baryon fraction assuming spherical symmetry. We adopt an ellipsoid approximation introduced in Popa et al. (2016). We outline this procedure here for completion. First, for each gas halo/cloud identified by our FOF finder, we consider an ellipsoidal surface that surrounds all of the constituent gas cells. Then the major axis of the ellipsoid is reduced by a small amount of 0.5%. We repeat this procedure until the condition

$$\frac{a_{\text{gas},n}}{a_{\text{gas},0}} > \frac{N_{\text{gas},n}}{N_{\text{gas},0}}, \quad (3.19)$$

or $N_{\text{gas},n}/N_{\text{gas},0} < 0.8$, is met, where $a_{\text{gas},0}$ is the major axis of the original ellipsoid and $a_{\text{gas},n}$ is that of the ellipsoid after the n th iteration. Similarly, $N_{\text{gas},0}$ and $N_{\text{gas},n}$ are the number of gas

cells. Note that the threshold value of the ratio $N_{\text{gas},n}/N_{\text{gas},0} = 0.8$ is determined by Popa et al. (2016), who have analyzed the ellipsoidal shape of SIGOs.

This iterative procedure successively shrinks the long axis of a gas halo while retaining the high-density region. We then calculate the gas fraction of each ellipsoid as

$$f_{\text{gas}} = \frac{M_{\text{gas}}}{M_{\text{gas}} + M_{\text{DM}}} \quad (3.20)$$

where M_{gas} and M_{DM} are the masses of the gas cells and DM particles within the defined ellipsoid, respectively. We note that the mass center of a SIGO is taken as the center of its ellipsoid, whereas Schauer et al. (2021a) take the highest-density point as a center of a gas clump. We have checked both coordinates of our SIGOs, and have found that the deviation is typically a small fraction (~ 0.1) of the size of the ellipsoid.

Finally, we identify SIGOs that satisfy the following two conditions:

- (1) The mass center of the gas cells is outside the virial radii of its closest DM halo(s)
- (2) there are at least 32 gas cells and the gas mass fraction is greater than 0.6 in each defined ellipsoid.

We note that the threshold value here is larger than the 0.4 adopted in Chiou et al. (2021). We have found that, when the critical value is set to 0.4, filamentary structures tend to be identified as SIGOs, especially in Run 0vH2, and many SIGOs are misidentified. We thus set $f_{\text{gas,crit}} = 0.6$.

3.2.4 High-resolution simulation with smaller Box Size

We are not able to follow the evolution of SIGOs to $z < 25$ in our parent simulation. This is because the gravitational and hydrodynamical time scales become too short in other high-density star-forming regions in the simulated volume, and the calculations do not proceed.

We thus reconfigure and continue the simulation by ignoring the evolution of the other halos and gas clouds far from a target SIGO, but with increasing the mass resolution in and around it. In practice, we cut out a cubic region of 10 physical kpc on a side centered at the SIGO. We then advance the "high-resolution" simulation by performing refinement of gas cells to ensure that the local Jeans length is always resolved with at least 64 cells. The simulation results are shown in 3.3.4. In both our parent and high-resolution simulations, we do not include a Lyman-Werner radiation background because the background intensity is expected to be significant only at $z < 15$ according to the cosmological simulations of Agarwal et al. (2012).

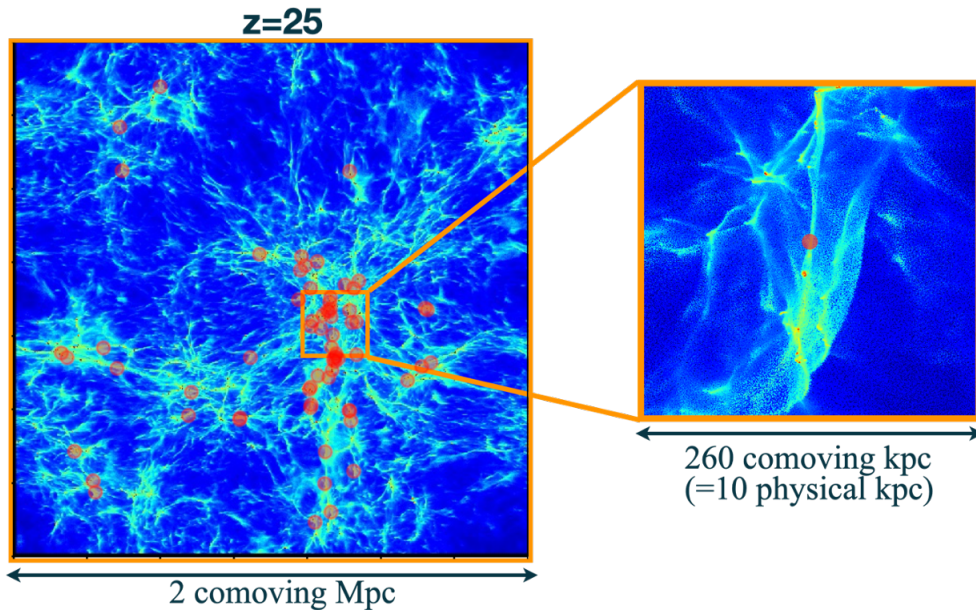


Figure 3.7: Overview of a high-resolution simulation. 68 SIGOs are identified in Run 2vH2 and are shown as red dots. In the further high-resolution simulation, we pick up one SIGO (S1) which is located in the center of the right panel. We cut off the region around S1 with a side length of 10 physical kpc.

Furthermore, we can justify the volume by simply examining possible boundary effects. After the high resolution simulation is initiated at $z = 25$, the boundary effect (if any) would propagate toward S1 at the center with soundspeed of a few km /sec. S1 collapses dynamically over a time of 33 million years (from $z = 25$ to 21), and any disturbance from the boundary propagates only ~ 0.1 kpc.

At $z = 25$, the distance to the neighboring fast contracting halo is 5.18 kpc (the coordinates relative to S1 are [0.0548, 3.4744, 3.85] (unit is [kpc])). The widest size of the area that was not affected by other halos in which we are not interested is 10 physical kpc.

3.3 Result

3.3.1 Density distribution for each run

Figure 3.8 shows gas density distribution in the hole boxsize for each run at $z = 25$. The left two panels (Run 0vH2 and Run 0vH) do not include SV but the right two panels (Run 2vH2 and 2vH) include SV. The effect of SV is clearly seen as coherent stream features from left to right in Run 2vH2 and 2vH. Gas is swept away in the direction of SV ($+x$ direction) and small-scale structure formation is suppressed. This result is consistent with that of Schauer et al. (2021a,b). At $z = 25$, the number of isolated density peaks with $n > 10^3 \text{ cm}^{-3}$ identified in Run 2vH2, 2vH, 0vH2, 0vH is 831, 642, 2508, 1758, respectively. With SV, there are 68 and 36 SIGOs in Run 2vH2 and 2vH. SV causes the gas density peaks to move fast with respect to the underlying DM, and some gas clouds start contracting while being outside of any DM halo. Note also that

twice as many SIGOs are formed in Run 2vH2 than in Run 2vH case at $z = 25$. SV causes the gas density peaks to move fast with respect to the underlying DM, and some gas clouds start contracting while being outside of any DM halo. Note also that twice as many SIGOs are formed in Run 2vH2 than in Run 2vH case at $z = 25$. This is caused by the effective gas contraction by H_2 radiative cooling.

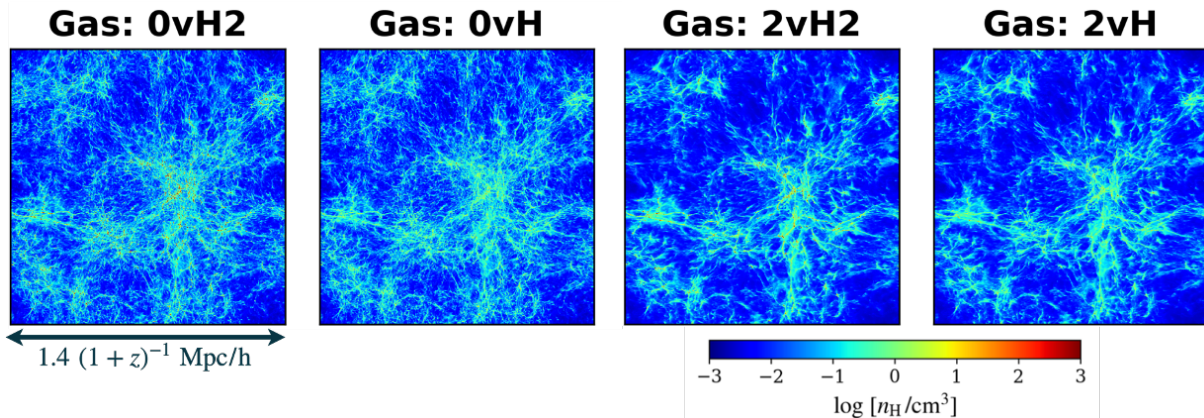


Figure 3.8: The projected gas number density distributions in our simulations, without SV (Run 0vH2, 0vH; left two figures) and with SV (Run 2vH2, 2vH; right two figures). Run 0vH and Run 2vH do not include H_2 chemistry. Each colormap shows a region with a side length and a depth of $1.4/h$ comoving kpc. We use the outputs at $z = 25$.

3.3.2 Evolution of SIGO (S1)

As explained in section 3.2.4, we focus on the evolution of a particular gas cloud "S1" that is identified as a SIGO in Run 2vH2 at $z = 25$. Figure 3.9 represents gas and DM structures around S1 from $z = 31$ to $z = 25$. S1 is located in the center of the right panel as a small gas clump. S1 is fitted as an ellipsoid and its major axis has a length of 1.15 kpc (see Figre 3.11).

First of all, filamentary DM structures are formed at $z = 31$ and the corresponding gas structures are formed with filamentary shape. At this time, SV is flown in the direction of left to right, which makes gas density peak displaced to right. The value of SV at $z = 31$ is

$$v_{\text{bc}} \sim 2\sigma_{\text{bc,rec}} \frac{1+z}{1+z_{\text{rec}}} = 1.9 \text{ km s}^{-1}. \quad (3.21)$$

As DM large structures evolve, the gas filament starts "moving back toward" the gravitational potential of the DM structure from $z = 31$ to $z = 25$. Figure 3.10 shows the velocity distribution of gas filament. The gas filament is compressed from both side; from left velocity due to SV and from right velocity due to the gravitational potential for DM filamentary structure located on the left of S1. Intrestingly, gas movement from both directions makes a shock on the gas filament. Gas temprature is as high as $\sim 10^4$ K at the shock front. This can be seen in only runs with SV cases; 2vH and 2vH2.

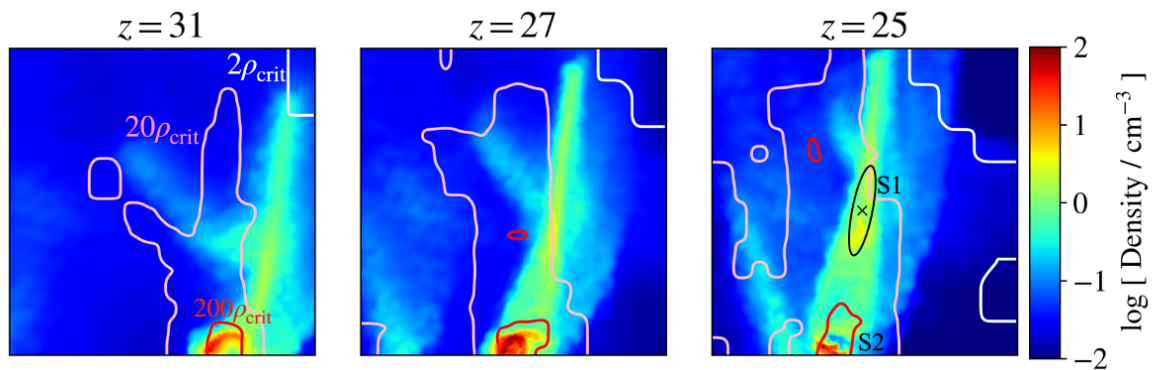


Figure 3.9: The projected density distribution of gas and DM around a gas cloud S1 in Run 2vH2. SV works from left to right in each panel. The colormap shows the gas number density and the countour lines represent the DM mass density. White, pink and red contour lines indicate 2, 20, 200 times the critical density of the universe, respectively. The black line shows S1 ellipsoid and the mark X is the mass center of S1. The other gas clump which is located in the bottom of S1 and has a high density of over 100 cm^{-3} is named S2. S2 is hosted by the closest DM halo and identified as a non-SIGO. Each panel shows the region with a side length of 40 comoving kpc.

At $z = 25$, there is no obvious DM halos around S1 and the local baryon fraction is $f_{\text{gas}} = 0.67$. The closest DM halos of S1 is located in the bottom in Figure 3.9, which represents in a red contour line. The distance between S1 and the closest DM is 1.1 physical kpc, which is over 4 times larger than the virial radius of the DM halo. S1 has the central density of 8.0 cm^{-3} and the temperature of $\sim 500 \text{ K}$, which implies that S1 is on the way of contracting by H_2 cooling.

In order to see the stability of S1 quantitatively, we calculate the ratio of the enclosed mass M_{enc} to the Jeans mass,

$$M_J = \frac{\pi}{6} \frac{c_s^3}{G^{3/2} \rho^{1/2}}, \quad (3.22)$$

where ρ is the density, c_s is the speed of sound and G is the gravitational constant. We take averaged ρ and c_s by weighting mass within radius r ². The right panel of Figure 3.11 shows the radial profile of S1 at $z = 25$ and we see that S1 is still Jeans stable at all radii. This result is consistent with Schauer et al. (2021a), who also find similar gas clumps located outside of their closest DM halos due to the SV.

Furthermore, the closest DM halo of S1 contains another massive and dense gas clump "S2" as indicated in the bottom of Figure 3.9. S2 can contract much faster than S1 due to the additional gravity from the host DM mini-halo and it has already formed the first unstable cloud at $z = 28$ with $M_J \sim 10^5 M_{\odot}$. $n_{\text{gas}} \sim 10^3 \text{ cm}^{-3}$, which is corresponding the primordial

²Hirano et al. (2017) calculate Jeans mass with including SV as a turbulence term;

$$M_J = \frac{\pi}{6} \frac{(c_s^2 + v_{\text{bc}}^2)^{3/2}}{G^{3/2} \rho^{1/2}} \quad (3.23)$$

This is because they focus on gas clouds in the DM halos and SV flows more gas into the DM halo, which leads turbulence in the cloud. However, SIGO (S1) is not hosted by DM halo, thus SV contributes to the translational motion of S1. Therefore, we do not include SV term in the equation of Jeans mass.

gas cloud in 2σ SV case in Hirano et al. (2018)³. The distance between S1 and S2 is ~ 30 comoving kpc (Figure 3.9; there is also a separation of ~ 20 comoving kpc in z direction). Therefore, radiative feedback effect from S2 is unlikely to affect the star formation in S1 (more quantitative estimation is described in section 3.3.5). Also, the separation does not cause tidal effect on S1.

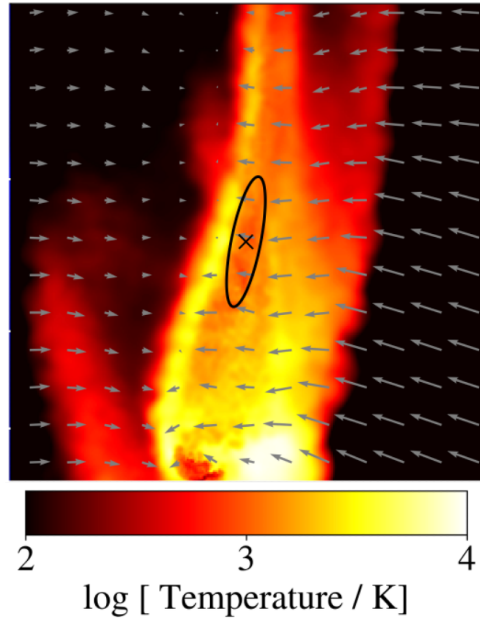


Figure 3.10: Temperature distribution and velocity distribution around S1 at $z = 25$. Colormap shows the gas temperature distribution and black arrows indicate gas velocity. S1 is located in the center of the figure as shown in a black ellipsoid and an X mark. One side of length and depth is 40 comoving kpc.

3.3.3 Comparison with each run

We have checked whether a similar SIGO forms at or near the same position as S1 in Run 0vH2 and 2vH. Figure 3.12 shows the density distribution for gas (colormap) and DM (contour lines) in Run 0vH2, 2vH2 and 2vH at the same redshift $z = 25$. In the left most panel, Run 0vH2 does not include SV, thus the location of DM filamentary structures and gas filaments are coincided with each other. However, Run 2vH2 and 2vH include SV and there is an offset of density peak of DM and gas. The offset delays the gas contraction for small gas clumps. Run 2vH, particularly, has only atomic cooling, which is effective gas with 8000 K (Barkana & Loeb 2001b). Therefore, gas cannot contract to high density and no gas clumps are detected in Run 2vH in the region of Figure 3.12.

On the other hand, Run 0vH2 contains H_2 cooling, which is an effective coolant for primordial gas with temperature $200 \text{ K} \lesssim T_{\text{gas}} \lesssim$ a few 1000 K. The molecular cooling forms a gas clump

³When we calculate Jeans mass for non-SIGO, we adopt the equation 3.23, the same as Hirano et al. (2017, 2018).

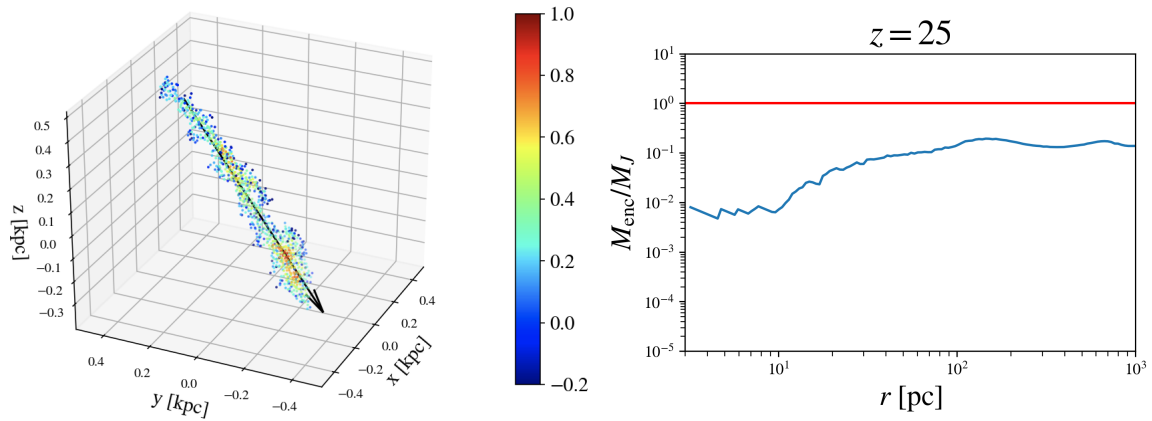


Figure 3.11: Left: Color dots indicate the number density of S1. The black arrow is the direction vector toward the closest DM halo. Right: Ratio of enclosed gas mass to the local Jeans mass at $z = 25$. When the curve exceeds $M_{\text{enc}}/M_J = 1$ (a red horizontal line), the gas cloud became Jeans unstable.

”S3” corresponding to S1 as shown in Figure 3.12. In order to check whether S3 is SIGO or not, we also calculate baryon fraction (F_{bar}) of S3 and compare the value with that of S1. Figure 3.13 shows the F_{bar} radial profiles of S1 and S3 at $z = 25$, and mean cosmic baryon fraction as a green line. F_{bar} of S1 is larger than the cosmic mean fraction in the all radii within $\sim 10^3$ pc. F_{bar} of S3, however, is smaller than the mean cosmic baryon fraction in the region of $r \lesssim 10^3$ pc. In consequence, S3 is a non-SIGO which is hosted by a DM mini-halo. The physical properties of S3 is summarized in Table3.2.

From the comparison with Run 0vH2, 2vH2 and 2vH, we conclude that SIGOs are formed via combined effect of Stream velocity and H_2 cooling; SV causes the density offset between DM and gas, and H_2 cools and contracts gas clumps to high densities.

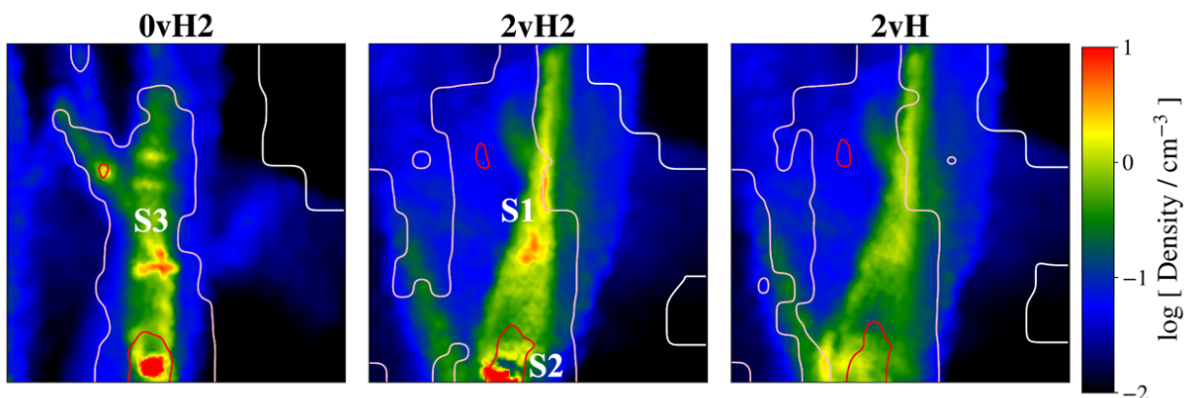


Figure 3.12: The projected density distribution for gas and DM, the same as Figure 3.9. Panels from left to right indicate the case of Run 0vH2, 2vH and 2vH. S3 in Run 0vH2 is located in almost the same position as S1. The one side length of each colormap is 40 comoving kpc.

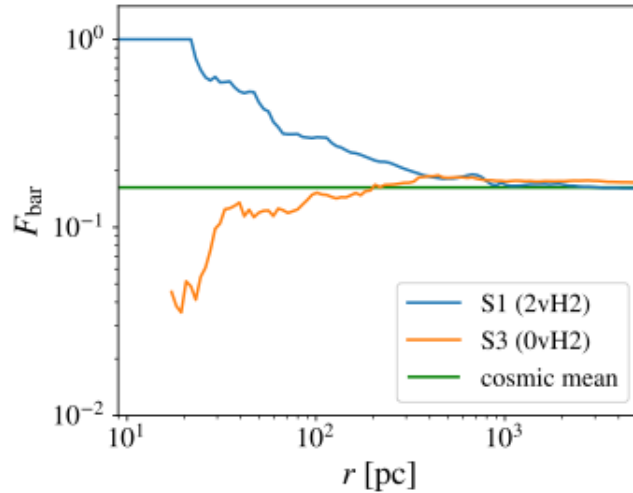


Figure 3.13: Baryon fraction radial profiles of S1(Run 2vH2) and S3(Run 0vH2) at $z = 25$. The horizontal green line shows the cosmic mean values of baryon fraction; $\Omega_b/\Omega_m = 0.044/0.27 = 0.16$. The baryon fraction is calculated as (enclosed gas mass)/(enclosed (DM+gas) mass).

Properties	S1	S2	S3
Run	2vH2	2vH2	0vH2
Classification	SIGO	non-SIGO	nonSIGO
Density [cm^{-3}]	7.97	6.89×10^3	11.6
Mass [M_\odot]	3.8×10^5	8.2×10^5	1.4×10^5
Radius [kpc]	0.20	0.21	0.20
Host DM halo mass [M_\odot]	-	6.2×10^6	8.5×10^5
local baryon fraction (f_{gas})	0.67	0.21	0.18

Table 3.2: Gas clump properties at $z = 25$. S1 is a SIGO in Run 2vH2, S2 is a non-SIGO which is the closest clump to S1, and S3 is the corresponding halo to S1.

3.3.4 High-resolution simulation with refinement

As explained in section 3.2.4, we perform high-resolution simulation around S1 with gas cell refinement. Figure 3.14 indicates the further evolution of S1 from $z = 25$ to $z = 21.4$, where S1 has reached Jeans instability. The colormap and contour lines indicate gas number density and DM mass over-density respectively. The distance between S1 and its closest DM halo is over four times larger than the halo's virial radius. Figure 3.15 shows various physical properties of S1 at $z = 21.4$ as a function of radius. Panel A indicates that S1 keeps a high baryon fraction and it is even larger than the cosmic mean baryon fraction within $r \lesssim 200$ pc, where the gas density is over 200 times critical density (Panel D). Panel B shows the ratio of the enclosed gas mass to Jeans mass and S1 becomes Jeans unstable (the ratio is over 1) at radius $r = 50 - 100$ pc. Panel C is a temperature-density phase plot of S1 and it is clear that S1 cools to 200 K via H_2 radiative cooling and becomes Jeans unstable at $n_{\text{gas}} \sim 100 \text{ cm}^{-3}$. The H_2 mass fraction in panel E is $f_{\text{H}_2} \sim 10^{-3}$, which is consistent with the result of Yoshida et al. (2006), who follow

the chemothermal evolution of primordial gas. Panel F shows the comparison of the speed of sound and stream velocity and SV is subsonic in cloud S1. We follow further evolution of S1 and find that S1 proceeds the runaway collapse and exceeds the density of $n_{\text{gas}} = 10^5 \text{ cm}^{-3}$ at $z = 20.0$. The ratio of contraction time ($t_{\text{cont}} = \rho/\dot{\rho}$) to free-fall time t_{ff} for S1 is also calculated and we find that t_{cont} is comparable to t_{ff} , and also to H_2 cooling time scale.

From the information in Figure 3.14, Jeans mass is calculated as $M_J = 5 \times 10^4 M_{\odot}$, which is 50 times larger than that of a typical primordial gas cloud hosted by a DM mini-halo. This is because the density when S1 becomes Jeans unstable is low ($\sim 100 \text{ cm}^{-3}$) owing to slow contraction of gas-only self-gravity, without DM gravitational potential. The large Jeans mass is consistent with the mass estimation of Naoz & Narayan (2014) and interestingly comparable to the conclusion of Peebles & Dicke (1968) who studied the formation of primordial star clusters that are not hosted by DM halos.

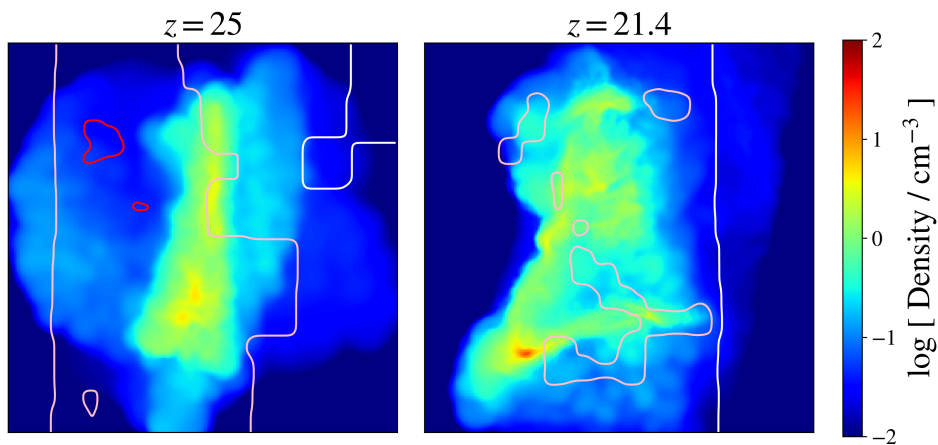


Figure 3.14: The projected density distribution for gas and DM, the same as Figure 3.9. The left and right panel shows the density distribution of S1 at $z = 25$ and $z = 21.4$ respectively. The projection region has a side length of 1 physical kpc.

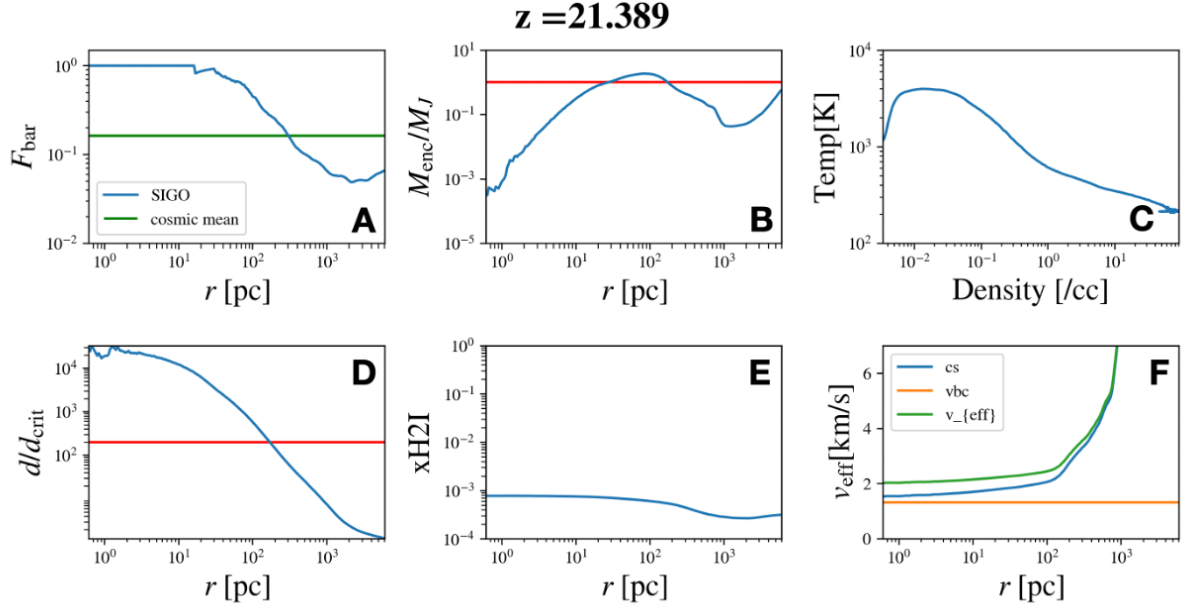


Figure 3.15: Radial profiles of various physical quantities at $z = 21.4$, when S1 reaches Jeans instability. Panel A: baryon fraction. A green line indicate cosmic mean baryon fraction $\Omega_b/\Omega_m = 0.044/0.27 = 0.16$. Panel B: ratio of enclosed gas mass to the local Jeans mass. A red line indicates $M_{\text{enc}}/M_J = 1$. Panel C: thermal evolution. Panel D: gas number density divided by the critical density of gas. A red line indicates the gas density is 200 times the critical density. Panel E: the mass fraction of molecular hydrogen. Panel F: the local speed of sound (blue), stream velocity at $z = 21.4$ (orange), and effective speed of sound $v_{\text{eff}} = (c_s^2 + v_{\text{bc}}^2)^{3/2}$ (green).

3.3.5 Caveats

radiative feedback from neighboring non-SIGO

We examine the possibility that Lyman-Werner radiation from a local source which is located at 30 ckpc away from S1 following Susa (2007). The effect of the LW radiation can be judged by comparing two time scales, H_2 dissociation time by Lyman-Werner radiation t_{dis} and the free fall time t_{ff} . If $t_{\text{dis}} = t_{\text{ff}}$, the Lyman-Werner radiation effective quench cooling and collapse of the gas cloud.

The critical distance where $t_{\text{dis}} = t_{\text{ff}}$ is given by equation (18) of Susa (2007)

$$D_{\text{cr}} = \alpha \times 113 \text{ pc} \left(\frac{L_{\text{LW}}}{10^{24} \text{ erg s}^{-1}} \right)^{-1/2} \left(\frac{n_{\text{N}}}{10^3 \text{ cm}^{-3}} \right)^{-7/16} \left(\frac{T}{600 \text{ K}} \right)^{-3/4}, \quad (3.24)$$

where L_{LW} is the LW luminosity of the source, n_{N} and T are the density and the temperature of the cloud center. Also, Susa (2007) suggests that $\alpha \sim 0.4$ is consistent with the result of its numerical simulations.

Regarding to S1 at $z = 25$, $n_{\text{N}} \sim 10 \text{ cm}^{-3}$ and $T \sim 500 \text{ K}$. Let us assume $L_{\text{LW}} \sim 1$ in units of $10^{24} \text{ erg s}^{-1}$. A Pop III star with $120 M_{\odot}$ has a luminosity in the LW band of $L_{\text{LW}} = 5.34 \times 10^{23} \text{ erg s}^{-1}$ according to Schaerer (2002) and Hasegawa et al. (2009). The critical

distance is then $D_{\text{cr}} = \alpha \times 0.97 \text{ kpc} = 0.39 \text{ kpc}$. Thus, we conclude that the Lyman-Werner radiation from stars formed in the gas cloud which is 30 ckpc (1.2 physical kpc) away from S1 does not affect the collapse of S1.

3.3.6 Comparison with the result of Schauer et al. (2021a)

A recent study by Schauer et al. (2021a) also performs simulation incorporating non-equilibrium chemical reactions and follows a formation and evolution of SIGOs. They conclude that SIGOs have a small gas number density of 10 cm^{-3} and all of them are Jeans stable and do not start gravitational collapse (Figure 3.16). They calculate the metallicity required to make the gas clump gravitationally unstable and find that if the gas contains the metal of $Z \sim 10^{-3} Z_{\odot}$ it can be cooled and condensed enough to runaway collapse.

In our study, we perform high-resolution simulations with gas cell refinements after S1 reaches $n_{\text{gas}} \sim 10 \text{ cm}^{-3}$ and that enables us to follow the SIGO's Jeans instability with H_2 cooling. It is important to calculate the long-term chemo-thermal evolution of gas clouds in order to confirm that some SIGOs can finally reach the gravitational collapse phase (see the detail in section 3.3.4).

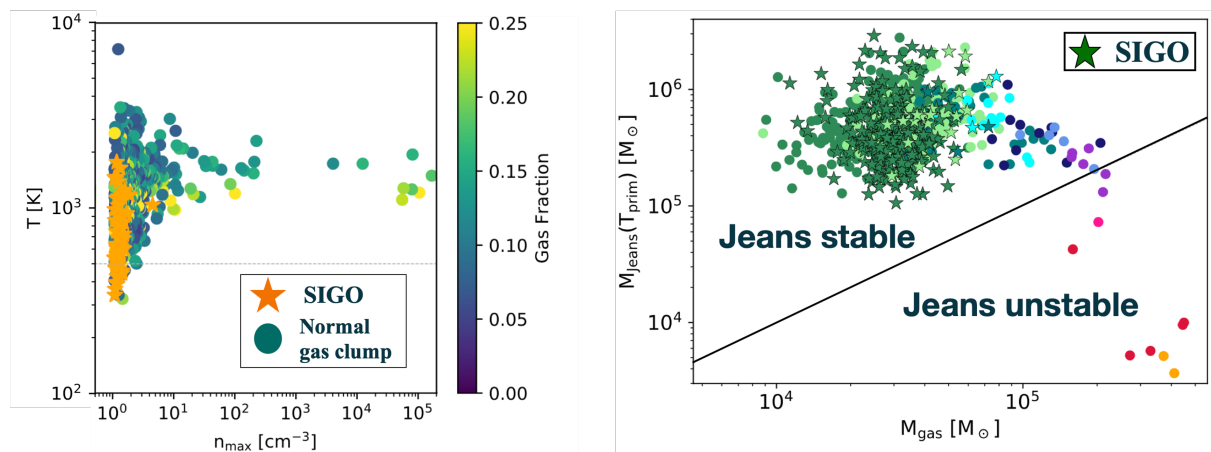


Figure 3.16: Left: Averaged temperature of gas clumps as a function of the averaged gas number density of clumps. Orange stars indicate SIGOs-like gas-rich objects which have over 40% gas fraction. Colored dots show non-SIGOs with a color bar of gas fraction. Right: Jeans mass as a function of mass of gas clumps. A black line represents the threshold where gas clump mass is equal to its Jeans mass. Green stars indicate SIGOs-like gas objects which exist outside the half-mass radius of their closest DM halos. Colored dots show non-SIGOs and only high-dense non-SIGOs (reddish dots) are Jeans unstable. Adopted from Schauer et al. (2021a) and added captions in the figure.

3.4 Statistics of SIGOs

In section 3.3, we select one SIGO (S1) and follow its formation and evolution until its Jeans instability. From here, we also follow evolution of other 50 SIGOs identified in Run 2vH2 and statistics of evolution pathway of SIGOs.

3.4.1 SIGOs identified at $z = 25$ in Run 2vH2

We find 68 SIGOs at $z = 25$ in Run 2vH2 as shown in Figure 3.7. Table 3.3 summarizes the properties of the 50 SIGOs at $z = 25$, whose evolutions are further followed. Detailed evolutions of the gas clumps labeled F1, F2, S1, and S2 are described in Sections 3.5.1, 3.5.2, and 3.5.3 respectively. Our hydrodynamical simulations show that only 6 cases successfully collapse to a star-forming SIGO out of the 50 samples. Bar graphs and dashed lines in Figure 3.17 show the evolution of the clump number and maximum density of SIGO candidates and non-SIGOs respectively. The numbers of both non-SIGO and SIGO-candidate clumps are increasing monotonically. Also, the SIGOs' number is 1/10 of that of non-SIGOs (Notice that the vertical axis is log scale). Regarding the density evolution, we can see that non-SIGO clumps grow rapidly by being hosted by DM halos. In contrast, the maximum density of SIGO candidate clumps does not change largely because SIGOs shrink slowly without being hosted by DM halos. At $z = 25$, the maximum density for non-SIGOs goes to over 10^{10} cm^{-3} , on the other hand, that for SIGOs stays around 10 cm^{-3} (See also Figure 3.18).

Figure 3.18 shows the relationship between the distance of clumps from the nearest DM halos and the density of the gas clumps at $z = 25$. The distance ratio d/R_{200} is taken as the vertical axis, where d is a distance between each clump and its closest DM halo (, which is equal to the distance between the both mass center points) and R_{200} is the virial radius of the DM halo. We take the highest density of each gas clumps as the horizontal axis. In the case of non-SIGOs, the larger the highest density point, the massive and the smaller the distance ratio non-SIGOs become. Notice that there are some non-SIGO clumps that the distance ratio is over 1. This is because the FOF algorithm sometimes detects DM halos which are on the way of merge as one big DM halo. That causes the mass center of a DM halo to be far from the mass center of gas clumps. However, the non-SIGOs whose distance ratios are over 1 are identified as “non-SIGO” correctly thanks to the second condition for SIGOs. This FOF tendency is also seen in Figure 3 of Schauer et al. (2021a). For SIGO candidates, the distance ratios are all greater than 1 by definition. At $z = 25$, the highest density does not reach 100 cm^{-3} for all gas clumps. (as seen in the T-rho diagram), and these SIGOs do not reach Jeans instability. Also, the mass is $\sim 10^5 M_{\odot}$. This result is in agreement with Schauer et al. (2021a) ⁴.

⁴Caveat to the comparison our results and ones of Schauer et al. (2021a) directly. We use the value of σ_8 as 1.8 to see over-density regions, while Schauer et al. (2021a) use $\sigma_8 = 0.8$.

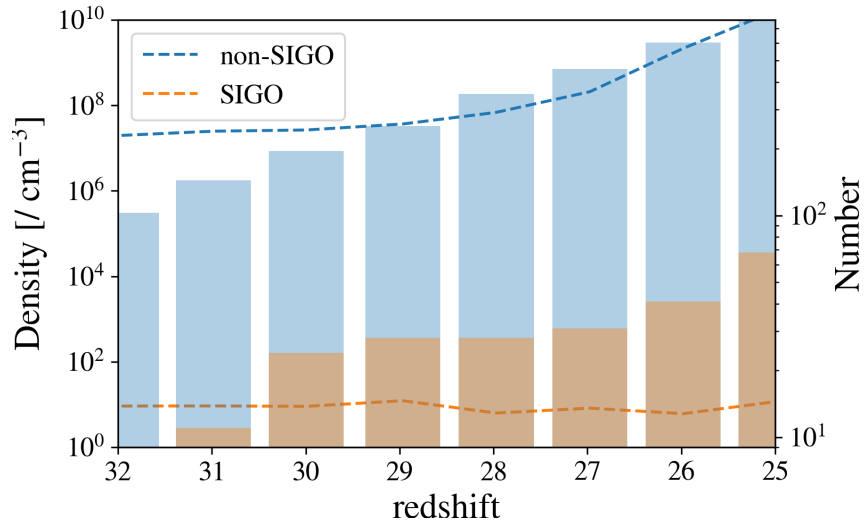


Figure 3.17: The evolution of clump number and density. Blue and orange bars represent the number of non-SIGOs and SIGOs respectively. Blue and orange dashed lines show the evolution of the maximum density of non-SIGOs and SIGOs. The highest density at each redshift is averaged with the mass weighting of each gas clump.

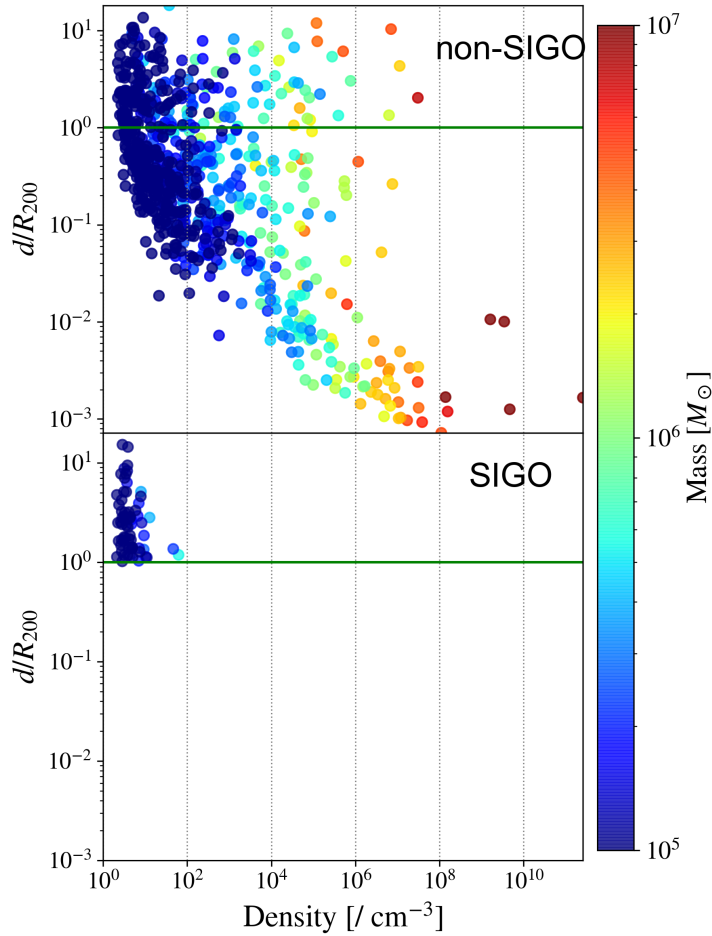


Figure 3.18: Distribution of the distance ratio d/R_{200} at $z = 25$ as a function of density. The color plots represent the mass distribution of each gas clump. Density in the horizontal axis shows the highest number density of gas clumps. The upper and the bottom panels are for non-SIGOs and SIGOs respectively.

3.5 Collapse of SIGO candidate clumps

We carry out high-resolution hydrodynamical simulations to follow the subsequent evolution of the gas clouds that are not hosted by DM halos. The calculations are performed for 50 clumps out of the 68 samples extracted from our parent simulation. We find 6 "successful" cases, where the gas clumps reach Jeans unstable. It is highly expected that stars will be formed in such a gas cloud. For the other cases, however, the clouds do not collapse, often because the gas clumps merge with a nearby DM-hosted halo before the cloud collapses. We find there are two types of hosting paths explained in the following section 3.5.1 and section 3.5.2). We focus on the evolution of four SIGO candidate clumps, which are listed as F1, F2, and S1 (ID456, ID411, ID197 in Table 3.3, respectively). F1 and F2 are the failed cases, whereas S1 is successful one.

Table 3.3: Properties of SIGO candidate gas clumps.

ID	M_{clump} ($10^5 M_{\odot}$)	M_{DM} ($10^5 M_{\odot}$)	F_{bar}	d/R_{200}	$n_{\text{gas,max}}$ [cm^{-3}]
144	5.49	35.65	0.67	1.19	62.52
197	3.80	7.71	0.67	5.12	7.97
215	3.97	361.13	0.77	2.81	12.79
257	2.72	17.41	0.80	1.34	9.28
286	2.23	19.65	0.63	1.36	46.67
306	1.97	35.37	0.72	1.85	9.39
314	1.95	37.16	0.64	1.03	7.04
318	1.88	33.41	0.62	3.92	7.08
338	1.76	6.91	0.96	2.92	6.67
344	1.79	150.83	0.61	2.42	4.73
348	1.66	55.67	0.83	2.75	4.17
349	1.65	6.95	0.66	2.68	4.66
357	1.53	8.81	0.82	6.32	3.70
370	1.58	8.43	0.68	1.13	10.38
378	1.44	84.80	0.62	1.38	7.18
392	1.36	35.13	0.85	1.18	4.33
400	1.33	15.92	0.78	2.49	8.27
406	1.19	7.25	0.65	8.75	3.19
411	1.21	14.41	0.61	2.74	3.80
421	1.14	21.52	0.72	8.29	3.76
456	1.07	361.13	0.69	4.59	7.90
462	1.05	137.64	0.75	1.68	4.61
473	1.10	18.15	0.85	1.11	10.97
480	0.95	18.15	0.62	3.19	4.08
494	0.92	45.07	0.60	5.09	3.56
496	1.02	7.59	0.75	2.76	4.30
509	0.89	328.82	1.00	5.11	3.14
530	0.80	28.91	0.69	2.86	4.44
555	0.77	21.94	0.68	14.41	3.91
561	0.73	25.14	0.64	1.86	4.35
585	0.68	32.86	0.66	2.25	3.87
609	0.65	13.29	0.67	1.71	4.12
616	0.63	6.67	0.64	4.23	2.77
643	0.58	83.17	0.65	4.76	2.13
664	0.60	56.35	0.65	1.75	3.27
667	0.59	12.43	0.73	1.79	3.16
677	0.58	12.93	0.68	9.43	3.81
682	0.54	58.60	0.67	3.78	2.39
692	0.54	9.23	0.77	3.17	3.31
693	0.50	50.09	0.67	1.18	3.86
697	0.52	38.55	0.77	1.64	3.12
698	0.51	18.15	0.86	3.31	5.92
701	0.53	108.15	0.93	2.35	3.60

continues to the next page

continued

ID	M_{clump} ($10^5 M_{\odot}$)	M_{DM} ($10^5 M_{\odot}$)	F_{bar}	d/R_{200}	$n_{\text{gas,max}}$ [cm^{-3}]
707	0.51	68.80	0.77	1.42	4.93
708	0.49	8.77	0.86	15.22	2.89
713	0.48	16.36	0.79	1.13	2.13
726	0.51	31.48	0.68	1.37	4.88
733	0.50	337.18	0.74	1.27	7.48
736	0.46	64.48	0.69	1.48	2.67

Table 3.3: Note of Table 3.3. Column (1):ID of the SIGO detected at $z = 25$. Column (2):Mass of the SIGO candidate gas clump. Column (3):Mass of the closest DM halo. Column (4):local baryon fraction. Its definition is explained in 3.2.3. Column (5): the ratio of the distance between SIGO candidate and its closest DM, and the virial radius of the DM halo. Column (6):maximum gas density of SIGO candidate clump.

Table end

3.5.1 Case F1: Hosted by a nearby large DM halo

F1 is located outside of the closest DM halo at $z = 25$ as shown in Figure 3.19. However, the DM halo mass is over $\sim 3 \times 10^7 M_\odot$ and its strong gravitational potential pulls F1. F1 is finally hosted and becomes Jeans unstable inside the host DM halo at $z = 21.9$. We see from Figure 3.19 that F1 is stretched toward the closest DM halo. We find $\sim 60\%$ of SIGO candidates are finally hosted by this scenario.

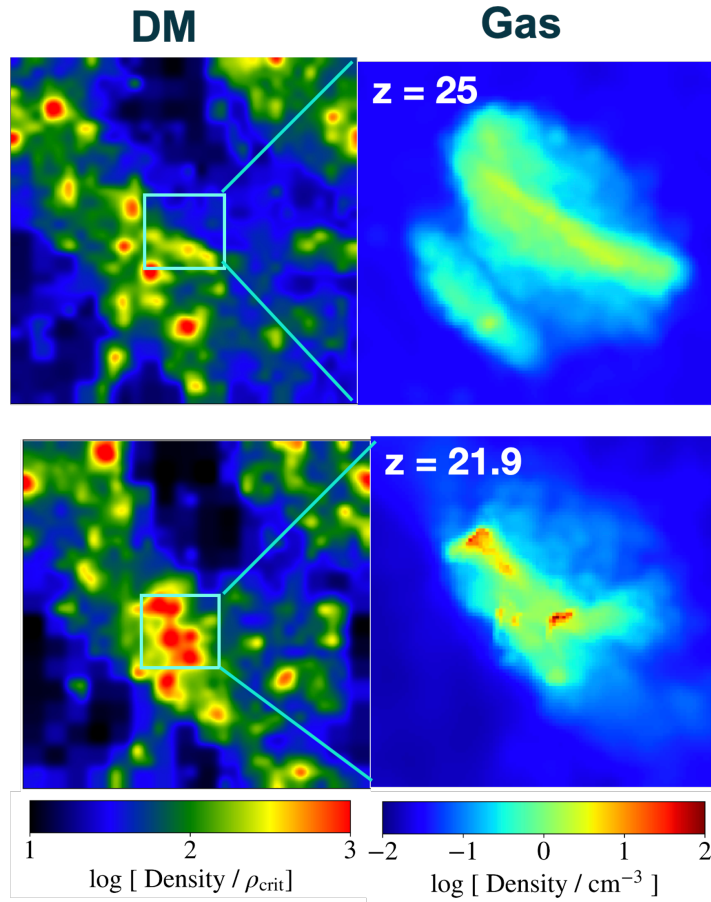


Figure 3.19: Time evolution of the F1 halo at $z = 25$ and 21.9 , where F1 becomes Jeans unstable. Left: projected DM density distribution around F1 normalized by the critical density of the universe. The color scale represents the DM column density. One side length is 2 physical kpc. Right: projected gas density distributions around F1. The center of the figure shows F1. The color scale represents the gas number density.

3.5.2 Case F2: Hosted by DM halos through merger

We also find that halo merger often cause SIGO candidate halos to be finally hosted by neighbor DM halos. F2 is also formed from gases flown away outside DM halos by SV. The counterpart DM halo mass is $\sim 10^6 M_{\odot}$, which is much less than that of host DM halos of F1. However, several DM clumps start to merge together and become a large DM halo. At the same time, F2 merges with the other gas clumps and is hosted by DM halos at $z = 21.8$. This merger event compresses the gas clumps, increases density, and leads Jeans instability. We find $\sim 30\%$ of SIGO candidates experience the same hosted scenario as F2.

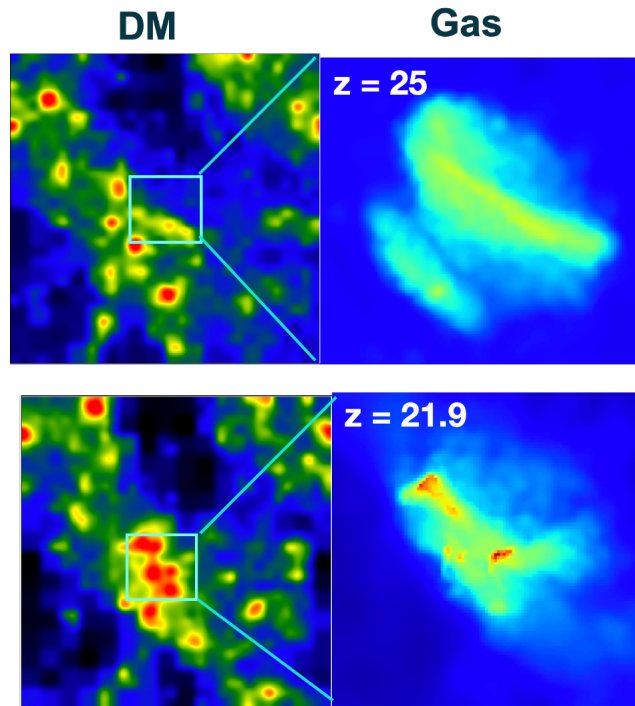


Figure 3.20: Same as Figure 3.19, but the redshift in each figure is $z = 25$ and 21.8 .

3.5.3 Case S1 : Star-forming SIGOs

S1 is a successful surviving case of SIGOs. At $z = 25$, the closest DM halo mass is as small as $\sim 7 M_\odot$ and the distance is over 5 times larger than the virial radius of the DM halo, whose separation is much larger than that of F1 and F2. S1 reaches Jeans unstable at $z = 21.4$ as mentioned in section 3.3.4. Figure 3.21 clearly shows that S1 grows independently from DM halos. We find $\sim 10\%$ of SIGO candidates finally evolve to star-forming SIGOs, which become Jeans unstable without being hosted by the closest DM halos. Such surviving SIGOs have the same large Jeans mass of $\sim 5 \times 10^4 - 10^5 M_\odot$.

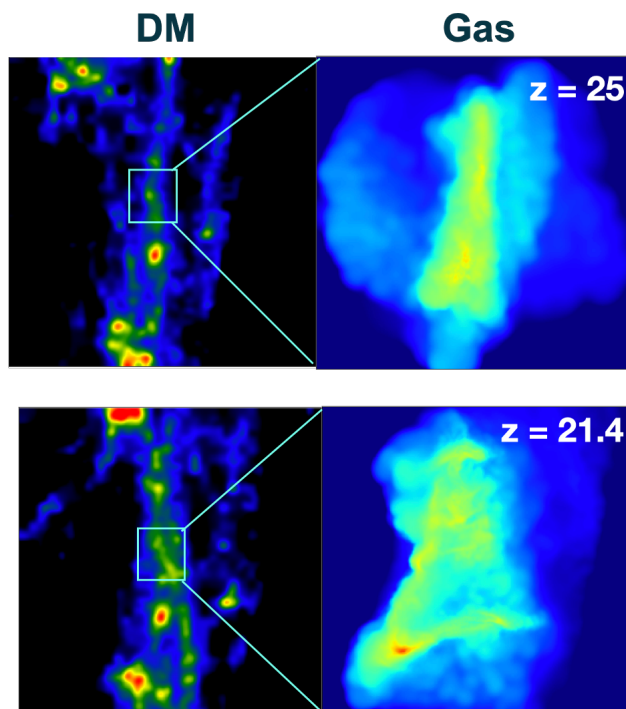


Figure 3.21: Same as Figure 3.19, but the redshift in each figure is $z = 25$ and 21.4 , where S1 becomes Jeans unstable. Note that the left figure has one side length of 5 kpc.

Whether SIGOs survive or not is investigated analytically by Lake et al. (2022). We find that the survival of SIGOs depends on the following timescales; (1) cooling time scale for SIGOs to cool via molecular hydrogen and to become Jeans unstable (t_{cool}), (2) free-fall(collapse) time scale (t_{ff}) and (3) fall-back time scale to be hosted the closest DM halos (t_{fall}). SIGOs with $t_{\text{cool}} < t_{\text{fall}}$ and $t_{\text{ff}} < t_{\text{fall}}$ can form stars outside DM halos.

3.6 Star formation in SIGOs

Further star formation in SIGOs is also studied in Lake et al. in prep (incl. Y. Nakazato). We find that 8 SIGOs start to form stars and the abundance of such SIGOs is 1 cMpc^{-3} . We show the evolution of one SIGO from $z = 20$ to $z = 15$ in Figure 3.22. The SIGO starts star formation at $z = 22$ and it is outside of the closest DM halo until $z = 20$. At $z = 18$, the SIGO

begins to merge with its parent halo and the halo also merge with a massive protogalaxy located in the bottom-right portion of the middle panel of Figure 3.22. When the SIGO falls into the protogalaxy, the large gravitational potential of the nucleus of the protogalaxy strips the gas of the (outer part of) SIGO at $z = 15$, while the stars remain as a bound cluster. Finally, the SIGO consists of stars with the stellar mass of $7.3 \times 10^4 M_\odot$ and evolves as a satellite of the host galaxy with a mass of $10^9 M_\odot$.

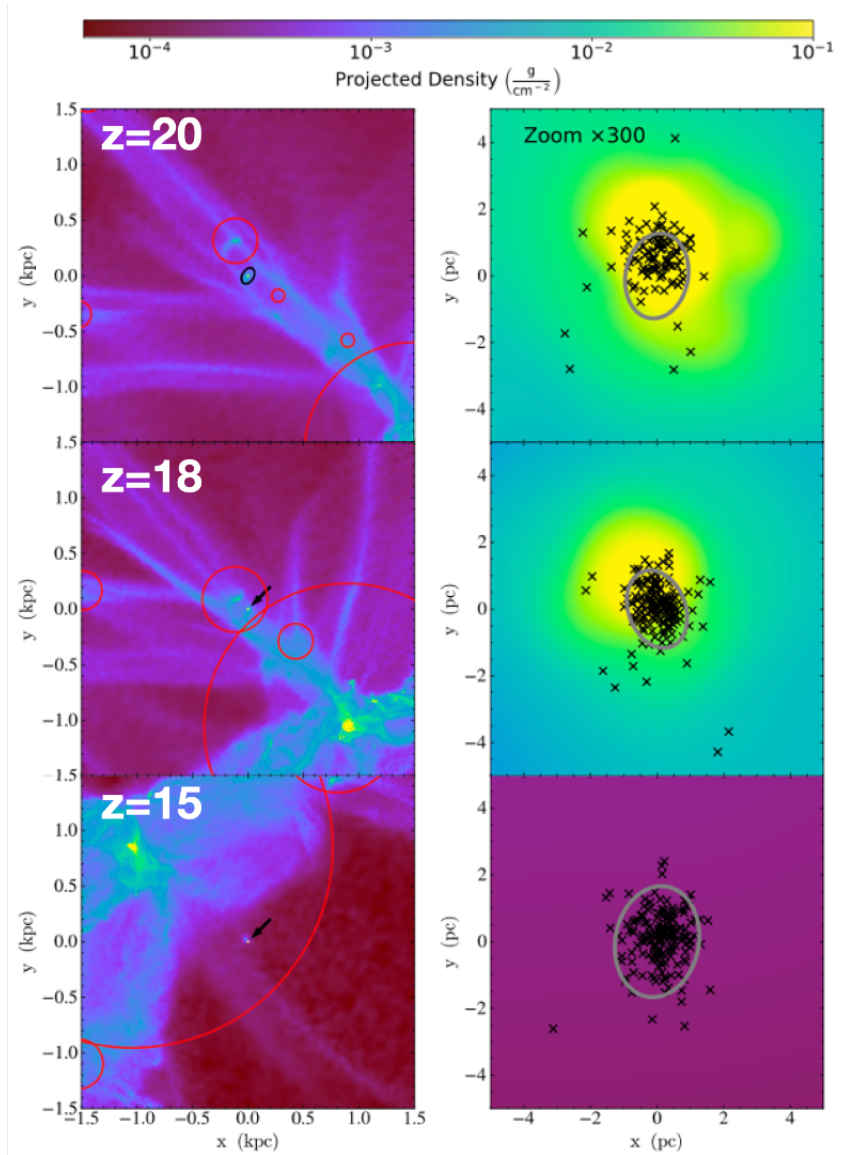


Figure 3.22: Projected density distributions around a SIGO at $z = 20$ (top), $z = 18$ (middle), and $z = 15$ (bottom). Left: A SIGO is signified as a black circle or arrow, and nearby DM halos are indicated by red circles. Right: Zoomed-in density projections of a SIGO in the center of the left panels. Black crosses represent stars and gray ellipsoids are ellipsoidal fits to the stellar distributions. Each colormap shows a region with a side length and a depth of 3 kpc (left) and 10 pc (right), respectively. Adopted from Lake et al. in prep.

3.7 Discussion and summary

In this Chapter, we perform 3D hydrodynamical simulations including stream velocities (SV) and follow the formation and evolution of Supersonically Induced Gas Objects (SIGOs). We find, for the first time, that a SIGO forms under the influence of SV and condenses via H_2 cooling enough to become Jeans unstable. The SIGO is expected to undergo runaway collapse and become a star-forming cloud. We also investigate physical properties of the other 50 SIGOs which are located in Run-2vH2 to study statistics. We run additional 50 high-resolution simulations and examine the rate of SIGOs which collapse without being hosted or swallowed by the nearby halos. Most of the SIGOs are found to be hosted by the closest large DM halos (60 %) or by experiencing merger (30 %). Only 10% of SIGOs evolve to Jeans instability without being hosted nearby DM halos. This is due to the distance between a SIGO and its closest DM halo and the mass of the DM halo. The relationship between SIGO's contraction timescale and fall-back timescale, on which SIGOs fall into the parent halos, is calculated by a recent study (Lake et al. 2022).

We also follow further evolution of SIGOs to see if they form star clusters. We find that some SIGOs form stars and are accreted into nearby massive protogalaxies. During the accretion process, gases in SIGOs are stripped by the potential well of the protogalaxies and the SIGOs evolve to star clusters with stellar masses of $10^5 M_\odot$. The SIGOs exist as a substructure within the galaxies, which are similar to present-day globular clusters. Proto-globular cluster candidates at $z = 6$ have been observed by Vanzella et al. (2017) and recent JWST observations report star cluster candidates around the lensed clusters SMACS-0723 (Pascale et al. 2022), Abell 2744 (Vanzella et al. 2022a), and Sunrise arc (Vanzella et al. 2022b).

We remark that S1, one SIGO we select, consists of only primordial gas, while observed globular clusters have some metallicities. Therefore, internal or external metal enrichment is significant to confirm SIGOs finally have some metals. It is likely that internal enrichment occurs after Pop-III star formation in S1, and external enrichment can happen from the closest non-SIGOs (S2). Non-SIGOs evolve much faster than SIGOs because they can contract to high-density with the help of the gravitational potential of the host DM halos. Such non-SIGOs are expected to form Pop-III stars early and massive stars will end their lives as supernovae, which have strong energy enough to enrich gas outside the halo. Further simulations incorporating the metal enrichment will be carried out in the near future. For the star formation in SIGOs in section 3.6, we do not include stellar feedback such as radiation and supernovae, which may give non-negligible effects on morphologies of SIGOs' star clusters. Future studies will reveal the kinematics of star-forming phase and metal enrichment inside SIGOs, and finally clarify the relationship between SIGOs and globular clusters.

Chapter 4

Line emission from galaxies

4.1 Chemical evolution of galaxies

To understand chemical evolution of galaxies, it is crucial to overview the star-forming processes inside galaxies. Figure 4.1 summarizes the processes.

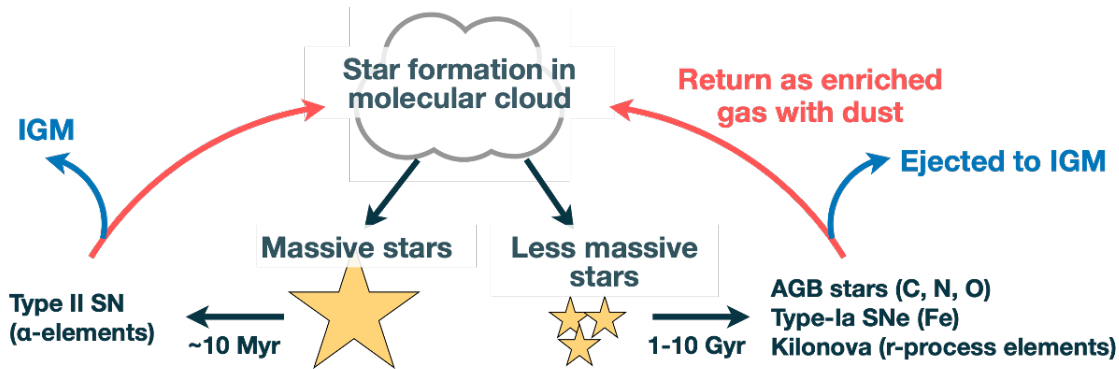


Figure 4.1: Schematic illustration of metal enrichment in galaxies.

The left path for massive stars may be important in high-redshift galaxies i.e. low-metallicity environments. This is because stellar mass is thought to scale with cloud mass (Jeans mass), which is proportional to $T_{\text{cloud}}^{3/2}$ (see eq. 2.93). Low-metallicity means a small number of coolants, thus T_{cloud} is higher than that in higher-metallicity environments.¹

Figure 4.2 shows the production timescale for four major elements: oxygen, nitrogen, carbon, and iron by using single stellar population models. Here we clearly see that the core-collapse supernovae (CCSN) are dominant during the first 30-40 Myr and produce oxygen and carbon. About 30 Myrs after the star formation, Type-Ia supernovae start to occur and iron production

¹The evolutionary paths for high-mass (left) and mid-/low-mass (right) stars are characterized as follows,

- high-mass stars :
Main Sequence → Red Supergiant/ Blue Supergiant/ Luminous Blue Variables/ Wolf-Rayet stars → CCSN
- mid-/low-mass stars:
Main Sequence → Red Giant Branch → Asymptotic Giant Branch → Thermal Pulsing-AGB → Planetary Nebula/ White Dwarf

is significant. Nitrogen is supplied mainly by AGB stars ~ 40 Myrs after star formation.

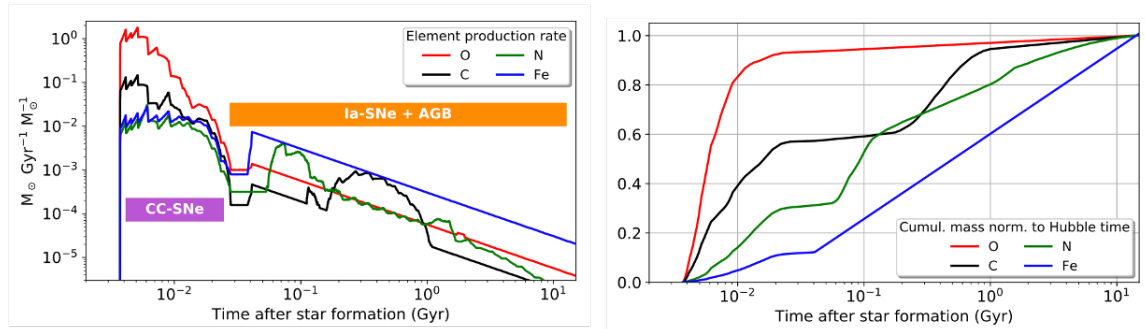


Figure 4.2: Production timescales of metals; oxygen(red), nitrogen(green), carbon(black), and iron (Fe). Formation and evolution of a single stellar population are assumed. Left: metal production rate normalized by $1 M_{\odot}$ of formed stars. Right: Cumulative production rate normalized by the current abundance. The model adopts Kroupa IMF (Kroupa et al. 1993), solar metallicity, stellar lifetime model from (Kobayashi 2004), metal release model and delay time distribution of Type Ia-SNe (Iwamoto et al. 1999; Maoz & Mannucci 2012). Adopted from Maiolino & Mannucci (2019).

Metallicity(Z) is determined by the **mass** of all the metals which are heavier than helium relative to the mass of baryons as

$$Z \equiv \frac{M_{\text{metal}}}{M_{\text{baryon}}}. \quad (4.1)$$

Solar metallicity is $Z_{\odot} = 0.02$ (Anders & Grevesse 1989). Metallicity of a star is often expressed by the abundance ratio of iron and hydrogen;

$$[\text{Fe}/\text{H}] = \log(M_{\text{Fe}}/M_{\text{H}}) - \log(M_{\text{Fe}}/M_{\text{H}})_{\odot} \quad (4.2)$$

$$= \log(N_{\text{Fe}}/N_{\text{H}}) - \log(N_{\text{Fe}}/N_{\text{H}})_{\odot}. \quad (4.3)$$

For gas-phase metallicity, **number** ratio of oxygen to hydrogen is often used in the literature;

$$12 + \log(\text{O}/\text{H}) \equiv 12 + \log(N_{\text{O}}/N_{\text{H}}). \quad (4.4)$$

The derived abundance is different from simulation to simulation, for instance, $12 + \log(\text{O}/\text{H})_{\odot} = 8.6$ (Asplund et al. 2009) and 8.9 (Woosley & Weaver 1995).

4.2 Star-forming regions in a galaxy

Star-forming regions consist of three main regions; HII regions, photodissociation regions, and molecular gas regions as shown in Figure 4.3. Each region mainly consists of ionized hydrogen, neutral hydrogen atom, and molecular hydrogen. Other heavier elements (metals) are also found. The emission lines from metals are indispensable to study the characteristic of star-forming regions. Detailed emission mechanism of metal lines is explained in section 4.3.

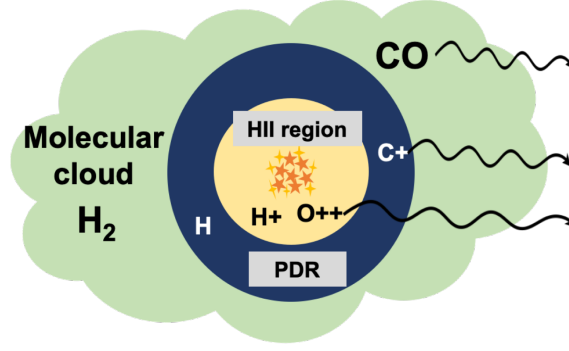


Figure 4.3: Illustration of star-forming regions. HII region, PDR, and molecular cloud are located closer to the central stars.

4.2.1 HII regions

Massive stars such as O-type and B-type stars emit ionizing photons, i.e. $h\nu > 13.6$ eV. An ionized gas surrounds such ionization sources which is called HII region.

Let us consider the recombination rate by using N_{rec} [$\text{cm}^{-3}\text{sec}^{-1}$]; the number of recombination per unit volume per unit time.

$$N_{\text{rec}} = n_{\text{p}}n_{\text{e}}\langle\sigma_{\text{e}}v_{\text{e}}\rangle = n_{\text{p}}n_{\text{e}}\alpha(T), \quad (4.5)$$

where σ_{e} is the cross section for electron capture and $\langle\sigma_{\text{e}}v_{\text{e}}\rangle$ is a velocity-averaged value

$$\langle\sigma_{\text{e}}v_{\text{e}}\rangle = \int_{-\infty}^{\infty} \sigma_{\text{e}}f(v_{\text{e}})v_{\text{e}}dv. \quad (4.6)$$

Hydrogen is a dominant component and thus $n_{\text{p}} \sim n_{\text{e}}$. Eq. 4.5 is re-written

$$N_{\text{rec}} = \alpha(T)n_{\text{e}}^2 = \alpha(T)x^2n_{\text{H}}^2 \left(x \equiv \frac{n_{\text{e}}}{n_{\text{H}}} \right), \quad (4.7)$$

where n_{H} is the total number of hydrogen atoms including both ionized and neutral ones, and x is the ionized fraction.

Let us assume that the gas is "optically thick"², which means no ionizing photons escape from the nebula, and let us further assume that the above situation is satisfied in a spherical region with radius R_{S} . Then N_{rec} is integrated over the sphere, and we obtain the balance equation as follows,

$$Q_0 = \int N_{\text{rec}}dV \quad (4.8)$$

$$= \frac{4\pi}{3}R_{\text{S}}^3\epsilon x^2n_{\text{H}}^2\alpha(T), \quad (4.9)$$

where Q_0 is the ionizing photon number per unit time emitted from the source stars. In eq. 4.9, we introduced filling factor ϵ (Gutiérrez & Beckman 2008), which is defined as following

$$\epsilon \equiv \frac{(\text{volume occupied by the clumps})}{(\text{total volume of HII region})}. \quad (4.10)$$

²In this sentence, optically thick *globally*.

Real HII regions do not have perfectly spherical but complex shapes, and consist of highly dense and fully ionized gas clumps and otherwise nearly empty fields (e.g. Osterbrock & Flather 1959). Hence ϵ traces inhomogeneous morphologies of HII regions.

Let us assume that the gas within R_S is totally ionized ($x = 1$) and case B approximation is valid. A gas is optically thick³ to all Lyman Series photons and ionizing photons with $h\nu > 13.6$ eV. Such photons are immediately absorbed by other atoms nearby ("on-the-spot approximation"). Then, eq. 4.9 becomes

$$Q_0 = \frac{4\pi}{3} R_S^3 n_{\text{HII}}^2 \epsilon \alpha_B, \quad (4.11)$$

where n_{HII} is the density of HII region, and α_B is effective recombination coefficient for hydrogen atoms. α_B is expressed as

$$\alpha_B(\text{H}^0, T) = \alpha_A(\text{H}^0, T) - \alpha_1(\text{H}^0, T) \quad (4.12)$$

$$= \sum_{n=2}^{\infty} \alpha_n(\text{H}^0, T) \quad (4.13)$$

$$= 2.6 \times 10^{-13} \left(\frac{T_e}{10^4 \text{ K}} \right)^{-0.85} \text{ cm}^3 \text{ s}^{-1}. \quad (4.14)$$

α_n is the recombination coefficient of free-bound transitions toward level n . From eq. 4.11, the size of HII region R_S is derived as follows;

$$R_S = \left(\frac{3Q_0}{4\pi n_{\text{HII}}^2 \epsilon \alpha_B} \right)^{1/3} \quad (4.15)$$

$$= 5.4 \left(\frac{n_{\text{HII}}}{10^2 \text{ cm}^{-3}} \right)^{-2/3} \left(\frac{Q_0}{5 \times 10^{49} \text{ s}^{-1}} \right)^{1/3} \text{ pc (for } T_e = 10^4 \text{ K, } \epsilon = 1), \quad (4.16)$$

which is called Strömngren radius.

Ionization parameter U is the ratio of the number of ionizing photons to that of hydrogen atoms. Ionization parameter quantifies the ionization state in the HII region, and traces star formation activity, since ionizing photons are produced by young massive stars. Ionization parameter is different from place to place, and the volume averaged ionization parameter is expressed by considering a spherical HII region with a uniform density (Panuzzo et al. 2003);

$$\langle U \rangle = \int_0^{R_S} \frac{U(r) 4\pi r^2}{\frac{4\pi}{3} R_S^3} dr, \quad (4.17)$$

$$U(r) = \frac{Q(r)}{4\pi r^2 n_{\text{HII}} c}, \quad (4.18)$$

where $Q(r)$ is the number of ionizing photons passing through a spherical shell of radius r per unit time,

$$Q(r) = \#(\text{total ionizing photons from the source}) - \#(\text{photons absorbed within } r) \quad (4.19)$$

$$= Q_0 - \frac{4\pi}{3} r^3 n_{\text{HII}}^2 \epsilon \alpha_B. \quad (\because \text{eq. 4.11}) \quad (4.20)$$

³In this sentence, optically thick *locally*.

Substituting eq. 4.11 and Strömgen radius (eq. 4.16) into eq. 4.18, we get

$$\langle U \rangle = \int_0^{R_S} \left(\frac{Q_0}{4\pi r^2 n_{\text{HII}} c} - \frac{r n_{\text{HII}} \alpha_B \epsilon}{3c} \right) \frac{3r^2 dr}{R_S^3} \quad (4.21)$$

$$= \frac{3Q_0}{4\pi n_{\text{HII}} c} \left(\frac{4\pi n_{\text{HII}}^2 \alpha_B \epsilon}{3Q_0} \right)^{2/3} - \frac{n_{\text{HII}} \alpha_B \epsilon}{4c} \left(\frac{3Q_0}{4\pi n_{\text{HII}}^2 \alpha_B \epsilon} \right)^{1/3} \quad (4.22)$$

$$= \frac{3\alpha_B^{2/3}}{4c} \left(\frac{3Q\epsilon^2 n_{\text{HII}}}{4\pi} \right)^{1/3} \quad (4.23)$$

$$= 1.0 \times 10^{-2} \left(\frac{n_{\text{HII}}}{10^2 \text{ cm}^{-3}} \right)^{1/3} \left(\frac{Q_0}{5 \times 10^{49} \text{ s}^{-1}} \right)^{1/3} \quad (\text{for } T_e = 10^4 \text{ K}, \epsilon = 1). \quad (4.24)$$

The radius which satisfies $\langle U \rangle = U(r)$ is derived from the equation $x^3 + (9/4)x^2 - 1 = 0$, where $x \equiv r/R_S$. The solution is $r \sim 0.6R_S$.

4.2.2 Photo dissociation regions (PDR)

Photons with energies below 13.6 eV reach outside HII region. Hydrogen molecules are photo-dissociated and exist as neutral hydrogen atoms, and we call such regions photo-dissociation regions, short for PDR. In PDR, carbon is first ionized (first ionization potential: 11.26 eV) and oxygen exists as neutral atoms (first ionization potential: 13.62 eV). Fine-structure lines such as [CII] 158 μm and [OI] 63 μm are emitted from PDR and their emissivity depends on the incident radiation field G within the Habing band (6 - 13.6 eV) and gas number density n . In reality, these properties have various distributions and HI gases have two-phase states; warm neutral medium (WNM, $T \sim 10^4 \text{ K}$, $n_{\text{H}} \sim 0.1 \text{ cm}^{-3}$) and cold neutral medium (CNM, $T \sim 10^2 \text{ K}$, $n_{\text{H}} \sim 10^1 - 10^2 \text{ cm}^{-3}$) as shown in Figure 4.4.

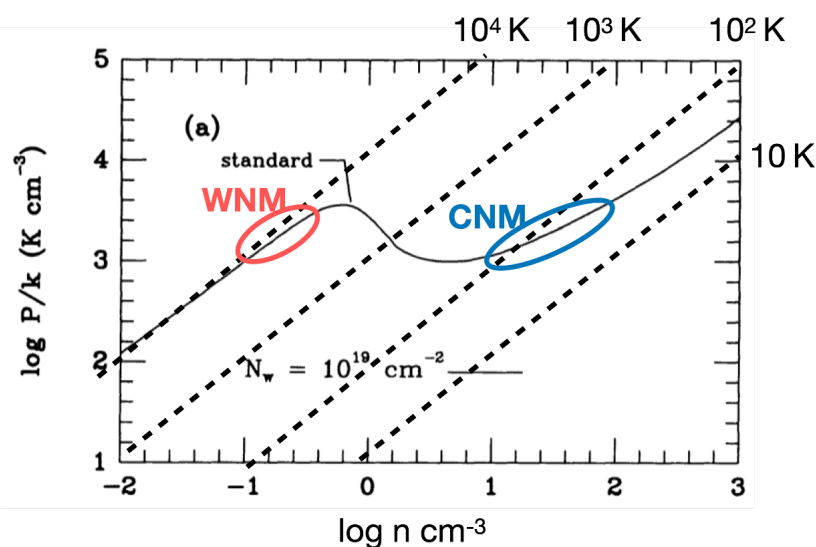


Figure 4.4: Phase diagram in HI region. Points on the black solid line satisfy radiative equilibrium between heating and cooling. Adopted from Wolfire et al. (1995) and added dashed lines indicating constant temperatures.

4.2.3 Molecular gas regions

Molecular hydrogen (H_2) gas regions exist outside PDR. The gas has highest density ($10^2 - 10^5 \text{ cm}^{-3}$) and the lowest temperature (a few tens of Kelvin) among the three regions. Under normal conditions, a molecular gas has a high pressure and contracts self-gravitationally, and can cause star formation. Due to such low temperature, emission lines from H_2 cannot be observed because its lowest excitation temperature is 512 K. Instead of H_2 , CO lines are thought to be good tracers for molecular gas regions.

4.3 Radiation processes

4.3.1 Selection rules and forbidden lines

The emission lines from electric dipole radiation are coined permitted lines, which satisfy the following selection rules;

1. $\Delta L = 0, \pm 1$ (but $L' = 0 \rightarrow L = 0$ is forbidden)
2. $\Delta J = 0, \pm 1$
3. $\Delta S = 0$,

where L is the orbital angular momentum, S is the spin quantum number, and J is the total angular momentum, i.e., $J = L + S$. However, even when transitions by electric dipole radiation are forbidden, transitions by magnetic dipole or electric quadrupole radiation are permitted. These transitions can happen in low-density environments, where collisional reverse excitation is unlikely to occur. The corresponding emission lines are called forbidden lines and are generally denoted by brackets around the ion, such as [OIII] or [CII].

Also, there are the other emission lines coined semi-forbidden lines, which are electric dipole radiation but with changes of $\Delta S = \pm 1$. The semi-forbidden lines are denoted by] around the ion, such as CIII].

4.3.2 Collisionally excited line emission and critical density

Collisionally excited line emission such as [OII], [OIII], and [NII] is a crucial radiative process. The abundance of these ions is small relative to hydrogen (eg. $N_{\text{O}}/N_{\text{H}} \sim 10^{-3.2}$, $N_{\text{N}}/N_{\text{H}} \sim 10^{-4.0}$ for solar abundance (Grevesse & Sauval 1998). However, their excitation potential of a few electron Volt can be a dominant radiation in a diffuse nebula. The details are described in Osterbrock & Ferland (2006); Seaton (1954, 1960).

We consider two-level systems. In Figure 4.5, X_{21} shows the coefficient from higher level 2 to lower level 1, and $A_{21} [\text{sec}^{-1}]$ is the Einstein coefficient of radiative de-excitation and $q_{21} [\text{cm}^{-3}\text{s}^{-1}]$ is the collisional de-excitation rate per unit time per unit volume.

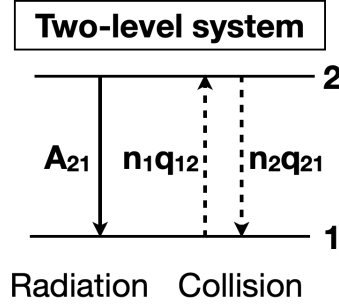


Figure 4.5: Transitions through radiation (solid) and collision (dashed) in two-level systems. n_1q_{12} and A_{21} , n_2q_{21} is excitation and de-excitation rate per unit time, respectively.

We calculate the collision excitation/de-excitation rate q_{12} , q_{21} . The relationship between q_{12} and q_{21} is derived by the principle of detailed balance, which means that an elementary process such as collisions is in equilibrium with its reverse process in a microscopic system in thermal equilibrium. In thermal equilibrium,

$$\begin{aligned} & \text{(the rate of collisional excitation with relative velocities of } u_1 \sim u_1 + du_1) \\ & = \text{(the rate of collisional de-excitation with relative velocities of } u_2 \sim u_2 + du_2). \end{aligned}$$

We can express this by using the collisional cross section σ and Maxwell-Boltzmann velocity distribution $f(u) = \frac{4}{\sqrt{\pi}} \left(\frac{m}{2kT}\right)^{3/2} u^2 \exp\left(-\frac{mu^2}{2kT}\right)$ as follows,

$$n_e n_1 u_1 \sigma_{12}(u_1) f(u_1) du_1 = n_e n_2 u_2 \sigma_{21}(u_2) f(u_2) du_2 \quad (4.25)$$

$$\therefore \frac{n_2}{n_1} = \frac{u_1 du_1 \sigma_{12}(u_1) f(u_1)}{u_2 du_2 \sigma_{21}(u_2) f(u_2)} \quad (4.26)$$

$$= \frac{\sigma_{12}(u_1) u_1^2}{\sigma_{21}(u_2) u_2^2} \exp\left[-\frac{m}{2kT}(u_1^2 - u_2^2)\right] \quad (4.27)$$

Here, u_1 and u_2 have the following relationship;

$$\frac{1}{2}mu_1^2 = \chi + \frac{1}{2}mu_2^2, \quad (4.28)$$

where χ is the excitation potential.

In thermal equilibrium, the Boltzmann distribution between the two levels gives

$$\frac{n_2}{n_1} = \frac{\omega_2}{\omega_1} \exp\left(-\frac{\chi}{kT}\right), \quad (4.29)$$

where ω_i is a statistical weight. From eq. 4.27 and eq. 4.29, we can derive

$$\omega_2 u_2^2 \sigma_{21}(u_2) = \omega_1 u_1^2 \sigma_{12}(u_1). \quad (4.30)$$

When $\frac{1}{2}mu_1^2 > \chi$, the collisional excitation can occur and its cross section σ_{12} scales as $\sigma_{12} \propto u^{-2}$ due to the electronic repulsion as following (Hebb & Menzel 1940),

$$\sigma_{12}(u_1) = \frac{\pi \hbar^2}{m^2 u_1^2} \frac{\Omega(1,2)}{\omega_1}, \quad (4.31)$$

where $\Omega(1,2)$ is collision strength and is a quantum mechanically determined quantity. The cross section of collisional de-excitation σ_{21} is also calculated by eq. 4.30 and eq. 4.31,

$$\sigma_{21}(u_2) = \frac{\pi \hbar^2}{m^2 u_2^2} \frac{\Omega(1,2)}{\omega_2} \quad (4.32)$$

Finally, the collisional de-excitation rate per unit time per unit volume is

$$q_{21} = \int_0^\infty u_2 \sigma_{21} f(u_2) du_2 \quad (4.33)$$

$$= \left(\frac{2\pi}{kT} \right)^{1/2} \frac{\hbar^2}{m^{3/2}} \frac{\Upsilon_{(1,2)}}{\omega_2} \left(\Upsilon_{(1,2)} \equiv \int_0^\infty \Omega_{(1,2)} \exp\left(-\frac{mv_2^2}{2kT_e}\right) d\left(\frac{mv_2^2}{2kT_e}\right) \right) \quad (4.34)$$

$$= \frac{8.629 \times 10^{-6}}{T^{1/2}} \frac{\Upsilon(1,2)}{\omega_2} [\text{cm}^{-3} \text{sec}^{-1}], \quad (4.35)$$

where $\Upsilon_{(1,2)}$ is the averaged collisional strength $\Omega_{(1,2)}$. The cross section of collisional excitation is also calculated in the same way,

$$q_{12} = \frac{n_2}{n_1} q_{21} = \frac{8.629 \times 10^{-6}}{T^{-1/2}} \frac{\Upsilon_{(1,2)}}{\omega_1} \exp\left(-\frac{\chi}{kT}\right) [\text{cm}^{-3} \text{sec}^{-1}] \quad (4.36)$$

Since electrons can be excited by collision⁴ and be de-excited by collision or radiation, the balance equations is

$$n_e n_1 q_{12} = n_e n_2 q_{21} + n_2 A_{21} \quad (4.37)$$

$$\therefore \frac{n_2}{n_1} = \frac{n_e q_{12}}{A_{21} \left[1 + \frac{n_e q_{21}}{A_{21}}\right]}, \quad (4.38)$$

The value of A_{21} is determined by quantum physics, and the value of q_{12} and q_{21} is calculated by eq. 4.36 and eq. 4.35, respectively. When the collisionally de-excitation and radiative de-excitation occurs at the same rate, the corresponding density is termed critical density;

$$n_{\text{crit}} \equiv \frac{A_{21}}{q_{21}}. \quad (4.39)$$

From eq. 4.38, the emission rate ϵ_{12} [erg/s/cm³] is

$$\epsilon_{21} = n_2 A_{21} h\nu_{21} = n_e n_1 q_{12} \frac{1}{1 + \frac{n_e}{n_{\text{crit}}}} h\nu_{21}. \quad (4.40)$$

When the electron density is very low ($n_e \ll n_{\text{crit}}$), collisional de-excitation can be neglected;

$$\epsilon_{21} = n_2 A_{21} h\nu_{21} = n_e n_1 q_{12} h\nu_{21} \quad (4.41)$$

$$= n_e n_1 \nu_{21} \frac{8.629 \times 10^{-6}}{T^{1/2}} \frac{\Upsilon_{(1,2)}}{\omega_1} \exp\left(-\frac{\chi}{kT}\right) \quad (4.42)$$

We see that the emission rate is proportional to $n_e n_1$ in the low density limit, which implies that ϵ_{21} becomes maximum around $n_e = n_{\text{crit}}$.

⁴Electrons are primary collision particles in HII regions.

When the electron density is high ($n_e \gg n_{\text{crit}}$), collisional de-excitation is dominant and eq. 4.40 becomes

$$\epsilon_{21} = n_2 A_{21} h\nu_{21} \quad (4.43)$$

$$= n_1 \frac{n_2}{n_1} A_{21} h\nu_{21} \quad (4.44)$$

$$= n_1 \frac{\omega_2}{\omega_1} \exp\left(-\frac{\chi}{kT}\right) A_{21} h\nu_{21}. \quad (\because \text{Boltzmann distribution}) \quad (4.45)$$

We see that $\epsilon_{12} \propto n_1$ at given T , and the emission rate is much smaller than that of low-density ($n_e < n_{\text{crit}}$) case because $n_1 \ll n_e$.

In reality, ions have several levels. For example, ions whose configurations are $2p^q$ or $3p^q$ ($q = 2, 3, 4$) have five levels. The thermal equilibrium at level i is

$$\sum_{j \neq i} n_j n_e q_{ji} + \sum_{j > i} n_j A_{ji} = \sum_{j \neq i} n_i n_e q_{ij} + \sum_{j < i} n_i A_{ij} \quad \left(\sum_j n_j = n \right) \quad (4.46)$$

From eq. 4.46, we can derive the critical density for multiple level systems;

$$n_c(i) = \frac{\sum_{j < i} A_{ij}}{\sum_{j \neq i} q_{ij}}. \quad (4.47)$$

Notice that we have to consider both collisional excitation rates in the multiple systems.

Figure 4.6 shows the emissivity (ϵ) of [OIII] 5007Å as a function of electron density. The middle panel indicates $\epsilon \propto n_e^2$ (n_e) for low(high)-density limit as shown in eq. 4.42 and eq. 4.45. The volume of HII region satisfies $V \propto n_e^{-2}$ and the total luminosity decreases as $L \propto n_e^{-1}$ for high-density limit.

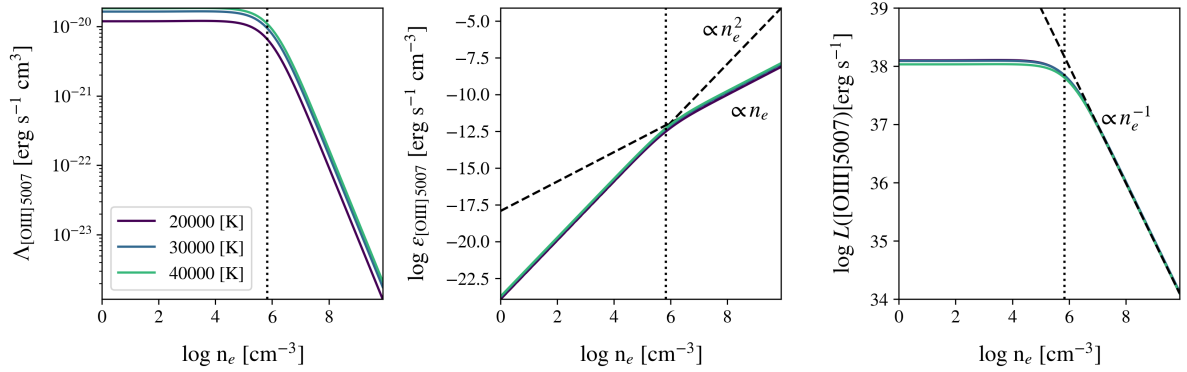


Figure 4.6: (left) cooling rate of [OIII] 5007 Å, (middle) emissivity of [OIII] 5007 Å. Emissivity is calculated from $\epsilon = n_e n_{\text{O}^{++}} \Lambda$ by assuming $n_{\text{O}^{++}} = 10^{-4} n_e$. (right) total luminosity of [OIII] 5007Å from HII region. Luminosity is calculated from $L = \epsilon \times V = \epsilon \times Q_0 / (n_e^2 \alpha_B)$ by assuming $Q_0 = 5 \times 10^{49}$ [1/s]. The dotted vertical lines represent the critical density of [OIII] 5007 Å.

Table 4.1 shows the critical density and excitation temperature of emission lines which are especially important in a diffuse nebula. The ion whose ionization potential (E_{ion}) is larger than

13.6 eV exists only in HII regions, and collides with free electrons. The ion whose ionization potential is lower than 13.6 eV can exist both in HII region and PDR and collides with free electrons and neutral hydrogen atoms, respectively. Notice that [SII] 6717Å and 6731Å have lower ionization potential but have high excitation temperature of $T_{\text{exc}} > 10^4$ K, which suggests the lines are emitted from (the edge of) HII region rather than PDR. On the other hand, [CII] 158 μm has also lower ionization potential and low excitation temperature of ~ 100 K, which makes [CII] 158 μm originate from both HII region and PDR.

Table 4.1: Properties of significant forbidden lines from HII regions. 'config': electron configurations, E_{ion} : ionization potential, n_{crit}^e : critical density with colliders of electrons (hydrogen atoms) at the temperature of 10^4 K. T_{exc} : excitation energy from the ground state ($\equiv E_{j0}/k$). Values are adopted from Osterbrock & Ferland (2006) and Draine (2011).

ion	config	$E_{\text{ion}}[\text{eV}]$	transition ($u - l$)	wavelength	$T_{\text{exc}}[\text{K}]$	$n_{\text{crit}}^e [\text{cm}^{-3}]$
CII	$2p^1$	11.3	$^2P_{3/2} - ^2P_{1/2}$	158 μm	91.2	50
NII	$2p^2$	14.5	$^3P_2 - ^3P_0$	122 μm	188	310
			$^3P_1 - ^3P_0$	205 μm	70	80
			$^1D_2 - ^3P_1$	6548 Å	2.20×10^4	6.60×10^4
			$^1D_2 - ^3P_2$	6584 Å	2.20×10^4	6.60×10^4
NIII	$2p^1$	29.6	$^2P_{3/2} - ^2P_{1/2}$	57 μm	302	1.50×10^3
OII	$2p^3$	13.6	$^2D_{5/2} - ^4S_{3/2}$	3727 Å	3.86×10^4	3.40×10^3
			$^2D_{3/2} - ^4S_{3/2}$	3729 Å	3.86×10^4	1.50×10^4
OIII	$2p^2$	35.1	$^3P_2 - ^3P_1$	52 μm	441	3.60×10^3
			$^3P_1 - ^3P_0$	88 μm	163	5.10×10^2
			$^1S_0 - ^1D_2$	4363 Å	6.12×10^4	2.78×10^7
			$^1D_2 - ^3P_1$	4959 Å	2.91×10^4	6.80×10^5
			$^1D_2 - ^3P_2$	5007 Å	2.91×10^4	6.80×10^5
NeIII	$2p^4$	41	$^1S_0 - ^1D_2$	3343 Å	8.02×10^4	1.37×10^8
			$^1D_2 - ^3P_1$	3968 Å	3.72×10^4	9.50×10^6
			$^1D_2 - ^3P_2$	3869 Å	3.72×10^4	9.50×10^6
SII	$2p^3$	10.4	$^2D_{5/2} - ^4S_{3/2}$	6717 Å	2.14×10^4	1.57×10^3
			$^2D_{3/2} - ^4S_{3/2}$	6731 Å	2.14×10^4	1.49×10^4
SIII	$2p^2$	23.3	$^3P_2 - ^3P_1$	18 μm	1.20×10^3	1.31×10^4
			$^3P_1 - ^3P_0$	33 μm	429	4.22×10^3
			$^1S_0 - ^1D_2$	6312 Å	3.91×10^4	1.52×10^7

4.4 Nebula diagnostics by line ratios

The emission rate of the transition $j \rightarrow i$ ($j > i$) is

$$\epsilon_{ji} = E_{ji} A_{ji} n_j \quad (4.48)$$

$$A_{ji} = \frac{1}{(2L_j + 1)(2S_j + 1)} \sum_{J_j, J_i} (2J_j + 1) A(L_j, S_j, J_j \rightarrow L_i, S_i, J_i), \quad (4.49)$$

where A_{ji} is averaged over initial J -levels and summed by final J -levels.

4.4.1 T_e estimation

Hydrogen recombination lines have little dependence on electron temperature T_e but depend on cascade, i.e., Einstein coefficient. Table 4.2 shows emissivities of hydrogen spectrum relative to $H\beta$.

Table 4.2: Hydrogen emission line intensities relative to $H\beta$ described as $X/H\beta \equiv j_X/j_{H\beta}$. We assume Case B approximation and low density limit. Values are adopted from (Osterbrock & Ferland 2006).

Temperature [K]		2,500	5,000	10,000	20,000
$4\pi j_{H\beta}/(n_e n_p)$ [erg/s/cm ³]		2.70×10^{-25}	1.54×10^{-25}	8.30×10^{-26}	4.21×10^{-26}
Lyman series	$Ly\alpha/H\beta$	33	32.5	32.7	34
Balmer series	$H\alpha/H\beta$	3.42	3.1	2.86	2.69
	$H\gamma/H\beta$	0.439	0.458	0.47	0.485
	$H\delta/H\beta$	0.237	0.25	0.262	0.271
Paschen series	$P\alpha/H\beta$	0.684	0.562	0.466	0.394
	$P\beta/H\beta$	0.267	0.241	0.216	0.196

Instead of hydrogen lines, metal forbidden lines are useful to examine T_e of a HII region. Estimating T_e is crucial for estimating metallicity, as explained in section 4.4.3. The electron temperature is calculated by line ratio of the same ions with different levels and we derive T_e based on Seaton (e.g. 1954, 1960).

The electron configurations of ions are $2p^q$ or $3p^q$ ($q = 2, 3, 4$) and let us denote $n = 3, 2, 1$ as shown in Figure 4.7.

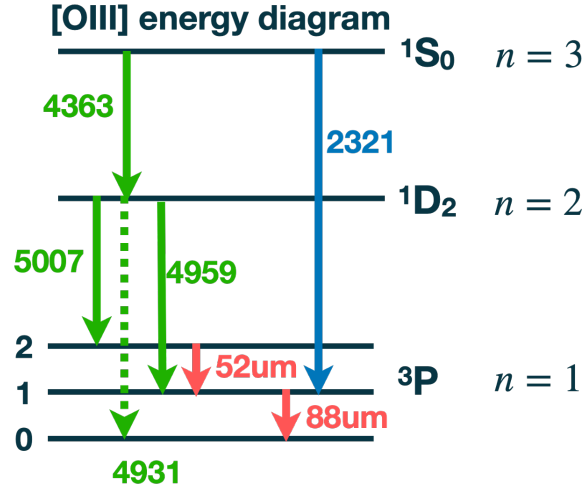


Figure 4.7: [OIII] energy diagram. Blue, green and red arrows indicate UV, optical and FIR emission lines, respectively. [OIII] 4931Å is emitted only by an electric-quadrupole transition and its emission is weak.

In equilibrium, the number of ions entering level n is the same as the number of ions leaving

as follows

$$(n = 2) \quad n_1 q_{12} + n_3 (A_{32} + C_{32}) = n_2 (A_{21} + C_{21} + C_{23}) \quad (4.50)$$

$$(n = 3) \quad n_1 C_{13} + n_2 C_{23} = n_3 (A_{31} + A_{32} + C_{31} + C_{32}). \quad (4.51)$$

C_{ji} is a collision rate per unit time,

$$C_{ji} \equiv n_e q_{ji}, \quad (4.52)$$

and q_{ji} is the collision rate per unit time per unit volume as derived in eq. 4.35. Eliminating n_1 from eq. 4.50 and eq. 4.51, we obtain

$$\frac{n_2}{n_3} = \frac{C_{12}}{C_{13}} \left\{ \frac{(A_{31} + C_{31}) + (A_{32} + C_{32}) [1 + C_{13}/C_{12}]}{(A_{21} + C_{21}) + (C_{12}C_{23}/C_{13}) [1 + C_{13}/C_{12}]} \right\}. \quad (4.53)$$

From eq. 4.52, eq. 4.35, we get

$$\frac{C_{13}}{C_{12}} = \frac{n_e q_{13}}{n_e q_{12}} = \frac{\Upsilon_{(1,3)}}{\Upsilon_{(1,2)}} \exp\left(-\frac{E_{32}}{kT_2}\right). \quad (4.54)$$

In the low-density limit, we can neglect collisional de-excitation from $n = 3$;

$$\frac{\Upsilon_{(1,3)}}{\Upsilon_{(1,2)}} \ll 1, \quad A_{31} \gg C_{31}, \quad A_{32} \gg C_{32} \quad (4.55)$$

$$\therefore \frac{C_{13}}{C_{12}} \ll 1. \quad (4.56)$$

Then we can simplify eq. 4.53 as

$$\frac{n_2}{n_3} = \frac{C_{12}}{C_{13}} \left\{ \frac{A_{31} + A_{32}}{A_{21} + C_{21} (C_{31} + C_{32}) / C_{31}} \right\}. \quad (4.57)$$

Finally, the line ratio $\epsilon_{21}/\epsilon_{3i}$ is derived by using eq. 4.57,

$$\frac{\epsilon_{21}}{\epsilon_{3i}} = \frac{E_{21} A_{21} n_2}{E_{3i} A_{3i} n_3} = \frac{E_{21} A_{21} C_{12}}{E_{3i} A_{3i} C_{13}} \left\{ \frac{A_{31} + A_{32}}{A_{21} + C_{21} (C_{31} + C_{32}) / C_{31}} \right\} \quad (4.58)$$

$$= \left[\frac{E_{21}}{E_{3i}} \frac{\Upsilon_{(1,2)}}{\Upsilon_{(1,3)}} \exp\left(\frac{E_{32}}{kT_e}\right) \frac{A_{31} + A_{32}}{A_{3i}} \right] \frac{1}{1 + \frac{C_{21}}{A_{21}} \frac{C_{31} + C_{32}}{C_{31}}} \quad (4.59)$$

$$= \left[\text{same} \right] \frac{1}{1 + \frac{n_e}{A_{21}} \frac{q_{21}(q_{31} + q_{32})}{q_{31}}} \quad (4.60)$$

$$= \left[\text{same} \right] \frac{1}{1 + \frac{n_e}{T_e^{1/2}} \frac{\Upsilon_{(1,2)}}{A_{21} \omega_2} \left(\frac{\Upsilon_{(3,1)} + \Upsilon_{(3,2)}}{\Upsilon_{(3,1)}} \right)} \quad (4.61)$$

$$= \frac{K_1 \exp\left(\frac{E_{32}}{kT_e}\right)}{1 + K_2 \frac{n_e}{T_e^{1/2}}} \quad (4.62)$$

For [OIII] line ratio for $i = 2$, we can calculate K_1, K_2, E_{32} as given in Table 4.3.

$$\frac{\epsilon_{21}}{\epsilon_{32}} = \frac{j_{4959} + j_{5007}}{j_{4363}} = \frac{7.90 \exp(3.29 \times 10^4 / T_e)}{1 + 4.5 \times 10^{-4} n_e / T_e^{1/2}} \quad (4.63)$$

Table 4.3: Values of K_1, K_2, E_{32} for line ratios of [OIII], [NII], [NeIII], [SII], adopted from Osterbrock & Ferland (2006).

ion	λ_{21} [Å]	λ_{32} [Å]	K_1	K_2	E_{32}/k
[OIII]	4959+5007	4363	7.90	4.5×10^{-4}	3.29×10^4
[NII]	6548+6583	5755	8.23	4.4×10^{-3}	2.50×10^4
[NeIII]	3869+3968	3343	13.7	3.8×10^{-5}	4.30×10^4
[SIII]	9532+9069	6312	5.44	3.5×10^{-4}	2.28×10^4

Other ions NII, NeIII and SIII have same electron configuration of np^2 , thus their line ratios also trace electron temperature. The values of K_1, K_2, E_{32} are tabulated in Table 4.3.

Figure 4.8 shows the line ratio for each ion as a function of T_e at $n_e = 100 \text{ cm}^{-3}$.

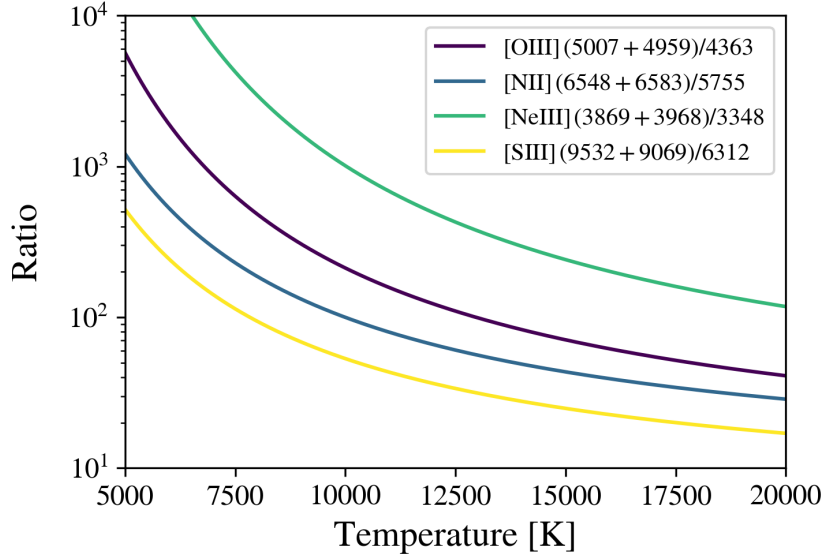


Figure 4.8: Line ratio as a function of electron temperature with the electron density of $n_e = 100 \text{ cm}^{-3}$.

4.4.2 Density estimation

The electron density n_e is calculated by the line ratio of the same ion with the same lower state, i.e., having only a different spin state.

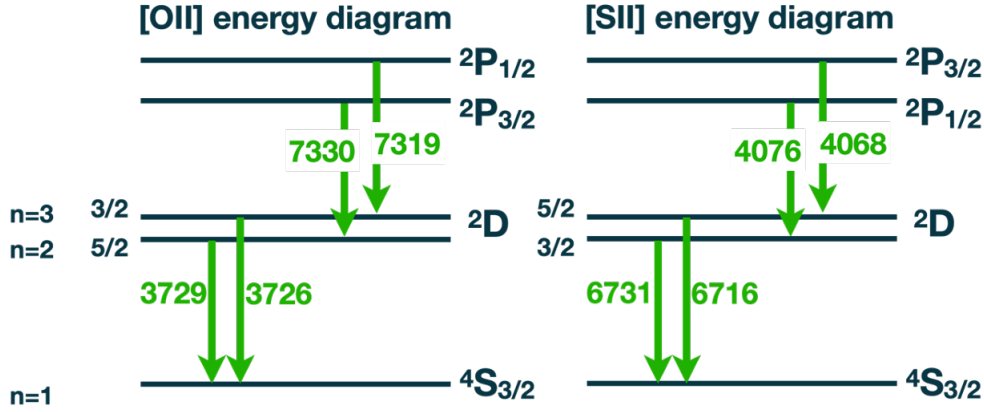


Figure 4.9: The first five energy diagram of OII and SII, which have np^3 configuration. Note that only the main optical emission lines are drawn as green arrows.

Figure 4.9 shows that the energy levels of upper state $D_{3/2}$ and lower state $D_{5/2}$ are almost the same and have little temperature dependence because their exciting energy is very close. However, they have different critical densities. Therefore, the line ratio is a good tracer of electron density. Notating $D_{3/2}$, $D_{5/2}$, S_0 as 3, 2, 1, and using eq. 4.40, we can write the line ratio as ⁵

$$\frac{j_{21}}{j_{31}} = \frac{\epsilon_{21}}{\epsilon_{31}} = \frac{q_{12}h\nu_{21}}{1 + \frac{n_e}{n_{\text{crit},21}}} \frac{1 + \frac{n_e}{n_{\text{crit},31}}}{q_{13}h\nu_{31}} \quad (4.64)$$

$$= \frac{q_{12}\nu_{21}n_{\text{crit},21}}{q_{13}\nu_{31}n_{\text{crit},31}} \cdot \frac{n_{\text{crit},31} + n_e}{n_{\text{crit},21} + n_e} \quad (4.65)$$

$$\equiv a \frac{b + n_e}{c + n_e} \quad (4.66)$$

The electron density is expressed by using the line ratio $R \equiv \frac{j_{21}}{j_{31}}$ and a, b, c defined in eq. 4.66,

$$n_e(R) = \frac{cR - ab}{a - R}. \quad (4.67)$$

In the case of low-density limit, the ratio becomes

$$\frac{j_{21}}{j_{31}} = \frac{\epsilon_{21}}{\epsilon_{31}} \quad (4.68)$$

$$\sim \frac{q_{12}h\nu_{21}}{q_{13}h\nu_{31}} \quad (4.69)$$

$$= \frac{\omega_2}{\omega_1} \exp\left(-\frac{E_{21}}{kT}\right) E_{21} \frac{\omega_1}{\omega_3} \exp\left(+\frac{E_{31}}{kT}\right) E_{31} \quad (4.70)$$

$$= \frac{\omega_2}{\omega_3} \exp\left(\frac{E_{32}}{kT}\right) \frac{E_{21}}{E_{31}} \sim \frac{\omega_2}{\omega_3} \quad (4.71)$$

where ω_i is a statistical weights at level i and the last approximation is from the assumption of $E_{32} \ll kT$ and $E_{32} \ll E_{21}$. This is because q_{12} and q_{13} have almost same collisional strength

⁵In these $D_{3/2} - S_0$, $D_{5/2} - S_0$ transitions, we can treat them as two-level systems.

$\Upsilon_{(1,2)} \sim \Upsilon_{(1,3)}$ and excitation energy $E_{12} \sim E_{13}$. For [OII] lines, low-density limit makes the ratio

$$\frac{j_{\lambda 3729}}{j_{\lambda 3726}} \rightarrow 1.5. \quad (\text{low density limit}) \quad (4.72)$$

In the case of high-density limit ($n_e \rightarrow \infty$), the ratio becomes

$$\frac{j_{21}}{j_{31}} \rightarrow \frac{q_{12} n_{\text{crit},21}}{q_{13} n_{\text{crit},31}} \quad (4.73)$$

$$= \frac{q_{12} q_{31} A_{21}}{q_{21} q_{13} A_{31}} \quad (4.74)$$

$$= \frac{n_2 n_1 A_{21}}{n_1 n_3 A_{31}} \quad (\because \text{eq. 4.36}) \quad (4.75)$$

$$= \frac{\omega_2 A_{21}}{\omega_3 A_{31}}. \quad (4.76)$$

The last term is from Boltzman distribution in thermal equilibrium (eq. 4.29). For [OII] line, we obtain

$$\frac{j_{\lambda 3729}}{j_{\lambda 3726}} \rightarrow \frac{3 \cdot 3.6 \times 10^{-5}}{2 \cdot 1.6 \times 10^{-4}} = 0.34. \quad (\text{high density limit}) \quad (4.77)$$

Figure 4.10 shows the [OII] and [SII] line ratio as a function of electron density.

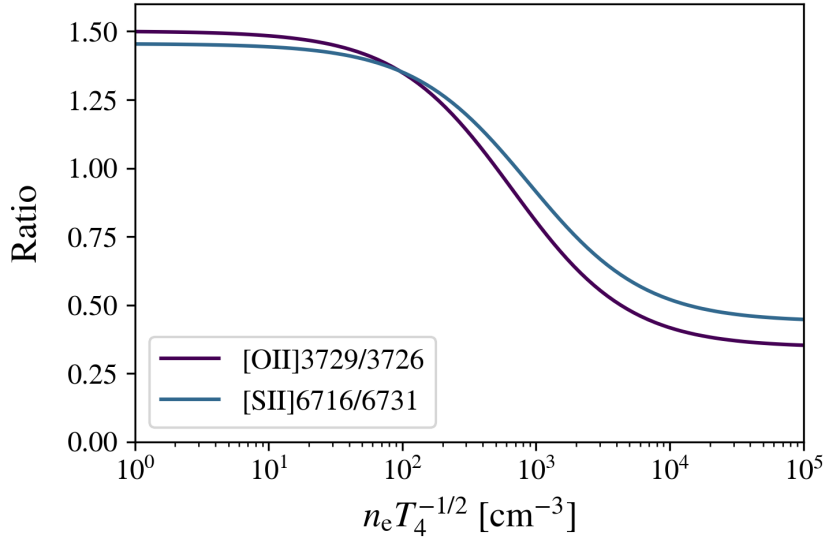


Figure 4.10: Line ratio as a function of electron density at $T_e = 10^4$ K.

[OIII] 52, 88 μm line ratio is also a useful indicator of electron density. Notating the electron configuration 3P_2 , 3P_1 , 3P_0 as 2, 1, 0, the [OIII] line ratio is written by using eq. 4.40,

$$\frac{j_{52}}{j_{88}} = \frac{j_{21}}{j_{10}} = \frac{n_2 A_{21} h \nu_{21}}{n_1 A_{10} h \nu_{10}} \quad (4.78)$$

We have to $\frac{n_2}{n_1}$ by considering three-level systems neglecting population of the fine-structure levels by radiative de-excitation from higher terms as shown in Figure 4.11.

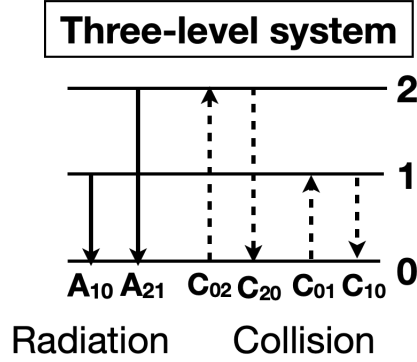


Figure 4.11: Transition through radiation (solid) and collision (dashed) in three-level systems.

The number of ions entering and leaving from level n ($n = 2, 1$) in equilibrium is written as the same as eq. 4.50 and eq. 4.51,

$$(n = 2) \quad C_{02}n_0 + C_{12}n_1 = (C_{20} + A_{20} + C_{21} + A_{21})n_2 \quad (4.79)$$

$$(n = 1) \quad C_{01}n_0 + (C_{21} + A_{21})n_2 = (C_{10} + A_{10} + C_{12})n_1 \quad (4.80)$$

Eliminating n_0 from the above two equations, we get

$$\frac{n_2}{n_1} = \frac{C_{02}(C_{10} + A_{10}) + C_{02}C_{12} + C_{12}C_{01}}{C_{01}(C_{20} + A_{20}) + C_{01}(C_{21} + A_{21}) + (C_{21} + A_{21})C_{02}}. \quad (4.81)$$

In eq. 4.78, in the case of low-density limit, we can neglect $O(C^2)$,

$$\frac{n_2}{n_1} \sim \frac{C_{02}A_{10}}{C_{01}(A_{20} + A_{21}) + A_{21}C_{02}} \sim \frac{C_{02}A_{10}}{(C_{01} + C_{02})A_{21}} \quad (\because A_{20} \ll A_{21}). \quad (4.82)$$

Therefore,

$$\frac{j_{52}}{j_{88}} = \frac{j_{21}}{j_{10}} \sim \frac{C_{02}A_{10}}{(C_{01} + C_{02})A_{21}} \cdot \frac{A_{21}h\nu_{21}}{A_{10}h\nu_{10}} \quad (4.83)$$

$$= \frac{q_{20}e^{-E_{21}/kT}}{q_{10} + q_{20}e^{-E_{21}/kT}} \cdot \frac{E_{21}}{E_{10}}. \quad (\text{low density limit}) \quad (4.84)$$

In the case of high-density limit, the system becomes thermalized and the level population follows Boltzmann distribution

$$\frac{n_2}{n_1} = \frac{g_1}{g_2} e^{-E_{21}/kT}. \quad (4.85)$$

The emission line ratio is

$$\frac{j_{52}}{j_{88}} = \frac{j_{21}}{j_{10}} \sim \frac{g_2}{g_1} e^{-E_{21}/kT} \frac{A_{21}E_{21}}{A_{10}E_{10}}. \quad (\text{high density limit}) \quad (4.86)$$

Collisional exciting and de-exciting rate C_{ij} ($i > j$), C_{ji} scales with $n_e/T_e^{1/2} \times \exp(-E_{ji}/kT_e)$ and $n_e/T_e^{1/2}$, respectively. Therefore, the line ratio of [OIII] 52 μ m and 88 μ m can be described as a function of $n_e T_e^{-1/2}$ as shown in Figure 4.12.

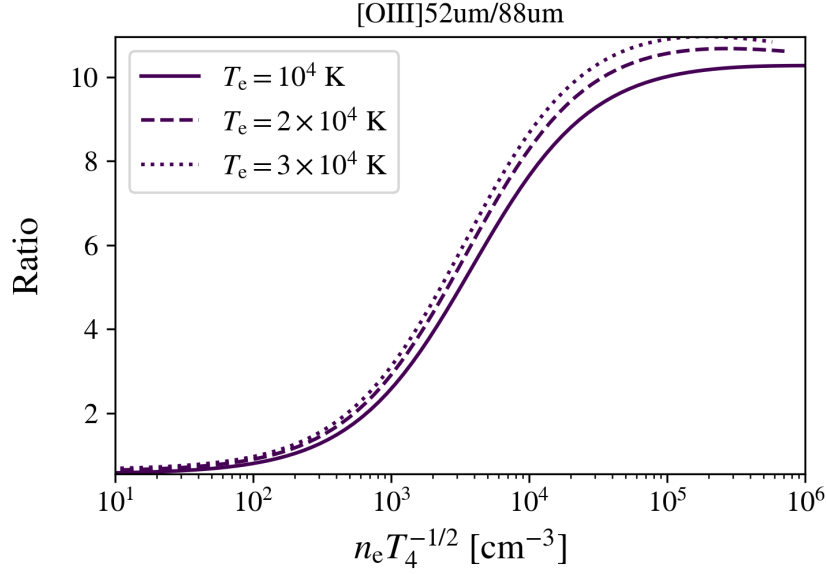


Figure 4.12: Line ratio $[\text{OIII}] 52\mu\text{m} / 88\mu\text{m}$ as a function of $n_e T_e^{-1/2}$ with different electron temperatures of $T_e = 10^4$ (solid), 2×10^4 (dashed), and 3×10^4 K (dotted).

4.4.3 Metallicity estimation

T_e direct method

Oxygen atoms are ionized in HII region and the oxygen abundance relative to hydrogen is expressed as

$$\frac{\text{O}}{\text{H}} = \frac{\text{O}^+}{\text{H}^+} + \frac{\text{O}^{++}}{\text{H}^+}. \quad (4.87)$$

$\frac{\text{O}^{++}}{\text{H}^+}$ is obtained from line ratio of $[\text{OIII}]$ and $\text{H}\beta$. We calculate emissivity of $[\text{OIII}] 5007, 4959\text{\AA}$ by using eq. 4.42,

$$\epsilon_{\lambda 5007} + \epsilon_{\lambda 4959} = \frac{4}{3} \epsilon_{\lambda 5007} = \frac{4}{3} n_e n_2 q_{32} h\nu_{32} \propto n_e n(\text{O}^{++}) T_e^{-1/2} \exp\left(-\frac{E_{32}}{kT_e}\right), \quad (4.88)$$

where $\epsilon_{\lambda 5007} : \epsilon_{\lambda 4959} = 3 : 1$ from quantum physics. The emissivity of $\text{H}\beta$ is written as

$$\epsilon_{\text{H}\beta} = n_e n_p \alpha_{\text{H}\beta}^{\text{eff}} E_{\text{H}\beta} \propto n_e n(\text{H}^+) T_e^{-1}. \quad (4.89)$$

Therefore,

$$\frac{\epsilon_{\lambda 5007} + \epsilon_{\lambda 4959}}{\epsilon_{\text{H}\beta}} = C_1 \frac{n(\text{O}^{++})}{n(\text{H}^+)} T_e^{1/2} \exp\left(-\frac{E_{32}}{kT_e}\right), \quad (4.90)$$

where coefficient C_1 is determined quantum mechanically and its temperature dependence is generally small.

The abundance ratio $\frac{\text{O}^+}{\text{H}^+}$ is obtained in the same way;

$$\frac{\epsilon_{\lambda 3726} + \epsilon_{\lambda 3729}}{\epsilon_{\text{H}\beta}} = C_2 \frac{n(\text{O}^+)}{n(\text{H}^+)} T_e^{1/2} \left[\exp\left(-\frac{E_{\lambda 3726}}{kT_e}\right) + \exp\left(-\frac{E_{\lambda 3729}}{kT_e}\right) \right]. \quad (4.91)$$

From eq. 4.90 and 4.91, we can derive oxygen abundance relative to hydrogen

$$\frac{\text{O}}{\text{H}} = \frac{\epsilon_{\lambda 3727}}{\epsilon_{\text{H}\beta}} \times D_1(T_e) + \frac{\epsilon_{\lambda 5007} + \epsilon_{\lambda 4959}}{\epsilon_{\text{H}\beta}} \times D_2(T_e), \quad (4.92)$$

where T_e is determined directly as described in section 4.4.1. However, auroral line $[\text{OIII}] \lambda 4363 \text{ \AA}$ can be emitted only at high electron temperature, it is difficult to detect the line and estimate T_e .

Strong-line method

Instead of direct T_e method, strong line method combining strong lines of $[\text{OII}]$, $[\text{OIII}]$, $\text{H}\beta$, or combining strong lines of $[\text{NII}]$ and $\text{H}\alpha$ can be used.

We take the strong line relative to $\text{H}\beta$ defined as

$$R_{23} \equiv \frac{[\text{OII}]_{\lambda 3727} + [\text{OIII}]_{\lambda 4959, 5007}}{\text{H}\beta_{\lambda 4861}}. \quad (4.93)$$

It is empirically known that R_{23} depends on gas-phase metallicity as shown in the left of Figure 4.13 (e.g. Curti et al. 2017, 2020; Maiolino et al. 2008; McGaugh 1991; Nagao et al. 2006; Pagel et al. 1979). Notice that R_{23} is a two-valued function of metallicity. Also, R_{23} can be easily affected by dust extinction and its correction is important.

The other strong line $[\text{NII}] \lambda 6584 \text{ \AA}$ is also useful as a metallicity indicator,

$$N2 \equiv \frac{[\text{NII}]_{\lambda 6584}}{\text{H}\alpha_{\lambda 6563}}, \quad (4.94)$$

which is useful because $[\text{NII}]$ and $\text{H}\alpha$ are close in wavelength and dust extinction does not quite affect the line ratio, and it is a single value function of metallicity as shown in the right of Figure 4.13. It is known that $[\text{NII}]$ is too weak to be observed for low-metallicity environments, since the main nitrogen source is AGB stars, which contribute after 40 million years after star formation as explained in section 4.1.

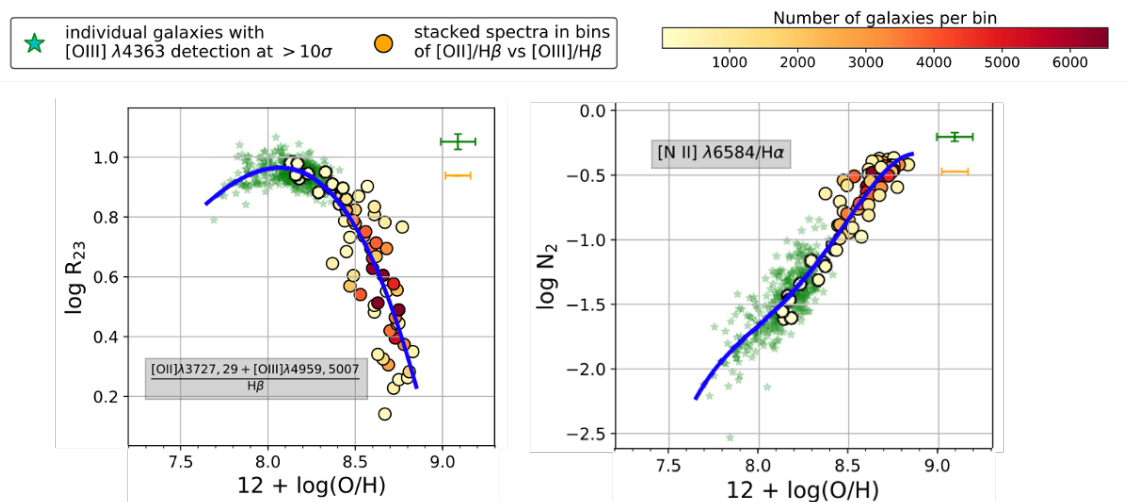


Figure 4.13: The flux ratio of R_{23} and $N2$ as a function of gas-phase metallicity. Green stars shows individual galaxies and colored circles are stacked galaxies. The blue lines in each panel are fitting lines to the data points. Adopted from Curti et al. (2020).

4.5 Observation of high-redshift galaxies

4.5.1 Dropout method

Dropout method is commonly used for detecting high-redshift galaxies using photometric data. Star-forming galaxies emit UV continuum, but photons with $\lambda_{\text{rest}} < 912\text{\AA}$ are absorbed when neutral hydrogen atoms exist in the IGM⁶. Galaxies detected by this method are termed Lyman Break Galaxies (LBGs). LBGs at $z \sim 3$ are firstly detected (Steidel et al. 1996, 1995). Following observations have detected $z \sim 6 - 7$ LBGs (e.g. Bouwens et al. 2010). After selecting high-redshift galaxy candidates by Lyman break method, the accurate redshift is determined by follow-up spectroscopic observations. LBGs at $z \lesssim 7$ tend to emit strong Lyman- α and such galaxies are called Lyman Alpha Emitters (LAEs). Spectroscopic observations for LBGs have also been performed to detect Ly α emission line.

However, the cosmic reionization is on-going at $z \gtrsim 8$ and Lyman- α photons are scattered by neutral hydrogen atoms in inter-galactic medium (IGM). Currently, the most distant galaxies detected by Ly α is located at $z = 8.78$ (GN-z10-3 Laporte et al. 2021), and no galaxies at $z > 9$ have been observed by Ly α ⁷. Using other emission lines is promising to detect galaxies at $z \gtrsim 8$.

4.5.2 Detection of $z \sim 6 - 9$ galaxies by ALMA

Atacama Large Millimeter/submillimeter Array (ALMA) can detect rest-frame FIR emission lines. As explained in section 4.2.2, [CII] $158\mu\text{m}$ ($^2P_{3/2} \rightarrow ^2P_{1/2}$) line originates from HII region and PDR, and is expected to be a good tracer of star-forming regions in high-redshift galaxies. However, [CII] is not detected in bright LAE (Ota et al. 2014; Ouchi et al. 2013; Schaerer et al. 2015), which implies that characters of ISM may be quite different from that of local ones. Some simulations and ISM models suggest that [CII] emission may decrease owing to low metallicity ISM, excitation by high CMB temperature, and low-density PDR generated by stellar feedback (Pallottini et al. 2017a,b; Vallini et al. 2013, 2015), but all of them have not been established.

[OIII] $88\mu\text{m}$ is emitted from HII regions and is known as one of the strongest FIR emission lines. [OIII] lines in local low-metallicity dwarf galaxies are stronger than [CII] line (Cormier et al. 2012; Madden et al. 2013), which suggests that high-redshift galaxies with low-metallicities can also be bright [OIII] emitters (Inoue et al. 2014). A qualitative explanation for [OIII] increase in the low-metallicity environment is the following; cooling of gas is inefficient in low-metallicity environments. Jeans mass of a star-forming cloud is large and massive stars tend to be born as explained in section 4.1. Massive stars have a short life of a few - 40 Myrs and end in Type-II SNe. The dissipated metals by Type-II SN contain large amounts of Oxygen (Woosley & Weaver 1995) as shown in Figure 4.2.

[OIII] $88\mu\text{m}$ emission line from a galaxy at $z = 7.2$ is first detected by ALMA (Inoue et al. 2016), and since then, other galaxies have been detected by [OIII] $88\mu\text{m}$ (Carniani et al. 2017;

⁶UV continuum at wavelengths shorter than the Lyman break is strongly absorbed by the IGM. The wavelength of Lyman break is in the range of 912\AA and 1216\AA (Ly α).

⁷There is a Ly α detection with significance with 4σ in the galaxy MACS1149-JD1 at $z = 9.1$ (Hashimoto et al. 2018).

Harikane et al. 2020; Hashimoto et al. 2018, 2019; Inoue et al. 2016; Laporte et al. 2017; Tadaki et al. 2022; Tamura et al. 2019; Witstok et al. 2022; Wong et al. 2022).

4.5.3 Latest observation by JWST

James Webb Space Telescope was launched on December 25th, 2021 and the first images were published on July 12th, 2022. Most distant galaxy candidates are detected by NIRCam, and their redshifts are (will be) determined by spectroscopic observation with NIRSpec (and also by ALMA).

NIRCam observation

Galaxy candidates are selected by dropout method as explained in section 4.5.1. Figure 4.14 shows a set of model SEDs of high-redshift galaxies at $z = 7 - 10$. The SED has the Lyman break at $\sim 1216 \text{ \AA}$ in the rest-frame⁸.

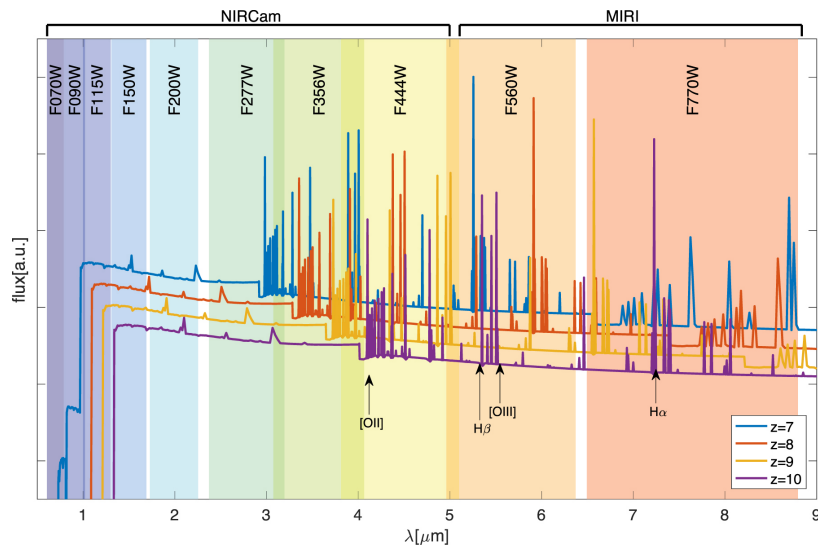


Figure 4.14: SED models for galaxies. Blue, red, orange, and purple lines indicate galaxy SEDs at $z = 7, 8, 9, 10$, respectively. Colored areas show photometric bands for NIRCam and MIRI. The clear flux drop at observed wavelength of $\lambda \sim 1 \mu\text{m}$ is Lyman break. Adopted by Bisigello et al. (2017).

Figure 4.15 shows color-color diagrams for galaxies at $z \sim 9, 12, 17$ identified by Lyman break. As shown in Figure 4.14, the dropout filter is different at different redshift. For example, $z \sim 9$ galaxies show Lyman break in their SED between F115W-F150W.

⁸Some SEDs with mature stellar age have Balmer breaks at $\sim 4000 \text{ \AA}$ in the rest-frame.

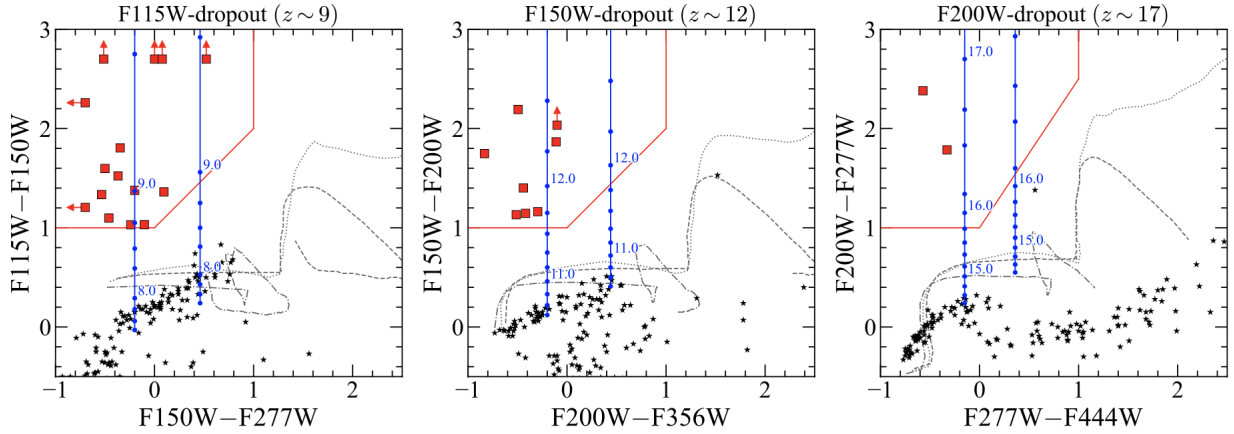


Figure 4.15: Two color diagrams for selection of galaxies at $z \sim 9$ (left), $z \sim 12$ (middle), and $z \sim 17$ (right). Each vertical axis detects Lyman break at each redshift. High-redshift objects are distinguished by a red line, which is drawn to avoid interlopers such as local galaxies and dwarf stars. Adopted from Harikane et al. (2022a).

Notice that the photometric redshift estimation may contaminate low-redshift galaxies. There can be possibilities that the dropout is not originated from a Lyman break but a Balmer break of low-redshift galaxies as shown in Figure 4.16.

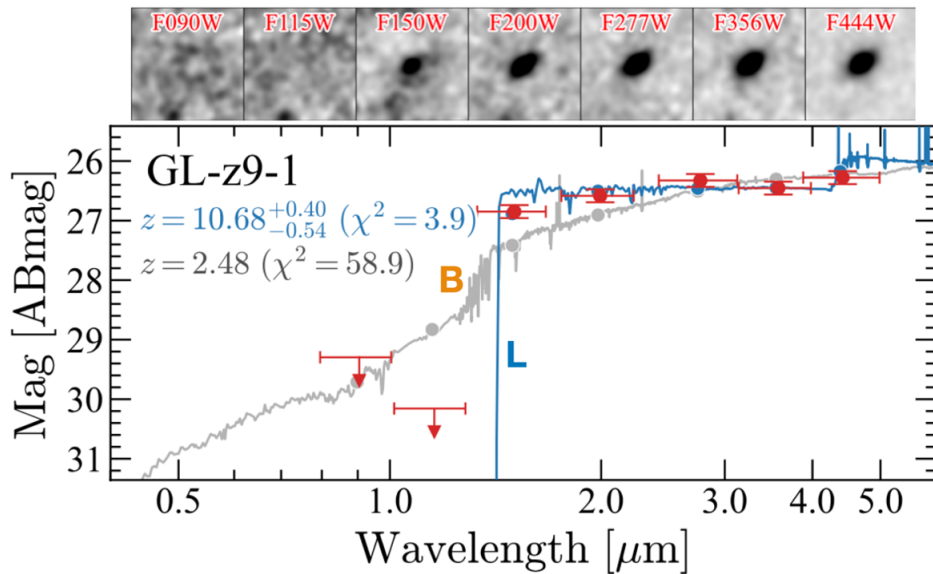


Figure 4.16: (top) NIRCcam images of galaxy GL-z9-1. There appears to be a drop at F115W. (bottom) SED fitting to a $z \sim 9$ galaxy candidate. The blue (gray) line indicates a SED model for a $z \sim 9$ ($z \sim 2.5$) galaxy assuming the dropout originates from Lyman (Balmer) break. Adopted by Harikane et al. (2022a) and added some captions.

So far, JWST have discovered bright galaxy candidates at unprecedentedly high redshifts of $z > 9$ by NIRCcam (e.g. Castellano et al. 2022; Donnan et al. 2022; Finkelstein et al. 2022;

Harikane et al. 2022a; Naidu et al. 2022). For instance, Harikane et al. (2022a) detect 25 galaxy candidates at $z > 9$ which are bright in UV ($M_{UV} \gtrsim -21$).

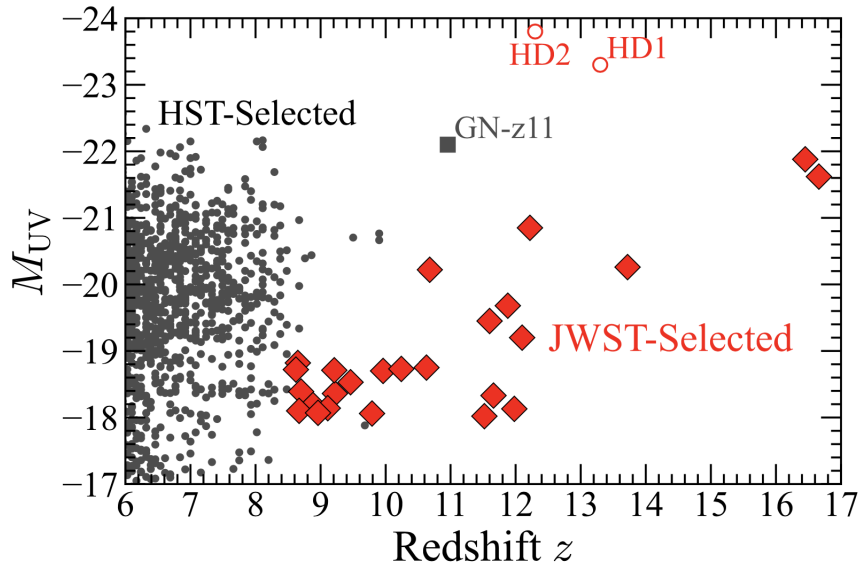


Figure 4.17: Absolute UV magnitude for galaxies at $z = 6 - 17$. Galaxies with red diamonds, red open circles, gray symbols are selected by NIRC*am* Images, and by a combination of Spitzer and ground-based telescope, HST images, respectively. GNz-11 is the farthest confirmed galaxy (Jiang et al. 2021; Oesch et al. 2016). Adopted from Harikane et al. (2022a).

In order to determine the redshift accurately, spectroscopic observations are required. In the JWST Cycle 1, several observation results of NIRS*pec* have been published (Curti et al. 2022; Roberts-Borsani et al. 2022; Schaerer et al. 2022; Williams et al. 2022).

NIRS*pec* observation

JWST NIRS*pec* can observe rest-frame optical emission lines from high-redshift galaxies. Figure 4.18 shows the spectrum of $z = 8.5$ galaxy (Carnall et al. 2023; Curti et al. 2022; Heintz et al. 2022; Katz et al. 2022; Schaerer et al. 2022; Trump et al. 2022). Several rest-frame optical lines are detected clearly, especially [OIII] 5007 Å, 4959 Å, H β , and [OIII] 3727 Å. Surprisingly, [OIII] 4363 Å is also detected, which enables us to estimate electron temperature in the nebula by direct method as explained in section 4.4.1.

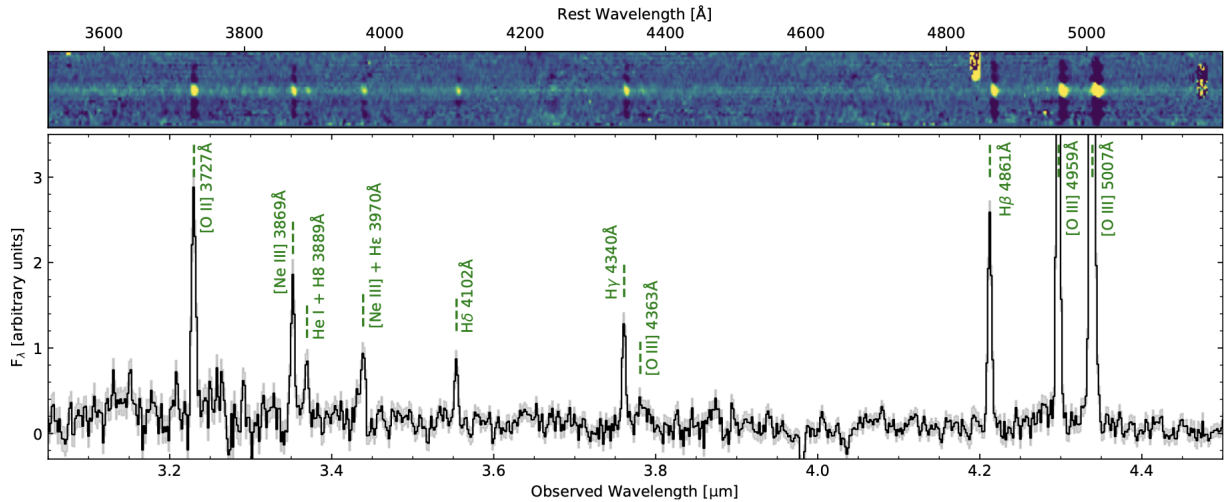


Figure 4.18: 2D (top) and 1D (bottom) spectrum of a $z = 7.6$ galaxy observed by JWST NIRSpec. Adopted by Schaerer et al. (2022).

Rest-frame optical lines detected by NIRSpec not only determine the accurate redshift but also allow estimating the fundamental physical properties of galaxies such as the ISM temperature, density, and metallicity. Rest-frame optical lines from low-redshift galaxies have already been observed by HST, and physical properties have been studied using emission line ratios (e.g. Maiolino et al. 2008).

4.5.4 Synergy of JWST and ALMA

For the galaxy candidates introduced in section 4.5.3, several follow-up ALMA observations have attempted to detect FIR emission lines such as [OIII] $88\mu\text{m}$ and [CII] $158\mu\text{m}$, which ended in reporting detections with significance with less than 4σ (Bakx et al. 2022; Fujimoto et al. 2022; Kaasinen et al. 2022; Popping 2022; Yoon et al. 2022). Figure 4.19 shows all of the galaxies at $z = 6 - 9$, where detection of [OIII] $88\mu\text{m}$ has been confirmed. Three galaxy candidates at $z > 10$ are observed with only upper limit detection of [OIII] $88\mu\text{m}$. In comparison with local galaxies, high-redshift galaxies tend to emit stronger [OIII] lines.

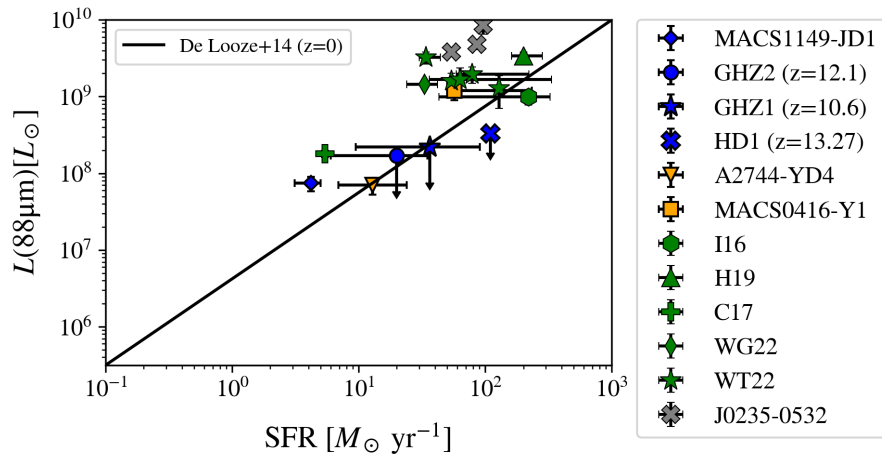


Figure 4.19: The [OIII] 88 μm luminosity versus SFR for observed galaxies at $z > 9$ (blue), $z = 8$ (orange), $z = 7$ (green), and $z = 6$ (gray). For comparison, we show the [OIII]-SFR relation derived from observations of local galaxies by De Looze et al. (2014). Galaxies at $z > 9$ from Hashimoto et al. (2018)(MACS1149-JD1), Bakx et al. (2022)(GHZ2), Yoon et al. (2022)(GHZ1), and Harikane et al. (2022b). $z \sim 8$ galaxies from Laporte et al. (2017)(A2744-YD4) and Tamura et al. (2019)(MACS0416-Y1). $z \sim 7$ galaxies from Inoue et al. (2016)(I16), Hashimoto et al. (2019)(H19), Carniani et al. (2017)(C17), Wong et al. (2022)(WG22) and Witstok et al. (2022)(WT22). $z \sim 6$ galaxies from Harikane et al. (2020).

For the upcoming observations to be conducted by JWST, it is urgently needed to study the population of high-redshift galaxies with high resolution in a fully cosmological context. In the following, we use the outputs of FirstLight simulation (Ceverino et al. 2017). The simulation suite is motivated to produce a statistically significant number of galaxies with very high resolution at the epoch of reionization. Thanks to the mass and volume complete sample of more than 60 massive galaxies and to the high-resolution of ~ 20 pc, we can investigate the internal structure as well as statistics of the high-redshift galaxies.

Chapter 5

Simulations of high-redshift [OIII] emitters: Chemical evolution and multi-line diagnostics

5.1 FirstLight simulation

We use mass-selected galaxy samples selected from the FirstLight simulation suite (Ceverino et al. 2017). The simulations are performed with ART code (Ceverino & Klypin 2009; Ceverino et al. 2014; Kravtsov 2003; Kravtsov et al. 1997), which follows gravitational N -body dynamics and Eulerian gas dynamics using an adaptive mesh refinement (AMR) method. Besides gravity and hydrodynamics, the code incorporates astrophysical processes relevant to galaxy formation.

First of all, DM-only simulations are conducted with a low-resolution of 128^3 . The cosmological simulations are performed from $z = 150$ to $z = 5$ in a cosmological volume of 40 Mpc/h box on a side. Massive dark halos are selected that have maximum circular velocity (V_{\max}) higher than 178 km/s at $z = 5$. After the host haloes are selected in a low-resolution N -body only simulation, refined initial conditions are generated using a standard zoom-in technique (Klypin et al. 2011). The refinement sets the dark matter particle mass of $m_{\text{DM}} = 8 \times 10^4 M_{\odot}$, the minimum star particle mass of $10^3 M_{\odot}$ as shown in Figure 5.1, and the maximum spatial resolution achieved is 17-32 proper parsec depending on the refinement level, with the effective resolution of 8192^3 .

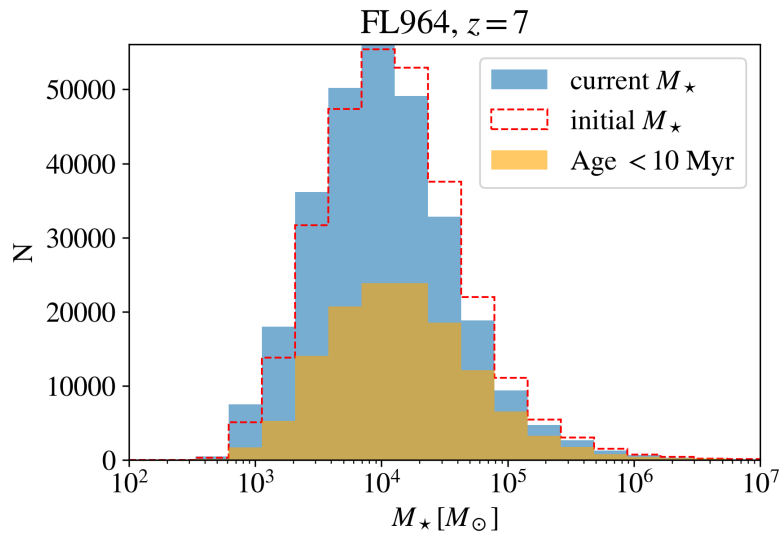


Figure 5.1: The star particle mass distribution for a one galaxy sample (FL964) at $z = 7$. Blue, red-dotted, and orange histograms represent the initial, current, and younger than 10 Myr stellar particle distributions, respectively. Current stellar particles have experienced mass-loss events. We select stars within a rectangular region of $0.3 R_{\text{vir}}$ on a side.

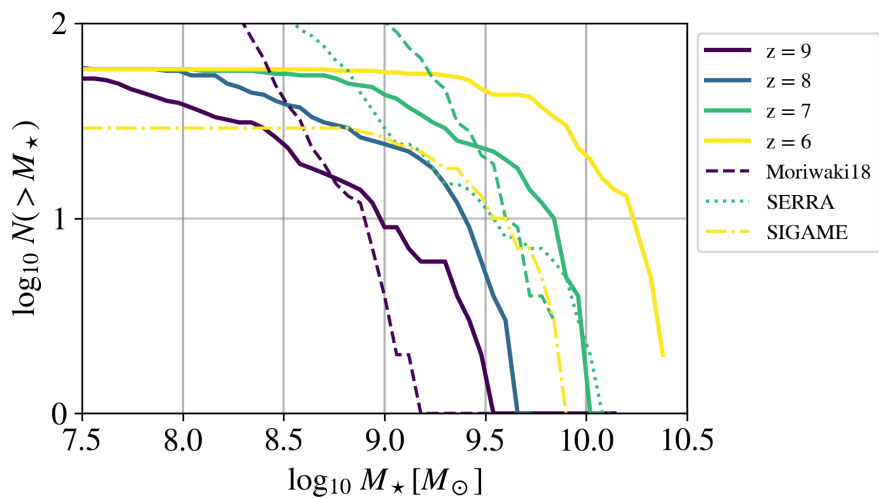


Figure 5.2: Cumulative distribution of stellar mass for massive galaxy samples ($V_{\text{max}} > 187 \text{ km/s}$) in FirstLight simulation. Dashed lines are results from Moriwaki et al. (2018) (purple and green), a green dotted line and a yellow dashdot line are results from SERRA simulation (Pallottini et al. 2022) and SIGAME simulation Olsen et al. (2017), respectively. Each color represents different redshifts.

Figure 5.2 shows the cumulative stellar mass distribution for 62 massive galaxies at $z = 6 - 9$ in our high resolution simulation. For comparison, we plot the stellar distribution from other

simulations, which have calculated [OIII] emission lines for their galaxy samples and shown the emission statistics (Moriwaki et al. (2018), SERRA simulation (Pallottini et al. 2022) and SÍGAME simulation (Olsen et al. 2017).) It is clear that our simulation samples cover massive galaxies than other simulations; for instance, $M_\star \gtrsim 10^{8.7} M_\odot$ at $z = 9$, $M_\star \gtrsim 10^{9.5} M_\odot$ at $z = 7$, and $M_\star \gtrsim 10^{8.7} M_\odot$ at $z = 6$. Therefore, our samples are comparable to observable massive galaxies by HST, ALMA and JWST (e.g. Barrufet et al. 2022; Graziani et al. 2020; Leethochawalit et al. 2022; Tacchella et al. 2022; Topping et al. 2022; Trussler et al. 2022). We have also checked the stellar mass histories for all of our samples from $z = 9.5$ to $z = 5$ in Figure 5.3. Interestingly, two galaxy samples with orange and blue have lower stellar mass of $\sim 10^8 M_\odot$ than others, finally have most/least massive stellar masses at $z = 5$. This implies that the observed $z = 6$ galaxies are not descendants of the observed $z = 9$ galaxies.

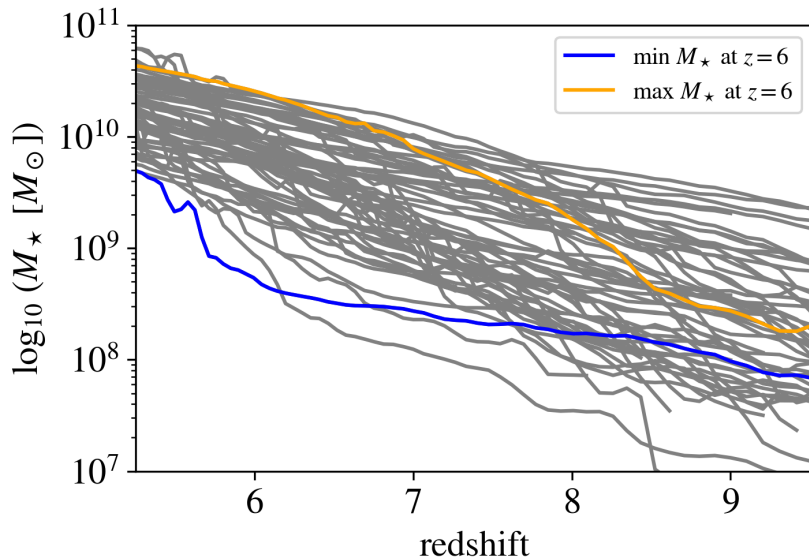


Figure 5.3: stellar mass histories of the main galaxies from $z = 9.5$ to $z = 5.5$. Those galaxies have a large circular velocity of $V_c > 178$ km/s at $z = 5$. An orange (blue) line traces the evolution of a galaxy which has the maximum (minimum) stellar mass at $z = 6$.

5.1.1 Subgrid physics

Besides the two processes, the code incorporates astrophysical processes relevant to galaxy formation. The so-called subgrid physics includes atomic and molecular cooling of hydrogen and helium, photoionization heating by a cosmological UV background with partial self-shielding, and star formation and the associated stellar feedback. Details are described in Ceverino et al. (2017). The simulations track metals released from SNe-Ia and from SNe-II, using supernovae yields from Woosley & Weaver (1995). In order to simulate a galaxy formation, we need to consider baryon physics as a subgrid model. The subgrid models are based on previous studies by Ceverino et al. (2010, 2012); Ceverino & Klypin (2009); Ceverino et al. (2014). The detailed subgrid models are explained in Appendix B.

5.1.2 Definition of notation

Here, we introduce the following notation for metallicity, and density. Direct outputs from the simulations are physical quantities for gas cells and stellar particles. A gas cell contains the information of cell size, number density, metallicity ($= Z_{\text{gas}}$), velocity, and coordinates. A stellar particle contains the information of mass, age, metallicity ($= Z_{\star}$), velocity, and coordinate. Apart from the simulation outputs, we arrange gas grids with a side length of 100 pc (details in the next section 5.2). Each grid has averaged density $n_{\text{gas,grid}}$ from all of the cells inside the grid. Metallicity of a gas grid is denoted $Z_{\text{gas,grid}}$ and averaged by weighting density of each cell. When we refer metallicity for each galaxy, we denote it nebular metallicity, averaging $Z_{\text{gas,grid}}$ by weighting [OIII] emissivity in each gas grid. Figure 5.4 summarize the distinction of each physical quantity.

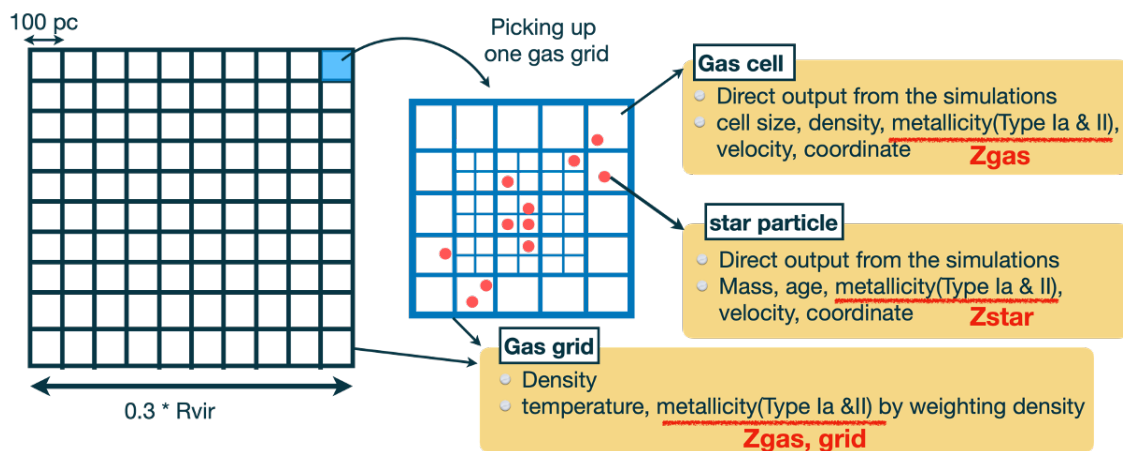


Figure 5.4: Schematic illustration of simulation output and re-arrangement of gas grid.

5.2 Line emissivity calculation

We model HII regions and calculate line emissivities as a post-processing and the procedures are overviewed in Figure 5.5.

We generate emission-line maps for our galaxy samples. First, we choose a region enclosed by 0.3 times the virial radius of each galaxy as same as Mandelker et al. (2017, 2014) and configure 3D grids with a side length of 100 pc, which is sufficiently large, and Strömgren sphere around star particle does not exceed the grid size (Ceverino et al. 2021). We have also tried changing the size from 50 pc to 300 pc, and have found that the luminosity is the same in the all cases.

We locate the star particles and gas elements within each grid, and store the mass of stars younger than 10 Myr, the average density of the gas with $n_{\text{H}} > 0.1 \text{ cm}^{-3}$, and the average metallicity of the cold/warm gas with $T < 5 \times 10^4 \text{ K}$. These physical quantities assigned to the individual grids are then used to compute the line emissivities in a similar manner to those in Gutkin et al. (2016); Hirschmann et al. (2017); Moriwaki et al. (2018). We generate a library of emission lines using CLOUDY (Ferland et al. 2013). The library covers a wide range of gas

metallicity Z , ionization parameter U as given in Table 5.2.

The library lists the line luminosity, L_{line} , normalized by the $\text{H}\beta$ line luminosity with the case-B approximation (Dopita & Sutherland 2003), $L_{\text{H}\beta}^{\text{caseB}}$, as

$$L_{\text{line}} = (1 - f_{\text{esc}}) C_{\text{line}}(Z_{\text{gas,grid}}, U, n_{\text{HII}}) L_{\text{H}\beta}^{\text{caseB}}, \quad (5.1)$$

where f_{esc} is the Lyman continuum escape fraction and C_{line} is the line luminosity ratio. Since individual HII regions are not resolved in our simulations, we resort to a physical model of the ISM structure to calculate the line emissivities of HII regions. We characterize the ISM by the local gas density n and metallicity Z , and a volume-averaged ionization parameter $\langle U \rangle$ as explained in the following.

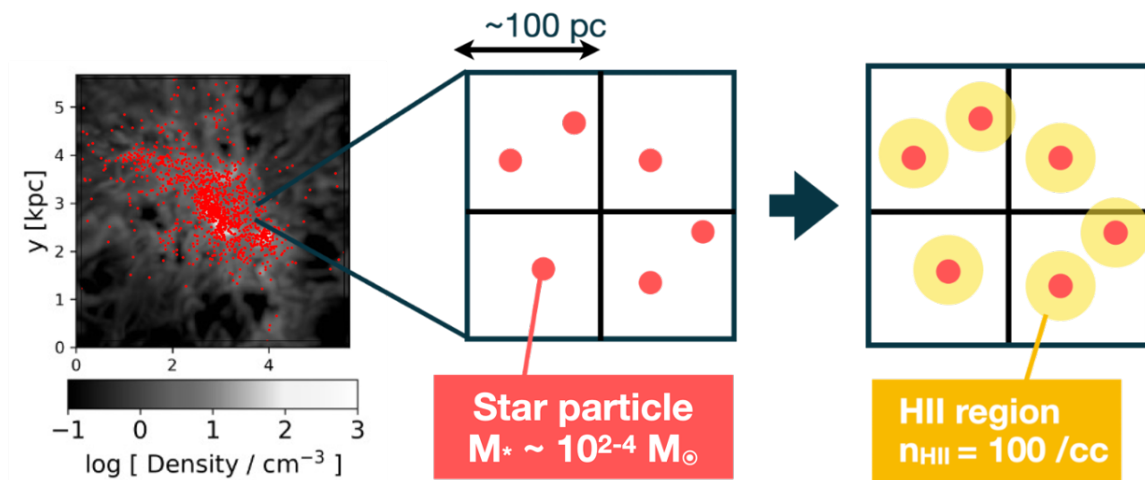


Figure 5.5: A simple cartoon of the modeling of HII regions. Left: Gas number density distribution with gray colormap and stellar particles younger than 10 Myr with red dots. One side length of the region is $0.3R_{\text{vir}}$. Middle: an enlargement of the grids, which have a side length of 100 pc. Each grid contains several stellar particles. Right: HII regions around stellar particles as yellow circles. We assume spherical HII regions with a Strömgen radius.

5.2.1 Escape fraction f_{esc}

We set $f_{\text{esc}} = 0.1$, which is consistent with previous radiative transfer simulations for massive galaxies with $M_{\text{halo}} > 10^{10-11} M_{\odot}$ (Kimm & Cen 2014; Paardekooper et al. 2015; Wise et al. 2014; Xu et al. 2016; Yajima et al. 2011), also consistent with observation results at $z \sim 6-8$ (Castellano et al. 2017; Robertson et al. 2013). We also note that some galaxies have been reported to have high escape fraction of over 20 % (e.g. Bian & Fan 2020; Fletcher et al. 2019; Flury et al. 2022; Marques-Chaves et al. 2022; Vanzella et al. 2016) at $z < 4$.

electron density n_{HII}

Our fiducial model assumes a constant gas density in HII regions $n_{\text{HII}} = 100 \text{ cm}^{-3}$ (e.g. Hirschmann et al. 2017, 2022; Osterbrock & Ferland 2006). We have also checked the case of $n_{\text{HII}} =$

86 Simulations of high-redshift [OIII] emitters: Chemical evolution and multi-line diagnostics

50, 300 cm^{-3} , and shown that the [OIII] emissivity does not change by an order. Furthermore, even though we set n_{HII} as gas number density in grids as same as Moriwaki et al. (2018), the total emissivity of [OIII] and its distribution inside galaxies do not change. This is because our fixed n_{HII} model can also trace gas density distribution by introducing the following factor ϵ .

5.2.2 Ionization parameter U

We assume a constant gas density n_{HII} in a spherical HII region surrounding a star particle (e.g. Hirschmann et al. 2017, 2022; Panuzzo et al. 2003) as explained the above section. A volume-averaged ionization parameter is derived in section 4.2.1 as

$$\langle U \rangle = \frac{3\alpha_{\text{B}}^{2/3}}{4c} \left(\frac{3Q\epsilon^2 n_{\text{HII}}}{4\pi} \right)^{1/3}. \quad (5.2)$$

The volume-filling factor of the gas ϵ is defined by

$$\epsilon = \frac{(\text{volume occupied by the clumps})}{(\text{total volume of HII region})} \equiv \frac{n_{\text{gas,grid}}}{n_{\text{HII}}}, \quad (5.3)$$

where $n_{\text{gas,grid}}$ is the gas number density in each grid. In rare cases where the volume-averaged gas density exceeds the adopted hydrogen density in the ionized regions ($\epsilon > 1$), we set the filling factor to unity. Note that a larger $n_{\text{gas,grid}}$ at fixed n_{HII} implies a larger filling factor ϵ , i.e., more compact gas clumps around the ionizing source. To calculate the ionization photon production rate Q , we use the value from Binary Population and Spectral Synthesis (BPASS) model (Byrne et al. 2022).

5.2.3 Ionizing photon rate Q from a population synthesis model

We compute the production rate of ionizing photons Q of the simulated galaxies using publicly available tables from the Binary Population and Spectral Synthesis (BPASS) model (Byrne et al. 2022). All physical properties we have selected are summarized in Table 5.1.

Table 5.1: BPASS table. We select the same population and IMF for all stellar particles. The rest four parameters are chosen for each stellar particle.

population	single stellar population
IMF	$\alpha_1 = -1.3, \alpha_2 = -2.35, M_1 = 0.5, M_{\text{max}} = 300 M_{\odot}$
$[\alpha/\text{Fe}]$	$\Delta(\log(\alpha/\text{Fe})) = -0.2, +0.0, +0.2, +0.4, +0.6$
metallicity (Z_{\star})	$10^{-5}, 10^{-4}, 10^{-3}, 0.002, 0.004, 0.008, 0.01, 0.02(Z_{\odot}), 0.03, 0.04$
Age	50 logarithmic bins in [1 Myr, 100 Gyr]; $10^{(6+0.1n)}$ $n = 0 - 50$
Mass	Fixed stellar particle mass of $10^6 M_{\odot}$ in BPASS data

Our simulations adopt the stellar initial mass function modeled by broken power laws as

$$N(M < M_{\text{max}}) \propto \int_{0.1}^{M_1} \left(\frac{M}{M_{\odot}} \right)^{\alpha_1} dM + M_1^{\alpha_1} \int_{M_1}^{M_{\text{max}}} \left(\frac{M}{M_{\odot}} \right)^{\alpha_2} dM \quad (5.4)$$

We re-assign all of young stellar age in order to remove the time step effect of a star formation process in the simulations. This is because our simulations produce new stellar particles with a times step of $\Delta t_{\text{SF}} = 5$ Myr (see details in Appendix 5.1.1) and each galaxy usually has only two kinds of stellar age younger than 10 Myr as shown in Figure 5.2.3. Most emission lines from HII regions are originated from young less than 10 Myr. For BPASS SED of a single stellar population, the number of ionizing photons will decrease over 2 dex from age 1 Myr to 10 Myr (Xiao et al. 2018), which might change the emissivity of each line for 2 dex from eq. 5.1 and eq. 5.8.

Then, we re-assign the stellar age as follows.

1. Consider stellar particle younger than 15 Myr. Notate three stellar ages T_1 , T_2 , T_3 ($T_1 < T_2 < T_3$) [Myr].
2. Reassign stellar age randomly within the range of $[T_3, T_2]$, $[T_2, T_1]$, and $[T_1, 1]$ Myr, respectively.

Figure 5.2.3 shows stellar age-mass distribution for one galaxy sample at $z = 7$ and $z = 6$.

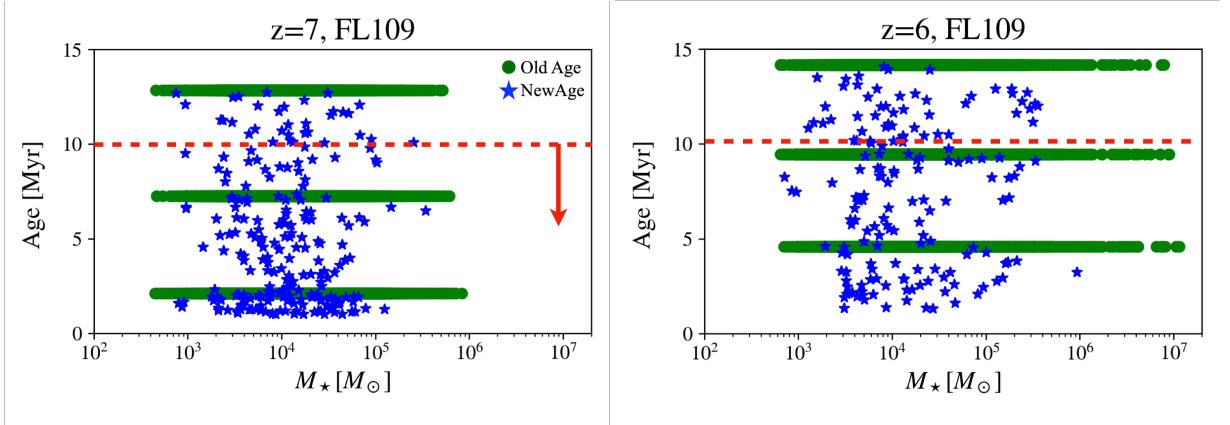


Figure 5.6: Stellar age - mass distribution. Green dots show the stellar ages before re-assignment, and blue stars show the new ages. Notice that blue stars are plotted by thinning out by 100 for visualization. A red dashed line indicates the threshold age of 10 Myr.

After re-assigning stellar age, we calculate ionizing photon rate Q for each young stellar particle (< 10 Myr) by multiplying the BPASS data by $(M_*/10^6 M_\odot)$. From Figure 5.2.3, we clearly see that Q_{new} at $z = 6$ have much larger amount of high values over 10^{51} [s^{-1}], and the total amount of Q_{new} is 1 dex larger than that of before re-assignment Q_{old} .

We also consider stellar atmosphere models with different elemental compositions, i.e., different values of $[\alpha/\text{Fe}]$. In the BPASS_v2.3 (Byrne et al. 2022), there are five models with the mass fractions in α -elements relative to iron of $\Delta(\log(\alpha/\text{Fe}))$ as shown in Table 5.1. For the calculation of $[\alpha/\text{Fe}]$, the α -element abundance is approximated by the oxygen abundance ($\log N_{\text{O}}$) assuming that half of the mass in metals produced by SNI are in the form of oxygen atoms;

$$\log N_{\text{O}} = \log(f_{\text{O}} z_{\text{SNI}}/A_{\text{O}}), \quad (5.5)$$

where f_{O} , z_{SNI} are the fraction of oxygen released by Type-II SNe, and the mass fraction of metals released from Type-II SNe, respectively. Here, the atomic weight of oxygen is $A_{\text{O}} = 16$

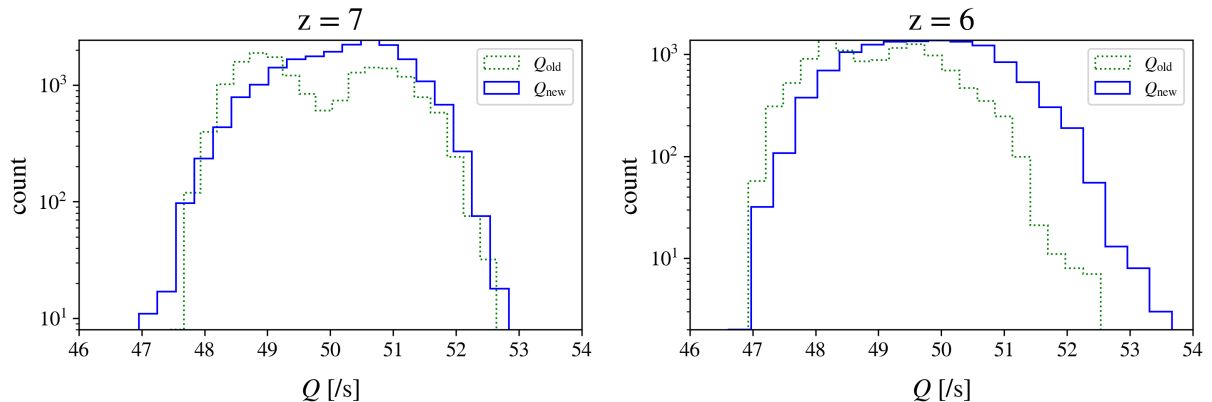


Figure 5.7: Ionizing photon rate Q distribution for a galaxy FL109 at $z = 7$ (left) and $z = 6$ (right). Dashed green (solid blue) histogram represents Q before (after) age re-assignment.

and we assume $f_{\text{O}} = 0.5$ (Woosley & Weaver 1995). We calculate the iron abundance ratio considering both contributions from Type-Ia and II SNe as

$$N_{\text{Fe}} = \frac{(f_{\text{Fe,Ia}} z_{\text{SNIa}} + f_{\text{Fe,II}} z_{\text{SNIa}})}{A_{\text{Fe}}}, \quad (5.6)$$

where z_{SNIa} is the mass fraction of metals released from Type-Ia SNe and $A_{\text{Fe}} = 56$. We set the fractions $f_{\text{Fe,Ia}} = 0.5$ (Thielemann et al. 1986) and $f_{\text{Fe,II}} = (0.026, 0.033)$ for metal mass ratio between zero and solar metallicity (Ceverino et al. 2019; Nomoto et al. 2006), respectively. Finally, $[\alpha/\text{Fe}]$ is obtained from

$$[\alpha/\text{Fe}] = \log N_{\text{O}} - \log N_{\text{Fe}} - \log(N_{\text{O}}/N_{\text{Fe}})_{\odot}, \quad (5.7)$$

where $(N_{\text{O}}/N_{\text{Fe}})_{\odot} = 1.17$ is the solar value of O/Fe abundance ratio.

5.2.4 CLOUDY calculation

We generate a library of emission lines using CLOUDY (Ferland et al. 2013). The library covers a wide range of gas metallicity Z_{gas} , ionization parameter U as given in Table 5.2. We adopt SEDs from BPASS single stellar population with the same set of Z_{gas} . For each case of Z_{gas} , we input the corresponding stellar spectrum into the code because of $Z_{\star} \sim Z_{\text{gas}}$. We assume the plane-parallel geometry for all the calculations. Notice that CLOUDY codes set the abundance of elements to be the solar one by default. The electron temperatures in the nebulae are calculated in the code with energy balance between heating and cooling rates. Especially, metal element works as a coolant and ionization parameter works as a heating source. Notice that when we substitute the ionization parameter to the CLOUDY Table 5.2, we use the value U_{inner} at the inner surface of HII region. For plane-parallel case, U_{inner} is twice $\langle U \rangle$. The library lists the line luminosity, L_{line} , normalized by the $\text{H}\beta$ line luminosity with the case-B approximation (Dopita & Sutherland 2003).

parameter	values
$\log_{10} Z_{\text{gas}}$	0.001, 0.004, 0.008, 0.02 (Z_{\odot}), 0.04
$\log_{10} U$	-4.0, -3.9, ..., -1.1, -1.0
$\log_{10} (n_{\text{HII}}/\text{cm}^{-3})$	2.0 (fixed)

Table 5.2: The parameters used to calculate the line luminosities with CLOUDY.

We also interpolate the table values with log-scale space.

5.2.5 H β luminosity calculation in case B

H β is emitted from the transition of $n = 4 \rightarrow n' = 2$ and its line luminosity is

$$L_{nn'}^{\text{caseB}} = 4\pi j_{nn'} V = h\nu_{nn'} \left(\frac{\alpha_{nn'}^{\text{eff}}}{\alpha_B} \right) Q, \quad (5.8)$$

where $j_{\text{H}\beta}$ is the H β emission rate per unit volume per unit time per unit solid angle, and $\alpha_{\text{H}\beta}^{\text{eff}}$ is an effective recombination coefficient $V = Q/(n_{\text{HII}}^2 \alpha_B)$ is a volume of HII region and $\alpha_{nn'}^{\text{eff}}$ is an effective recombination coefficient. $h\nu_{nn'}$ is a transition energy $n = 4 \rightarrow n' = 2$, i.e., $h\nu_{\text{H}\beta} = 2.55$ eV. The effective recombination coefficient for H β line is

$$\alpha_{\text{H}\beta}^{\text{eff}} = 3.72 \times 10^{-13} \text{ cm}^3/\text{s} \quad (\text{for } T_e = 10^4 \text{ K}). \quad (5.9)$$

5.3 Results

We focus on rest-frame sub-millimeter and optical lines from high- z galaxies, which are essential for ALMA and JWST observations.

5.4 $L_{[\text{OIII}]}$ vs SFR

Figure 5.8 shows the [OIII] 88 μm luminosity against star formation rate (SFR) for our galaxy samples. The color-bar indicates the nebular metallicity Z_{neb} , which is the line luminosity-weighted gas metallicity. We compare with the observed local galaxies SFR from De Looze et al. (2014). and with the observed [OIII] 88 μm luminosities of high-redshift galaxies.

At $z = 9$ to $z = 7$, most of our simulated galaxies are located above the local galaxy relation (solid line), similar to the simulated results of Arata et al. (2020); Moriwaki et al. (2018); Pallottini et al. (2022), but Katz et al. (2019b) shows the opposite trend (see the details in section 5.4.1). At $z = 7 - 9$, some of our galaxy samples are distributed around the observed galaxies. It is interesting that luminous galaxies are already chemically enriched with $\log(Z/Z_{\odot}) \sim -0.5$ at the early epochs. Our simulations predict a slightly steeper relation with

$$L_{[\text{OIII}]88} \propto \left(\frac{\text{SFR}}{M_{\odot} \text{ yr}^{-1}} \right)^{0.9-1.2}. \quad (5.10)$$

We find three galaxies with $L_{[\text{OIII}]} > 10^9 L_{\odot}$ at $z = 7$, which are as bright as several observed galaxies. We study the structure of one of them (sample FL964) in detail. It has

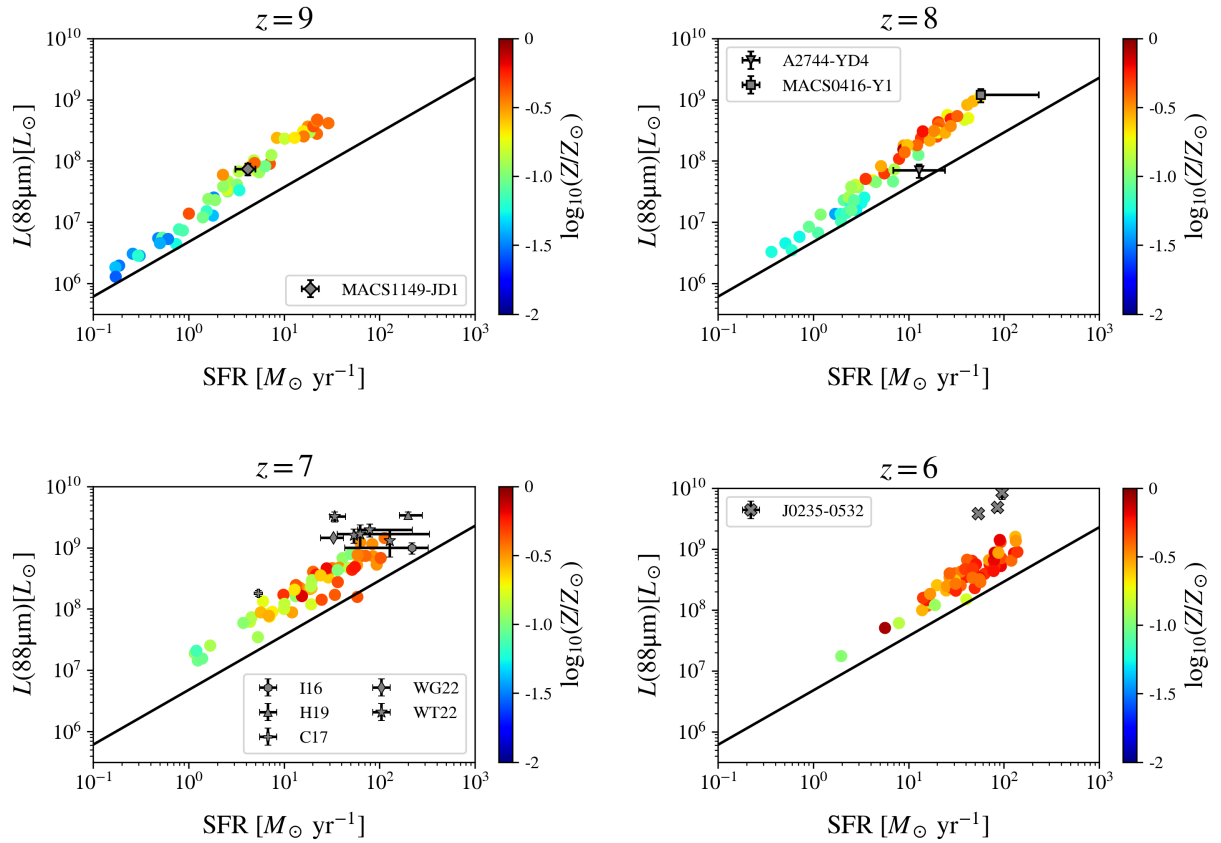


Figure 5.8: SFR versus [OIII] 88 μm luminosity for our 62 simulated galaxies at $z = 9$ (top left), $z = 8$ (top right), $z = 7$ (bottom left), and $z = 6$ (bottom right). We indicate the gas metallicity by the color of each point. For comparison, we show the [OIII]-SFR relation measured from $z = 0$ galaxies from De Looze et al. (2014). We also plot the observational results of high- z ($z > 6$) galaxies as gray points with error bars. We adopt 15 observation results from Hashimoto et al. (2018); Laporte et al. (2017); Tamura et al. (2019), Inoue et al. (2016)(I16), Hashimoto et al. (2019), Carniani et al. (2017)(C17), Wong et al. (2022)(WG22), Witstok et al. (2022)(WT22, 5 plots) and Harikane et al. (2020)(3 plots).

$M_{\text{gas}} = 6.41 \times 10^9 M_{\odot}$, $M_{\star} = 9.96 \times 10^9 M_{\odot}$, and a specific SFR of 11 Gyr at $z = 7$. Figure 5.9 shows the projected maps of gas number density, ionization parameter, and $[\text{OIII}] 88\mu\text{m}$. Clearly, regions with high ionization parameters of $\log U \sim -2$ cause high emissivities, consistent with the observation by Harikane et al. (2020) and also with recent simulations by Kohandel et al. (2022). The total luminosity of $[\text{OIII}] 5007\text{\AA}$ of FL964 is $7.60 \times 10^9 L_{\odot}$, which is about 5 times larger than $L_{[\text{OIII}],88}$.

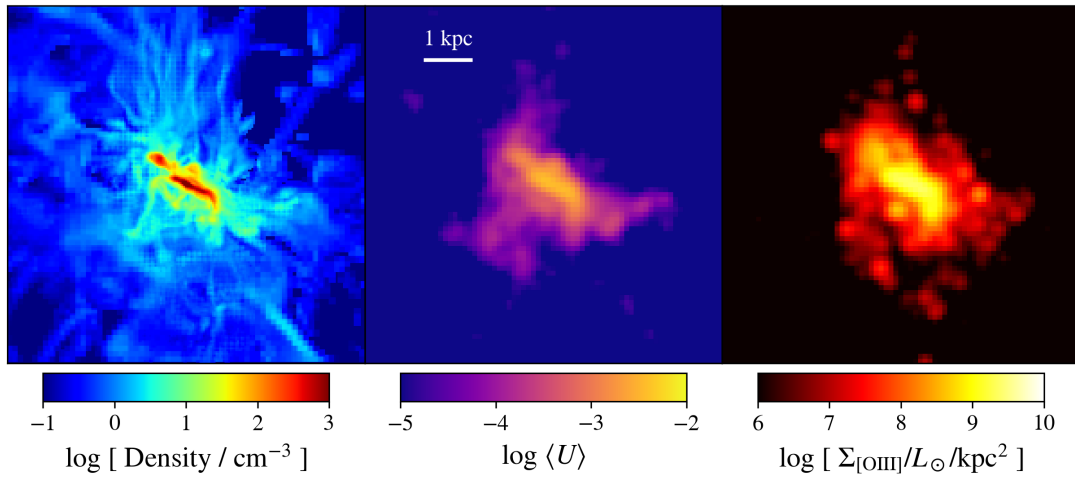


Figure 5.9: Projected gas density, averaged ionization parameter, $[\text{OIII}] 88\mu\text{m}$ distribution for a galaxy sample (FL964) at $z = 7$. Each colormap shows a region with a side length and depth of $0.3R_{\text{vir}} (= 7.4 \text{ kpc})$. The direction of the galaxy is random.

Figure 5.10 shows metallicity (Z) - ionization parameter (U) distribution of our simulated samples. We compared our distribution to the photoionization model of Sugahara et al. (2022), who have estimated the region of $Z - U$ diagram which satisfies the observed $L_{[\text{OIII}],88}/\text{SFR}$ and $L_{[\text{CII}],158}/\text{SFR}$ of $z > 6$ galaxies. Our galaxy samples with high luminosity of $L_{[\text{OIII}],88} > 10^8 L_{\odot}$ are located in the region of Sugahara et al. (2022), which implies that high luminosity of $[\text{OIII}]$ requires both high-metallicity of $Z/Z_{\odot} \sim (-0.7, -0.2)$ and high-ionization parameter of $\langle U \rangle \sim (-2.5, -2.0)$.

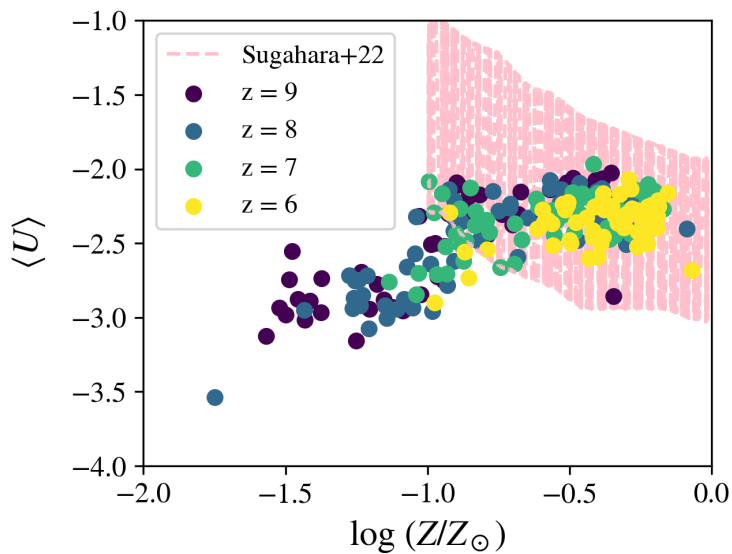


Figure 5.10: Phase diagram of Metallicity and ionization parameter for simulated samples at $z = 6, 7, 8, 9$. Pink shaded regions indicate the best parameter regions which satisfy $L_{[\text{OIII}],88}/\text{SFR}$ and $L_{[\text{CII}],158}/\text{SFR}$ values of observed $z > 6$ galaxies (Sugahara et al. 2022).

5.4.1 Comparison to other simulations

We compare our massive galaxy samples with the other simulation results from $z = 6$ to $z = 9$ in Figure 5.11. Katz et al. (2019b) adopts zoom-in radiation simulations named Aspen simulations (Katz et al. 2019a), which model Lyman Break Galaxies and follow their evolution until $z = 9.2$. Moriwaki et al. (2018) calculated [OIII] emissivity by using cosmological hydrodynamical simulation (Shimizu et al. 2016) with a box size of $(50 \text{ cMpc}/h)^3$. SEERA (Pallottini et al. 2022) is a suite of zoom-in simulations and focuses on massive galaxies with stellar mass $10^7 M_\odot \lesssim 5 \times 10^{10} M_\odot$. SÍGAME (Olsen et al. 2017) uses zoom-in simulations called MUFASA (Davé et al. 2017, 2016) and targets main-sequence galaxies with SFR $3 - 23 M_\odot/\text{yr}$, stellar masses $0.7 - 8 \times 10^9 M_\odot$ at $z \simeq 6$. In order to compare SFR- $L_{[\text{OIII}]}$ relationship with metallicity, we also plot previous simulation results with a color bar of metallicity in Figure 5.12. The trend that SFR- $L_{[\text{OIII}]}$ relationship is above the local one (De Looze et al. 2014) at $z = 9$ is consistent with both theoretical predictions from Moriwaki et al. (2018) and observational results in Figure 5.8. However, Katz et al. (2019b) results are opposite to Moriwaki et al. (2018) and our results. The reasons why Katz et al. (2019b) simulated systems fall below the observed and other theoretical relationships are not only for the different simulation scheme but also relatively low metallicity samples ($\log(Z/Z_\odot) = -1.3 - -0.88$ at $z = 9.2$).

In comparison with SERRA simulations at $z = 8$, our results locate in their dispersion of them and the SFR- $L_{[\text{OIII}]}$ slopes are almost the same. Our results at $z = 7$ also have the same trend with Moriwaki et al. (2018) but we follow more luminous samples. This is because our samples have both larger SFR and higher metallicities than Moriwaki et al. (2018) simulated

galaxies.

At $z = 6$, SÍGAME simulation appears to produce low emissivity of $[\text{OIII}] 88 \mu\text{m}$. This is because they do not explicitly model HII regions.

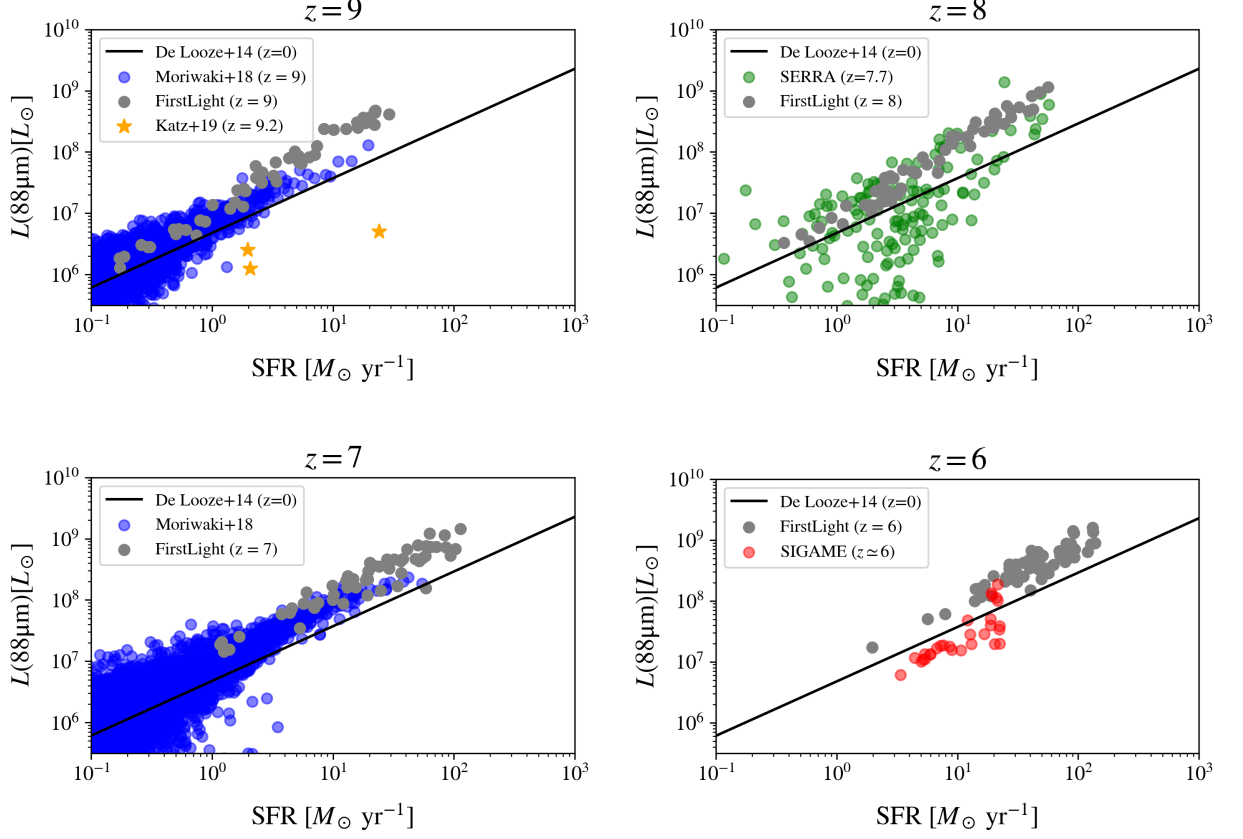


Figure 5.11: SFR versus $[\text{OIII}] 88 \mu\text{m}$ luminosity for our 62 massive galaxy samples from $z = 9$ to $z = 6$. At $z = 9$, we refer the results from Moriwaki et al. (2018) and Katz et al. (2019b)(3 plots). At $z = 8$, we compare the results with SERRA simulations from Pallottini et al. (2022). Their simulation results are for $z = 7.7$. At $z = 7$, we adopt Moriwaki et al. (2018) for comparison. At $z = 6$, we use SÍGAME simulation results Olsen et al. (2017).

5.5 The mass-metallicity relation

It is important to examine the so-called mass-metallicity relation (MZR) for our simulated galaxies. We calculate the metallicity for individual galaxies using both the gas-phase and stellar metallicities. Figure 5.13 shows the stellar mass-gas phase oxygen abundance relation. We calculate the gas phase oxygen abundance by adopting the conversion equation of Mandelker et al. (2014);

$$\frac{\text{O}}{\text{H}} = \frac{f_{\text{O}} z_{\text{SNII}}}{XA} \quad (5.11)$$

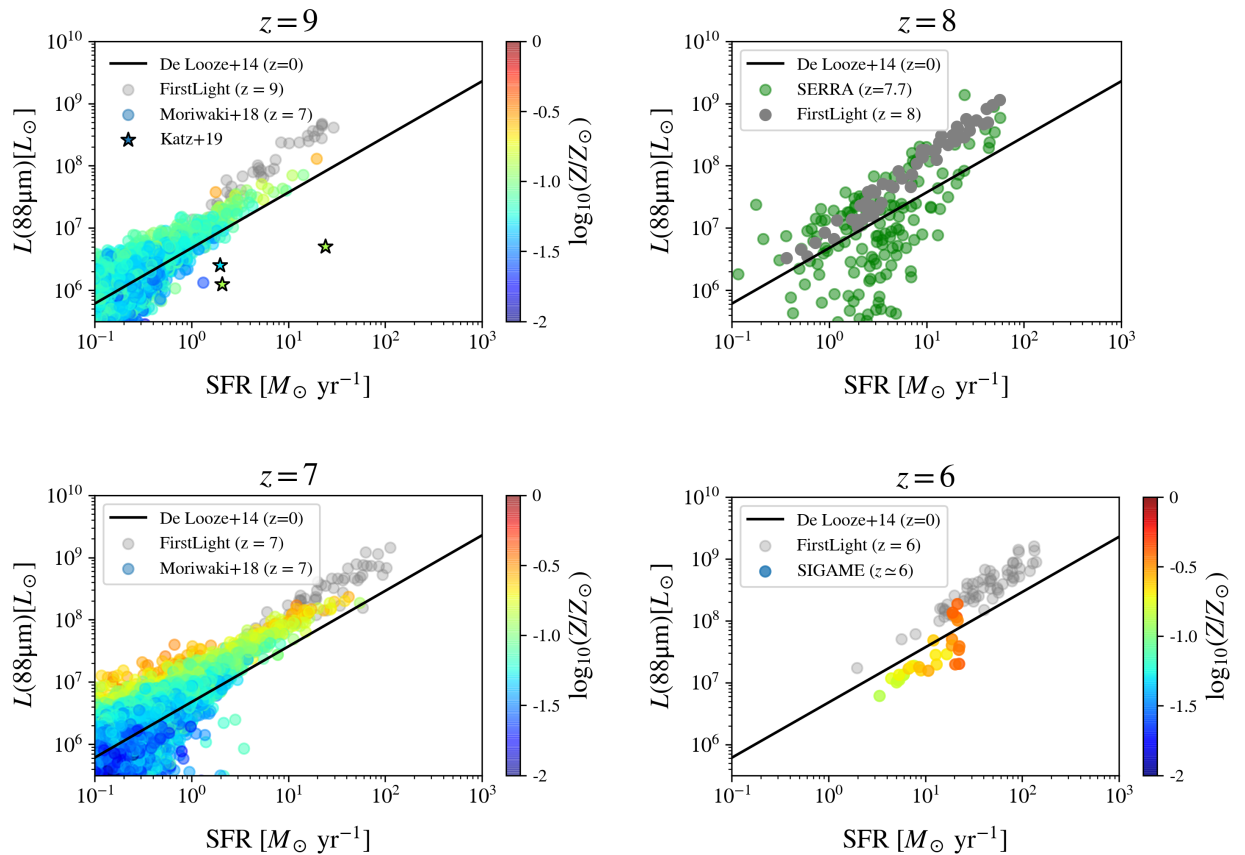


Figure 5.12: The same as Figure 5.11 but with colorbars of metallicity. We calculate metallicity from gas metallicity by weighting $L[\text{OIII}]$ luminosity. Notice that each simulation adopts different calculation strategies. (See the details in the text.)

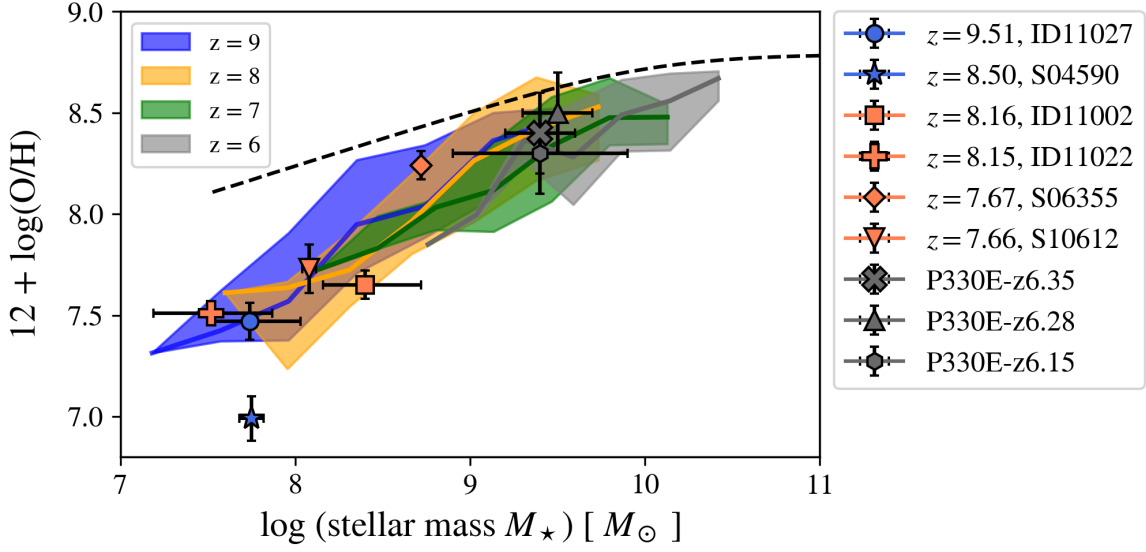


Figure 5.13: as-phase metallicity versus stellar mass for our galaxy samples from $z = 9$ to $z = 6$. The solid lines show the median and the colored bands indicate the sample dispersion in the range of 5%- 95%. The dashed line is the local mass-metallicity relation from Curti et al. (2020). Symbols with errorbars are JWST observation data of galaxies at $z \sim 6$ (gray), $z \sim 8$ (orange), and $z \sim 9$ (blue). The observed galaxies are located around the flux calibration star P330E (Sun et al. 2022), behind the galaxy cluster SMACS J0723.3–7327 (Curti et al. 2022), and the cluster RX J2129.4+0009 Langeroodi et al. (2022); Williams et al. (2022).

We set the hydrogen mass fraction $X = 0.755$ and the other values of f_{O} and A_{O} are the same as those of eq.(5.5), which adopts the solar oxygen abundance $12 + \log(\text{O}/\text{H}) = 8.9$. We then calculate the averaged z_{SNII} , weighted by the $[\text{OIII}]$ luminosity of each grid. This weighting method is valid for observation results by direct method or strong line method, which uses oxygen emission lines to estimate metallicities. Direct method uses three rest-frame optical $[\text{OIII}]$ emission lines of 4363\AA , 4959\AA , and 5007\AA and derives electron temperature, which can derive metallicity directly. Strong line method (e.g. Bian et al. 2018; Izotov et al. 2019) uses two emission line ratios; $\text{O32} = [\text{OIII}] 5007\text{\AA}/[\text{OII}] (3727+3729\text{\AA})$ and $\text{R23} = ([\text{OII}] 3727, 3729\text{\AA} + [\text{OIII}] 4959\text{\AA} + [\text{OIII}] 5007\text{\AA}) / \text{H}\beta$ and estimate metallicities from empirical calibration at local galaxies.

We calculate the mass of stars within the region of $0.3 R_{\text{vir}}$. In Figure 5.13, we also plot the MZR for local galaxies from Curti et al. (2020) (dashed line). Red, blue, and purple symbols show the mass and metallicity of the $z > 7$ galaxies observed in SMACS J0723 field (Curti et al. 2022), $z \sim 6$ galaxies observed by JWST/ NIRCcam WFSS mode (Sun et al. 2022), and $z = 8.1 - 9.5$ galaxies observed in the cluster RX J2129.4+0009 field (Langeroodi et al. 2022; Williams et al. 2022), respectively. Curti et al. (2022) estimated metallicities of SMACS field galaxies by direct method, Sun et al. (2022) adopt strong line calibration by Bian et al. (2018) using O32, and Langeroodi et al. (2022) and Williams et al. (2022) adopt strong line method by

Izotov et al. (2019).

Our simulated galaxies have similar metallicities (oxygen abundance) to the observed galaxies. Note that Figure 5.13 shows the "evolution" for a fixed sample of simulated galaxies, rather than all the galaxies at respective epochs as shown in Figure 5.3. Namely, we select the galaxies at $z = 5$ by mass and plot their progenitors at $z = 6 - 9$. Hence we likely miss low-mass, low-metallicity galaxies at $z = 9$. Some galaxies with $M_\star > 10^9 M_\odot$ have already gas-phase metallicities of $12 + \log(\text{O}/\text{H}) \sim 8.5$ even at $z = 9$, suggesting that metal-enrichment can proceed rapidly in massive galaxies.

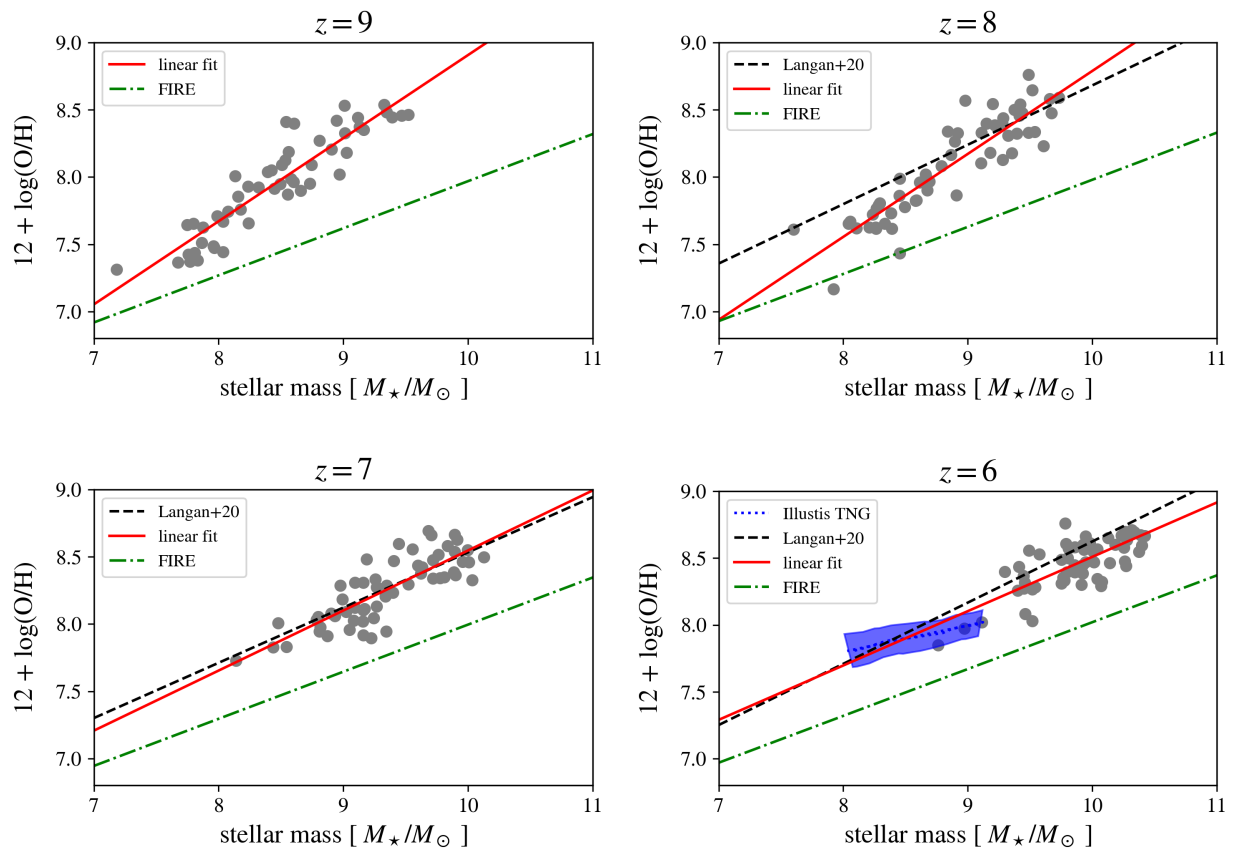


Figure 5.14: MZR evolution from $z = 9$ to $z = 6$. We plot our simulation samples as gray dots and their linear fitting line in red. For the comparison, we show extrapolated MZR lines from FIRE simulation (Ma et al. 2016) in a green dot-dashed line. For $z = 8, 7, 6$, we draw linear fitting lines (black dashed) from FirstLight for low mass samples (Langan et al. 2020). Also we show IllustrisTNG results at $z = 6$ in a blue dotted line (Torrey et al. 2019). The blue contour shows 1σ variation.

We also compare our results with other simulation results; FIRE simulations (Ma et al. 2016), Illustris TNG (Torrey et al. 2019), less massive samples from FirstLight simulations (Langan et al. 2020) in Figure 5.14.

Ma et al. (2016) use zoom-in simulations from FIRE project (Hopkins et al. 2014) and predict

the evolution of MZR based on galaxy samples in the range of $z = 0-6$ as the following equation,

$$12 + \log(\text{O}/\text{H}) = 9.0 + 0.35 [\log(M_*/M_\odot) - 10] + 0.93 \exp(-0.43z) - 1.05. \quad (5.12)$$

We extrapolate the above equation to $z = 9$ and draw as a green dot-dashed line in Figure 5.14. Langan et al. (2020) calculate MZR from FirstLight simulation data (Ceverino et al. 2018), which are the same simulation set as ours but target smaller stellar mass samples. They use 300 simulated galaxies with a maximum circular velocity V_{max} is less than 100 km/s at $z = 5$, but our study focuses on massive galaxies with V_{max} (see the details in 5.1). Torrey et al. (2019) analyze MZR evolution from $z = 0$ to $z = 6$ by using galaxy samples from Illustris TNG (Marinacci et al. 2018; Naiman et al. 2018; Nelson et al. 2018; Pillepich et al. 2018; Springel et al. 2018).

Figure 5.14 shows that metallicities of our simulated galaxies with gray dots are proportional to their stellar mass. This trend is consistent with previous high- z simulations listed above, and local or low- z observed trends ($z \sim 0$: Berg et al. (2012), MOSDEF samples at $z \sim 2.3, 3.3$: Sanders et al. (2021)).

We cover more massive galaxies than other simulations and MZR has a steep slope than other simulated galaxies which cover less massive galaxies. This implies that the massive galaxy experiences the faster chemical enrichment in high-redshift universe.

5.6 Far-IR/optical line ratios

For future observation analysis, we consider combing rest-frame FIR and optical emission lines to be observed by JWST and ALMA. It is timely to make theoretical predictions of luminosity functions for these lines have already been discussed in Jones et al. (2020); Moriwaki et al. (2018); Yang & Lidz (2020). It is interesting and timely to study theoretically the line ratios of three [OIII] fine structure emission lines; 88 μm , 52 μm and 5007 \AA (see, e.g. Osterbrock & Ferland (2006)). The former two lines are observed by ALMA whereas the latter is to be observed by JWST. Hereafter we denote the line luminosity ratios using the wavelength such as $R_{5007/88} = L_{5007\text{\AA}}/L_{88\mu\text{m}}$. Figure 5.15 shows $R_{5007/88}$ against $R_{52/88}$ for our simulated galaxies colored with the galaxies' gas metallicities. We also plot the model line ratios obtained by our set of CLOUDY calculations (Table 5.2).

Interestingly, $R_{5007/88}$ *appears* to trace metallicity in this plot. We argue that it is an indirect indicator because of the complex dependence of the line emissivities on the relevant physical quantities. Typically, the oxygen line emissivity increases with increasing oxygen abundance (metallicity), but there is a critical abundance beyond which the emissivity *decreases* because of the temperature decrease of HII regions owing to metal line cooling. Note also that the critical "peak" abundance is different for different lines. Hence the line ratios depend on the gas metallicity in a nonlinear manner as can be seen in Figure 5.15.

It is generally thought that $R_{52/88}$ can be used as a sensitive probe of the number density of HII regions as explained in section 4.4.2.

From the CLOUDY analysis in Figure 5.15, we see that $R_{52/88}$ at the same n_e increases as Z increases. In the case of $\log U = -1$, especially, $R_{52/88}$ at the fixed density of $n_e = 100 \text{ cm}^{-3}$ at the metallicity of $\log(Z/Z_\odot) = -0.4(0.0)$ is 1.7 (2.2) times larger than that of metallicity of $\log(Z/Z_\odot) = -1.3$. This is because electron temperature (T_e) in the nebulae are calculated in the CLOUDY code with energy balance between heating and cooling rates. Especially, metal works as a coolant and ionization parameter works as a heating source, which changes T_e in each parameter set. All our galaxies samples have fixed $n_e = 100 \text{ cm}^{-3}$ and galaxies with higher Z locates on the lower and righter area than low metallicity galaxies in Figure 5.15. Furthermore, in the case of high metallicity i.e. $Z \gtrsim Z_\odot$, $R_{52/88}$ has an U dependence slightly. For instance, for the yellow lines with $Z = Z_\odot$, $R_{52/88}$ increases at the same electron density. This is consistent with the results from Yang & Lidz (2020).

We also plot local metal-rich galaxies observed with both FIR (Brauer et al. 2008) and optical emission lines (Moustakas et al. 2006). The optical observation results are corrected for dust attenuation. The local planetary nebulae (Dinerstein et al. 1985) are also plotted as red stars. Dinerstein et al. (1985) have estimated that those planetary nebulae have electron densities of $n_e[\text{OIII}] = 10^{3-4} \text{ cm}^{-3}$, which are derived from [OII] lines.

We also see that the local galaxies in Figure 5.15 have over solar metallicities and electron densities of $n_e = 100 - 10^3 \text{ cm}^{-3}$. Only NGC 1569, the galaxy with $R_{5007/88} = 4.9$, has sub-solar metallicity of $\log(Z/Z_\odot) = -0.6$ (Israel 1988), which is located on the same metallicity line from CLOUDY analysis. Also, this galaxy has lower n_e of $\sim 50 \text{ cm}^{-3}$ than high- z galaxies.

To see the physical processes of line ratio trend in Figure 5.13, we have also investigated emissivities of [OIII] optical (5007, 4959 Å) and FIR (88, 52 μm) lines as a function of metallicity with a different ionization parameter in Figure 5.16. When Z is smaller than the threshold metallicity, Z_{th} , all the emissivities increase monotonically, and when $Z > Z_{\text{th}}$, the emissivities decrease monotonically. This trend is consistent with previous CLOUDY analysis for optical strong emission lines (Inoue 2011), and optical [OIII] observation for star forming galaxies at $z \sim 3.5$ (Maiolino et al. 2008), local galaxies at $z \sim 0$ (Curti et al. 2017, 2020), and local extremely metal-poor galaxies (Nakajima et al. 2022). Qualitative explanations for the trend are as follows:

In the case of $Z < Z_{\text{th}}$, the line emissivity increases with oxygen abundance. In the case of $Z > Z_{\text{th}}$, metal cools nebula gas efficiently and gas temperature becomes lower than the excitation temperature ($T_{\text{exc}} = E_{\text{exc}}/k_B$, Table 4.1), which the emissivity decreases. Optical lines [OIII] 5007 Å, 4959 Å have $\log(Z_{\text{th}}/Z_\odot) \simeq -0.4$ and the value is almost the same as that of Inoue (2011). FIR lines [OIII] 88 μm, 52 μm have $\log(Z_{\text{th}}/Z_\odot) \simeq 0$, which is larger than Z_{th} for optical lines. This is because FIR [OIII] lines have smaller excitation energies than optical [OIII] lines do. The line emissivities also depend on ionization parameter, but the dependence is weak as can be seen in Figure 5.16. When we fix the electron density, i.e. 100 cm^{-3} , U is proportional to $Q^{1/3}$, where Q is the number of ionizing photon (see eq. 5.2). Figure 5.16 shows that [OIII] emissivity decrease significantly in the case of $\log U = -3$. According to Section 5.4, our simulated galaxies have high U in the range of $\log U \sim (-3, -2)$, therefore we can treat $R_{5000/88}$ is dependent on metallicity chiefly for high- z galaxies.

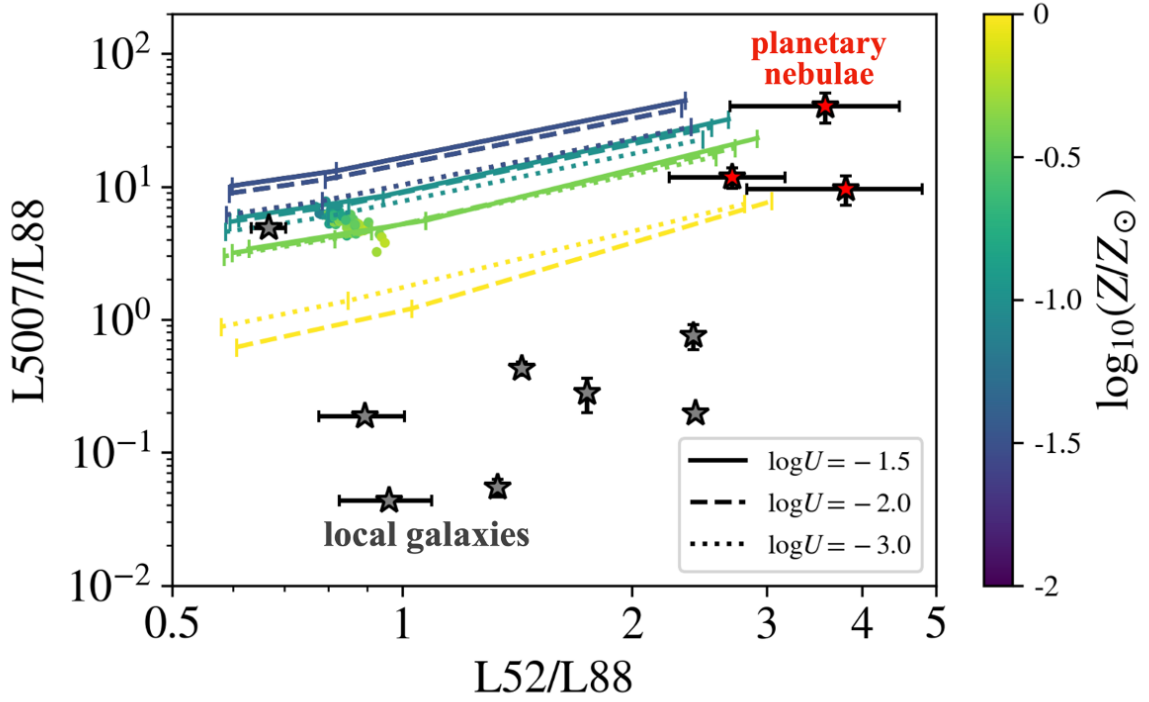


Figure 5.15: Line luminosity ratio $R_{5007/52}$ against $R_{52/88}$. Our simulated galaxies at $z = 7$ are represented by solid circles colored with gas metallicity. Gray star symbols show the local galaxies from Brauher et al. (2008); Moustakas et al. (2006) and red ones show the local planetary nebulae from Dinerstein et al. (1985). The results of CLOUDY calculations are represented by lines colored with metallicity ($\log(Z/Z_{\odot}) = -1.30, -0.70, -0.40, 0.0$). Solid, dashed, and dotted lines are the case of $\log U = -1.5, -2, -3$ respectively. The number densities of HII region $\log n_{\text{HII}}[\text{cm}^{-3}] = 1, 2, 3$ are also marked by ticks from left to right on each CLOUDY line.

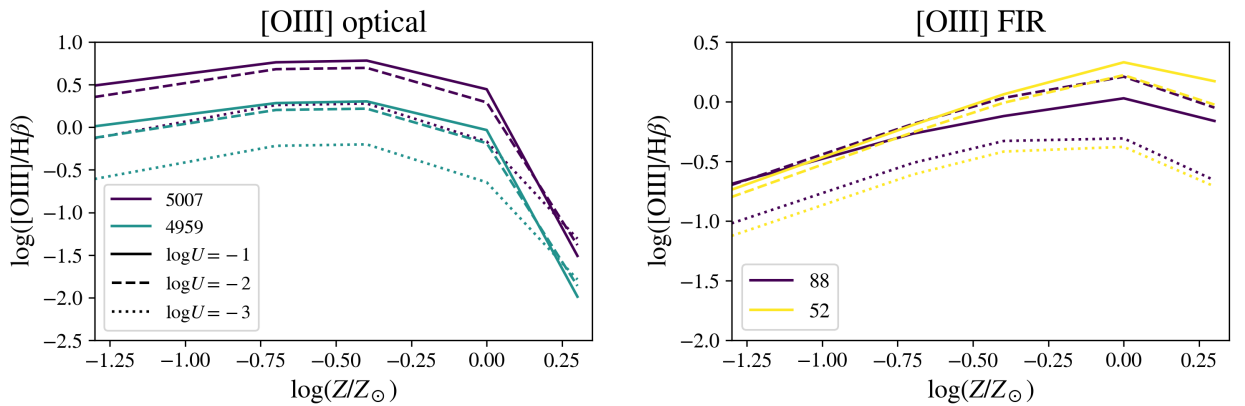


Figure 5.16: Emissivities relative to $\text{H}\beta$ of four [OIII] emission lines (left: rest-frame optical 5007 Å and 4959 Å, right: rest-frame Far-IR 88 μm and 52 μm). All lines are calculated from CLOUDY with the fixed electron density of $n_e = 100 \text{ cm}^{-3}$. Solid, dashed and dotted lines are the cases of $\log U = -1, -2$ and -3 respectively.

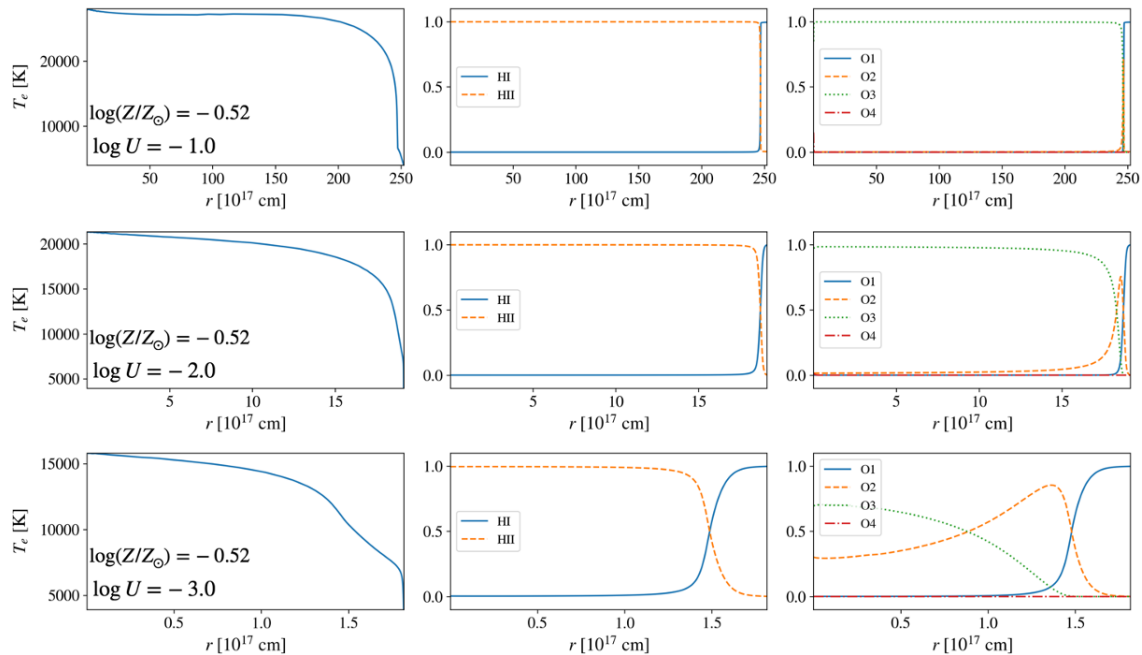


Figure 5.17: Radial profiles in HII region calculated by CLOUDY with the same metallicity of $\log(Z/Z_{\odot}) = -0.52$ and different ionization parameters; $\log U = -1.0$ (top), -2.0 (middle), -3.0 (bottom). For columns, Left: Electron temperature, Middle: the fraction of hydrogen in the form of HI and HII. Right: the fraction of oxygen in the form of OI(O1), OII(O2), OIII(O3), and OIV(O4). We use BPASS single stellar population SED at 10 Myr, and stop CLOUDY calculation when the electron fraction reaches $n_e/n(\text{H}) = 10^{-3}$.

Figure 5.17 shows the radial profiles in HII region calculated by CLOUDY. With fixed metallicity, ionization parameter contributes high ionizing photon rate Q_0 ¹ and heating in HII region and increases electron temperature T_e and Strömgen sphere R_s . The ionization fraction of hydrogen drops sharply as ionization parameter increases. The large ionization parameter ($\log U \gtrsim -2$) ionizes most oxygen atoms doubly. We clearly see that metallicity (Z) and ionization parameter (U) makes the complicated HII structures and that may change the ratio $R_{52/88}$ slightly even at the fixed electron density.

5.7 Mock data for NIRSpec observation

Generating mock data is indispensable for coming high-redshift galaxy observations, especially observations by JWST NIRSpec IFU mode.

IFU spectroscopy is an observing technique that provides 3D information; spectral information(1D) and 2D field of view, by using instruments coined Integral Field Units (IFUs).

From IFU observations, we can obtain spatially resolved maps of important spectral features

¹Input SED is normalized at the CLOUDY calculation and gives only the shape of SED. U determines the number of photons.

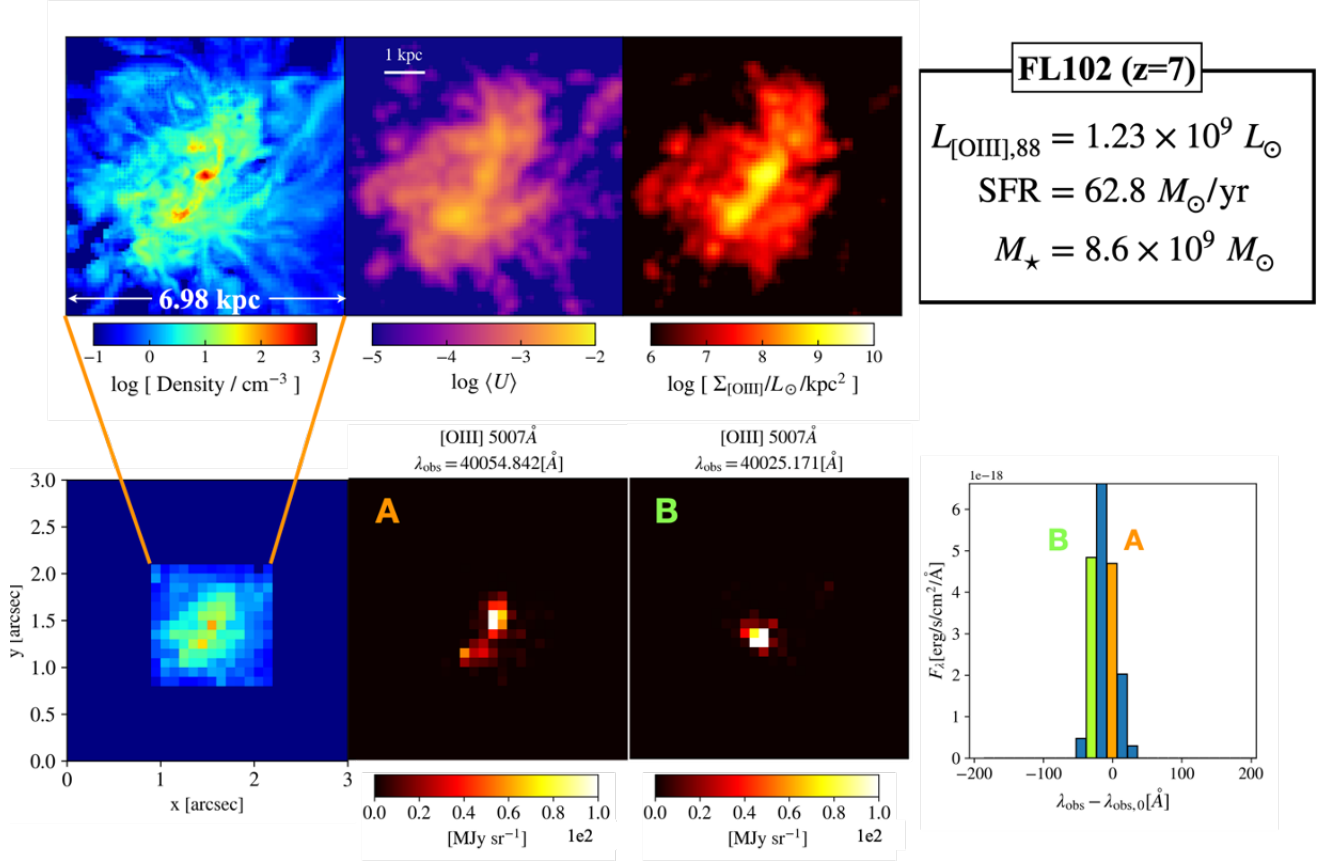


Figure 5.18: Projection map of a galaxy sample (FL102) at $z = 7$ with simulation resolution (top) and NIRSpect resolution (bottom). The top panels are the same as Figure 5.9 and the region has a side length and depth of $0.3 R_{\text{vir}} (= 6.98 \text{ kpc})$. The field of view of bottom panels is $3'' \times 3''$, which is larger than $0.3 R_{\text{vir}}$ where we treat for line calculation. The most left bottom panel shows the gas density distribution as same as the most left top panel. Panel A and B are moment 0 mapping of non-shifted and blue-shifted $[\text{OIII}] 5007\text{\AA}$. The bottom right panel shows the spectrum of $[\text{OIII}] 5007\text{\AA}$ of the entire galaxy (FL102). We colored the corresponding bars with range (panel A) and green yellow (panel B), respectively.

which encapsulate galaxy properties such as velocity (gas kinematics), elemental abundances, and star formation histories. As a test, we generate an intensity map of one galaxy sample (FL102) at $z = 7$ assuming the observation by NIRSpec IFU with a spectrum resolution of $R = 2700$ and a field of view $3'' \times 3''$ as shown in Figure 5.18. The flux distribution of [OIII] 5007 Å is quite different with different wavelength due to complex gas kinematics such as feedback or rotation. Notice that we do not input noise data into the mock data in Figure 5.18, which can cause different flux distribution following noise pattern. Since we have modeled HII region, we can generate other emission lines coming from HII region such as [OIII] 4363 Å, [OII] 3727 Å, [NII] 6584 Å, H β and so on. Taking the ratio of these lines in each IFU pixel, we will be able to see the distribution of gas density, temperature and metallicity.

5.8 Discussion

In this thesis, we have studied the chemical evolution of massive galaxies from $z = 9$ to $z = 6$ by using zoom-in hydrodynamical simulation, First Light simulation (Ceverino et al. 2017). We find that galaxies with stellar masses of $M_\star = 10^{9-9.5} M_\odot$ has large ionization parameter of $\log U = -2$ and metallicity of $\log(Z/Z_\odot) \sim -1 - -0.5$ become metal enriched for ~ 0.5 dex in a few $\times 100$ Myr.

Previous observation and simulation studies (e.g. Harikane et al. 2020; Katz et al. 2019b) have examined [OIII] emissivities at $z = 6 - 9$ collectively as a trend of high- z galaxies. Our studies have revealed, for the first time, the chemical evolution and [OIII] emission for each period in EoR. Furthermore, we also propose line combination of [OIII] 5007 Å, 88 μm , and 52 μm for the future observational collaboration of JWST and ALMA. For instance, several [OIII] 88 μm emitters will be observed by NIRSpec (GO-1740, PI: Harikane, three high- z galaxies at $z = 6$, and GO-1840, PI: Álvarez-Márquez & Hashimoto, 14 high- z galaxies at $z = 6 - 9$). Such galaxies are expected to emit [OIII] optical lines such as 5007 Å and 4959 Å. Recent ALMA observation detect [OIII] 52 μm of a galaxy at $z = 7$ for the first time (Killi et al. 2022) and estimate the value of U and $R_{52/88}$ as $\log U = -1$ and $R_{52/88} < 1.1$. According to Figure 5.15, we can also estimate $R_{5007/88}$ as ~ 1 .

Recent studies of Noel et al. (2022) also investigate MZR from $z = 5$ to $z = 10$ by using Cosmic Reionization on Computers (CROC) simulations. Their simulations are not zoom-in ones and focus on relatively lower-mass galaxies (eg. $M_\star = 10^{5.5-8}$ at $z = 9$) than our simulated galaxies. Their simulated MZR is always lower than observed ones for $z = 5 - 10$. Our zoom-in simulation selects massive, observable samples and shows that the more massive galaxies, the faster evolve chemically. Our MZR results are consistent with up-to-date JWST observation.

There is a caveat that this study focuses on the chemical evolution of massive galaxies during EoR, not including less massive galaxies, which exist more universally. Also, we calculate gas metallicity or oxygen abundance for each galaxy by taking average in each grid, weighting [OIII] emission lines. This is because JWST observations derive metallicity by [OIII] or [OII] emissions and physical values should be biased by these lines. When we consider luminosity function at each redshift, considering only massive galaxies will bring some bias. Also,

our simulations do not include dust. Recent ALMA surveys report the existence of dust in star-forming galaxies at $z \sim 6$ (Burgarella et al. 2022; Fudamoto et al. 2020), at $z \sim 7$ (Inami et al. 2022; Schouws et al. 2022), $z \sim 8$ (Bakx et al. 2022; Tamura et al. 2019), and $z \sim 9$ (Hashimoto et al. 2018). When observers take the line ratio between [OIII] $88\mu\text{m}$ and 5007\AA , values of dust absorption are to be estimated accurately.

In this thesis, we follow the statistics of massive high- z galaxies and compare several observational results. However, our simulation can also follow the star-formation history of each galaxy. From Figure 5.8 and 5.13, we have some galaxy samples that have fairly similar physical properties of M_* , SFR, and metallicity. Furthermore, our zoom-in simulations have quite a high resolution of ~ 20 pc, thus we can see the distribution of emission lines and can investigate metal and density distribution, and gas dynamics inside galaxies. Cameron et al. (2022) argues that real galaxies have fluctuating electron temperature T_e and previous T_e method might have underestimated metallicity at low-stellar mass galaxies. NIRSpec IFU observation can resolve 2D flux map for each emission line to some extent. IFU Spectroscopy has a pixel scale of 0.1 [arcsec/pixel]², which resolves 13×13 pixels for $0.3 \times R_{\text{vir}} = 7$ kpc size galaxies at $z = 7$. We will create mock data for our simulated galaxies with the same resolution of NIRSpec IFU and realistic noise from JWST Exposure Time Calculator and investigate whether the mock data can reproduce physical properties (n, T, Z) which are output from simulations. In a forthcoming paper, we will study the observational biases qualitatively.

²<https://jwst-docs.stsci.edu/jwst-near-infrared-spectrograph>

Chapter 6

Summary and future prospects

Formation and evolution of stars and galaxies during the first billion years after the Big Bang are being unveiled from both theoretical and observational perspectives. Cosmological hydrodynamical simulations have been conducted to follow structure formation and evolution of chemically pristine gas toward the star formation at $z \sim 30 - 20$. Recent observations from JWST and ALMA have reported detection of high-redshift galaxies, including some candidates at $z \sim 15 - 20$. They may contribute greatly to filling the gap of the evolution scenario of our Universe. In this thesis, we have studied formation of star clusters considering the relative motions between baryons and dark matter in the early Universe. We have also studied the chemical evolution of high-redshift galaxies by combing observational data.

In Chapter 3, we have performed cosmological hydrodynamical simulations incorporating the stream velocity (SV) and non-equilibrium chemical reactions of 15 species. We identify particular gas clouds that contract by molecular hydrogen cooling without being hosted by dark matter halos. SIGOs remain outside the virial radii of their closest halos, and they become Jeans unstable when the central gas-particle density reaches $\sim 100 \text{ cm}^{-3}$ with a temperature of $\sim 200 \text{ K}$. The corresponding Jeans mass is $\sim 10^5 M_{\odot}$, which is ~ 100 times larger than typical primordial gas clumps hosted by dark matter halos. This is because SIGOs condensate slowly with their self-gravity. When SIGOs become Jeans unstable, they collapse gravitationally and initiate the formation of primordial stars or a star cluster. We conduct the same set-up but with/without incorporating SV and molecular chemistry to see the existence of SIGOs. Through the comparison of these runs, we have confirmed that gas-rich objects can be formed in the early universe by the combined effects of streaming motions and molecular hydrogen cooling.

We study further evolution of the SIGOs by focusing on the region in and around each gas clump and running higher resolution simulations from $z = 25$. We find that some gas-rich objects identified at $z \sim 25$ cannot survive as SIGOs. Some gas clumps are eventually hosted by neighboring large dark matter halos, other gas clumps merge together, while sub-halos merge and become a bigger halo. After being hosted by dark matter halos, gas clumps can easily contract to high density with the large gravitational potential from halos and evolve essentially in the same manner as typical primordial gas clouds. Through the analysis of various evolution paths for gas-rich objects, we conclude that $\sim 10\%$ of gas-rich objects can survive without being

hosted by dark matter halos. Also, some of gas-clouds which are finally hosted by the closest halos can exist as satellites and behave as low-mass galaxies or star clusters similar to globular clusters. As the James Webb Space Telescope comes online, future observations will further constrain the link between SIGOs and globular clusters.

Chemical enrichment of SIGOs will be an important research topic in the future. In this thesis, we follow the evolution of SIGOs which consists of only primordial gas, while star clusters which are already observed contain a finite amount of metals. Internal or external metal enrichment is crucial to determine the further evolution pathway of SIGOs. External enrichment from the closest stars and/or galaxies is promising because non-SIGOs can evolve and form Pop-III stars faster than SIGOs and the formed stars end in supernovae and can expel metal-enriched gas. Further simulations incorporating metal-enrichment will be carried out in the near future.

In Chapter 5, we have used the outputs of FirstLight simulation, which owns a statistically significant number of galaxies (~ 60) with very high resolution (~ 20 pc) at the epoch of reionization. We model HII regions around all the young stellar particles with considering the inhomogeneous distribution of HII regions by introducing filling factor. We, for the first time, consider *fine* stellar ages in order to avoid the effect of time step resolution of the simulations. We calculate [OIII] line emission from each HII regions by using one-dimensional radiative transfer code CLOUDY. We find that oxygen line emission galaxies with stellar masses of $M_{\star} = 10^{9-9.5} M_{\odot}$ and similar luminosity to observed high-redshift galaxies have large ionization parameter of $\log U \sim -2$ and metallicity of $\log(Z/Z_{\odot}) \sim (-1, -0.5)$. In these galaxies, metal-enrichment occurs early and quickly over a few hundred million years. This rapid chemical evolution at high redshift is also seen in the resulting mass-metallicity relationship, which is consistent with up-to-date JWST observations. We also propose line-ratio diagnostics for future synergies of JWST and ALMA. We argue that the ratio of [OIII] 5007 Å and 88 μm may trace metallicity and the ratio of [OIII] 52 μm and 88 μm can trace electron density with different ionization parameters. We emphasize that the information of physical properties such as metallicity and ionization parameter is useful to understand chemical evolution of high-redshift galaxies *globally* rather than fundamental physical quantities such as electron temperatures. This is because the distribution of electron density and the abundance of highly ionized elements within HII regions depend critically and non-trivially on the metallicity and ionization parameter. For instance, when we estimate the high temperature from line-ratio, it is difficult to solve the degeneracy of temperature sources, owing either to low metallicity or to high ionization parameter and so on. We expect that our line-ratio diagnostics can categorize objects into high-redshift, low-redshift galaxies, and planetary nebulae. Furthermore, we generated mock data for coming JWST IFU observations.

For future studies, dust extinction should be considered. Several ALMA observation reports detections of dust in galaxies at the epoch of reionization. Since rest-frame optical lines are considerably subjective to dust attenuation, it is important to construct realistic dust extinction model with consistency of observations. Also, the FirstLight simulation suites achieve high-resolution enough to investigate the inner structure of each galaxy sample. We can apply the line diagnostics to each simulated pixels and see the distribution of physical properties.

IFU observation data can also be applied. Some of the simulated galaxy samples have similar properties to observed galaxies. We will follow their galaxies in each snapshot, investigate the gas dynamics, bursty star-formation, metal-enrichment, and finally see how the observed massive galaxies have evolved to what they are.

Finally, our research in this thesis may help to comprehensively understand the formation and evolution of star clusters and galaxies at high redshift, and to facilitate synergy of JWST and ALMA.

Appendix A

Primordial Chemical Reactions

We list the primordial chemical reactions installed in extended GRACKLE (Chiaki & Wise 2019). Chiaki & Wise (2019) add three more species: HeH^+ , D^- and HD^+ . The reaction rates are summed up in Nagakura et al. (2009).

Reaction Number	Reactions
1	$\text{H} + \text{e}^- \rightarrow \text{H}^+ + 2\text{e}^-$
2	$\text{H}^+ + \text{e}^- \rightarrow \text{H} + \gamma$
3	$\text{He} + \text{e}^- \rightarrow \text{He}^+ + 2\text{e}^-$
4	$\text{He}^+ + \text{e}^- \rightarrow \text{He} + \gamma$
5	$\text{He}^+ + \text{e}^- \rightarrow \text{He}^{++} + 2\text{e}^-$
6	$\text{He}^{++} + \text{e}^- \rightarrow \text{He}^+ + \gamma$
7	$\text{H} + \text{e}^- \rightarrow \text{H}^- + \gamma$
8	$\text{H} + \text{H}^- \rightarrow \text{H}_2 + \text{e}^-$
9	$\text{H} + \text{H}^+ \rightarrow \text{H}_2^+ + \gamma$
10	$\text{H}_2^+ + \text{H} \rightarrow \text{H}_2^* + \text{H}^+$
11	$\text{H}_2 + \text{H}^+ \rightarrow \text{H}_2^+ + \text{H}$
12	$\text{H}_2 + \text{e}^- \rightarrow 2\text{H} + \text{e}^-$
13	$\text{H}_2 + \text{H} \rightarrow 3\text{H}$
14	$\text{H}^- + \text{e}^- \rightarrow \text{H} + 2\text{e}^-$
15	$\text{H}^- + \text{H} \rightarrow 2\text{H} + \text{e}^-$
16	$\text{H}^- + \text{H}^+ \rightarrow 2\text{H}$
17	$\text{H}^- + \text{H}^+ \rightarrow \text{H}_2^+ + \text{e}^-$
18	$\text{H}_2^+ + \text{e}^- \rightarrow 2\text{H}$
19	$\text{H}_2^+ + \text{H}^- \rightarrow \text{H} + \text{H}_2$
20	$\text{D}^+ + \text{e}^- \rightarrow \text{D} + \gamma$
21	$\text{D} + \text{H}^+ \rightarrow \text{D}^+ + \text{H}$
22	$\text{D}^+ + \text{H} \rightarrow \text{D} + \text{H}^+$
23	$\text{D} + \text{H} \rightarrow \text{HD} + \gamma$
24	$\text{D} + \text{H}_2 \rightarrow \text{H} + \text{HD}$
25	$\text{HD}^+ + \text{H} \rightarrow \text{H}^+ + \text{HD}$
26	$\text{D}^+ + \text{H}_2 \rightarrow \text{H}^+ + \text{HD}$
27	$\text{HD} + \text{H} \rightarrow \text{H}_2 + \text{D}$

continues

28	$\text{HD} + \text{H}^+ \rightarrow \text{H}_2 + \text{D}^+$
29	$\text{D} + \text{H}^+ \rightarrow \text{HD}^+ + \gamma$
30	$\text{D}^+ + \text{H} \rightarrow \text{HD}^+ + \gamma$
31	$\text{HD}^+ + \text{e}^- \rightarrow \text{H} + \text{D}$
32	$\text{D} + \text{e}^- \rightarrow \text{D}^- + \gamma$
33	$\text{D}^+ + \text{D}^- \rightarrow 2\text{D}$
34	$\text{H}^+ + \text{D}^- \rightarrow \text{D} + \text{H}$
35	$\text{H}^- + \text{D} \rightarrow \text{H} + \text{D}^-$
36	$\text{D}^- + \text{H} \rightarrow \text{D} + \text{H}^-$
37	$\text{D}^- + \text{H} \rightarrow \text{HD} + \text{e}^-$
38	$\text{H} + \text{H} + \text{H} \rightarrow \text{H}_2 + \text{H}$
39	$\text{H} + \text{H} + \text{H}_2 \rightarrow \text{H}_2 + \text{H}_2$
40	$\text{H}_2 + \text{H}_2 \rightarrow \text{H} + \text{H} + \text{H}_2$
41	$\text{H} + \text{H} \rightarrow \text{H}^+ + \text{e}^- + \text{H}$
42	$\text{He} + \text{H}^+ \rightarrow \text{He}^+ + \text{H}$
43	$\text{He}^+ + \text{H} \rightarrow \text{He} + \text{H}^+$
44	$\text{He} + \text{H}^+ \rightarrow \text{HeH}^+ + \gamma$
45	$\text{He} + \text{H}^+ \rightarrow \text{HeH}^+ + \gamma$
46	$\text{He} + \text{H}_2^+ \rightarrow \text{HeH}^+ + \text{H}$
47	$\text{He}^+ + \text{H} \rightarrow \text{HeH}^+ + \gamma$
48	$\text{HeH}^+ + \text{H} \rightarrow \text{He} + \text{H}_2^+$
49	$\text{HeH}^+ + \text{e}^- \rightarrow \text{He} + \text{H}$

Appendix B

Subgrid Models in FirstLight

Hydrodynamics of gas and N-body calculation in the simulations solve the following fundamental equations:

$$\boxed{\text{eq. of continuity}} \quad \frac{\partial \rho_{\text{gas}}}{\partial t} + \nabla \cdot (\rho_{\text{gas}} \mathbf{u}) = \mathcal{S}_{\rho_{\text{gas}}}, \quad (\text{B.1})$$

$$\boxed{\text{eq. of momentum}} \quad \frac{\partial \mathbf{u}}{\partial t} + (\mathbf{u} \cdot \nabla) \mathbf{u} = -\nabla \Phi - \frac{\nabla P_{\text{tot}}}{\rho_{\text{gas}}} + \mathcal{S}_{\mathbf{u}}, \quad (\text{B.2})$$

$$\boxed{\text{eq. of energy}} \quad \frac{\partial E}{\partial t} + \nabla \cdot [(E + P_{\text{thermal}}) \mathbf{u}] = -\rho_{\text{gas}} \mathbf{u} \cdot \nabla \Phi + (\Gamma - \Lambda) + \mathcal{S}_E, \quad (\text{B.3})$$

$$\boxed{\text{Poisson eq.}} \quad \nabla^2 \Phi = 4\pi G \rho_{\text{tot}} - \Lambda_{\text{cos}}, \quad (\text{B.4})$$

$$\boxed{\text{EoS}} \quad \varepsilon = \frac{1}{\gamma - 1} \frac{P_{\text{thermal}}}{\rho_{\text{gas}}}, \quad (\text{B.5})$$

where ρ_{gas} , \mathbf{u} , P are mass density of gas, gas velocity, and gas pressure, respectively. The total gas energy density is denoted $E = \rho_{\text{gas}}(\varepsilon + \mathbf{u}^2)$, and ε is the internal energy of the gas per unit mass. Λ_{cos} is the cosmological constant. ρ_{tot} is the density of all components of matter including gas, stars and dark matter. In our simulation, we only follow hydrogen atoms, thus the value of adiabatic index is $\gamma = 5/3$. Γ is a heating rate from stellar winds and supernovae explained in section B.3 and Λ is a cooling rate by radiation from metals explained in section B.1.

$\mathcal{S}_{\rho_{\text{gas}}}$, $\mathcal{S}_{\mathbf{u}}$ and \mathcal{S}_E are source/ sink terms and are determined by the processes of star formation and stellar mass loss.

In addition to the hydrodynamical equations, we solve the self-consistent advection of metals produced in stars and released into the gas by SNe, stellar winds, and evolved stars.

$$\boxed{\text{metals in gas}} \quad \frac{\partial \rho_{Z_i}}{\partial t} + \nabla \cdot (\rho_{Z_i} \mathbf{u}) = \mathcal{S}_{Z_i, \text{FD}} + \mathcal{S}_{Z_i, \text{ML}} + \mathcal{S}_{Z_i, \text{SF}}, \quad (\text{B.6})$$

where FD, ML, and SF stand for feedback, mass loss, and star formation, respectively. Z_i represents two types of metals from Type-II supernovae and Type-Ia supernovae; $i = \text{SNII}, \text{SNIa}$. ρ_{Z_i} is mass density of ejected metals.

B.1 Radiative cooling

The radiative cooling rate Λ in eq.B.3 are tabulated by CLOUDY calculations (Ferland et al. 1998) and $\Lambda' \equiv \Lambda/n_{\text{H}}^2$ is available for given gas density, temperature, metallicity and UV background. The coolants are atomic hydrogen, helium, metals and molecular hydrogen.

B.2 Subgrid physics

In order to simulate galaxy formation, we need to consider baryon physics as a subgrid model. The so-called subgrid physics include atomic (H, He) and molecular (H_2) cooling, photoionization heating by a cosmological UV background with partial self-shielding, star formation and feedback, as described in the followings. The subgrid models are based on previous studies by Ceverino et al. (2010, 2012); Ceverino & Klypin (2009); Ceverino et al. (2014).

B.2.1 Star formation

Stars form in high-density ($\rho > \rho_{\text{th}}$) and low-temperature ($T < T_{\text{th}}$) gas clouds. In our simulations, $\rho_{\text{th}} = 0.035 M_{\odot} \text{ pc}^{-3}$ ($n_{\text{th}} = 1 \text{ cm}^{-3}$) and $T_{\text{th}} = 10^4 \text{ K}$. In simulations of Ceverino et al. (2014), which have adopted the same subgrid model as Ceverino et al. (2017), over 90 % stars are formed at $T < 10^3 \text{ K}$, and over 50% the stars form at 300 K. Satisfying the above conditions, stellar particles are formed with a single stellar population (SSP). SSP is characterized by IMF, age and metallicity. Chabrier IMF (Chabrier 2005) is adopted in our simulations.

We also set star formation rate density ($\dot{\rho}_{\star}$) which follows Kennicutt-Schmidt law (Kennicutt 1998) ($\dot{\rho}_{\star} \propto \rho^{1.5}$);

$$t_{\star} \propto t_{\text{dyn}} \propto \rho_{\text{gas}}^{-1/2} \quad (\text{B.7})$$

$$\dot{\rho}_{\star} = \frac{\rho}{t_{\star}} = C_{\star} \frac{\rho}{t_{\text{dyn}}} \propto \rho^{1.5}, \quad (\text{B.8})$$

where t_{\star} is a timescale of star formation for gas cell with density of ρ_{gas} and a parameter C_{\star} is calibrated to match observations. Stars form in a time step of $\Delta t_{\text{SF}} = 5 \text{ Myr}$ which is determined by Courant condition. During the time step Δt_{SF} , star formation in a gas cell with density of ρ_{gas} occurs with the following probability,

$$P_{\star} = \min \left(0.2, \sqrt{\frac{\rho_{\text{gas}}}{1000 \rho_{\text{th}}}} \right) \quad (\text{B.9})$$

Also, SFR for a single stellar particle formation is proportional to the gas density as the following (Kravtsov 2003):

$$\frac{d\rho_{\star, \text{young}}}{dt} = \frac{\rho_{\text{gas}}}{\tau}, \quad (\text{B.10})$$

where τ is a constant star formation time scale which is set to be $\tau = 12 \text{ Myr}$ in our simulation, which is consistent with the gas consumption time scale. The mass of new stellar particles is determined by integrating eq.B.10,

$$m_{\star, \text{young}} = m_{\text{gas}} \frac{dt_{\text{SF}}}{\tau}, \quad (\text{B.11})$$

where m_{gas} is the gas mass. Notice that eventhough star formation time step is set to $dt_{\text{SF}} = 5$ Myr, gas dynamics are calculated with a maximum time resolution of ~ 1 kyr.

The conversion of gas into stars evacuates the gas density, momentum and total energy. Therefore, eq.B.1, B.2, and B.3 have the *sink* terms $\mathcal{S}_{\rho_{\text{gas}}}$, $\mathcal{S}_{\mathbf{u}}$, \mathcal{S}_E when star formation occurs;

$$\mathcal{S}_{\rho_{\text{gas}},\text{SF}} = -\frac{\rho_{\text{gas}}}{\tau} \quad (\text{B.12})$$

$$\mathcal{S}_{\mathbf{u},\text{SF}} = -\frac{\mathbf{u}}{\tau} \quad (\text{B.13})$$

$$\mathcal{S}_{E,\text{SF}} = -\frac{E}{\tau} \quad (\text{B.14})$$

At the same time, metals in the gas are also evacuated at the star formation and the corresponding sink terms in eq.B.6 are

$$\mathcal{S}_{Z_i,\text{SF}} = -\frac{\rho_{Z_i}}{\tau} \quad (i = \text{SNII}, \text{SNIa}). \quad (\text{B.15})$$

B.3 Stellar feedback

Stellar feedback occurs from stellar winds and supernova (SN) explosions (Ostriker & Shetty 2011). and works as a heating source. The heating rate Γ in eq.B.3 is given as

$$\Gamma = \frac{1}{V} \sum_i M_i \Gamma'(t_{\text{age},i}), \quad (\text{B.16})$$

where M_i, t_i is the mass and the age of each stellar particle. The specific heating rate is denoted Γ' and the feed back type is different from the age of star particles as follows,

- $0 < t_{\text{age}} < 40$ Myr: stellar winds by massive stars and Type-II SNe
- $t_{\text{age}} > 40$ Myr : stellar winds from AGB stars
- $t_{\text{age}} \sim 1$ Gyr: Type-Ia SNe.

Stellar winds are driven by massive stars with $M \geq 5 M_{\odot}$ during the first 6 Myr of stellar evolution (Lamers & Cassinelli 1999), and we incorporate the thermal feedback as a constant heating rate for over 40 Myr, which is the typical age of the lightest star that explodes as a core-collapse supernova¹. The constant heat rate Γ' is $\Gamma' = 1.18 \times 10^{34}$ erg/s/ M_{\odot} , which corresponds to the injection of $E_{\text{SNII}} = 2 \times 10^{51}$ erg from stellar winds and SN explosions of massive stars with $M > 8 M_{\odot}$.

After 40 Myr, thermal feedback comes from stellar winds from AGB stars, whose injection rate is 6 orders lower than the previous thermal feedback in the first 40 Myr.

Also, we assume SNIa injection with a time scale of 1 Gyr and the event rate is 3 orders lower than that of CCSNe and the corresponding specific heating rate is

$$\Gamma'_{\text{SNIa}}(t_{\text{age}}) = E_{\text{SNIa}} \times \frac{dN_{\text{SNIa}}}{dt dM}(t_{\text{age}}), \quad (\text{B.17})$$

¹In the first few Myr, stellar winds from massive stars such as OB main-sequence stars and WR stars are dominant. The later energy injection is CCSNe. The stellar winds, SNe have roughly the same momentum ejection (Agertz et al. 2013).

where the energy of one SNIa is $E_{\text{SNIa}} = 10^{51}$ erg and the SNIa event rate is written as the following formula;

$$\frac{dN_{\text{SNIa}}}{dt dM}(t_{\text{age}}) = \frac{f_{\text{SNIa}}}{1.75 t_{\text{peak}}} e^{-x^2} \sqrt{x}, \quad x = \frac{t_{\text{peak}}}{t_{\text{age}}}, \quad (\text{B.18})$$

where f_{SNIa} is the number of SNIas per solar mass calculated by assumed IMF, and $t_{\text{peak}} = 1$ Gyr is the peak time scale of the SNIa event rate. The heating rate Γ' from SNIa is 3 orders lower than that from SNII.

B.4 Metal enrichment

The metal enrichment of from SNII and SNIa is considered separately because both supernova time-scales and release metal yields are quite different.

Single stellar particles release SNII metals in the first 40 Myrs as explained in section B.3. The total mass of heavy elements from SNII is $F_{Z,\text{SNII}} M_{\star}$, where M_{\star} is the mass of the stellar population and $F_{Z,\text{SNII}}$ is the metal mass fraction averaged over the IMF $\psi(m)$ within the range of $[m_{\text{min}}, m_{\text{max}}]$;

$$F_{Z,\text{SNII}} = \frac{\int_8^{m_{\text{max}}} m \psi(m) f_{Z,\text{SNII}}(m) dm}{\int_{m_{\text{min}}}^{m_{\text{max}}} m \psi(m) dm}, \quad (\text{B.19})$$

where $f_{Z,\text{SNII}}(m)$ is the mass fraction in metals from a Type-II SNe of a star with mass m and is modeled as the following by Woosley & Weaver (1995);

$$f_{Z,\text{SNII}}(m) = \min(0.2, 0.01m - 0.06). \quad (\text{B.20})$$

Finally, the feedback source term $\mathcal{S}_{Z_i,\text{FD}}$ is expressed as

$$\mathcal{S}_{Z_{\text{SNII}},\text{FD}} = \frac{F_{Z,\text{SNII}} \rho_{\star}}{40 \text{ Myr}}. \quad (\text{B.21})$$

For a single SNIa, we set a fixed mass of ejected metal of $m_{Z_{\text{SNIa}}} = 1.3 M_{\odot}$ for $3 - 8 M_{\odot}$ stars, and the feedback source term becomes

$$\mathcal{S}_{Z_{\text{SNIa}},\text{FD}} = m_{Z,\text{SNIa}} \frac{dN_{\text{SNIa}}}{dt dM} \rho_{\star}. \quad (\text{B.22})$$

B.5 Stellar mass loss

A stellar population loses mass through SNe and stellar winds from massive stars, WR or AGB stars. Stellar mass loss events inject mass, momentum, energy and metals to the surrounding gas. We introduce mass loss rate $f_{\text{loss}}(t_{\text{age}})$ as a function of the age of a single stellar population t_{age} provided by Jungwiert et al. (2001);

$$f_{\text{loss}}(t_{\text{age}}) \equiv -\frac{M_{\star}(t_{\text{age}})}{M_{\star}(t_{\text{age}} = 0)} = \frac{c_0}{t_{\text{age}} + T_0}, \quad (\text{B.23})$$

where coefficients have the constant values of $c_0 = 0.05$ and $T_0 = 5$ Myr. Therefore, the mass of SSP at age t_1 is obtained by integrating eq.B.23,

$$\int_0^{t_1} f_{\text{loss}}(t) dt = \frac{M(t_1) - M(0)}{M(0)} = \int_0^{t_1} \frac{c_0}{t_{\text{age}} + T_0} dt \quad (\text{B.24})$$

$$\therefore M(t_1) = \left[1 - c_0 \log \left(\frac{t_1 + T_0}{T_0} \right) \right] M(0) \quad (\text{B.25})$$

For example, the SSP with age $t_1 = 40$ Myr has mass of $M(40 \text{ Myr}) = 0.89 M(0)$, which indicates that 10% of the stellar mass is lost during the first 40 Myr by SNII and stellar winds from massive stars.

Finally, the source term in the continuity equation (eq.B.1) coming from stellar mass loss can be expressed as;

$$\mathcal{S}_{\rho_{\text{gas,ML}}} = \sum_i \rho_{\star}(t_{\text{age},i} = 0) f_{\text{loss}}(t_{\text{age},i}), \quad (\text{B.26})$$

where the sum includes all stellar particles within a given gas cell with an initial stellar density of $\rho_{\star}(t_{\text{age},i} = 0)$ and an age $t_{\text{age},i}$. Based on $\mathcal{S}_{\rho_{\text{gas,ML}}}$, the source terms in the momentum, energy, metal equations (eq.B.2, B.3, B.6) can be expressed as

$$\mathcal{S}_{\mathbf{u},\text{ML}} = \frac{\mathcal{S}_{\rho_{\text{gas,ML}}}}{\rho_{\text{gas}}} \bar{\mathbf{v}} \quad (\text{B.27})$$

$$\mathcal{S}_{E,\text{ML}} = \mathcal{S}_{\rho_{\text{gas,ML}}} (\mathbf{u} \cdot \bar{\mathbf{v}} + \mathbf{u}^2/2) \quad (\text{B.28})$$

$$\mathcal{S}_{Z_{\text{SNII}},\text{ML}} = \mathcal{S}_{\rho_{\text{gas,ML}}} F_{Z,\text{SNII}} \quad (\text{B.29})$$

$$\mathcal{S}_{Z_{\text{SNIa}},\text{ML}} = \mathcal{S}_{\rho_{\text{gas,ML}}} F_{Z,\text{SNIa}}, \quad (\text{B.30})$$

where $\bar{\mathbf{v}}$ is the velocity averaged over all stellar particles in the given gas cell, \mathbf{u} is the gas velocity, and $F_{Z,\text{SNII}}$ and $F_{Z,\text{SNIa}}$ are the mass fractions of metals obtained in eq. B.19.

B.6 Runaway stars

We also consider the effect of runaway stars, which has large velocity of 30 km/s. Runaway stars are mainly OB massive stars (Blaauw 1961) and one of their origins is kick due to SNe of the counterpart star of its binary system. Our simulation assigns a kick velocity of ~ 10 km/s to 30% of the newly formed stellar particles.

B.7 Radiative Pressure Feedback

Massive stars produce quite amounts of ionizing photons and radiation pressure P_{rad} is added as a non-thermal pressure. This ionizing radiation injects momentum of gas cells which contain stellar particles younger than 5 Myr and whose column density is $N_{\text{HI}} > 10^{21} / \text{cm}^2$.

$P_{\text{rad,UV}}$ is expressed by the intensity I , the mass of a stellar mass particle m_{star} , the luminosity of ionizing photons per unit stellar mass Γ' , and an assumed spherical area A ,

$$P_{\text{rad,UV}} = \frac{4\pi}{3c} I = \frac{4\pi}{3c} \frac{\Gamma' m_{\star}}{A} = \frac{\Gamma' m_{\star}}{R^2 c} \quad (\because A = 4\pi R^2) \quad (\text{B.31})$$

The value of Γ' is $\Gamma' = 10^{36}$ erg/s/ M_{\odot} from STARBURST99 (Leitherer et al. 1999), and is the time-averaged luminosity per unit mass of the ionizing radiation for the first 5 Myr of the SSP evolution. When $N_{\text{HI}} > 10^{21}$ /cm², the gas cloud is optically thick and the ionizing radiation is trapped effectively.

Furthermore, our simulations include infrared(IR) radiation pressure, which is effective when the gas density is $n_{\text{gas}} > 300$ cm⁻³. IR photons are absorbed by dust and scattered many times and can be enhanced significantly. This multiple scattering increases the radiation pressure $P_{\text{rad,IR}}$ in proportion to the dust optical depth (Agertz et al. 2013; Hopkins et al. 2011; Murray et al. 2010). $P_{\text{rad,IR}}$ is given by

$$P_{\text{rad,IR}} = (1 + \tau_{\text{IR}})P_{\text{rad}}, \quad \tau_{\text{IR}} = \frac{n_{\text{gas}}}{300 \text{ cm}^{-3}}. \quad (\text{B.32})$$

The total pressure P_{tot} is the sum of thermal and radiative pressure,

$$P_{\text{tot}} = P_{\text{thermal}} + P_{\text{rad,UV}} + P_{\text{rad,IR}}. \quad (\text{B.33})$$

B.8 Other effects

We set a uniform UV background with redshift dependence (Haardt & Madau 1996) where the $n_{\text{gas}} < 0.1$ cm⁻³. In the case of $n_{\text{gas}} > 0.1$ cm⁻³, UV background is suppressed significantly and we use the value of 5.9×10^{26} erg/s/cm²/Hz, which reproduces the partial self-shielding of dense gas. This shielding effect allows dense gas to cool to ~ 300 K. The heating rate is calculated by the feedback models explained above.

We did not include AGN feedback on sub- L_{*}^2 galaxies because it is a minor effect.

² L_{*} is a characteristic luminosity.

Appendix C

stellar mass - SFR relationship

We study not only the metallicity evolution of high- z galaxies, but also study another important relationship, M_\star -SFR relationships. There is a strong correlation between the star formation rate (SFR) and the stellar mass (M_\star) of main sequence galaxies observed at a given redshift. The stellar mass gives the information on star formation mechanisms and its efficiencies, such as gas accretion rates, feedback and so on. The M_\star -SFR relationships have been well studied and have a highly consistent framework from $z = 6$ to $z = 0$ by (Speagle et al. 2014). In this section, we investigate the redshift evolution of the stellar mass-SFR relationships from $z = 6$ to $z = 9$ in Figure C.1. We compare our FirstLight samples with galaxies which [OIII] $88\mu\text{m}$ lines are observed by ALMA, the new samples in CANDELS field by HST (Tacchella et al. 2022), and the latest data from JWST observation; GLASS-JWST ERS program by NIRCcam (Leethochawalit et al. 2022), and three galaxies around the galaxy cluster SMACS J0723 (Curti et al. 2022). We show the extrapolation from Speagle et al. (2014) at $z = 6$ as a dashed line.

To strengthen the reliability of our results, we also compare FirstLight simulation results with other samples from independent numerical simulations; FLARES simulations (Lovell et al. 2021), with the dustyGadget simulations (Di Cesare et al. 2022; Graziani et al. 2020), large-scale cosmological simulations (Moriwaki et al. 2018; Shimizu et al. 2016), SERRA simulations (Pallottini et al. 2022), and SIGAME simulations (Olsen et al. 2017). FLARES, SERRA, and SIGAME simulations adopt a zoom-in technique as the same as our simulations. dustyGadget implements dust models into their cosmological simulations to follow the evolution of dusty galaxies at $z \geq 4$. Despite differences of simulation methods, the predicted stellar mass-SFR relationships agree with each other.

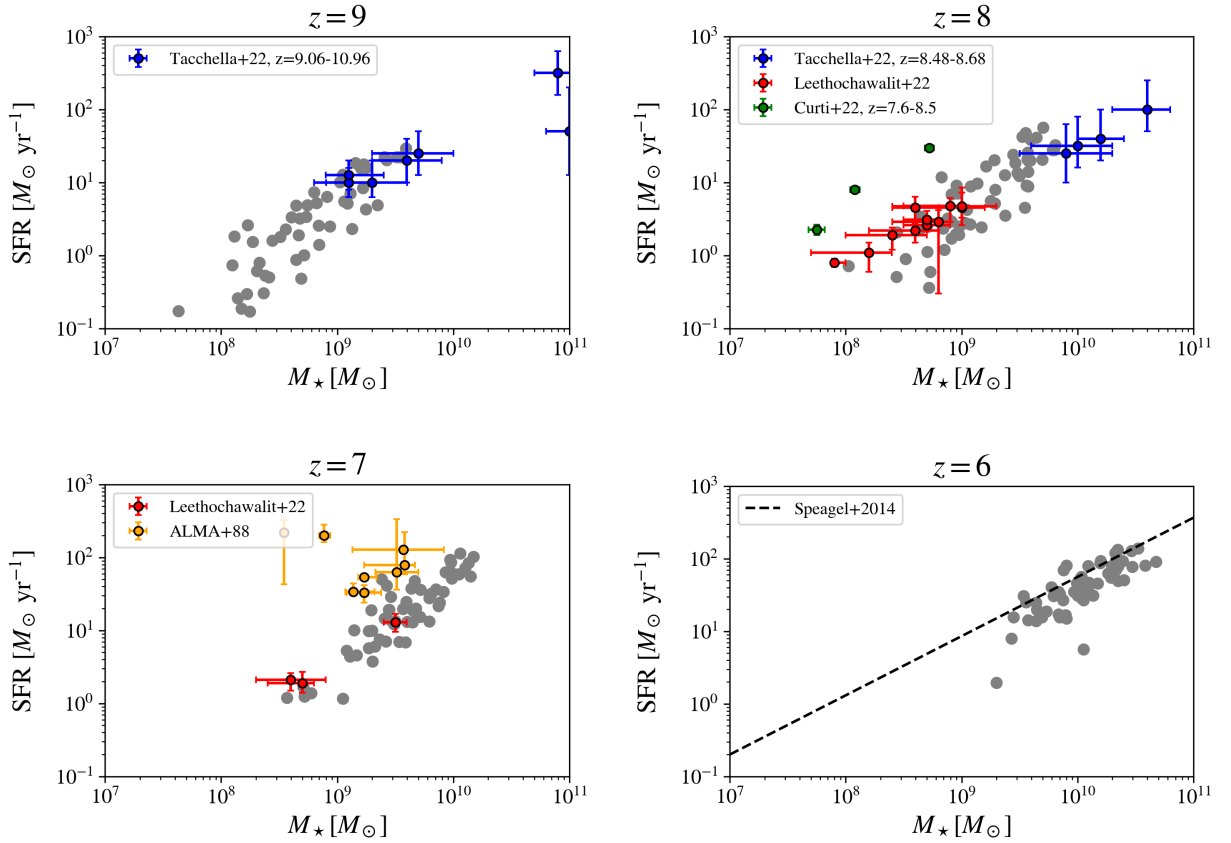


Figure C.1: Stellar mass and SFR in the redshift range between 9 (top left) and 6 (bottom right). Plots with errorbars in green, blue and red are the works from Tacchella et al. (2022), Leethochawalit et al. (2022) and Curti et al. (2022). The ALMA observation plots in $z = 7$ (bottom left) are from Hashimoto et al. (2019); Inoue et al. (2016); Wong et al. (2022) and Witstok et al. (2022). A black dashed line in $z = 6$ (bottom right) is a fitting function from Speagle et al. (2014).

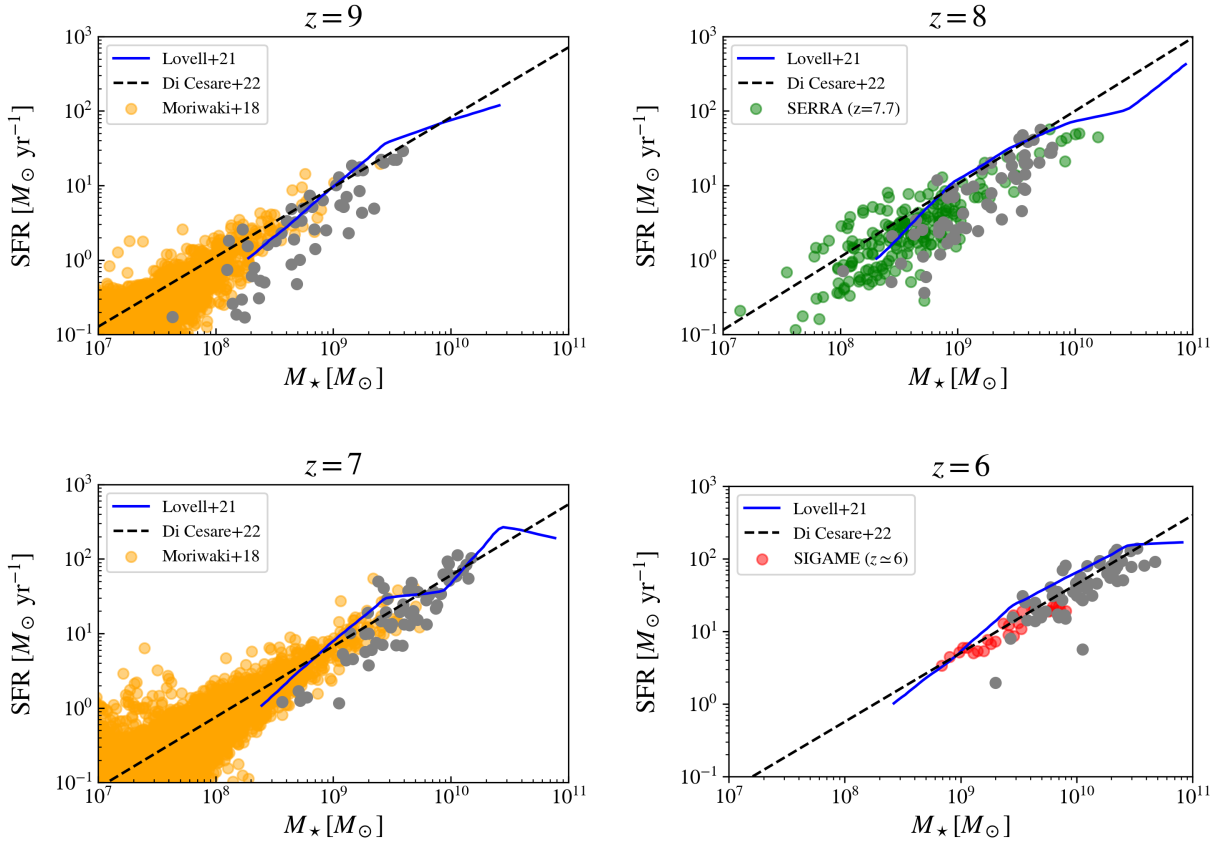


Figure C.2: Comparison of M_* - SFR between our work and other simulations. Gray plots are our galaxy samples, black-dashed lines are linear fit from the dustyGadget simulation (Di Cesare et al. 2022; Graziani et al. 2020), and blue-solid lines show the predictions from the FLARES simulation (Lovell et al. 2021). Orange, green and red plots are simulated samples of Moriwaki et al. (2018), Pallottini et al. (2022), and Olsen et al. (2017).

Appendix D

Flux density calculation

The line emissivity from each HII region around a star particle is calculated in a unit of [erg/s/one HII region]. We then sum the emissivity and calculate the emissivity from each grid (3D) in a unit of [erg/s/grid (3D)]. A real observation does not have the information of z -direction, and we project the pixel emissivity into x-y plane and get the 2D pixel emissivity in a unit of [erg/s/pixel (2D)].

The NIRSPEC IFU observation data is obtained in a unit of [MJy/sr] for IFU data, and a unit of [erg/s/cm²/Å] for spectrum. Therefore, we have to convert our simulated output unit into an observation unit to produce mock data.

D.1 Surface flux density calculation

We consider one galaxy sample (FL939) at $z = 6.93$, which have [OIII] 88 μm luminosity of

$$L_{[\text{OIII}]88}(z = 6.93) = 2.52 \times 10^{41} \text{ erg/s/pixel(2D)}. \quad (\text{D.1})$$

The comoving distance to $z = 6.93$ is $D_c = 8804 \text{ Mpc} = 2.71 \times 10^{28} \text{ cm}$. The luminosity in eq. D.1 is the value at $z = 6.93$. One second at $z = 6.93$ is $1 \times (1 + z)$ seconds at $z = 0$ and the luminosity for an observer at $z = 0$ is

$$L_{[\text{OIII}]88}(z = 0) = L_{[\text{OIII}]88}(z = 6.93)/(1 + z) \text{ erg/s/pixel}. \quad (\text{D.2})$$

The observed flux at $z = 0$ is

$$F(z = 0) = \frac{L(z = 0)}{4\pi D_c^2} = \frac{2.52 \times 10^{41}/(1 + 6.93)}{4\pi \times (2.71 \times 10^{28})^2} = 3.422 \times 10^{-18} \text{ [erg/s/cm}^2\text{/pixel]}. \quad (\text{D.3})$$

For the calculation of flux density, we have to consider the flux **per frequency** (/Hz). Notice that the wavelength is stretched by redshift. Let us assume the linewidth is $\Delta v(z = 6.93) =$

100 km/s. From the doppler shift relationship $v/c = -(\nu - \nu_0)/\nu_0$, we obtain $\Delta\nu$ as the following,

$$\Delta\nu(z = 6.93) \equiv \nu_0 - \nu = \frac{\Delta v}{c} \nu_0 \quad (\text{D.4})$$

$$= \frac{1.0 \times 10^7 \text{ cm/s}}{3.0 \times 10^{10} \text{ cm/s}} \times 3406 \times 10^9 \text{ Hz} \quad (\because 3406 \text{ GHz for [OIII] } 88\mu\text{m}) \quad (\text{D.5})$$

$$= 1.13 \times 10^9 \text{ Hz}. \quad (\text{D.6})$$

The frequency $\Delta\nu(z = 0)$ is decreased by redshift;

$$\Delta\nu(z = 0) = \frac{\Delta\nu(z = 6.93)}{(1 + z)}. \quad (\text{D.7})$$

The flux density at $z = 0$ is

$$f_\nu(z = 0) = \frac{F(z = 0)}{\Delta\nu(z = 0)} = \frac{3.422 \times 10^{-18}}{1.13 \times 10^9} \text{ Jy/pixel}. \quad (\text{D.8})$$

For the calculation of integral flux density at $z = 0$, we multiply the flux density $f_\nu(z = 0)$ by Δv [cm/s]¹. We obtain the integral flux density as the following,

$$\mathcal{F}_\nu(z = 0) = f_\nu(z = 0) \times \Delta v \times 10^{-5} \text{ [Jy km/s/pixel]} \quad (\text{D.9})$$

$$= \frac{F(\nu = 0)}{\Delta\nu(z = 0)} \times \Delta v \times 10^{-5} \quad (\text{D.10})$$

$$= F(\nu = 0) \times \frac{c(1 + z)}{\Delta v \nu_0} \times \Delta v \times 10^{-5} \text{ [erg/s/cm}^2\text{/Hz} \cdot \text{km/s/pixel]} \quad (\text{D.11})$$

$$= F(\nu = 0) \frac{c(1 + z)}{\nu_0} \times 10^{-5} \times 10^{23} \text{ [Jy km/s/pixel]} \quad (\text{D.12})$$

$$= 3.422 \times 10^{-18} \times \frac{3 \times 10^{10} \times (1 + 6.93)}{3406 \times 10^9} \times 10^{-5} \times 10^{23} \quad (\text{D.13})$$

$$= 0.239 \text{ Jy km/s/pixel} \quad (\text{D.14})$$

Notice that we do not need the information of line width Δv for the calculation of integral flux density.

One side length of the pixel is 0.1 pkpc = 0.1/5.378 arcsec. Therefore, 1 pixel satisfies

$$1 \text{ pixel} = 3.46 \times 10^{-4} \text{ arcsec}^2. \quad (\text{D.15})$$

The surface flux density at $z = 0$ is

$$\mathcal{S}_\nu(z = 0) = \frac{\mathcal{F}_\nu(z = 0)}{3.46 \times 10^{-4}} \times 10^3 \text{ [mJy km/s arcsec}^2\text{]}. \quad (\text{D.16})$$

The unit of surface flux density [mJy km/s arcsec²] is often used by ALMA observation.

¹ Δv has a unit of [km/s] and the redshift effects on the distance and time are canceled and the value of Δv is same at both $z = 6.93$ and $z = 0$.

D.2 NIRSpec IFU

D.2.1 Spectrum in a unit of [erg/s/cm²/Å]

Let us consider the emission line [OIII] 5007Å from $z = z_i$, i.e., the observed wavelength is $\lambda_{\text{obs}} = 5007 \times (1 + z_i)$ Å. We have line emissivities in each 3D grid as $L_{[\text{OIII}]5007}(z = z_i)$ [erg/s/grid(3D)]. We assume that the line width depends on only wavelength resolution as

$$\Delta v = \frac{\Delta \lambda_{\text{obs,reso}}}{\lambda_{\text{obs}}} \cdot c = \frac{c}{R} \sim 111 \text{ km/s}. \quad (\text{D.17})$$

We calculate the flux for each grid (3D) as same as eq. D.3

$$F(z = 0) = \frac{L_{[\text{OIII}]5007}(z = 0)}{4\pi D_c^2} \quad (\text{D.18})$$

$$= \frac{L_{[\text{OIII}]5007}(z = z_i)}{(1 + z_i)4\pi D_c^2} \quad [\text{erg/s/cm}^2/\text{grid}], \quad (\text{D.19})$$

where D_c is comoving distance to $z = z_i$ ². NIRSpec observation has a wavelength resolution of $R = 2700$ and the minimum wavelength interval $\Delta \lambda_{\text{obs,reso}}$ is

$$\Delta \lambda_{\text{obs,reso}} = \frac{\lambda_{\text{obs}}}{R} = \frac{\lambda_{\text{rest}} \times (1 + z)}{2700} (= 14.8 \text{ Å for } [\text{OIII}] 5007 \text{ Å}). \quad (\text{D.23})$$

The flux density f_λ is calculated by dividing the flux F by $\Delta \lambda$. $\Delta \lambda(z = z_i)$ is derived by using doppler shift relationship $(\lambda - \lambda_0)/\lambda_0 = \Delta v/c$,

$$\Delta \lambda(z = z_i) = \lambda - \lambda_0 \quad (\text{D.24})$$

$$= \frac{\Delta v}{c} \cdot \lambda_0 \quad (\text{D.25})$$

$$= \frac{\Delta \lambda_{\text{obs,reso}}}{\lambda_{\text{obs}}} c \cdot \frac{\lambda_0}{c} \quad (\because \text{eq. D.17}) \quad (\text{D.26})$$

$$= \frac{\lambda_0}{R} \quad (\text{D.27})$$

$$\therefore \Delta \lambda(z = 0) = \Delta \lambda(z = z_i) \times (1 + z_i) = \frac{\lambda_{\text{obs}}}{R} = \Delta \lambda_{\text{obs,reso}} \quad (\text{D.28})$$

We then obtain the flux density as following,

$$f_\lambda(z = 0) = \frac{F(z = 0)}{\Delta \lambda(z = 0)} = \frac{F(z = 0)}{\Delta \lambda_{\text{obs,reso}}} \quad [\text{erg/s/cm}^2/\text{Å}/\text{grid}]. \quad (\text{D.29})$$

Next, we have to convert 3D grid information (x, y, z) into 3D IFU information (x, y, λ) . The line-of-sight velocity v_{LOS} of each grid is calculated as the average of z -direction velocity

²The comoving distance at $z = z_i$ can be derived as

$$D_c = \int_0^{z_i} \frac{cdz}{H(z)} \quad (\text{D.20})$$

$$H = H_0 \sqrt{\Omega_{r0}(1 + z_i)^4 + \Omega_{m0}(1 + z_i)^3 + \Omega_{K0}(1 + z_i)^2 + \Omega_{\Lambda 0}} \quad (\text{eq. 1.37}) \quad (\text{D.21})$$

$$= H_0 \sqrt{\Omega_{m0}(1 + z_i)^3 + \Omega_{\Lambda 0}} \quad (\text{for flat and matter-dominant universe}). \quad (\text{D.22})$$

of gas cells, which is weighted by density. The wavelength of the emitted line from each grid is doppler-shifted as the following,

$$\lambda_{\text{obs}} = \lambda_{\text{obs},0} + \Delta\lambda \quad (\text{D.30})$$

$$= \lambda_{\text{obs},0} + \frac{v_{\text{LOS}}}{c} \lambda_{\text{obs},0} \quad (\text{D.31})$$

$$= \left(1 + \frac{v_{\text{LOS}}}{c}\right) \lambda_{\text{obs},0}. \quad (\text{D.32})$$

The flux density in eq. D.29 is equals to

$$f_{\lambda}(z=0) \text{ [erg/s/cm}^2/\text{\AA}/\text{grid}] \iff f_{\lambda}(z=0) \text{ [erg/s/cm}^2/\text{\AA}/\text{pixel}] \text{ at } \lambda = \lambda_{\text{obs}}. \quad (\text{D.33})$$

We sum the flux density [erg/s/cm²/Å/pixel], whose λ_{obs} is in the range of $[\lambda_{\text{obs}} \pm \Delta\lambda_{\text{obs,reso}}]$, and finally obtain the spectrum for one whole galaxy in a unit of [erg/s/cm²/Å]³.

D.2.2 Flux density in a unit of MJy/sr

We calculate flux density for each grid (eq. D.29) and sum up the flux density at each 2D pixel at each wavelength $\lambda = \lambda_{\text{obs}}$.

$$f_{\nu}(z=0) = \frac{F(z=0)}{\Delta\nu(z=0)} = \frac{F(z=0)}{\Delta\nu_{\text{obs,reso}}} \text{ [erg/s/cm}^2/\text{Hz}/\text{grid}], \quad (\text{D.34})$$

where $\Delta\nu_{\text{obs,reso}} = \nu_{\text{obs}}/R$ assuming the line width as Δv . Then we get the 2D flux distribution in a unit of [erg/s/cm²/Hz/pixel] at each wavelength. Finally we convert the unit from [erg/s/cm²/Hz/pixel] to [MJy/sr].

D.2.3 Conversion of kpc to arcsec

Angular diameter distance at $z = z_i$ is written as

$$d_{\text{A}}(z_i) = \frac{S_k[D_{\text{c}}(z_i)]}{1 + z_i}. \quad (\text{D.35})$$

where $S_k(D_{\text{c}})$ is

$$S_k(x) = \begin{cases} \frac{\sinh(\sqrt{-K}x)}{\sqrt{-K}} & (K < 0) \\ x & (K = 0) \\ \frac{\sin(\sqrt{K}x)}{\sqrt{K}} & (K > 0) \end{cases} \quad (\text{D.36})$$

Here x is comoving distance ($= D_{\text{c}}$). In the flat universe, i.e., $K = 0$, the angular distance is

$$d_{\text{A}}(z_i) = \frac{D_{\text{c}}(z_i)}{1 + z_i}. \quad (\text{D.37})$$

³Notice that the unit does not include per pixel

The conversion factor C is calculated as following,

$$1 \text{ arcsec} = C \text{ kpc} \quad (\text{D.38})$$

$$= d_A(z_i) \text{ [kpc]} \times \theta \text{ [radian]} \quad (\text{D.39})$$

$$= d_A(z_i) \times \frac{1 \text{ arcsec} \times \pi}{180 \times 3600} \text{ [kpc]} \quad (\text{D.40})$$

The conversion from arcsec^2 to sr is

$$1 \text{ arcsec}^2 = 2.35 \times 10^{-11} \text{ str} \quad (\text{D.41})$$

For instance, the comoving distance to $z = 7$ is $D_c = 8.826 \times 10^6$ kpc and the conversion is

$$1 \text{ arcsec} = \frac{8.826 \times 10^6}{1 + 7} \times \frac{1 \times \pi}{180 \times 3600} = 5.349 \text{ kpc}. \quad (\text{D.42})$$

NIRSpec observation has a spatial resolution of $dl_{\text{obs}} = 0.1$ [arcsec/pixel]. Therefore, the conversion of pixel to sr is

$$1 \text{ pixel} = dl_{\text{obs}}^2 \times 2.35 \times 10^{-11} \text{ sr} \quad (\text{D.43})$$

Acknowledgement

Words cannot express my gratitude to my supervisor, Professor Naoki Yoshida for his invaluable support and sincere guidance, and funding to make my master student life fruitful. His inspiration, innovative feedback, and critical comments always helped me a lot in my research as well as in improving my thesis. Every discussion with him encourages me to investigate things thoroughly and work hard. He also gave me wonderful opportunities to start my research of high-z galaxies and to join JWST observation team collaborating with Japan and Spain. Through hole two years of research, I was able to do comprehensive research from formation of the first stars to evolution of high-z galaxies.

Next, I would like to thank my closest collaborator, Gen Chiaki, who has taught me almost everything such as the way to perform cosmological simulations, to analyze simulation outputs even though the first one and a half years of research was conducted totally remotely. He also corrected my research proposal, conference abstract, and presentation slides over and over again. Without his help, it would not have been possible to carry out my research.

I am also grateful to my research collaborator, Daniel Ceverino, who provides FirstLight simulation data and always gives me lots of helpful comments on my research. I would like to express my appreciation to Professor Smadar Naoz for accepting me as a remote member of her group at the University of California, Los Angels, and giving me an amazing research topic on Stream Velocity in the early universe. I would like to thank Chiou Yeou, and William Lake for providing me with the initial conditions for cosmological simulations and giving me insightful comments on my paper. I have not met all of them listed above in person due to the covid pandemic, but it was an honor to conduct my research with them.

I would like to thank my thesis committee members; Prof. Naoki Yoshida, Prof. Kotaro Kono and Prof. Kipp Cannon for all of their guidance through this process.

Thanks should also go to Shingo Hirano, who mentors the first star *zemi* during the whole my master course, teaches me star formation processes from scratch, and provides constructive discussions. His attitude toward work also motivates me to pursue my study.

I would like to express my gratitude to the following people: Kana Moriwaki, for teaching me lots of things about emission line modeling, and basic knowledge of galaxies; Tilman Hartwig, for fruitful discussions on stream velocity and mentoring stellar *zemi*; Hiroto Mitani, for mentoring *zemi* from undergrad, and correcting my research proposal many times; Yuta Tarumi, for helping me analyzing AREPO outputs, extending my astrophysics knowledge, and providing entertainment for me. I thank all the other members of the University of Tokyo Theoretical Astrophysics Group and Research Center for the Early Universe for many fruitful discussions. I am also very much thankful to the members of *zemi* I have joined.

Special thanks to my best friend, Hiroka, who is always listening to me whenever I am happy or depressed, and is always on my side for over 10 years. I am proud of having such a nice friend who I the most respect for her personality and activeness. Finally, I deeply thank my parents, brothers, and grandmother who always believe and understand me, and give tremendous

moral support. This achievement of my life would not be possible without their support and cooperation.

I acknowledge the support from International Graduate Program for Excellence in Earth-Space Science (IGPEES) of the University of Tokyo. The work made use of v2.3 of the Binary Population and Spectral Synthesis (BPASS) models as described in Byrne et al. (2022) and Stanway & Eldridge (2018). Parts of the calculations in this work were carried out on Cray XC50 and analysis servers at Center for Computational Astrophysics, National Astronomical Observatory of Japan.

Bibliography

- Abbott, B. P., Abbott, R., Abbott, T. D., et al. 2016, *Phys. Rev. Lett.*, 116, 061102, doi: 10.1103/PhysRevLett.116.061102
- Abel, T., Bryan, G. L., & Norman, M. L. 2002, *Science*, 295, 93, doi: 10.1126/science.295.5552.93
- Agarwal, B., Khochfar, S., Johnson, J. L., et al. 2012, *MNRAS*, 425, 2854, doi: 10.1111/j.1365-2966.2012.21651.x
- Agertz, O., Kravtsov, A. V., Leitner, S. N., & Gnedin, N. Y. 2013, *ApJ*, 770, 25, doi: 10.1088/0004-637X/770/1/25
- Anders, E., & Grevesse, N. 1989, *Geochim. Cosmochim. Acta*, 53, 197, doi: 10.1016/0016-7037(89)90286-X
- Aoki, W., Tominaga, N., Beers, T. C., Honda, S., & Lee, Y. S. 2014, *Science*, 345, 912, doi: 10.1126/science.1252633
- Arata, S., Yajima, H., Nagamine, K., Abe, M., & Khochfar, S. 2020, *MNRAS*, 498, 5541, doi: 10.1093/mnras/staa2809
- Asplund, M., Grevesse, N., Sauval, A. J., & Scott, P. 2009, *ARA&A*, 47, 481, doi: 10.1146/annurev.astro.46.060407.145222
- Bakx, T. J. L. C., Zavala, J. A., Mitsunashi, I., et al. 2022, arXiv e-prints, arXiv:2208.13642. <https://arxiv.org/abs/2208.13642>
- Barkana, R., & Loeb, A. 2001a, *Phys. Rep.*, 349, 125, doi: 10.1016/S0370-1573(01)00019-9
- . 2001b, *Phys. Rep.*, 349, 125, doi: 10.1016/S0370-1573(01)00019-9
- Barrufet, L., Oesch, P. A., Weibel, A., et al. 2022, arXiv e-prints, arXiv:2207.14733. <https://arxiv.org/abs/2207.14733>
- Berg, D. A., Skillman, E. D., Marble, A. R., et al. 2012, *ApJ*, 754, 98, doi: 10.1088/0004-637X/754/2/98
- Bian, F., & Fan, X. 2020, *MNRAS*, 493, L65, doi: 10.1093/mnras1/slaa007
- Bian, F., Kewley, L. J., & Dopita, M. A. 2018, *ApJ*, 859, 175, doi: 10.3847/1538-4357/aabd74
- Bisigello, L., Caputi, K. I., Colina, L., et al. 2017, *ApJS*, 231, 3, doi: 10.3847/1538-4365/aa7a14

- Blaauw, A. 1961, *Bull. Astron. Inst. Netherlands*, 15, 265
- Bouwens, R. J., Illingworth, G. D., Oesch, P. A., et al. 2010, *ApJ*, 709, L133, doi: 10.1088/2041-8205/709/2/L133
- Bovino, S., & Galli, D. 2019, in *Formation of the First Black Holes*, ed. M. Latif & D. Schleicher, 45–66, doi: 10.1142/9789813227958_0003
- Bovy, J., & Dvorkin, C. 2013, *ApJ*, 768, 70, doi: 10.1088/0004-637X/768/1/70
- Brauher, J. R., Dale, D. A., & Helou, G. 2008, *ApJS*, 178, 280, doi: 10.1086/590249
- Bromm, V., Coppi, P. S., & Larson, R. B. 2002, *ApJ*, 564, 23, doi: 10.1086/323947
- Bromm, V., & Loeb, A. 2003, *Nature*, 425, 812, doi: 10.1038/nature02071
- Burgarella, D., Bogdanoska, J., Nanni, A., et al. 2022, *A&A*, 664, A73, doi: 10.1051/0004-6361/202142554
- Byrne, C. M., Stanway, E. R., Eldridge, J. J., McSwiney, L., & Townsend, O. T. 2022, *MNRAS*, 512, 5329, doi: 10.1093/mnras/stac807
- Cameron, A. J., Katz, H., & Rey, M. P. 2022, arXiv e-prints, arXiv:2210.14234. <https://arxiv.org/abs/2210.14234>
- Carnall, A. C., Begley, R., McLeod, D. J., et al. 2023, *MNRAS*, 518, L45, doi: 10.1093/mnras1/slac136
- Carniani, S., Maiolino, R., Pallottini, A., et al. 2017, *A&A*, 605, A42, doi: 10.1051/0004-6361/201630366
- Castellano, M., Pentericci, L., Fontana, A., et al. 2017, *ApJ*, 839, 73, doi: 10.3847/1538-4357/aa696e
- Castellano, M., Fontana, A., Treu, T., et al. 2022, *ApJ*, 938, L15, doi: 10.3847/2041-8213/ac94d0
- Ceverino, D., Dekel, A., & Bournaud, F. 2010, *MNRAS*, 404, 2151, doi: 10.1111/j.1365-2966.2010.16433.x
- Ceverino, D., Dekel, A., Mandelker, N., et al. 2012, *MNRAS*, 420, 3490, doi: 10.1111/j.1365-2966.2011.20296.x
- Ceverino, D., Glover, S. C. O., & Klessen, R. S. 2017, *MNRAS*, 470, 2791, doi: 10.1093/mnras/stx1386
- Ceverino, D., Hirschmann, M., Klessen, R. S., et al. 2021, *MNRAS*, 504, 4472, doi: 10.1093/mnras/stab1206
- Ceverino, D., Klessen, R. S., & Glover, S. C. O. 2018, *MNRAS*, 480, 4842, doi: 10.1093/mnras/sty2124
- . 2019, *MNRAS*, 484, 1366, doi: 10.1093/mnras/stz079
- Ceverino, D., & Klypin, A. 2009, *ApJ*, 695, 292, doi: 10.1088/0004-637X/695/1/292

-
- Ceverino, D., Klypin, A., Klimek, E. S., et al. 2014, *MNRAS*, 442, 1545, doi: 10.1093/mnras/stu956
- Chabrier, G. 2005, in *Astrophysics and Space Science Library*, Vol. 327, *The Initial Mass Function 50 Years Later*, ed. E. Corbelli, F. Palla, & H. Zinnecker, 41, doi: 10.1007/978-1-4020-3407-7_5
- Chiaki, G., & Wise, J. H. 2019, *MNRAS*, 482, 3933, doi: 10.1093/mnras/sty2984
- Chiou, Y. S., Naoz, S., Burkhart, B., Marinacci, F., & Vogelsberger, M. 2019, *ApJ*, 878, L23, doi: 10.3847/2041-8213/ab263a
- . 2021, *ApJ*, 906, 25, doi: 10.3847/1538-4357/abc88f
- Chiou, Y. S., Naoz, S., Marinacci, F., & Vogelsberger, M. 2018, *MNRAS*, 481, 3108, doi: 10.1093/mnras/sty2480
- Chon, S., Hirano, S., Hosokawa, T., & Yoshida, N. 2016, *ApJ*, 832, 134, doi: 10.3847/0004-637X/832/2/134
- Chon, S., & Hosokawa, T. 2019, *MNRAS*, 488, 2658, doi: 10.1093/mnras/stz1824
- Clark, P. C., Glover, S. C. O., Smith, R. J., et al. 2011, *Science*, 331, 1040, doi: 10.1126/science.1198027
- Cormier, D., Lebouteiller, V., Madden, S. C., et al. 2012, *A&A*, 548, A20, doi: 10.1051/0004-6361/201219818
- Curti, M., Cresci, G., Mannucci, F., et al. 2017, *MNRAS*, 465, 1384, doi: 10.1093/mnras/stw2766
- Curti, M., Mannucci, F., Cresci, G., & Maiolino, R. 2020, *MNRAS*, 491, 944, doi: 10.1093/mnras/stz2910
- Curti, M., D'Eugenio, F., Carniani, S., et al. 2022, arXiv e-prints, arXiv:2207.12375. <https://arxiv.org/abs/2207.12375>
- Davé, R., Rafieferantsoa, M. H., Thompson, R. J., & Hopkins, P. F. 2017, *MNRAS*, 467, 115, doi: 10.1093/mnras/stx108
- Davé, R., Thompson, R., & Hopkins, P. F. 2016, *MNRAS*, 462, 3265, doi: 10.1093/mnras/stw1862
- De Looze, I., Cormier, D., Lebouteiller, V., et al. 2014, *A&A*, 568, A62, doi: 10.1051/0004-6361/201322489
- Di Cesare, C., Graziani, L., Schneider, R., et al. 2022, arXiv e-prints, arXiv:2209.05496. <https://arxiv.org/abs/2209.05496>
- Dinerstein, H. L., Lester, D. F., & Werner, M. W. 1985, *ApJ*, 291, 561, doi: 10.1086/163096
- Dolag, K., Borgani, S., Murante, G., & Springel, V. 2009, *MNRAS*, 399, 497, doi: 10.1111/j.1365-2966.2009.15034.x

- Donnan, C. T., McLeod, D. J., Dunlop, J. S., et al. 2022, arXiv e-prints, arXiv:2207.12356.
<https://arxiv.org/abs/2207.12356>
- Dopita, M. A., & Sutherland, R. S. 2003, *Astrophysics of the diffuse universe*
- Draine, B. T. 2011, *Physics of the Interstellar and Intergalactic Medium*
- Ferland, G. J., Korista, K. T., Verner, D. A., et al. 1998, *PASP*, 110, 761, doi: 10.1086/316190
- Ferland, G. J., Porter, R. L., van Hoof, P. A. M., et al. 2013, *Rev. Mexicana Astron. Astrofis.*, 49, 137. <https://arxiv.org/abs/1302.4485>
- Fialkov, A., Barkana, R., Tseliakhovich, D., & Hirata, C. M. 2012, *MNRAS*, 424, 1335, doi: 10.1111/j.1365-2966.2012.21318.x
- Fialkov, A., Barkana, R., Visbal, E., Tseliakhovich, D., & Hirata, C. M. 2013, *MNRAS*, 432, 2909, doi: 10.1093/mnras/stt650
- Finkelstein, S. L., Bagley, M. B., Haro, P. A., et al. 2022, *ApJ*, 940, L55, doi: 10.3847/2041-8213/ac966e
- Fletcher, T. J., Tang, M., Robertson, B. E., et al. 2019, *ApJ*, 878, 87, doi: 10.3847/1538-4357/ab2045
- Flury, S. R., Jaskot, A. E., Ferguson, H. C., et al. 2022, *ApJS*, 260, 1, doi: 10.3847/1538-4365/ac5331
- Fudamoto, Y., Oesch, P. A., Faisst, A., et al. 2020, *A&A*, 643, A4, doi: 10.1051/0004-6361/202038163
- Fujimoto, S., Finkelstein, S. L., Burgarella, D., et al. 2022, arXiv e-prints, arXiv:2211.03896.
<https://arxiv.org/abs/2211.03896>
- Galli, D., & Palla, F. 2013, *ARA&A*, 51, 163, doi: 10.1146/annurev-astro-082812-141029
- Graziani, L., Schneider, R., Ginolfi, M., et al. 2020, *MNRAS*, 494, 1071, doi: 10.1093/mnras/staa796
- Greif, T. H. 2015, *Computational Astrophysics and Cosmology*, 2, 3, doi: 10.1186/s40668-014-0006-2
- Greif, T. H., Bromm, V., Clark, P. C., et al. 2012, in *American Institute of Physics Conference Series*, Vol. 1480, *First Stars IV - from Hayashi to the Future -*, ed. M. Umemura & K. Omukai, 51–56, doi: 10.1063/1.4754327
- Greif, T. H., White, S. D. M., Klessen, R. S., & Springel, V. 2011, *ApJ*, 736, 147, doi: 10.1088/0004-637X/736/2/147
- Grevesse, N., & Sauval, A. J. 1998, *Space Sci. Rev.*, 85, 161, doi: 10.1023/A:1005161325181
- Gutiérrez, L., & Beckman, J. E. 2008, in *Lecture Notes and Essays in Astrophysics*, Vol. 3, 177–188
- Gutkin, J., Charlot, S., & Bruzual, G. 2016, *MNRAS*, 462, 1757, doi: 10.1093/mnras/stw1716

- Haardt, F., & Madau, P. 1996, *ApJ*, 461, 20, doi: 10.1086/177035
- Harikane, Y., Ouchi, M., Inoue, A. K., et al. 2020, *ApJ*, 896, 93, doi: 10.3847/1538-4357/ab94bd
- Harikane, Y., Ouchi, M., Oguri, M., et al. 2022a, arXiv e-prints, arXiv:2208.01612. <https://arxiv.org/abs/2208.01612>
- Harikane, Y., Inoue, A. K., Mawatari, K., et al. 2022b, *ApJ*, 929, 1, doi: 10.3847/1538-4357/ac53a9
- Hasegawa, K., Umemura, M., & Susa, H. 2009, *MNRAS*, 395, 1280, doi: 10.1111/j.1365-2966.2009.14639.x
- Hashimoto, T., Laporte, N., Mawatari, K., et al. 2018, *Nature*, 557, 392, doi: 10.1038/s41586-018-0117-z
- Hashimoto, T., Inoue, A. K., Mawatari, K., et al. 2019, *PASJ*, 71, 71, doi: 10.1093/pasj/psz049
- Hebb, M. H., & Menzel, D. H. 1940, *ApJ*, 92, 408, doi: 10.1086/144230
- Heintz, K. E., Giménez-Arteaga, C., Fujimoto, S., et al. 2022, arXiv e-prints, arXiv:2212.06877. <https://arxiv.org/abs/2212.06877>
- Hirano, S., & Bromm, V. 2017, *MNRAS*, 470, 898, doi: 10.1093/mnras/stx1220
- Hirano, S., Hosokawa, T., Yoshida, N., & Kuiper, R. 2017, *Science*, 357, 1375, doi: 10.1126/science.aai9119
- Hirano, S., Hosokawa, T., Yoshida, N., et al. 2014, *ApJ*, 781, 60, doi: 10.1088/0004-637X/781/2/60
- Hirano, S., & Machida, M. N. 2022, *ApJ*, 935, L16, doi: 10.3847/2041-8213/ac85e0
- Hirano, S., Yoshida, N., Sakurai, Y., & Fujii, M. S. 2018, *ApJ*, 855, 17, doi: 10.3847/1538-4357/aaaaba
- Hirschmann, M., Charlot, S., Feltre, A., et al. 2017, *MNRAS*, 472, 2468, doi: 10.1093/mnras/stx2180
- . 2022, arXiv e-prints, arXiv:2212.02522. <https://arxiv.org/abs/2212.02522>
- Hopkins, P. F., Kereš, D., Oñorbe, J., et al. 2014, *MNRAS*, 445, 581, doi: 10.1093/mnras/stu1738
- Hopkins, P. F., Quataert, E., & Murray, N. 2011, *MNRAS*, 417, 950, doi: 10.1111/j.1365-2966.2011.19306.x
- Hosokawa, T., Omukai, K., Yoshida, N., & Yorke, H. W. 2011, *Science*, 334, 1250, doi: 10.1126/science.1207433
- Hummel, J. A., Stacy, A., & Bromm, V. 2016, *MNRAS*, 460, 2432, doi: 10.1093/mnras/stw1127
- Hummel, J. A., Stacy, A., Jeon, M., Oliveri, A., & Bromm, V. 2015, *MNRAS*, 453, 4136, doi: 10.1093/mnras/stv1902

- Inami, H., Algera, H. S. B., Schouws, S., et al. 2022, MNRAS, 515, 3126, doi: 10.1093/mnras/stac1779
- Inayoshi, K., & Omukai, K. 2012, MNRAS, 422, 2539, doi: 10.1111/j.1365-2966.2012.20812.x
- Inoue, A. K. 2011, MNRAS, 415, 2920, doi: 10.1111/j.1365-2966.2011.18906.x
- Inoue, A. K., Shimizu, I., Tamura, Y., et al. 2014, ApJ, 780, L18, doi: 10.1088/2041-8205/780/2/L18
- Inoue, A. K., Tamura, Y., Matsuo, H., et al. 2016, Science, 352, 1559, doi: 10.1126/science.aaf0714
- Inoue, S., & Yoshida, N. 2020, MNRAS, 491, L24, doi: 10.1093/mnras1/slz160
- Israel, F. P. 1988, A&A, 194, 24
- Iwamoto, K., Brachwitz, F., Nomoto, K., et al. 1999, ApJS, 125, 439, doi: 10.1086/313278
- Izotov, Y. I., Guseva, N. G., Fricke, K. J., & Henkel, C. 2019, A&A, 623, A40, doi: 10.1051/0004-6361/201834768
- Jiang, L., Kashikawa, N., Wang, S., et al. 2021, Nature Astronomy, 5, 256, doi: 10.1038/s41550-020-01275-y
- Jones, T., Sanders, R., Roberts-Borsani, G., et al. 2020, ApJ, 903, 150, doi: 10.3847/1538-4357/abb943
- Jungwiert, B., Combes, F., & Palouš, J. 2001, A&A, 376, 85, doi: 10.1051/0004-6361:20010966
- Kaasinen, M., van Marrewijk, J., Popping, G., et al. 2022, arXiv e-prints, arXiv:2210.03754. <https://arxiv.org/abs/2210.03754>
- Katz, H., Laporte, N., Ellis, R. S., Devriendt, J., & Slyz, A. 2019a, MNRAS, 484, 4054, doi: 10.1093/mnras/stz281
- Katz, H., Galligan, T. P., Kimm, T., et al. 2019b, MNRAS, 487, 5902, doi: 10.1093/mnras/stz1672
- Katz, H., Saxena, A., Cameron, A. J., et al. 2022, arXiv e-prints, arXiv:2207.13693. <https://arxiv.org/abs/2207.13693>
- Kennicutt, Robert C., J. 1998, ARA&A, 36, 189, doi: 10.1146/annurev.astro.36.1.189
- Killi, M., Watson, D., Fujimoto, S., et al. 2022, arXiv e-prints, arXiv:2211.01424. <https://arxiv.org/abs/2211.01424>
- Kimm, T., & Cen, R. 2014, ApJ, 788, 121, doi: 10.1088/0004-637X/788/2/121
- Kinugawa, T., Inayoshi, K., Hotokezaka, K., Nakauchi, D., & Nakamura, T. 2014, MNRAS, 442, 2963, doi: 10.1093/mnras/stu1022
- Kinugawa, T., Miyamoto, A., Kanda, N., & Nakamura, T. 2016, MNRAS, 456, 1093, doi: 10.1093/mnras/stv2624

- Klypin, A. A., Trujillo-Gomez, S., & Primack, J. 2011, *ApJ*, 740, 102, doi: 10.1088/0004-637X/740/2/102
- Kobayashi, C. 2004, *MNRAS*, 347, 740, doi: 10.1111/j.1365-2966.2004.07258.x
- Kohandel, M., Ferrara, A., Pallottini, A., et al. 2022, arXiv e-prints, arXiv:2212.02519. <https://arxiv.org/abs/2212.02519>
- Komatsu, E., Dunkley, J., Nolta, M. R., et al. 2009, *ApJS*, 180, 330, doi: 10.1088/0067-0049/180/2/330
- Kravtsov, A. V. 2003, *ApJ*, 590, L1, doi: 10.1086/376674
- Kravtsov, A. V., Klypin, A. A., & Khokhlov, A. M. 1997, *ApJS*, 111, 73, doi: 10.1086/313015
- Kroupa, P., Tout, C. A., & Gilmore, G. 1993, *MNRAS*, 262, 545, doi: 10.1093/mnras/262.3.545
- Kulkarni, M., Visbal, E., & Bryan, G. L. 2020, in *American Astronomical Society Meeting Abstracts*, Vol. 235, American Astronomical Society Meeting Abstracts #235, 153.07
- Lake, W., Naoz, S., Burkhart, B., et al. 2022, arXiv e-prints, arXiv:2208.05987. <https://arxiv.org/abs/2208.05987>
- Lamers, H. J. G. L. M., & Cassinelli, J. P. 1999, *Introduction to Stellar Winds*
- Langan, I., Ceverino, D., & Finlator, K. 2020, *MNRAS*, 494, 1988, doi: 10.1093/mnras/staa880
- Langeroodi, D., Hjorth, J., Chen, W., et al. 2022, arXiv e-prints, arXiv:2212.02491. <https://arxiv.org/abs/2212.02491>
- Laporte, N., Meyer, R. A., Ellis, R. S., et al. 2021, *MNRAS*, 505, 3336, doi: 10.1093/mnras/stab1239
- Laporte, N., Ellis, R. S., Boone, F., et al. 2017, *ApJ*, 837, L21, doi: 10.3847/2041-8213/aa62aa
- Larson, R. B. 1969, *MNRAS*, 145, 271, doi: 10.1093/mnras/145.3.271
- Latif, M. A., Khochfar, S., Schleicher, D., & Whalen, D. J. 2021, *MNRAS*, 508, 1756, doi: 10.1093/mnras/stab2708
- Latif, M. A., Schleicher, D. R. G., Bovino, S., Grassi, T., & Spaans, M. 2014, *ApJ*, 792, 78, doi: 10.1088/0004-637X/792/1/78
- Leethochawalit, N., Trenti, M., Santini, P., et al. 2022, arXiv e-prints, arXiv:2207.11135. <https://arxiv.org/abs/2207.11135>
- Leitherer, C., Schaerer, D., Goldader, J. D., et al. 1999, *ApJS*, 123, 3, doi: 10.1086/313233
- Long, H., Givans, J. J., & Hirata, C. M. 2022, *MNRAS*, 513, 117, doi: 10.1093/mnras/stac658
- Lovell, C. C., Vijayan, A. P., Thomas, P. A., et al. 2021, *MNRAS*, 500, 2127, doi: 10.1093/mnras/staa3360
- Ma, X., Hopkins, P. F., Faucher-Giguère, C.-A., et al. 2016, *MNRAS*, 456, 2140, doi: 10.1093/mnras/stv2659

- Madden, S. C., Rémy-Ruyer, A., Galametz, M., et al. 2013, *PASP*, 125, 600, doi: 10.1086/671138
- Maiolino, R., & Mannucci, F. 2019, *A&A Rev.*, 27, 3, doi: 10.1007/s00159-018-0112-2
- Maiolino, R., Nagao, T., Grazian, A., et al. 2008, *A&A*, 488, 463, doi: 10.1051/0004-6361:200809678
- Mandelker, N., Dekel, A., Ceverino, D., et al. 2017, *MNRAS*, 464, 635, doi: 10.1093/mnras/stw2358
- . 2014, *MNRAS*, 443, 3675, doi: 10.1093/mnras/stu1340
- Maoz, D., & Mannucci, F. 2012, *PASA*, 29, 447, doi: 10.1071/AS11052
- Marinacci, F., Vogelsberger, M., Pakmor, R., et al. 2018, *MNRAS*, 480, 5113, doi: 10.1093/mnras/sty2206
- Marques-Chaves, R., Schaerer, D., Álvarez-Márquez, J., et al. 2022, *MNRAS*, 517, 2972, doi: 10.1093/mnras/stac2893
- McDowell, M. R. C. 1961, *The Observatory*, 81, 240
- McGaugh, S. S. 1991, *ApJ*, 380, 140, doi: 10.1086/170569
- McQuinn, M., & O’Leary, R. M. 2012, *ApJ*, 760, 3, doi: 10.1088/0004-637X/760/1/3
- Moriwaki, K., Yoshida, N., Shimizu, I., et al. 2018, *MNRAS*, 481, L84, doi: 10.1093/mnras1/sly167
- Moustakas, J., Kennicutt, Robert C., J., & Tremonti, C. A. 2006, *ApJ*, 642, 775, doi: 10.1086/500964
- Murray, N., Quataert, E., & Thompson, T. A. 2010, *ApJ*, 709, 191, doi: 10.1088/0004-637X/709/1/191
- Nagakura, T., Hosokawa, T., & Omukai, K. 2009, *MNRAS*, 399, 2183, doi: 10.1111/j.1365-2966.2009.15423.x
- Nagao, T., Maiolino, R., & Marconi, A. 2006, *A&A*, 459, 85, doi: 10.1051/0004-6361:20065216
- Naidu, R. P., Oesch, P. A., van Dokkum, P., et al. 2022, arXiv e-prints, arXiv:2207.09434. <https://arxiv.org/abs/2207.09434>
- Naiman, J. P., Pillepich, A., Springel, V., et al. 2018, *MNRAS*, 477, 1206, doi: 10.1093/mnras/sty618
- Nakajima, K., Ouchi, M., Xu, Y., et al. 2022, *ApJS*, 262, 3, doi: 10.3847/1538-4365/ac7710
- Naoz, S., & Barkana, R. 2005, *MNRAS*, 362, 1047, doi: 10.1111/j.1365-2966.2005.09385.x
- Naoz, S., Barkana, R., & Mesinger, A. 2009, *MNRAS*, 399, 369, doi: 10.1111/j.1365-2966.2009.15282.x
- Naoz, S., & Narayan, R. 2014, *ApJ*, 791, L8, doi: 10.1088/2041-8205/791/1/L8

-
- Naoz, S., Yoshida, N., & Gnedin, N. Y. 2012, *ApJ*, 747, 128, doi: 10.1088/0004-637X/747/2/128
- . 2013, *ApJ*, 763, 27, doi: 10.1088/0004-637X/763/1/27
- Nelson, D., Pillepich, A., Springel, V., et al. 2018, *MNRAS*, 475, 624, doi: 10.1093/mnras/stx3040
- Noel, I., Zhu, H., & Gnedin, N. 2022, arXiv e-prints, arXiv:2210.16750. <https://arxiv.org/abs/2210.16750>
- Nomoto, K., Tominaga, N., Umeda, H., Kobayashi, C., & Maeda, K. 2006, *Nucl. Phys. A*, 777, 424, doi: 10.1016/j.nuclphysa.2006.05.008
- Oesch, P. A., Brammer, G., van Dokkum, P. G., et al. 2016, *ApJ*, 819, 129, doi: 10.3847/0004-637X/819/2/129
- Olsen, K., Greve, T. R., Narayanan, D., et al. 2017, *ApJ*, 846, 105, doi: 10.3847/1538-4357/aa86b4
- Omukai, K. 2000, *ApJ*, 534, 809, doi: 10.1086/308776
- Omukai, K., & Nishi, R. 1998, *ApJ*, 508, 141, doi: 10.1086/306395
- Omukai, K., & Palla, F. 2001, *ApJ*, 561, L55, doi: 10.1086/324410
- . 2003, *ApJ*, 589, 677, doi: 10.1086/374810
- O’Shea, B. W., & Norman, M. L. 2008, *ApJ*, 673, 14, doi: 10.1086/524006
- Osterbrock, D., & Flather, E. 1959, *ApJ*, 129, 26, doi: 10.1086/146592
- Osterbrock, D. E., & Ferland, G. J. 2006, *Astrophysics of gaseous nebulae and active galactic nuclei*
- Ostriker, E. C., & Shetty, R. 2011, *ApJ*, 731, 41, doi: 10.1088/0004-637X/731/1/41
- Ota, K., Walter, F., Ohta, K., et al. 2014, *ApJ*, 792, 34, doi: 10.1088/0004-637X/792/1/34
- Ouchi, M., Ellis, R., Ono, Y., et al. 2013, *ApJ*, 778, 102, doi: 10.1088/0004-637X/778/2/102
- Paardekooper, J.-P., Khochfar, S., & Dalla Vecchia, C. 2015, *MNRAS*, 451, 2544, doi: 10.1093/mnras/stv1114
- Pagel, B. E. J., Edmunds, M. G., Blackwell, D. E., Chun, M. S., & Smith, G. 1979, *MNRAS*, 189, 95, doi: 10.1093/mnras/189.1.95
- Palla, F., Salpeter, E. E., & Stahler, S. W. 1983, *ApJ*, 271, 632, doi: 10.1086/161231
- Pallottini, A., Ferrara, A., Bovino, S., et al. 2017a, *MNRAS*, 471, 4128, doi: 10.1093/mnras/stx1792
- Pallottini, A., Ferrara, A., Gallerani, S., et al. 2017b, *MNRAS*, 465, 2540, doi: 10.1093/mnras/stw2847
- . 2022, *MNRAS*, 513, 5621, doi: 10.1093/mnras/stac1281

- Panuzzo, P., Bressan, A., Granato, G. L., Silva, L., & Danese, L. 2003, *A&A*, 409, 99, doi: 10.1051/0004-6361:20031094
- Park, H., Shapiro, P. R., Komatsu, E., et al. 2013, *ApJ*, 769, 93, doi: 10.1088/0004-637X/769/2/93
- Park, J., Ricotti, M., & Sugimura, K. 2021, *MNRAS*, 508, 6193, doi: 10.1093/mnras/stab3000
- Pascale, M., Frye, B. L., Diego, J., et al. 2022, *ApJ*, 938, L6, doi: 10.3847/2041-8213/ac9316
- Peebles, P. J. E., & Dicke, R. H. 1968, *ApJ*, 154, 891, doi: 10.1086/149811
- Pillepich, A., Nelson, D., Hernquist, L., et al. 2018, *MNRAS*, 475, 648, doi: 10.1093/mnras/stx3112
- Popa, C., Naoz, S., Marinacci, F., & Vogelsberger, M. 2016, *MNRAS*, 460, 1625, doi: 10.1093/mnras/stw1045
- Popping, G. 2022, arXiv e-prints, arXiv:2208.13072. <https://arxiv.org/abs/2208.13072>
- Press, W. H., & Schechter, P. 1974, *ApJ*, 187, 425, doi: 10.1086/152650
- Press, W. H., & Vishniac, E. T. 1980, *ApJ*, 236, 323, doi: 10.1086/157749
- Ripamonti, E., Haardt, F., Ferrara, A., & Colpi, M. 2002, *MNRAS*, 334, 401, doi: 10.1046/j.1365-8711.2002.05516.x
- Roberts-Borsani, G., Treu, T., Chen, W., et al. 2022, arXiv e-prints, arXiv:2210.15639. <https://arxiv.org/abs/2210.15639>
- Robertson, B. E., Furlanetto, S. R., Schneider, E., et al. 2013, *ApJ*, 768, 71, doi: 10.1088/0004-637X/768/1/71
- Sanders, R. L., Shapley, A. E., Jones, T., et al. 2021, *ApJ*, 914, 19, doi: 10.3847/1538-4357/abf4c1
- Saslaw, W. C., & Zipoy, D. 1967, *Nature*, 216, 976, doi: 10.1038/216976a0
- Schaerer, D. 2002, *A&A*, 382, 28, doi: 10.1051/0004-6361:20011619
- Schaerer, D., Boone, F., Zamojski, M., et al. 2015, *A&A*, 574, A19, doi: 10.1051/0004-6361/201424649
- Schaerer, D., Marques-Chaves, R., Oesch, P., et al. 2022, arXiv e-prints, arXiv:2207.10034. <https://arxiv.org/abs/2207.10034>
- Schauer, A. T. P., Bromm, V., Boylan-Kolchin, M., Glover, S. C. O., & Klessen, R. S. 2021a, *ApJ*, 922, 193, doi: 10.3847/1538-4357/ac27aa
- Schauer, A. T. P., Glover, S. C. O., Klessen, R. S., & Ceverino, D. 2019, *MNRAS*, 484, 3510, doi: 10.1093/mnras/stz013
- Schauer, A. T. P., Glover, S. C. O., Klessen, R. S., & Clark, P. 2021b, *MNRAS*, 507, 1775, doi: 10.1093/mnras/stab1953

- Schouws, S., Stefanon, M., Bouwens, R., et al. 2022, *ApJ*, 928, 31, doi: 10.3847/1538-4357/ac4605
- Seaton, M. J. 1954, *MNRAS*, 114, 154, doi: 10.1093/mnras/114.2.154
- . 1960, *Reports on Progress in Physics*, 23, 313, doi: 10.1088/0034-4885/23/1/306
- Seljak, U., & Zaldarriaga, M. 1996, *ApJ*, 469, 437, doi: 10.1086/177793
- Sharda, P., Federrath, C., Krumholz, M. R., & Schleicher, D. R. G. 2021, *MNRAS*, 503, 2014, doi: 10.1093/mnras/stab531
- Shimizu, I., Inoue, A. K., Okamoto, T., & Yoshida, N. 2016, *MNRAS*, 461, 3563, doi: 10.1093/mnras/stw1423
- Sluder, A., Ritter, J. S., Safrank-Shrader, C., Milosavljević, M., & Bromm, V. 2016, *MNRAS*, 456, 1410, doi: 10.1093/mnras/stv2587
- Smith, B. D., Bryan, G. L., Glover, S. C. O., et al. 2017, *MNRAS*, 466, 2217, doi: 10.1093/mnras/stw3291
- Speagle, J. S., Steinhardt, C. L., Capak, P. L., & Silverman, J. D. 2014, *ApJS*, 214, 15, doi: 10.1088/0067-0049/214/2/15
- Springel, V. 2010, *MNRAS*, 401, 791, doi: 10.1111/j.1365-2966.2009.15715.x
- Springel, V., Pakmor, R., Pillepich, A., et al. 2018, *MNRAS*, 475, 676, doi: 10.1093/mnras/stx3304
- Stanway, E. R., & Eldridge, J. J. 2018, *MNRAS*, 479, 75, doi: 10.1093/mnras/sty1353
- Steidel, C. C., Giavalisco, M., Pettini, M., Dickinson, M., & Adelberger, K. L. 1996, *ApJ*, 462, L17, doi: 10.1086/310029
- Steidel, C. C., Pettini, M., & Hamilton, D. 1995, *AJ*, 110, 2519, doi: 10.1086/117709
- Sugahara, Y., Inoue, A. K., Fudamoto, Y., et al. 2022, *ApJ*, 935, 119, doi: 10.3847/1538-4357/ac7fed
- Sugimura, K., Omukai, K., & Inoue, A. K. 2014, *MNRAS*, 445, 544, doi: 10.1093/mnras/stu1778
- Sun, F., Egami, E., Pirzkal, N., et al. 2022, arXiv e-prints, arXiv:2209.03374. <https://arxiv.org/abs/2209.03374>
- Sunyaev, R. A., & Zeldovich, Y. B. 1970, *Ap&SS*, 7, 3, doi: 10.1007/BF00653471
- Susa, H. 2007, *ApJ*, 659, 908, doi: 10.1086/512670
- Susa, H., Hasegawa, K., & Tominaga, N. 2014, *ApJ*, 792, 32, doi: 10.1088/0004-637X/792/1/32
- Tacchella, S., Finkelstein, S. L., Bagley, M., et al. 2022, *ApJ*, 927, 170, doi: 10.3847/1538-4357/ac4cad
- Tadaki, K.-i., Tsujita, A., Tamura, Y., et al. 2022, *PASJ*, 74, L9, doi: 10.1093/pasj/psac018

- Tamura, Y., Mawatari, K., Hashimoto, T., et al. 2019, *ApJ*, 874, 27, doi: 10.3847/1538-4357/ab0374
- Tanaka, T. L., & Li, M. 2014, *MNRAS*, 439, 1092, doi: 10.1093/mnras/stu042
- Tegmark, M., Silk, J., Rees, M. J., et al. 1997, *ApJ*, 474, 1, doi: 10.1086/303434
- Thielemann, F. K., Nomoto, K., & Yokoi, K. 1986, *A&A*, 158, 17
- Topping, M. W., Stark, D. P., Endsley, R., et al. 2022, *MNRAS*, 516, 975, doi: 10.1093/mnras/stac2291
- Torrey, P., Vogelsberger, M., Marinacci, F., et al. 2019, *MNRAS*, 484, 5587, doi: 10.1093/mnras/stz243
- Trump, J. R., Arrabal Haro, P., Simons, R. C., et al. 2022, arXiv e-prints, arXiv:2207.12388. <https://arxiv.org/abs/2207.12388>
- Trussler, J. A. A., Adams, N. J., Conselice, C. J., et al. 2022, arXiv e-prints, arXiv:2207.14265. <https://arxiv.org/abs/2207.14265>
- Tseliakhovich, D., Barkana, R., & Hirata, C. M. 2011, *MNRAS*, 418, 906, doi: 10.1111/j.1365-2966.2011.19541.x
- Tseliakhovich, D., & Hirata, C. 2010, *Phys. Rev. D*, 82, 083520, doi: 10.1103/PhysRevD.82.083520
- Vallini, L., Gallerani, S., Ferrara, A., & Baek, S. 2013, *MNRAS*, 433, 1567, doi: 10.1093/mnras/stt828
- Vallini, L., Gallerani, S., Ferrara, A., Pallottini, A., & Yue, B. 2015, *ApJ*, 813, 36, doi: 10.1088/0004-637X/813/1/36
- Vanzella, E., de Barros, S., Vasei, K., et al. 2016, *ApJ*, 825, 41, doi: 10.3847/0004-637X/825/1/41
- Vanzella, E., Calura, F., Meneghetti, M., et al. 2017, *MNRAS*, 467, 4304, doi: 10.1093/mnras/stx351
- Vanzella, E., Castellano, M., Bergamini, P., et al. 2022a, *ApJ*, 940, L53, doi: 10.3847/2041-8213/ac8c2d
- Vanzella, E., Claeysens, A., Welch, B., et al. 2022b, arXiv e-prints, arXiv:2211.09839. <https://arxiv.org/abs/2211.09839>
- Visbal, E., Barkana, R., Fialkov, A., Tseliakhovich, D., & Hirata, C. M. 2012, *Nature*, 487, 70, doi: 10.1038/nature11177
- Williams, H., Kelly, P. L., Chen, W., et al. 2022, arXiv e-prints, arXiv:2210.15699. <https://arxiv.org/abs/2210.15699>
- Wise, J. H., Demchenko, V. G., Halicek, M. T., et al. 2014, *MNRAS*, 442, 2560, doi: 10.1093/mnras/stu979
- Witstok, J., Smit, R., Maiolino, R., et al. 2022, *MNRAS*, doi: 10.1093/mnras/stac1905

- Wolfire, M. G., Hollenbach, D., McKee, C. F., Tielens, A. G. G. M., & Bakes, E. L. O. 1995, *ApJ*, 443, 152, doi: 10.1086/175510
- Wong, Y. H. V., Wang, P., Hashimoto, T., et al. 2022, *ApJ*, 929, 161, doi: 10.3847/1538-4357/ac5cc7
- Woosley, S. E., & Weaver, T. A. 1995, *ApJS*, 101, 181, doi: 10.1086/192237
- Xiao, L., Stanway, E. R., & Eldridge, J. J. 2018, *MNRAS*, 477, 904, doi: 10.1093/mnras/sty646
- Xu, H., Wise, J. H., Norman, M. L., Ahn, K., & O'Shea, B. W. 2016, *ApJ*, 833, 84, doi: 10.3847/1538-4357/833/1/84
- Yajima, H., Choi, J.-H., & Nagamine, K. 2011, *MNRAS*, 412, 411, doi: 10.1111/j.1365-2966.2010.17920.x
- Yang, S., & Lidz, A. 2020, *MNRAS*, 499, 3417, doi: 10.1093/mnras/staa3000
- Yoon, I., Carilli, C. L., Fujimoto, S., et al. 2022, arXiv e-prints, arXiv:2210.08413. <https://arxiv.org/abs/2210.08413>
- Yoshida, N., Abel, T., Hernquist, L., & Sugiyama, N. 2003, *ApJ*, 592, 645, doi: 10.1086/375810
- Yoshida, N., Hosokawa, T., & Omukai, K. 2012, *Progress of Theoretical and Experimental Physics*, 2012, 01A305, doi: 10.1093/ptep/pts022
- Yoshida, N., Omukai, K., & Hernquist, L. 2008, *Science*, 321, 669, doi: 10.1126/science.1160259
- Yoshida, N., Omukai, K., Hernquist, L., & Abel, T. 2006, *ApJ*, 652, 6, doi: 10.1086/507978